

New Mexico Bureau  
of  
Geology and Mineral Resources

**COUPLING A FAULT-SCARP DIFFUSION MODEL WITH  
COSMOGENIC  $^{36}\text{Cl}$ : RUPTURE CHRONOLOGY OF THE SOCORRO  
CANYON FAULT, NEW MEXICO**

by

JOHN PETE AYARBE

Independent Study

Submitted in Partial Fulfillment of the Requirements for the Degree of

Masters of Science in Hydrology

New Mexico Institute of Mining and Technology

Socorro, New Mexico, August 2000

## Table of Contents:

ABSTRACT .....	V
<b>1.0 INTRODUCTION .....</b>	<b>1</b>
1.1 MORPHOLOGIC DATING.....	1
1.2 PROJECT OBJECTIVE .....	6
1.3 COSMOGENIC NUCLIDES.....	7
1.4 COSMOGENIC <sup>36</sup> CL SYSTEMATICS AND MODELED DISTRIBUTIONS.....	13
<b>2.0 CLARA.....</b>	<b>15</b>
2.1 MODEL (CLARA) OVERVIEW.....	15
2.2 MORPHOLOGIC DATING (FAULT-SCARP MORPHOLOGY).....	17
2.3 COSMOGENIC <sup>36</sup> CL PRODUCTION.....	20
2.3.1 <i>High-Energy Neutron (Spallation) Production</i> .....	21
2.3.2 <i>Low-Energy Neutron Capture</i> .....	30
2.4 COSMOGENIC <sup>36</sup> CL ACCUMULATION AND REDISTRIBUTION .....	38
<b>3.0 SOCORRO CANYON FAULT .....</b>	<b>41</b>
<b>4.0 METHODS AND MATERIALS .....</b>	<b>49</b>
4.1 CHLORINE-36 AND CHEMICAL ANALYSES.....	49
4.2 FAULT SCARP PROFILE .....	51
4.3 MODEL DOMAIN.....	51
<b>5.0 RESULTS AND MODELING.....</b>	<b>52</b>
5.1 ANALYTICAL RESULTS .....	52
5.2 MODELING.....	53
5.2.1 <i>Analysis of the Control Profile (Sample Inheritance and Terrace Age)</i> .....	55
5.2.2 <i>Analysis of the Footwall and Hanging Wall Profiles (Rupture History)</i> .....	57
<b>6.0 DISCUSSION.....</b>	<b>63</b>
<b>BIBLIOGRAPHY .....</b>	<b>68</b>

## Table of Figures:

Figure 1.1. Fault-Scarp Diffusion Profiles .....	3
Figure 1.2. Range of Geomorphic Diffusivities .....	3
Figure 1.3. Cosmogenic nuclide production rates as a function of elevation and latitude .....	10
Figure 1.4. Cosmogenic $^{36}\text{Cl}$ as function of depth and percentage of epithermal and thermal neutron production.....	10
Figure 1.5. Change in $^3\text{He}$ production rates as a function of time.....	12
Figure 1.6. Cosmogenic $^{36}\text{Cl}$ as a function of erosion rate.....	12
Figure 1.7. Cosmogenic $^{36}\text{Cl}$ production mechanisms .....	14
Figure 1.8. Hypothetical cosmogenic $^{36}\text{Cl}$ depth profiles .....	14
Figure 2.1. CLARA flowchart .....	16
Figure 2.2. Numerical Solution to the Diffusion Equation .....	22
Figure 2.3. Spherical Coordinate System.....	25
Figure 2.4. Calibration of the Numerical Solution for the Cosmic-Radiation Flux .....	27
Figure 2.5. Intercept of a Cosmic Ray with the Footwall Shortly After a Rupture .....	29
Figure 2.6. Five-Point Star Used in Finite Difference.....	34
Figure 2.7. Verification of the Low-Energy Flux Numerical Solutions.....	39
Figure 3.1. Field Site.....	42
Figure 3.2. Photo Showing the Geomorphic Surfaces .....	42
Figure 3.3. Simplified Trench Log near Fault Plane .....	45
Figure 3.4. Soil Trench Log near Fault Plane .....	46
Figure 3.5. Picture of Trench .....	47
Figure 3.6. Picture of the Graben .....	47
Figure 5.1. Cosmogenic $^{36}\text{Cl}$ of the Three Profiles .....	54
Figure 5.2. Regression Analysis of the Control Profile.....	54
Figure 5.3. Observed versus Modeled for the Control Profile .....	60
Figure 5.4. Contour Plot of the total Chi-squared-error as a function of the first and second ruptures.....	60
Figure 5.5. Observed versus Modeled for the Footwall and Hanging Wall Profile .....	62
Figure 5.6. Observed versus Modeled Socorro Canyon Fault Scarp Profiles .....	62
Figure 6.1. Defines the Parameters Used to Calculate the Dimensionless Width .....	67
Figure 6.2. Plot Showing the Analysis for Single Offset Scarps.....	67

## Table of Appendices:

Appendix 1.1. CLARA README FILE .....	A2
Appendix 2.1. Analytical Solution to the Diffusion Equation for Fault-Scarp Morphology.....	A4
Appendix 2.2. Analytical Solution for Spallation Production.....	A5
Appendix 2.3. Analytical Solution for the Epithermal Neutron Flux.....	A6
Appendix 2.4. Analytical Solution for the Thermal Neutron Flux.....	A7
Appendix 3.1. Trigonometric Relationships .....	A8
Appendix 3.2. Validation of CLARA's Numerical Solution.....	A12
Appendix 4.1. Influence of Boundary Locations on the Accuracy of the Fault-Scarp Diffusion Numerical Solution .....	A13
Appendix 4.2. Sensitivity to $\Delta\phi$ and $\Delta\theta$ .....	A14
Appendix 4.3. Source Term for High-Energy Neutrons .....	A17
Appendix 4.4. Upper and Lower Boundary Locations for the Numerical Low-Energy Flux Solutions...	A20
Appendix 5.1. Grain Size Log of Entire Trench .....	A22
Appendix 5.2. Grain Size Log near Fault Plane.....	A23
Appendix 5.3. Legend for the Grain Size Logs of Appendices 5.2 and 5.3 .....	A24
Appendix 6.1. Protocol for Sample Collection, Preparation, and Grinding (Zreda, 1994) .....	A26
Appendix 6.2. Protocol for Sample Leaching .....	A28
Appendix 6.3. Protocol for Extracting Cl for $^{36}\text{Cl}/\text{Cl}$ Analysis (Lui, 1994; and Zreda, 1994).....	A29
Appendix 6.4. Estimation of the Expected $^{36}\text{Cl}/\text{Cl}$ .....	A32
Appendix 6.5. Estimation of Chloride Content with a Chloride Electrode (Aruscavage and Campbell, 1983; and Elsheimer, 1987) .....	A33
Appendix 7.1. Tables of Sample Chemistry.....	A35
Appendix 8.1. Cosmogenic $^{36}\text{Cl}$ Accumulation and Production Parameters.....	A43
Appendix 9.1. Reduced Chi-Squared-Error Calculated from the Individual Profiles and Both Profiles ..	A45

## Abstract

Determining rupture chronologies is central to paleoseismology and in the assessment of earthquake hazards. In arid environments, the low abundance of organic carbon often prevents  $^{14}\text{C}$  dating of ruptures; therefore, in these regions, fault-scarp diffusion modeling has been applied to date ruptures based on the present day morphology of fault scarps. A drawback to this technique is that the ‘geomorphic diffusivity’, a proportional constant in the diffusion equation, is generally poorly constrained and must be estimated. The geomorphic diffusivity of unconsolidated material can vary over two orders of magnitude; thus, if the geomorphic diffusivity is unknown, a large amount of uncertainty is introduced into the calculated age of a scarp. By constraining the value of the geomorphic diffusivity with a cosmogenic nuclide, we can obtain better age estimates of fault scarps, and thus more accurate rupture chronologies.

We collected samples along three vertical transects accessed from a backhoe trench oriented perpendicular to the Socorro Canyon fault scarp, located in central New Mexico. We analyzed the  $^{36}\text{Cl}/\text{Cl}$  ratio and the whole rock chemistry in numerous small clasts retained from each sample. Two of the vertical transects were located  $\sim 1.5$  m on either side of the fault plane. These two profiles were used to calibrate the model CLARA, which couples equations describing the accumulation and production of cosmogenic  $^{36}\text{Cl}$  to a fault-scarp diffusion model. By calibrating CLARA to the two vertical cosmogenic  $^{36}\text{Cl}$  and fault-scarp profiles, we determined a rupture chronology for the Socorro Canyon fault scarp. The ages of the first and second ruptures are  $92^{+16}_{-13}$  ka and  $28^{+18}_{-23}$  ka, respectively. We sampled the third profile  $\sim 27$  m west of the fault plane on the footwall.

We used this profile and the model CHLOE to determine the age of the displaced terrace. The terrace age is  $122\pm 18$  ka.

CLARA links the accumulation and production of a cosmogenic nuclide to a mathematical model describing landscape evolution. Result from this study show that CLARA can be used to reconstructed rupture histories. Due to multiple offsets, we needed numerous samples to determine the rupture history of the Socorro Canyon fault scarp. However, for fault scarps produced from single offsets, the number of samples can be greatly reduced, making this a feasible approach for assessing regional tectonics from single rupture scarps.

# 1.0 Introduction

This thesis describes the development and application of a numerical model that provides the absolute ages of ruptures of a fault scarp in loosely consolidated material. The model couples the production and accumulation of cosmogenic  $^{36}\text{Cl}$  to a diffusion model for fault-scarp morphology. CLARA serves as the name of the model and is an acronym for Chlorine-36 Accumulation and Rupture Ages. Although CLARA does not yield the date and hour of the next major earthquake, it may provide insight to the frequency of prehistoric earthquakes. This information can be useful to those interested in assessing regional earthquake activity, such as paleoseismologists and structural engineers.

## 1.1 *Morphologic Dating*

Fault scarps in Quaternary sediments are a surficial expression of faulting and contain a record of paleo-faulting events. Morphologic dating of degraded fault scarps can assist in the development of earthquake chronologies (Nash, 1980; Colman and Watson, 1983), which can enhance our understanding of regional tectonics. Morphologic dating uses a diffusion equation to model the evolution of a fault scarp and has been referred to as diffusion modeling of fault-scarp morphology in addition to morphologic dating. Since its inception, morphologic dating has been applied to the dating of fault and terrace scarps in arid and semiarid environments (Nash, 1984; Enzel et al., 1994; Hanks, 1998). Geologists have applied morphologic dating in these environments due to the poor preservation of organic matter for  $^{14}\text{C}$  dating and because it is rapid and inexpensive. In an excellent review of morphologic dating from its inception, Hanks (1998) discusses the mathematics associated with morphologic dating as well as its application.

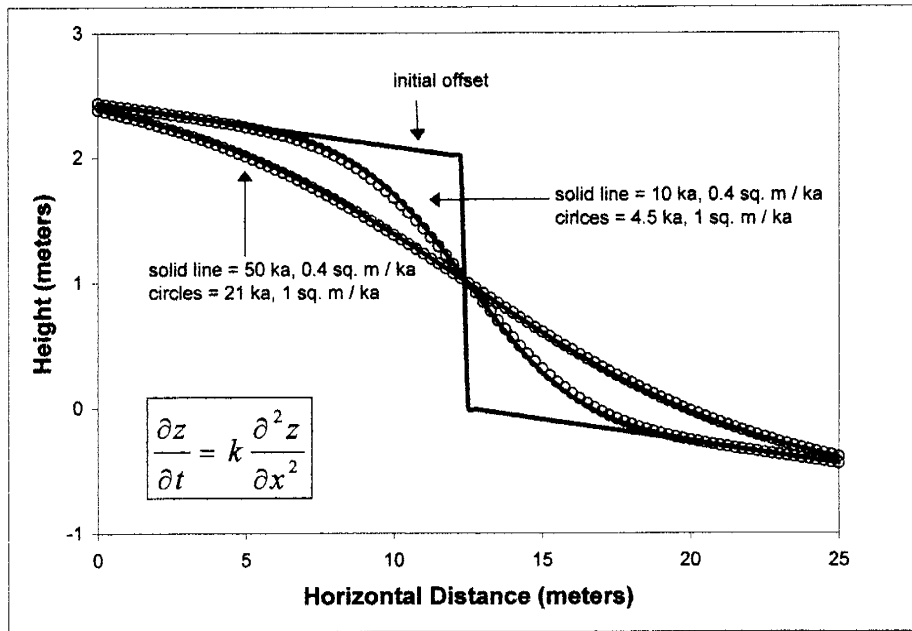
Wallace (1977) documented the geomorphic characteristics associated with fault scarps in unconsolidated sediments and proposed the use of these characteristics to date fault displacements. He noted that the slope of younger scarps was steeper than the slope of older scarps and that younger scarps were more angular than older scarps, all else being equal (i.e., scarp height and properties of the geologic material). Bucknam and Anderson (1979) expanded on this work in a study in western Utah with a more quantitative analysis for scarp age and morphology. This study provided relative ages for scarps in western Utah, but failed to yield a universal technique for the absolute dating of scarps. By applying a diffusion equation (Equation 1) to fault-scarp degradation, Nash (1980) pioneered morphologic dating, a simple and inexpensive method for dating earthquakes based on the present day morphology of a fault scarp. Nash's approach provides absolute ages, when the proportionality constant ( $K$ ) is known, and can be applied to any normal fault scarp in unconsolidated sediment. The technique involves surveying a profile of the scarp, perpendicular to its strike, and matching the observed profile to one generated from a solution to Equation 1.

$$\frac{\partial^2 z}{\partial x^2} = K \frac{\partial z}{\partial t} \quad (1)$$

In Equation 1,  $z$  is elevation,  $t$  is time,  $K$  is a proportionality constant termed the 'geomorphic diffusivity', and  $x$  is the horizontal coordinate perpendicular to the strike of the scarp. This model, Equation 1, states that the rate of change in elevation at a point along the scarp is proportional to the curvature of the scarp at that point. Assumptions associated with Equation 1 are (i) the rate of movement of material is proportional to the slope of the scarp, (ii) the fault trace is straight in plan view, and (iii)  $K$  is neither a function of time nor scarp height.

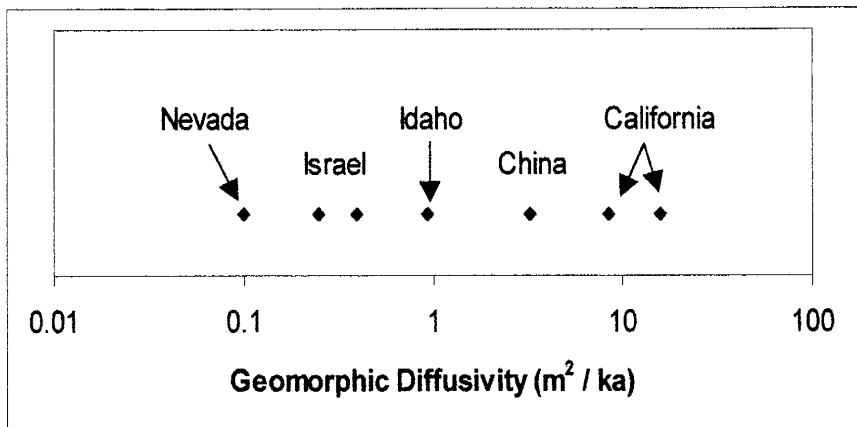
Figure 1.1 shows scarp profiles generated from a solution to Equation 1. The profiles generated from the diffusion equation concur with the observations of Wallace (1977). Given





**Figure 1.1.** Scarp profiles showing a rounding and reduction of scarp slope with increasing age. The figure also illustrates the non-uniqueness associated with the diffusion equation. Different combinations of  $K$  and age generate similar scarp profiles.

**Figure 1.2.** Data from Hanks (1998) demonstrates the range of variability in  $K$ .



the same geomorphic diffusivity and initial offset, the slopes of younger scarps are steeper than the slopes of older scarps, and younger scarps are more angular than older scarps. The figure also illustrates the non-uniqueness associated with morphologic dating. Different combinations of the rupture age and geomorphic diffusivity can yield identical fault-scarp profiles.

Morphologic dating is applicable to transport-limited scarps, which produce more loosened material than transport processes are capable of removing (Nash, 1986). The diffusion equation, Equation 1, describes the transport of alluvial material after the scarp has attained the angle of repose of alluvial material and transport mechanisms such as soil creep dominate (Nash, 1980; Nash, 1984). The diffusion equation does not describe the initial spalling and mass movement of alluvial material that occurs shortly after an offset. The angle of repose of alluvial material is  $\sim 30^\circ$ , and the time for the scarp to reach this angle is geologically short ( $<10$ - $100$  years) (Wallace, 1977). Because the time to obtain the angle of repose is short, modeling fault-scarp degradation with a diffusion equation will introduce little error into the calculated age of older scarps. For young scarps, non-diffusive transport processes can still be influencing or apparent in the scarp profile, and, therefore, the error may be much larger. By incorporating the angle of repose of alluvial material into the initial condition to Equation 1, Hanks and Andrew (1989) have demonstrated that the initial scarp angle does not significantly influence the morphology of older scarps. On the other hand, the regional slope (commonly referred to as the far-field slope in morphologic dating) of the displaced alluvial fan or terrace tread does affect the morphology of a scarp throughout its evolution (Hanks and Andrews, 1989).

Since 1980, many publications have expanded on and reviewed the concepts associated with morphologic dating. For example, several publications have enhanced the flexibility of morphologic dating by contributing to the mathematics of fault-scarp diffusion. Martin and

Church (1997) modified the diffusion coefficient (i.e., geomorphic diffusivity) so that fault-scarp diffusion analysis would accommodate episodic mass movements. Andrews and Buchnam (1987) introduced non-linear transport laws and applied these laws to fit synthetic scarp profiles to the Bonneville and Lahanton data. Andrews and Hanks (1985) applied inverse solutions to determine the age of scarps. In addition to the contributions made to the mathematics of fault-scarp diffusion, other publications have reviewed the application of morphologic dating to fault-scarp degradation. For example, Avouac (1993) evaluated the errors associated with morphologic dating. He attributed the errors to the uncertainty associated with the regional slope and modification of the scarp slope by three-dimensional geomorphic processes not accounted for in Equation 1. Pierce and Colman (1986) explored the influence of aspect (microclimate) and scarp height on the geomorphic diffusivity. Enzel et al. (1994) compared morphologic dating to other age-dating techniques. Their morphologic age estimates were in agreement with the other age-dating techniques (e.g. optical stimulated luminescence). They used morphologic dating in their tectonic analysis of the southern Arava, Israel. Recently, Niviere et al. (1998) applied morphologic dating to slowly evolving scarps in a temperate environment. Before this work, the focus of morphologic dating had been arid and semiarid environments.

Although researchers have made significant advances in morphologic dating over the past 30 years, the uncertainty associated with the geomorphic diffusivity is still the primary limitation of fault-scarp diffusion analysis. If both the age and geomorphic diffusivity are unknown, fault scarp diffusion analysis yields a morphologic age due to the non-uniqueness associated with Equation 1 (Figure 1.1). Morphologic ages are the product of the geomorphic diffusivity and scarp age. Grouping scarps in a region according to their morphologic ages is a relative age-dating technique, which fails to provide the absolute dates of ruptures. Figure 1.2 is a

compilation of geomorphic diffusivities from fault-scarps around the world. The figure shows that the geomorphic diffusivity can vary by two orders of magnitude. Therefore, if the geomorphic diffusivity cannot be accurately determined, a large amount of uncertainty is introduced into the calculated age of a scarp. By constraining the value of the geomorphic diffusivity, we can obtain better age estimates.

Additionally, for multiple rupture scarps the problem of non-uniqueness is further complicated by the uncertainty associated with each rupture age. Although numerical solutions to Equation 1 allow multiple ruptures to be included, the numerous unknowns (i.e., geomorphic diffusivity and each rupture) preclude the use of fault-scarp diffusion modeling in determining rupture ages.

## **1.2 *Project Objective***

The objective of this study is to provide a method for obtaining rupture chronologies of fault scarps by constraining the value of the geomorphic diffusivity with a cosmogenic nuclide. To meet this objective, we developed a model (CLARA) that couples fault-scarp diffusion to cosmogenic  $^{36}\text{Cl}$  accumulation. By calibrating CLARA to cosmogenic  $^{36}\text{Cl}$  measurements of samples from a fault scarp, the geomorphic diffusivity can be constrained and the timing of ruptures determined. The coupling of fault-scarp diffusion to the accumulation of a cosmogenic nuclide provides a new means for determining rupture chronologies for fault scarps in unconsolidated material. To test the feasibility of the approach, we use CLARA to reconstruct the rupture history of a portion of the Socorro Canyon fault scarp.

### 1.3 *Cosmogenic Nuclides*

Cosmogenic nuclides, such as  $^{36}\text{Cl}$ , are rare nuclides formed by the action of cosmic radiation in the upper few meters of geologic material at the land surface (Cerling and Craig, 1994; Gosse and Phillips, in press). Nuclear interactions between the atoms of the geologic material and cosmic ray particles produce cosmogenic nuclides. Because the accumulation of a cosmogenic nuclide records the period that geologic material has been exposed to cosmogenic radiation, they are applicable in geochronological studies (Phillips et al., 1986). The buildup of a cosmogenic nuclide is proportional to the intensity of the cosmic-ray flux and the concentration of target nuclides in minerals at the surface of the earth (Zreda et al., 1991). The intensity of the cosmic-ray flux varies temporally and spatially (Lal, 1991; Cerling and Craig, 1994). After separation of a cosmogenic nuclide from the geologic material, accelerator mass spectrometry (AMS) is commonly employed to measure the concentration of the cosmogenic nuclide (Elmore and Phillips, 1987). This concentration can then be used to assess the exposure history of the sample.

Cerling and Craig (1994), Zreda and Phillips (1998), and Gosse and Phillips (in press) are reviews describing the fundamentals of cosmogenic nuclides, the mathematical models that characterize the production and accumulation of cosmogenic nuclides, and the application of these nuclides to geochronological studies.

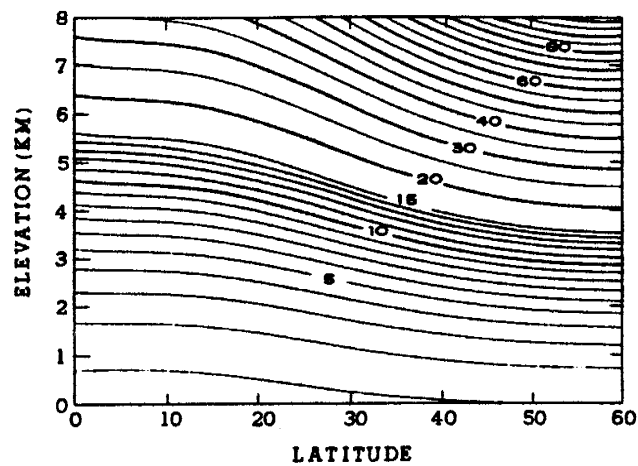
Secondary fast neutrons, thermal neutrons, and slow muons produce cosmogenic nuclides and are derived from the moderation of the primary cosmic-radiation flux (Zreda and Phillips, 1998). The majority of the primary cosmic radiation is generated outside our solar system and consists mostly of protons. The energy of the primary flux is in the TeV to MeV range (Zreda and Phillips, 1998). As the primary cosmic-radiation flux propagates through the atmosphere

and towards the surface of the Earth, its composition changes and the flux begins to lose energy (Gosse and Phillips, in press). These changes are the result of interactions between the cosmic-ray flux and atmospheric gases. At the surface of the Earth, the flux consists mostly of neutrons. The high-energy component of these neutrons, termed secondary fast neutrons (10-30 MeV), produce cosmogenic nuclides through spallation reactions (Gosse and Phillips, in press). A spallation reaction is the loss of neutrons and protons from the nucleus of an atom due to collision of a high-energy neutron with the atom. As the secondary fast neutrons lose energy as the result of collisions with surrounding nuclei, they enter the epithermal energy regime ( $\sim 0.1$  MeV to 0.5 eV) (Gosse and Phillips, in press). After further dissipation of energy and if they are not absorbed by the nuclei of surrounding atoms, the epithermal neutrons reach the thermal energy of the gas or solid containing the neutrons. These low-energy neutrons are called thermal neutrons and have energies of  $\sim 0.025$  eV (Gosse and Phillips, in press). Absorption of an epithermal or thermal neutron into the nucleus of an atom produces a cosmogenic nuclide. Muons are produced along with secondary fast neutrons, but muon reactivity is low (Gosse and Phillips, in press).. Therefore, these particles tend to penetrate deeply into geologic materials and are responsible for the majority of cosmogenic nuclide production at great depths.

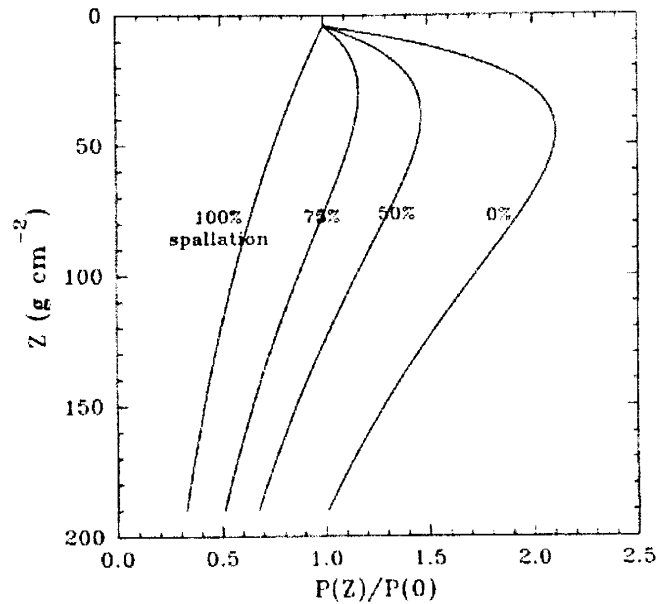
The production of cosmogenic nuclides varies spatially as a function of geomagnetic latitude, elevation, and sample depth. Because protons comprise the majority of the primary cosmic-radiation flux, the Earth's geomagnetic field deflects the flux towards the poles. This deflection results in greater cosmogenic nuclide production rates with increased distance from the equator (Lal, 1991). Production rates are also greater at higher elevations (Lal, 1991). As the cosmic-rays travel through the atmosphere, collisions of the cosmic-ray particles with atmospheric gases attenuate the intensity of the flux. At high elevation, there is less atmosphere

above the land surface; hence, the flux is greater than at lower elevations. Figure 1.3 shows the variation in cosmogenic nuclide production rates as a function of elevation and latitude. Lal (1991) provided a cubic polynomial that calculates a scaling factor based on the elevation and latitude of a sample for cosmogenic nuclide analysis. By scaling the production rate for elevation and latitude, this polynomial assists in the determination of the age of a sample. In a similar fashion to the atmospheric attenuation of the cosmogenic flux, the secondary cosmic-ray flux is exponentially attenuated as it passes through surficial material. Figure 1.4 shows the variability of cosmogenic  $^{36}\text{Cl}$  as function of depth and epithermal and thermal neutron production. As illustrated in Figure 1.4, as the fraction of epithermal and thermal neutron production increases, a bulge, just below the land surface, in the cosmogenic  $^{36}\text{Cl}$  depth profile becomes more pronounced. Due to the affinity of atmospheric nitrogen for low-energy neutrons, near the land surface a neutron gradient exists with the net direction of neutron transport being from the subsurface to the atmosphere. This loss of neutrons to the atmosphere reduces cosmogenic  $^{36}\text{Cl}$  production near the land surface and, hence, creates a bulge in the cosmogenic  $^{36}\text{Cl}$  depth profiles.

In addition to the spatial variability of cosmogenic nuclide production rates, the rates vary temporally due to variations in the Earth's magnetic dipole strength, the galactic cosmic-ray flux, the geomagnetic pole position, and solar cycles (Cerling and Craig, 1994; Gosse and Phillips, in press). Because variability in the geomagnetic pole position and solar cycles are significant on time scales of 10 and 100 years, their influence on production rates are averaged over large time intervals (Zreda and Phillips, 1998). However, fluctuations in the magnetic dipole strength operate over longer time scales ( $\sim 10^4$  years) and, therefore, these changes have a significant influence on the accumulation of cosmogenic nuclides in materials exposed for less



**Figure 1.3.** Contour plot showing the production rates of cosmogenic nuclides as function of geomagnetic latitude and altitude. Production rates are normalized to 1 for sea level and high latitudes. Source of figure: Cerling and Craig, 1994.



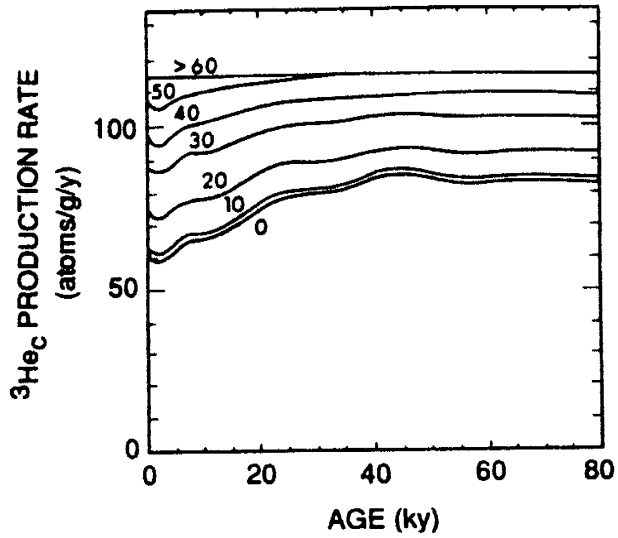
**Figure 1.4.** Cosmogenic  $^{36}\text{Cl}$  depth profiles with a varying component of spallation production. Vertical axis is mass depth (Z). The production rates (horizontal axis) have been normalized to sea level and high geomagnetic surface production. Source of figure: Lui et al., 1994.



than 20 ka (Cerling and Ciriag, 1994, Zreda and Phillips, 1998). Figure 1.5 shows the deviation in cosmogenic  $^3\text{He}$  production rates. The greatest deviation occurs at  $\sim 20$  ka. Currently, mathematical models describing the production and accumulation of cosmogenic nuclides assume the galactic cosmic-ray flux has been constant (Gosse and Phillips, in press).

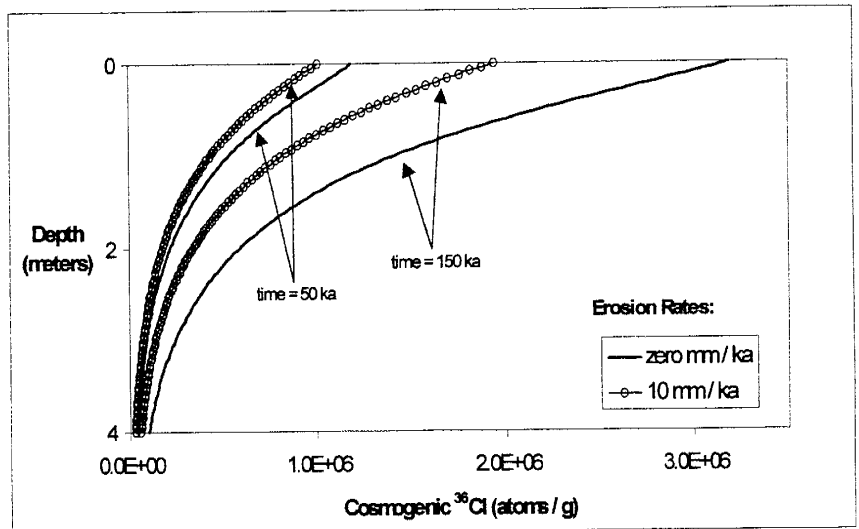
Surficial processes such as erosion influence cosmogenic  $^{36}\text{Cl}$  concentrations. Figure 1.6 presents cosmogenic  $^{36}\text{Cl}$  as a function of depth, erosion rate, and time. The figure shows that an increase in erosion results in a cosmogenic  $^{36}\text{Cl}$  depth profile with lower  $^{36}\text{Cl}$  concentrations. As erosion removes surface material with a greater accumulation of cosmogenic  $^{36}\text{Cl}$  relative to material at depth, previously buried material is exposed to a greater intensity of the cosmic-ray flux. Because surficial processes, such as erosion, and time influence the accumulation of a cosmogenic nuclide, the concentration of a cosmogenic nuclide in the geologic material of a fault scarp will record the timing of ruptures and reflect erosion and aggradation rates described by Equation 1.

Cosmogenic nuclides have been used to evaluate regional paleoseismicity. For instance, cosmogenic nuclides have been used to determine the earthquake recurrence interval for the Owens Valley fault in California (Bierman et al., 1995), the horizontal slip rate on the El Tigre fault in Argentina and Kunlun fault in China (Siame et al., 1997; Woerd et al., 1998), the time since faulting occurred on the Solitario Canyon fault (Bell et al., 1998), and the ages of paleoearthquakes along the Hebgen Lake fault (Zreda and Noller, 1998). In these previous studies, landscape evolution was given only qualitative treatment and used to interpret results from the cosmogenic nuclide analyses. This study differs in that it links the accumulation of a cosmogenic nuclide to a mathematical model that describes landscape evolution.



**Figure 1.5.** Plot shows the change in the integrated, normalized cosmogenic  $^3\text{He}$  production rate with time. The contours represent different geomagnetic latitudes. Source of figure: Cerling and Craig, 1994.

**Figure 1.6.** Increase in erosion rate reduces the cosmogenic  $^{36}\text{Cl}$  inventory yielding a younger apparent age.

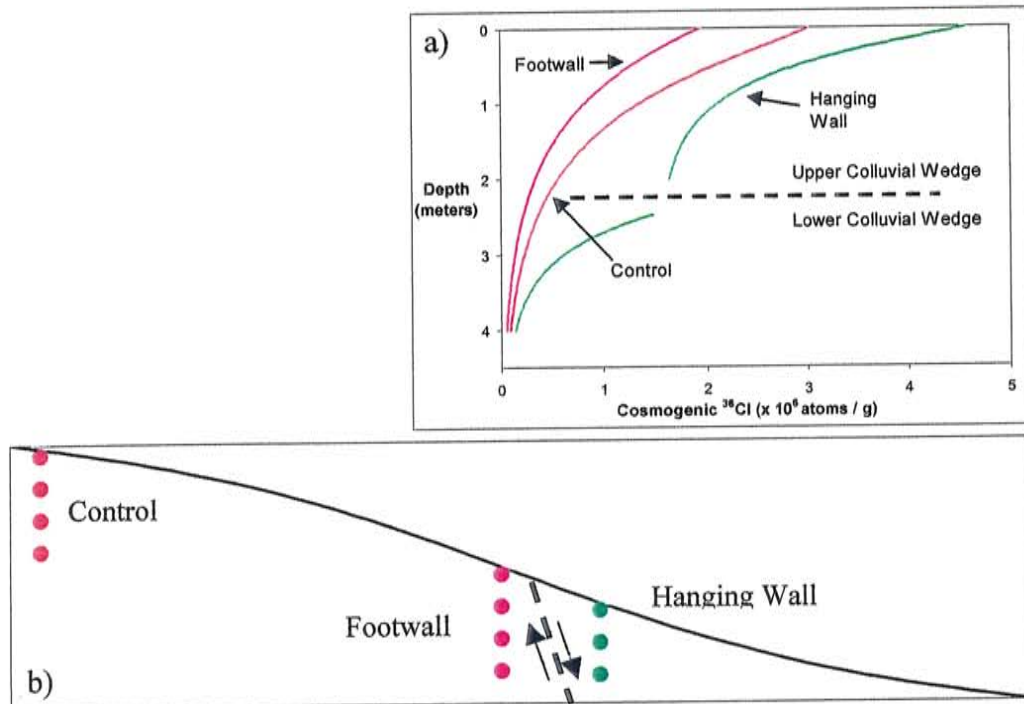
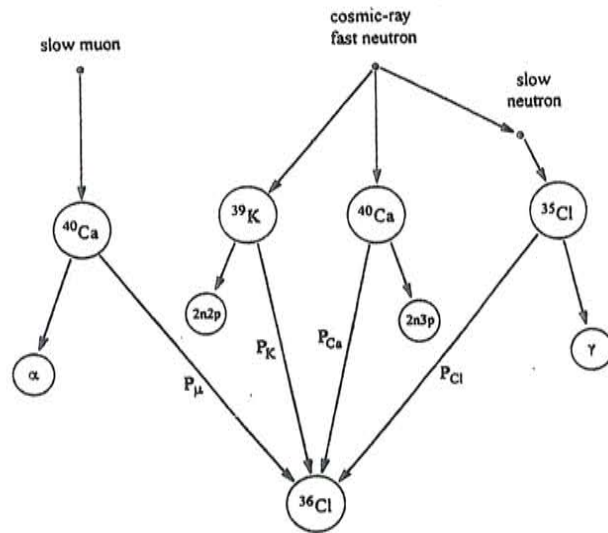


#### 1.4 *Cosmogenic $^{36}\text{Cl}$ Systematics and Modeled Distributions*

We selected cosmogenic  $^{36}\text{Cl}$  as the nuclide for analysis. Cosmogenic  $^{36}\text{Cl}$  is easily separated from meteoric  $^{36}\text{Cl}$ , it builds up to measurable levels over the period of the interest (Holocene to late Pleistocene), and its production mechanisms are well understood. Cosmogenic  $^{36}\text{Cl}$  is produced from spallation of  $^{40}\text{Ca}$  and  $^{39}\text{K}$  by high-energy nucleons and from thermal neutron activation by  $^{35}\text{Cl}$  (Phillips et al., 1986). Muon capture is responsible for the majority of cosmogenic  $^{36}\text{Cl}$  production at great depths (Stone et al. 1998). Because muon production is significant only at great depths, CLARA does not account for the production of  $^{36}\text{Cl}$  from muons. Figure 1.7 is a schematic showing the different  $^{36}\text{Cl}$  production mechanisms.

We use CLARA to construct the rupture chronology for a fault scarp of the Socorro Canyon fault. Figure 1.8 shows hypothetical cosmogenic  $^{36}\text{Cl}$  depth profiles of samples collected from vertical transects near and on both sides of the Socorro Canyon fault plane and a third profile distal the fault plane (control). Erosion along the footwall of the fault scarp will yield an apparently younger cosmogenic  $^{36}\text{Cl}$  profile relative to the control profile. Deposition and burial of material that was previously exposed to cosmogenic radiation at the surface will produce an apparently older hanging wall profile. In addition, the hanging wall profile will show a discontinuity between rupture events due to the mass movement of material shortly after an offset. Two rupture events are evidenced by colluvial wedges and buried soils in the soil geomorphology of the Socorro Canyon fault scarp.

**Figure 1.7.** Schematic shows the production mechanisms for cosmogenic  $^{36}\text{Cl}$ . Source of figure: Zreda and Phillips, 1998.

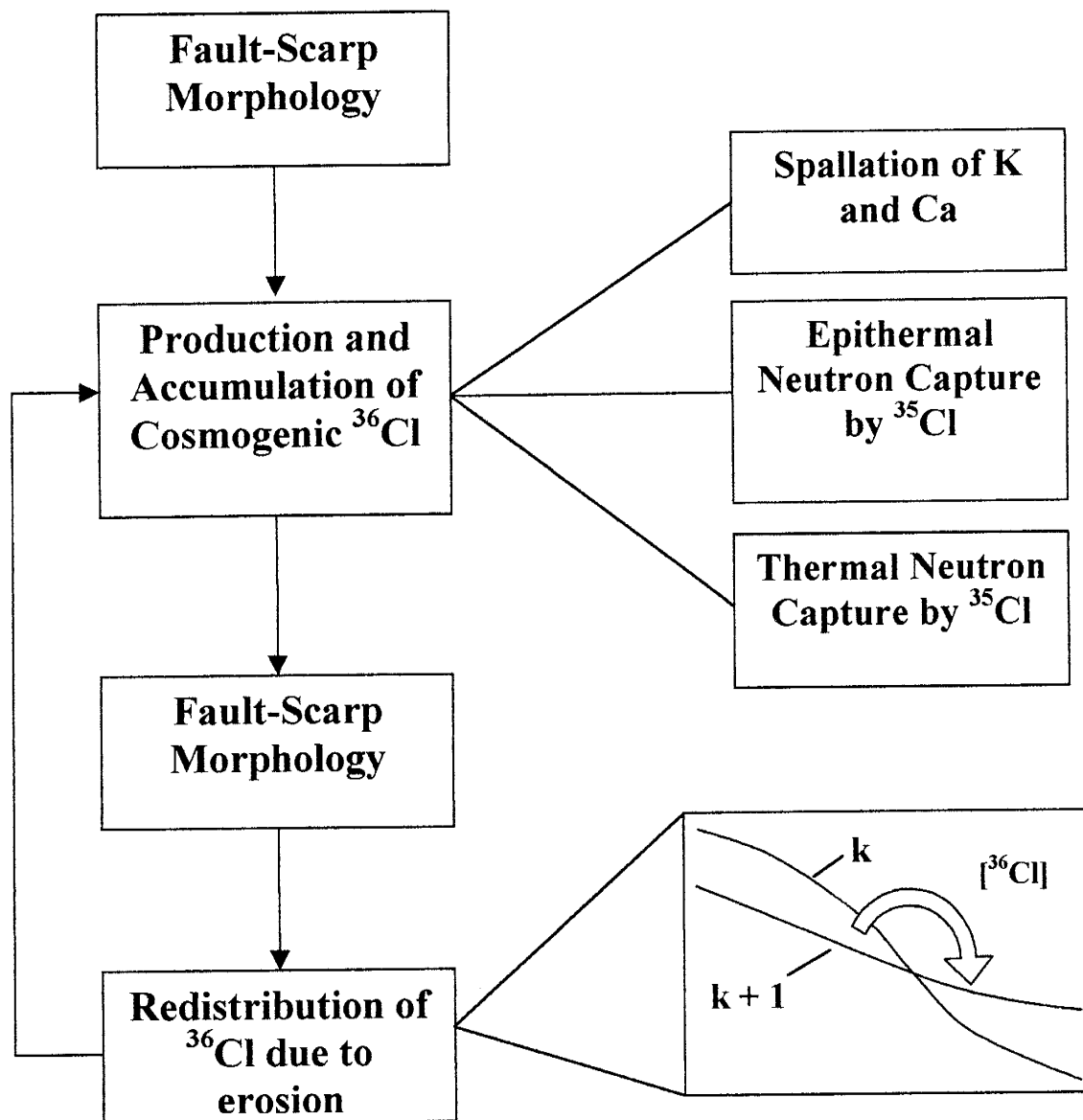


**Figure 1.8.** a) Hypothesized cosmogenic  $^{36}\text{Cl}$  depth profiles for the Socorro Canyon Fault. b) Different colored dots represent the sampled vertical transects. Red denotes control, green hanging wall, and violet footwall.

## 2.0 CLARA

### 2.1 *Model (CLARA) Overview*

We developed a program to simulate  $^{36}\text{Cl}$  accumulation under fault scarps using Matlab, a software package with programming language constructs and built-in mathematical routines. Matlab is a registered trademark of The Math Works, Inc. The program couples cosmogenic  $^{36}\text{Cl}$  production and accumulation to a model for fault-scarp morphology (Figure 2.1). Because the coupled model calculates the accumulation of cosmogenic  $^{36}\text{Cl}$  and assists in the determination of rupture chronologies, we have given the model the name CLARA (acronym for  $^{36}\text{Cl}$  Accumulation and Rupture Ages). The model for fault-scarp morphology creates a topographic surface for each timestep from the initial rupture to the present. At the model nodes, beneath each of these surfaces, CLARA assesses the production, accumulation, and redistribution of  $^{36}\text{Cl}$ . These nodes are spaced through discretization in the vertical ( $z$ ) and horizontal ( $x$ ) directions and are referenced, within this text and the program, by the row and column indexes  $i$  and  $j$ , respectively. The production of cosmogenic  $^{36}\text{Cl}$  is determined from the spallation of K and Ca and thermal neutron capture by  $^{35}\text{Cl}$ . Thermal neutron capture is assessed by considering two distinct energy ranges for these low-energy neutrons, epithermal ( $\sim 0.1$  MeV to 0.5 eV) and thermal ( $< 0.5$  eV). By summing the production of all timesteps, minus radioactive decay, CLARA accumulates cosmogenic  $^{36}\text{Cl}$ . Using the fault-scarp morphologies of consecutive timesteps, CLARA simulates the erosion of material from the footwall and its deposition onto the hanging wall through the redistribution of cosmogenic  $^{36}\text{Cl}$  values between nodes. Appendix 1.1 contains a README file for CLARA detailing the expected inputs and outputs and the role of each function in the program. The Matlab scripts for CLARA are on the appended 3.5" diskette.



**Figure 2.1.** Schematic illustrating the coupling of diffusion modeling of fault-scarp morphology and  $^{36}\text{Cl}$  production and accumulation.  $[\text{}^{36}\text{Cl}]$  is the average  $^{36}\text{Cl}$  concentration of the footwall nodes located between fault-scarps  $k$  and  $k+1$ . Arrow shows the redistribution of  $[\text{}^{36}\text{Cl}]$  between  $k$  and  $k+1$  of the hanging wall.

CLARA accounts for cosmogenic  $^{36}\text{Cl}$  production prior to the initial rupture. Before the first displacement, an equation of a line (either flat or sloping) represents the land surface, and the model assumes erosion and aggradation are negligible. CLARA calculates the production of cosmogenic  $^{36}\text{Cl}$  using analytical expressions for spallation, epithermal neutron, and thermal neutron production (Gosse and Phillips, in press; Phillips et al., in press). The accumulation of cosmogenic  $^{36}\text{Cl}$  is given by

$$N_{i,j} = \frac{P_{t,(i,j)}}{\lambda_{\text{decay}}} (1 - e^{-\lambda_{\text{decay}} t}) \quad (2.1)$$

where  $N_{i,j}$  is the accumulated cosmogenic  $^{36}\text{Cl}$  concentration (atoms  $^{36}\text{Cl}$   $\text{g}^{-1}$  rock) at node- $i,j$  located beneath the land surface,  $P_{t,(i,j)}$  is the total production rate (atoms  $^{36}\text{Cl}$   $\text{g}^{-1}$   $\text{y}^{-1}$ ) from spallation and epithermal and thermal neutrons,  $\lambda_{\text{decay}}$  is the radioactive decay coefficient of  $^{36}\text{Cl}$  ( $2.3 \times 10^{-6}$   $\text{y}^{-1}$ ), and  $t$  represents the time period between the deposition of the surface and first rupture.

## 2.2 Morphologic Dating (Fault-Scarp Morphology)

### *Diffusion equation solved using implicit finite difference*

As described in section 1.1, a diffusion equation can be used to model the degradation of a normal fault-scarp with time (Nash, 1980). Although analytical solutions for Equation 1.1 have been derived for single rupture scarps (Colman and Watson, 1983), CLARA uses a numerical solution so that multiple rupture events can be included. Equation 2.2 is the implicit finite difference approximation to Equation 1.1 (Wang and Anderson, 1982).

$$\frac{u_{j-1}^{k+1} - 2u_j^{k+1} + u_{j+1}^{k+1}}{(\Delta x)^2} = K \frac{u_j^{k+1} - u_j^k}{\Delta t} \quad (2.2)$$

In Equation 2.2,  $k$  and  $j$  index time and space, respectively,  $t$  is time,  $K$  is the geomorphic diffusivity,  $x$  is the horizontal coordinate, and  $u$  is the height of the fault scarp and is a function of  $x$  and  $t$ . The left-hand term is the central difference approximation to the space derivative evaluated at the advanced time step ( $k + 1$ ), and the right-hand term is the time derivative approximation.

CLARA uses Gaussian elimination to solve Equation 2.2. By placing the unknowns ( $u$ 's at  $k + 1$ ) on the left-hand side of the equal sign and the knowns ( $u$ 's at  $k$ ) on the right-hand side, Equation 2.2 can be rewritten as

$$u_{j-1}^{k+1} + \left( -2 - \frac{K(\Delta x)^2}{\Delta t} \right) u_j^{k+1} + u_{j+1}^{k+1} = -\frac{K(\Delta x)^2}{\Delta t} u_j^k \quad (2.3)$$

For a single timestep ( $k$ ), Equation 2.3 represents a set of algebraic expressions (one expression per  $j$ ). By representing the set of algebraic expressions as a matrix equation, Gaussian elimination solves the matrix equation directly. Equation 2.4 is an example matrix equation written for a hypothetical domain with 6 nodes.

$$\begin{bmatrix} -2 - \frac{K(\Delta x)^2}{\Delta t} & 1 & 0 & 0 \\ 1 & -2 - \frac{K(\Delta x)^2}{\Delta t} & 1 & 0 \\ & 1 & -2 - \frac{K(\Delta x)^2}{\Delta t} & 1 \\ & & 1 & -2 - \frac{K(\Delta x)^2}{\Delta t} \end{bmatrix} \begin{Bmatrix} u_2^{k+1} \\ u_3^{k+1} \\ u_4^{k+1} \\ u_5^{k+1} \end{Bmatrix} = \begin{Bmatrix} -\frac{K(\Delta x)^2}{\Delta t} u_2^k - u_1 \\ -\frac{K(\Delta x)^2}{\Delta t} u_3^k \\ -\frac{K(\Delta x)^2}{\Delta t} u_4^k \\ -\frac{K(\Delta x)^2}{\Delta t} u_5^k - u_6 \end{Bmatrix} \quad (2.4)$$



A general form of the matrix equation is

$$[A]\{x\} = \{f\} \quad (2.5)$$

where  $[A]$  is the tridiagonal coefficient matrix (first term of Equation 2.4),  $\{x\}$  is the matrix of unknown  $u$ 's at timestep  $k + 1$ , and  $\{f\}$  is the matrix of known  $u$ 's at timestep  $k$ . Gaussian elimination solves for the  $u$ 's at timestep  $k + 1$ . CLARA performs Gaussian elimination using Matlab's full matrix solver (backslash operator ( $\backslash$ )) at each timestep ( $k$ ) (Equation 2.6).

$$\{x\} = [A] \backslash \{f\} \quad (2.6)$$

Because  $[A]$  is a tridiagonal matrix, CLARA could solve Equation 2.5 using a Thomas algorithm in place of Gaussian elimination. The Thomas algorithm takes advantage of the tridiagonal feature of the matrix and is computationally more efficient than Gaussian elimination. Future development of CLARA should include the use of the Thomas algorithm to enhance computational efficiency.

To solve the diffusion model for fault-scarp morphology (Equation 1.1), an initial condition and two boundary conditions are required. The initial condition is the first rupture with the far-field slope superimposed (Figure 2.2a). The far-field slope is the regional slope of the offset alluvial fan or terrace tread. An initial scarp slope at the angle of repose of alluvial material ( $\sim 30^\circ$ ) is not included in the initial condition or after additional ruptures. Hanks and Andrews (1989) have demonstrated that the value of the initial scarp slope, whether infinite or at the angle of repose, influences modeled scarp profiles for only a short period ( $< 1$  ka) after the initial offset. The boundary conditions are specified heights ( $u$ ) and occur at  $j = 1$  and  $j = l_x$  where  $l_x$  is the total number of nodes in the  $x$  domain.

### *Model Verification*

We verified the numerical solution to the diffusion equation for fault-scarp morphology against the analytical solution presented in Hanks (1998). Appendix 2.1 provides the analytical solution of Hanks (1998). During the verification, the  $x$  domain was discretized using a uniform spacing of 1.0 meter, a timestep of 2000 years, and the boundaries were located 100 meters from the fault plane. Given these conditions, the numerical and analytical solutions are in excellent agreement (Figure 2.2b). Other parameter values used were a total offset of 5.0 meters and a geomorphic diffusivity of  $3.0 \text{ m}^2 \text{ ka}^{-1}$ .

In addition to model verification, we performed a sensitivity analysis of the numerical solution to the locations of the boundary conditions. The results of the analysis demonstrate that the numerical solution is sensitive to the locations of the boundary conditions. Appendix 4.1 presents the results of the sensitivity analysis. Therefore, users of CLARA should verify that their selected boundary locations are not impacting the accuracy of the model.

### **2.3 Cosmogenic $^{36}\text{Cl}$ Production**

To calculate the production of cosmogenic  $^{36}\text{Cl}$ , we have modified governing differential equations describing the fluxes of high-energy and low-energy neutrons (i.e., epithermal and thermal neutrons) from those of Gosse and Phillips (in press) and Phillips et al. (in press). The spatial distribution of these fluxes in the subsurface is necessary for calculating cosmogenic  $^{36}\text{Cl}$  production and accumulation. The analytical solutions of Gosse and Phillips (in press) and Phillips et al. (in press) may be used to assess the production of cosmogenic  $^{36}\text{Cl}$  or other cosmogenic nuclides beneath planar surfaces. The independent variable in the analytical solutions is referred to as the ‘mass depth’, which is the product of the bulk density of the geologic material and depth. Therefore, the solutions provide the production and accumulation

of cosmogenic  $^{36}\text{Cl}$  along a vertical transect. Because of the non-planar geometry of a fault scarp, the cosmogenic  $^{36}\text{Cl}$  production equations of CLARA solve for the distribution of the low-energy and high-energy neutron fluxes for a two-dimensional cross-section perpendicular to the strike of a fault scarp. The following sections describe the development of the mathematical expressions used to calculate the fluxes of low-energy and high-energy neutrons beneath a fault scarp, and thereby determine the production and accumulation of cosmogenic  $^{36}\text{Cl}$ . CLARA solves the high-energy and low-energy flux equations numerically. The numerical solutions of CLARA assume that bulk parameters can represent the material properties of a scarp and do not account for chemical and physical heterogeneity in the material of a scarp or variations that may occur through time. Although we modified the equations of Gosse and Phillips (in press) and Phillips et al. (in press), we have preserved the cosmogenic nuclide production theory presented in those publications.

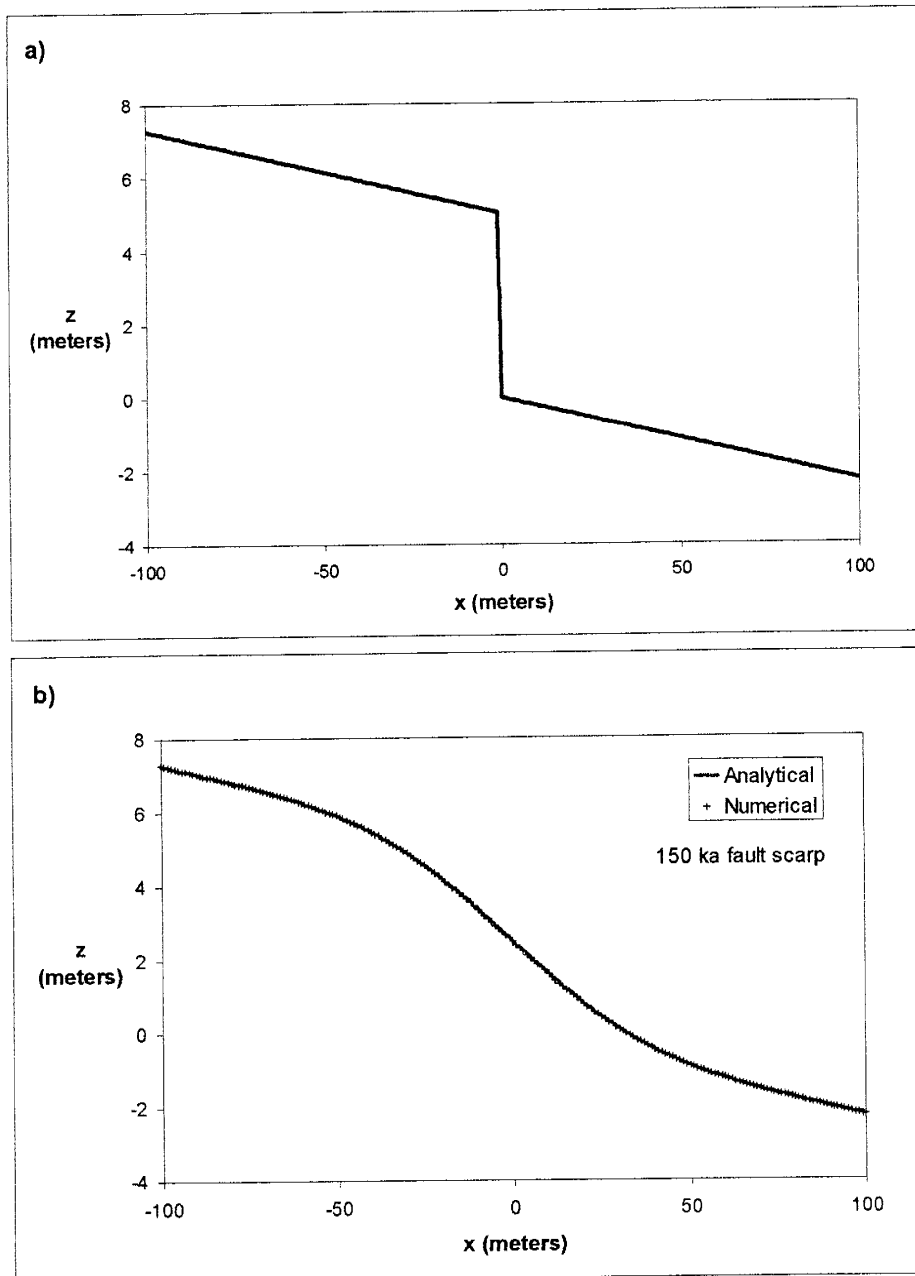
### 2.3.1 High-Energy Neutron (Spallation) Production

#### *Theory and Mathematics*

The production rate of cosmogenic  $^{36}\text{Cl}$  by spallation is proportional to the flux of high-energy neutrons (cosmic-ray flux), the abundance of K and Ca in surficial material, and the surface production rates of  $^{36}\text{Cl}$  from spallation of K and Ca (Gosse and Phillips, in press). The production of cosmogenic  $^{36}\text{Cl}$  is found by normalizing the cosmic-ray flux by the surface flux of cosmic radiation and is written as

$$P_{sp,i,j} = P_{sp}(0) \left( \frac{\Phi_{f,i,j}}{\Phi_f(0)} \right) \quad (2.7)$$

where,  $P_{sp,(i,j)}$  and  $\Phi_{f,(i,j)}$  are the production rate (atoms  $^{36}\text{Cl} \text{ g}^{-1} \text{ y}^{-1}$ ) and the cosmic-ray flux (neutrons  $\text{cm}^{-2} \text{ y}^{-1}$ ), respectively, at the node- $i,j$  located beneath the surface, and  $\Phi_f(0)$  and  $P_f(0)$



**Figure 2.2.** Verification of the numerical solution to the diffusion equation for fault-scarp morphology: a) morphology of the initial condition (the far-field slope ( $\theta_f$ ) is superimposed on the infinite scarp slope of the initial displacement); b) verification of the numerical solution (average absolute difference between modeled and observed z-values is 0.012 m).

are the cosmic-ray flux and production rate of cosmogenic  $^{36}\text{Cl}$ , respectively, at the land surface. The surface production rate is equal to the sum of the production rates from spallation of Ca and K (Equation 2.8).

$$P_{sp}(0) = P_{Ca}(0)[Ca] + P_K(0)[K] \quad (2.8)$$

In Equation 2.8,  $[Ca]$  and  $[K]$  are the concentrations of Ca and K in the surficial material (atoms  $\text{g}^{-1}$ ), and  $P_{Ca}(0)$  and  $P_K(0)$  are the Ca and K surface production rates (atoms  $^{36}\text{Cl}$  / atom Ca or K / y). Phillips et al. (in press) have empirically calibrated the surface production rates at  $66.1 \pm 6.8$  and  $137 \pm 60$  atoms  $^{36}\text{Cl}$   $\text{g}^{-1}$   $\text{y}^{-1}$  for Ca and K, respectively, for sea level and high latitude.

The cosmic-ray intensity must be integrated through solid angles, defined in spherical coordinates, across which the radiation is incident in order to obtain the total cosmic-ray flux (Gosse and Phillips, in press; Coulson, 1975) (Equation 2.9). Figure 2.3 is an illustration of the spherical coordinate system. We obtained Equation 2.9 by modifying the integration of the cosmic-ray flux described by Equation 3.56 in Gosse and Phillips (in press). Equation 2.9 differs from Equation 3.56 in that it includes an additional term describing the exponential attenuation of cosmic radiation with the linear distance traversed through surficial material.

$$\Phi_{f,i,j} = \int_{\theta=0}^{2\pi} \int_{\phi=0}^{\pi/2} F_0 \cos^m(\phi) \exp(d_t \rho_b / \lambda_t) \cos(\gamma) \sin(\phi) d\phi d\theta \quad (2.9)$$

In Equation 2.9,  $F_0$  is the maximum intensity of the cosmic radiation (i.e. in the vertical direction,  $\phi = 0$ ),  $\phi$  is the inclination angle with its origin vertically overhead, and  $\theta$  is the azimuth angle with its origin in the direction of the dip of the scarp. The maximum intensity ( $F_0$ ) is an unknown parameter; however, because the production rate is calculated by normalizing the cosmic-ray flux at depth by the surface flux,  $F_0$  cancels. The parameters associated with the exponential are as follows:  $d_t$  is the linear distance traveled by cosmic-rays in the subsurface

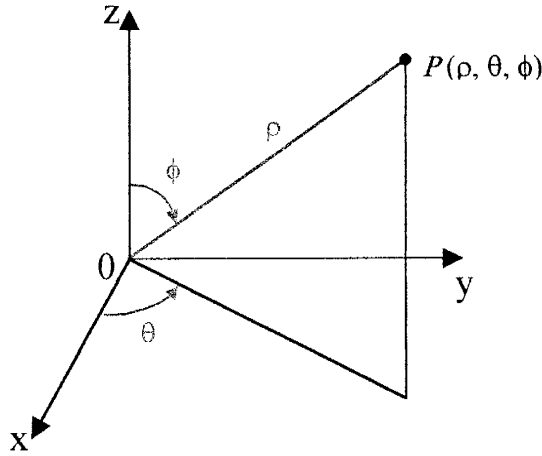
(surface to the production node- $i,j$ ),  $\rho_b$  is the bulk density of the surficial material, and  $\lambda_t$  is termed the true attenuation coefficient. The quotient  $\lambda_t/\rho_b$  represents the distance over which attenuation reduces the cosmic-ray flux by  $e^{-1}$ . Equation 2.9 incorporates the assumption that the rate of interaction between high-energy neutrons and the atoms comprising the surficial material is not dependent on the atomic arrangement of the geologic material but only on the material's mass density. The term  $\cos^m(\phi)$  accounts for the angular distribution of cosmic radiation at the base of the atmosphere (Gosse and Phillips, in press). The cosmic-ray intensity is greatest vertically overhead ( $\phi = 0$ ) where the atmospheric depth through which radiation must pass is shortest, and the cosmic-ray intensity diminishes towards the horizon as the atmospheric depth increases. The value of  $m$  that has typically been used in cosmogenic nuclide application is 2.3 (Gosse and Phillips, in press). The  $\cos(\gamma)$  term accounts for a foreshortening effect that is the result of cosmic radiation intercepting a surface at non-perpendicular angles (Gosse and Phillips, in press). Lower case gamma ( $\gamma$ ) is the angle between the normal to the surface and the incident cosmic ray ( $\phi$ ). The  $\sin(\phi)$  quantity accounts for the convergence of the spherical coordinate system toward the origin of  $\phi$ , and the limits of integration define a hemisphere.

Due to the non-planar geometry of fault scarps and difficulty in obtaining an analytical solution, CLARA uses the summations described by equation 2.10 to approximate the integrals of Equation 2.9.

$$\Phi_{f,i,j} = 2 \sum_{jj=1}^{n2} \sum_{ii=1}^{n1} F_0 \cos^m(\phi_{ii,jj}) \exp(d_{t,(ii,jj)} \rho_b / \lambda_t) \cos(\gamma_{ii,jj}) \sin(\phi_{ii,jj}) \Delta\theta \Delta\phi \quad (2.10)$$

where  $n2$  is  $(\pi/2)/\Delta\phi$ ,  $n1$  is  $\pi/\Delta\theta$ , and the multiplication by 2 completes the integration along  $\theta$  by taking advantage of the symmetry along the strike of a fault scarp. In the above

approximation, the midpoint of each solid angle is used to define  $\phi$ ,  $\theta$ ,  $\gamma$  and  $d_i$ . The values of these parameters are weighted by the area of the solid angle (product of  $\Delta\phi$  and  $\Delta\theta$ ).



**Figure 2.3.** Spherical Coordinate System.

The parameter  $d_i$  is a function of  $\phi$  and  $\theta$  and is calculated as

$$d_i = \Delta z \cos(\phi) \tag{2.11}$$

where  $\Delta z$  is the vertical distance between a node beneath the surface and the interception of the cosmic ray with the surface. The  $z$  coordinate where the cosmic-ray intercepts the surface ( $z_{int}$ ) is found by projecting the actual inclination angle ( $\phi$ ) onto the  $xz$ -plane ( $\phi'$ ), finding the surface interval containing  $z_{int}$ , and solving for  $z_{int}$ . The relationship between  $\phi$  and  $\phi'$  (the projected angle) is

$$\tan(\phi') = \tan(\phi) \cos(\theta) \tag{2.12}$$

We derived Equation 2.12 from trigonometric relationships (Appendix 3) and the assumption of symmetry along the strike of a fault scarp. The interval containing the projected angle ( $\phi'$ ) was found by constructing an algorithm that incorporated Matlab's built-in *find* routine. The

interception of the cosmic ray with the surface was calculated by representing the interval found from Matlab's *find* routine and the cosmic ray with separate linear equations and setting the equations equal (Appendix 3).

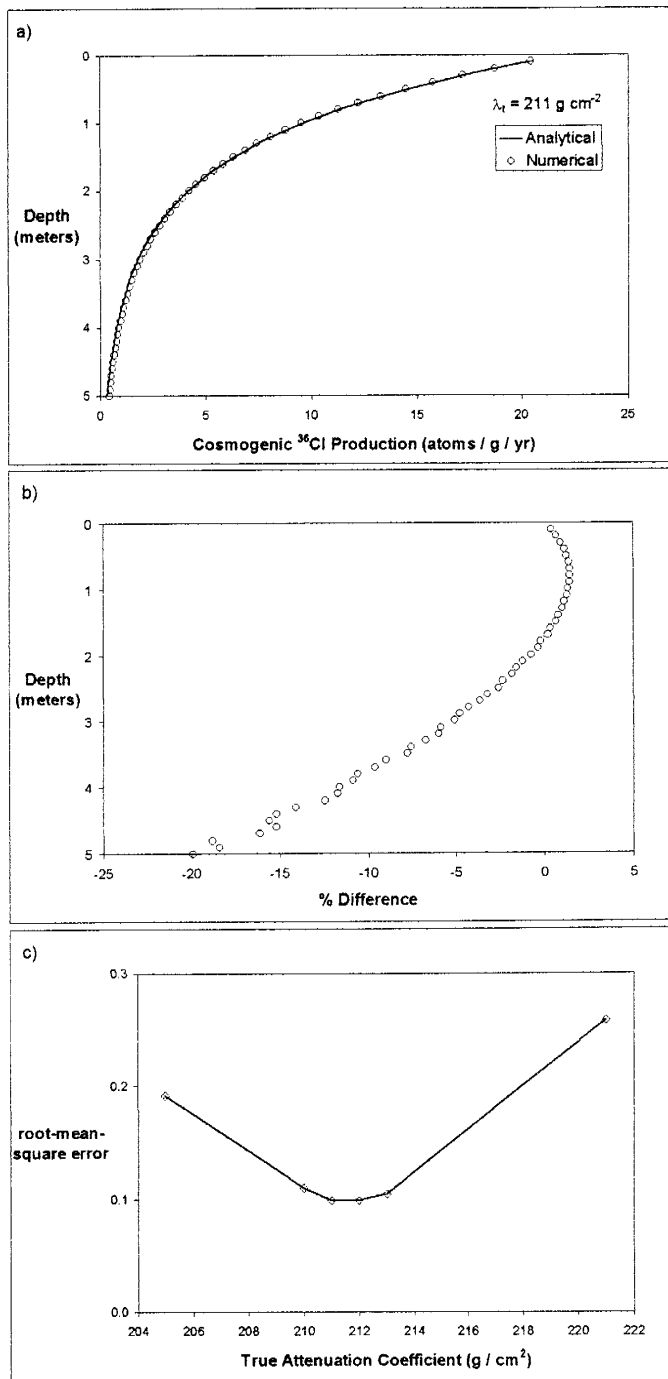
### *Calibration of the Numerical Solution*

We calibrated the numerical solution for cosmogenic  $^{36}\text{Cl}$  production (above) to an analytical solution for a flat surface. Appendix 2.2 provides the analytical solution. Using  $\lambda_t$  as a fitting parameter, the objective of the calibration was to minimize the root-mean-square error between the analytical and numerical solutions. A spacing of  $1.0^\circ$  was used for both  $\phi$  and  $\theta$ . Figure 2.4 presents the results of the calibration. The  $\lambda_t$  that provides the minimum root-mean-square error is  $211 \text{ g cm}^{-2}$ . Using this value for  $\lambda_t$ , the numerical solution overpredicts spallation production at depth as both the numerical and analytical solutions approach zero production. Nonetheless, the numerical solution does accurately (<5% difference) model spallation production at depths less than 3 m where the majority of cosmogenic  $^{36}\text{Cl}$  is produced.

In addition to the calibration, a sensitivity analysis of the numerical solution to the size of  $\Delta\phi$  and  $\Delta\theta$  was performed. Appendix 4.2 presents the results of the sensitivity analysis. The analysis shows that a spacing of  $6.0^\circ$  and  $10.0^\circ$  for  $\Delta\phi$  and  $\Delta\theta$ , respectively, can be used in order to reduce the computational cost associated with the finer spacing while preserving the accuracy of the numerical solution.

Additionally, in Appendix 4.3, we explored the difference in cosmogenic  $^{36}\text{Cl}$  production using two different solutions (i.e. equation 2.10 and the analytical solution of Gosse and Phillips (in press)) for the source of high-energy neutrons. High-energy neutrons contribute to cosmogenic  $^{36}\text{Cl}$  production through spallation reactions and as a source of epithermal neutrons. The depth we used in the analytical solution of Gosse and Phillips (in press) was the vertical



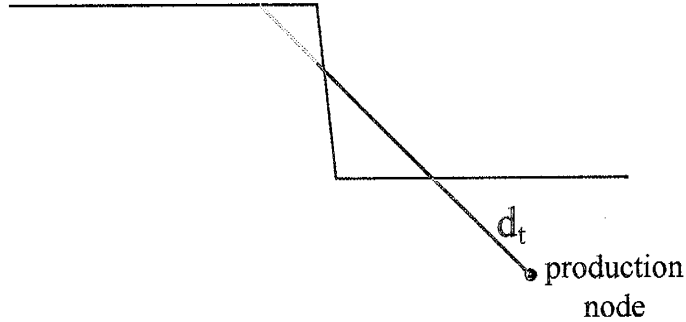


**Figure 2.4.** Calibration of the numerical solution for the cosmic-radiation flux: a) analytical and numerical spallation production solutions ( $\lambda_t = 211 \text{ g cm}^{-2}$  and  $\lambda_e = 170 \text{ g cm}^{-2}$ ); b) difference between the analytical and numerical solutions ( $[\text{analytical} - \text{numerical}] / \text{analytical}$ ), c) results of the root-mean-square error analysis.

distance between a node and the land surface. The results show that as the morphologic age of a scarp increases and thereby the scarp slope decreases the analytical solution provides an accurate approximation for the source of high-energy neutrons.

#### *Sources of Error and Recommendations for Future Improvements*

The method used to determine  $z_{int}$  hampers the numerical integration of the cosmic radiation flux. The algorithm, which incorporates the *find* function of Matlab, locates only a single interception of a cosmic ray with the surface; however, for steep, young scarps, a cosmic ray may intercept a surface three times (Figure 2.5). The result is a slight over-prediction of the flux and, hence, spallation production for nodes of the hanging wall located near the fault plane. The  $z_{int}$  found yields the shortest distance between the surface of a fault-scarp and the node- $i,j$  (Figure 2.5). The approach overestimates the intensity of a cosmic ray by failing to account for the attenuation of cosmic radiation as it intercepts and travels through a portion of the footwall before impinging upon the hanging wall. However, the error introduced by this overestimation is not large. Except for a brief period immediately after an offset, slopes of fault-scarp are generally at angles  $<30^\circ$  (or inclination angles  $>60^\circ$ ). Due to the angular distribution of the cosmic-ray intensity, the flux at inclination angles  $>60^\circ$  is attenuated by the atmosphere and, therefore, contributes little to total spallation production. The majority (87%) of high-energy production occurs at inclinations between zero and  $60^\circ$ . As the scarp evolves, the scarp slope (measured from the horizontal) decreases, and the accuracy of the numerical solution increases as the range of inclination over which the cosmic-radiation flux is integrated without traversing the footwall increases. Although the error associated with the numerical integration is expected to be small, future development of the model should correct this problem.



**Figure 2.5.** Source of error in the numerical integration. The red portion of the trajectory is attenuated by the footwall; however, this is currently not accounted for in CLARA. In the program, the cosmic-ray intensity is attenuated by only the distance of the blue line ( $d_t$ ).

A theoretical relationship between  $\lambda_t$  and the effective attenuation coefficient ( $\lambda_{f,e}$ ) of the analytical solution for the high-energy flux is given by

$$\lambda_t = \frac{3.3}{4.3} \lambda_{f,e} \quad (2.13)$$

where  $\lambda_{f,e}$  is the effective attenuation coefficient for cosmic-ray intensity (Gosse and Phillips, in press). Using this equation and a value of  $170 \text{ g cm}^{-2}$  for  $\lambda_{f,e}$ ,  $\lambda_t$  is  $221 \text{ g cm}^{-2}$ . This value for  $\lambda_t$  is  $\sim 5\%$  greater than the  $211 \text{ g cm}^{-2}$  determined from the calibration presented above. Due to this disparity between the two calculated values of  $\lambda_t$ , we compared the numerical solution presented in this section to a second numerical solution. This second numerical solution uses the same summations presented in Equation 2.10; however, it assumes a flat surface. Because a flat surface is assumed, Equation 2.11 can be used to calculate  $d_t$  without having to locate  $z_{ini}$ ; thus, simplifying the numerical routines from those described above in this section. The second numerical solution validates the trigonometry and numerical techniques of the numerical solution of CLARA (see Figure A3.3 in Appendix 3). The difference between  $\lambda_t$  calculated from

Equation 2.13 and the calibrated  $\lambda_t$  needs further investigation. Interestingly, if the term for foreshortening is included in the derivation of Equation 2.13 (see Equation 3.69 of Gosse and Phillips (in press)), the following expression is obtained

$$\lambda_t = \frac{4.3}{5.3} \lambda_{f,e} \quad (2.14)$$

Using this relationship and a value of  $170 \text{ g cm}^{-2}$  for  $\lambda_{f,e}$ ,  $\lambda_t$  is  $\sim 210 \text{ g cm}^{-2}$ .

### 2.3.2 Low-Energy Neutron Capture

#### *Theory and Mathematics*

By modeling the transport, production, and absorption of epithermal and thermal neutrons, the production of cosmogenic  $^{36}\text{Cl}$  from low-energy neutron capture by  $^{35}\text{Cl}$  can be calculated (Lui et al., 1994; Phillips et al., in press; Gosse and Phillips et al., in press). The production of cosmogenic  $^{36}\text{Cl}$  from low-energy neutrons is described by

$$P_{le,(i,j)} = \frac{f_{le,(i,j)}}{\Lambda_{le,(i,j)}} \Phi_{le,(i,j)} \quad (2.15)$$

where  $le$  denotes epithermal (*epi*) or thermal (*thn*) neutrons,  $f_{le,(i,j)}$  is the fraction of low-energy (epithermal or thermal) neutrons absorbed by  $^{35}\text{Cl}$ ,  $\Lambda_{le,(i,j)}$  is the attenuation coefficient for absorption of epithermal or thermal neutrons ( $\text{g cm}^{-2}$ ), and  $\Phi_{le,(i,j)}$  is the subsurface flux of epithermal or thermal neutrons ( $\text{neutrons cm}^{-2} \text{ y}$ ) (Gosse and Phillips, in press).

The epithermal and thermal neutron fluxes are modeled with diffusion equations (Equation 2.16 and 2.17, respectively). The subsurface distribution of low-energy neutrons depends on the atmospheric epithermal and thermal neutron distributions. Due to the large macroscopic low-energy neutron cross-section of the atmosphere, neutrons have a propensity to diffuse out of the

subsurface at the land/atmosphere interface (see Section 1.3). Therefore, Equations 2.16 and 2.17 describe the distributions of the fluxes in both the subsurface and atmosphere.

Other than the parameter values, the difference between the governing differential equations for the epithermal and thermal neutron fluxes is the source term. The source of epithermal neutrons is the moderation of secondary higher energy neutrons ( $>0.1$  MeV); whereas moderated epithermal neutrons, which have escaped capture by the atomic nuclei of gases of the atmosphere, are the source of thermal neutrons.

$$\frac{\partial}{\partial x} \left( D'_{epi} \frac{\partial \Phi_{epi}}{\partial x} \right) + \frac{\partial}{\partial z} \left( D'_{epi} \frac{\partial \Phi_{epi}}{\partial z} \right) = \frac{\Phi_{epi}}{\Lambda'_{epi}} - \rho R_{epi} P_f \quad (2.16)$$

$$\frac{\partial}{\partial x} \left( D'_{thn} \frac{\partial \Phi_{thn}}{\partial x} \right) + \frac{\partial}{\partial z} \left( D'_{thn} \frac{\partial \Phi_{thn}}{\partial z} \right) = \frac{\Phi_{thn}}{\Lambda'_{thn}} - R_{thn} \frac{\rho(E_{th})_a}{\Lambda'_{epi}} \Phi_{epi} \quad (2.17)$$

Values for the parameters of Equations 2.16 and 2.17 are dependent on the medium in which the node- $i,j$  is located. For nodes located above the land surface of the scarp, atmospheric values characterize the parameters; whereas, for nodes located beneath the surface of the scarp, subsurface values represent the parameters. The parameters of Equations 2.16 and 2.17 are as follows:  $D'$  is the diffusion coefficient for either epithermal or thermal neutrons (cm);  $\Lambda'$  is the attention coefficient for absorption for either epithermal or thermal neutrons (cm);  $R_{epi}$  and  $R_{thn}$  normalize production from epithermal and thermal neutrons, respectively, to that in the atmosphere;  $\rho$  is the bulk density ( $\text{g cm}^{-3}$ ) of air or colluvium;  $p(E_{th})_a$  is the resonance escape probability of a neutron from the epithermal energy regime, in the atmosphere; and  $P_f$  is the production rate of epithermal neutrons from high energy ( $\sim 1$  to  $10$  MeV) neutrons (neutrons  $\text{g}^{-1} \text{y}^{-1}$ ).

We modified the governing differential equations for the thermal and epithermal neutron fluxes presented in Phillips et al. (in press) in order to obtain the above expressions for the low-

energy neutron fluxes. The equations of Phillips et al. (in press) use the mass depth, which is the product of the material density and vertical depth below the land surface or height above the land surface, as the independent variable because their governing differential equations assume a planar surface and thus a one-dimensional variation of production with depth. We have recast the low-energy flux equations in two-dimensional form, in terms of the Cartesian coordinates  $x$  and  $z$ , in order to account for the non-planar geometries of fault scarps. By modeling the flux of low-energy neutrons with Equations 2.16 and 2.17, it is assumed that the low-energy neutron flux gradient along  $y$  is  $\sim 0$ . This assumption is consistent with an assumption in the model for fault-scarp morphology that the scarp is straight in plan view (along its strike). Because the equations for the low-energy fluxes have been written in terms of Cartesian coordinates, the diffusion and attenuation coefficients for epithermal and thermal neutrons are expressed in units of volume per area in order for the diffusion equations to maintain a unit balance. Modifying the coefficients in this manner is accomplished by dividing the atmospheric and subsurface diffusion and attenuation coefficients of Phillips et al. (in press) by the respective bulk densities of the media. Phillips et al. (in press) express their attenuation and diffusion coefficients in units of mass per area.

The diffusion and attenuation coefficient of Phillips et al. (in press) as well as  $R_{epi,ss}$  and  $R_{th,ss}$  are dependent on the chemical composition of the surficial material. For the sake of brevity, we did not include equations describing the calculations of these parameters here, and the reader is referred to Gosse and Phillips (in press), which provides the necessary equations and theory.

Due to the dimensionality (2D) and presence of the fault scarp, CLARA solves Equation 2.16 and 2.17 numerically. This is accomplished by replacing the partial differential equations with central difference approximations and using the iterative technique of Successive Over

Relaxation (SOR) to find a solution. Because of the similarities between the governing equations for the epithermal and thermal neutron fluxes, the following expressions are written in a general form and apply to both fluxes except where stated explicitly that an equation is specific to epithermal or thermal neutrons. The central difference approximation to the  $x$  derivative in Equations 2.16 and 2.17 is given by

$$\frac{\partial}{\partial x} \left( D' \frac{\partial \Phi_{le,(j)}}{\partial x} \right) = \frac{D'_{j+1/2} (\Phi_{le,(j+1)} - \Phi_{le,(j)}) + D'_{j-1/2} (\Phi_{le,(j-1)} - \Phi_{le,(j)})}{\Delta x^2} \quad (2.18)$$

where  $j$  references a nodal location along  $x$ . Similarly, for the  $z$  derivative

$$\frac{\partial}{\partial z} \left( D' \frac{\partial \Phi_{le,(i)}}{\partial z} \right) = \frac{D'_{i+1/2} (\Phi_{le,(i+1)} - \Phi_{le,(i)}) + D'_{i-1/2} (\Phi_{le,(i-1)} - \Phi_{le,(i)})}{\Delta z^2} \quad (2.19)$$

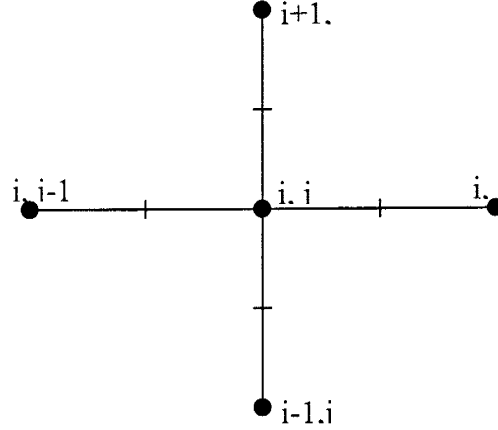
where  $i$  references a nodal location along  $z$ . Figure 2.6 is a five-point star illustrating the relationship between consecutive nodes. Tick marks, located midway between consecutive nodes, identify the locations where diffusion coefficients are evaluated. CLARA uses harmonic means (Equations 2.20a through 2.20d) to approximate the epithermal and thermal neutron diffusion coefficients ( $D'$ ) in the central difference approximations to the  $x$  and  $z$  derivatives (Equations 2.18 and 2.19). The heterogeneity in  $D'$  for both epithermal and thermal neutrons results from differences in the transport characteristics between the subsurface and atmosphere.

$$D'_{i+1/2,j} = \frac{2D'_{i,j}D'_{i+1,j}}{D'_{i,j} + D'_{i+1,j}} \quad (2.20a)$$

$$D'_{i-1/2,j} = \frac{2D'_{i,j}D'_{i-1,j}}{D'_{i,j} + D'_{i-1,j}} \quad (2.20b)$$

$$D'_{i,j-1/2} = \frac{2D'_{i,j}D'_{i-1,j}}{D'_{i,j} + D'_{i-1,j}} \quad (2.20c)$$

$$D'_{i,j+1/2} = \frac{2D'_{i,j}D'_{i+1,j}}{D'_{i,j} + D'_{i+1,j}} \quad (2.20d)$$



**Figure 2.6.** Discretization of  $x$  and  $z$ . The tick marks between nodes are the locations where  $D'$  is evaluated.

Applying Equations 2.20a through 2.20d and the central difference approximations of the space derivatives (Equations 2.18 and 2.19) to Equations 2.16 and 2.17, the following general expression for the epithermal and thermal neutron fluxes, at the node- $i,j$ , is obtained:

$$\Phi_{le,(i,j)} = \frac{(D'_{i,j-1/2}\Phi_{le,(i,j-1)} + D'_{i,j+1/2}\Phi_{le,(i,j+1)})\Delta z^2 + (D'_{i-1/2,j}\Phi_{le,(i-1,j)} + D'_{i+1/2,j}\Phi_{le,(i+1,j)})\Delta x^2 + S_{i,j}\Delta x^2\Delta z^2}{(D'_{i,j-1/2} + D'_{i,j+1/2})\Delta z^2 + (D'_{i-1/2,j} + D'_{i+1/2,j})\Delta x^2 + \frac{\Delta x^2\Delta z^2}{\Lambda'_{i,j}}} \quad (2.21)$$

In Equation 2.21,  $S$  is the source term for epithermal or thermal neutrons and is given by

$$S = \rho_{i,j}R_{epi,(i,j)}P_{f,(i,j)} \quad (2.22)$$

for epithermal neutrons and

$$S = R_{thn,(i,j)} \frac{\rho(E_{th})_a}{\Lambda'_{epi,(i,j)}} \Phi_{epi,(i,j)} \quad (2.23)$$



for thermal neutrons. The parameters of Equations 2.22 and 2.23 are described with Equations 2.16 and 2.17.

In the subsurface, the production rate of high-energy neutrons is given by

$$P_{f,(i,j)} = P_{f,s} (\Phi_{f,(i,j)} / \Phi_{f,s}) \quad (2.24)$$

where  $\Phi_{f,(i,j)}$  is the cosmic-ray flux at the node- $i,j$  located beneath the land surface and is calculated using Equation 2.10,  $\Phi_{f,s}$  is the surface flux of cosmic radiation for a horizontal surface, and  $P_{f,s}$  is the surface production rate of high-energy (fast) neutrons. The value of the surface production rate has been empirically calibrated at 626 neutrons  $\text{g}^{-1} \text{y}^{-1}$  (Phillips et al., in press).

Because the program used to solve the numerical integration for the cosmic-ray flux (section 2.3.1) is limited to nodes beneath the surface, the distribution of the high-energy neutron production rate in the atmosphere is approximated from an analytical solution presented in Gosse and Phillips (in press) (Equation 2.25).

$$P_{f,(i,j)} = P_{f,s} \exp\left(\frac{-Z_j}{\lambda_{f,e}}\right) \quad (2.25)$$

In Equation 2.25,  $Z$  is termed the mass depth and  $\lambda_{f,e}$  is the effective attenuation coefficient for secondary high-energy neutrons. The mass depth in the atmosphere is equal to the product of the vertical height above the scarp and the bulk density of the atmosphere. The origin for  $Z$  is the land surface with positive values representing depth beneath the surface and negative values for height above the surface.

CLARA uses the iterative method SOR to solve the numerical solutions for the low-energy neutron fluxes (Wang and Anderson, 1982).

$$\Phi_{i,j}^{m+1} = \omega \Phi_{i,j}^{m+1} + (1 - \omega) \Phi_{i,j}^m \quad (2.26)$$

In Equation 2.26,  $m$  denotes the iteration number and  $\omega$  is the relaxation factor. In general, the optimum range for  $\omega$  is between 1 and 2. Values in this range allow for quicker convergence while not permitting the solution to be overshoot (Wang and Anderson, 1982). A logic statement in CLARA stops the iterative technique when the difference between  $\Phi^{n+1}$  and  $\Phi^n$  is less than a specified tolerance for all nodes. Like all iterative methods, SOR requires an acceptable initial guess. The analytical solutions of Phillips et al. (in press) are used to calculate the initial guesses for both low-energy fluxes. Appendices 2.3 and 2.4 provide these analytical solutions. These solutions are expressed in terms of mass depth ( $Z$ ), which is calculated as the product of the vertical distance from the scarp's surface to the node- $i,j$  and either the bulk density of the geologic material or atmosphere depending on the location of the node- $i,j$ .

Four boundary conditions are required to solve the governing differential equations for the low-energy neutron fluxes. The boundaries are first-type boundary conditions, where the analytical solutions of Phillips et al. (in press) specify the low-energy fluxes. The lateral boundaries are defined at  $x_{j=1}$  and  $x_{j=l_x}$  where  $l_x$  is the total number of nodes along  $x$ . By specifying the low-energy flux with analytical solutions, it is assumed that at these boundary locations the slope of the surface is gentle ( $\theta_j < 5^\circ$ ) and the distance from the scarp is large so that the geometry of the scarp does not influence the low-energy fluxes. The user of CLARA specifies the lateral extent of the horizontal domain. The domain needs to be large enough so the boundaries do not have an influence on the numerical solution for the low-energy fluxes. Equations 2.27a and 2.27b describe the lower subsurface and upper atmospheric boundary conditions, respectively. By expressing these boundary conditions in terms of the coordinate system used in CLARA, we obtained Equations 2.27a and 2.27b from modification of the

boundary conditions presented in Phillips et al. (in press), which were used to obtain the analytical solutions presented in Appendices 2.3 and 2.4.

$$\Phi(z) = 0 \quad \text{at } z = -\infty \quad (2.27a)$$

$$\Phi(z) = \frac{P_f(0)}{\Sigma_{le,a} - D_{le,a}\lambda_{f,e}^{-2}} \exp\left(\frac{-z\rho_a}{\lambda_{f,e}}\right) \quad \text{at } z \gg 0 \quad (2.27b)$$

Equation 2.27a (lower boundary) states that at an infinite depth the low-energy fluxes are totally attenuated. Equation 2.27b (upper boundary) state that at large distance above the land surface the low-energy neutron fluxes are in spatial equilibrium with the atmospheric high-energy neutron flux. In Equation 2.27b,  $a$  denotes atmosphere,  $P_f(0)$  is the surface production rate of high-energy neutrons,  $D_{le,a}$  is the epithermal or thermal diffusion coefficient in the atmosphere ( $\text{g cm}^{-2}$ ),  $\Sigma_{le,a}$  is the macroscopic epithermal neutron loss cross-section or macroscopic thermal neutron absorption cross-section in the atmosphere, and the other parameters have been previous defined. CLARA uses the analytical solutions of Phillips et al. (in press) to specify the upper and lower boundaries. Approximating the location of the upper and lower boundary conditions in this manner requires that they be placed a large enough distance from the land surface that they do not influence the low-energy flux calculations near the land surface.

#### *Verification of the Numerical Solutions for the Low-Energy Neutron Fluxes*

We verified the numerical solutions for the epithermal and thermal neutron fluxes against the analytical solutions of Phillips et al. (in press) (solutions provided in Appendix 2). For the verification, the analytical and numerical solutions solved for the distributions of the low-energy neutron fluxes beneath and above a flat surface. The spreadsheet model CHLOE (Plummer and Philips, 1996) calculated the low-energy flux parameters based on the average whole-rock chemistry of colluvial samples collected from the Socorro Canyon fault field site. We used a

spatial discretization of 0.5 meters for  $\Delta x$  and 0.1 meters for  $\Delta z$ . The lateral boundaries were located 50 meters from the fault plane. The upper atmospheric boundary condition was placed 10 meters above the surface, and the lower subsurface boundary condition was located 5 meters below the surface. Figure 2.7 shows the results of the verification and accuracy of the numerical solutions for the low-energy fluxes. The average absolute deviation between the numerical and analytical solutions for the epithermal and thermal neutron fluxes is 0.034% and 0.29%, respectively. For the thermal neutron flux depth profile, the largest difference is just below the land surface, in the ‘thermal neutron bulge’.

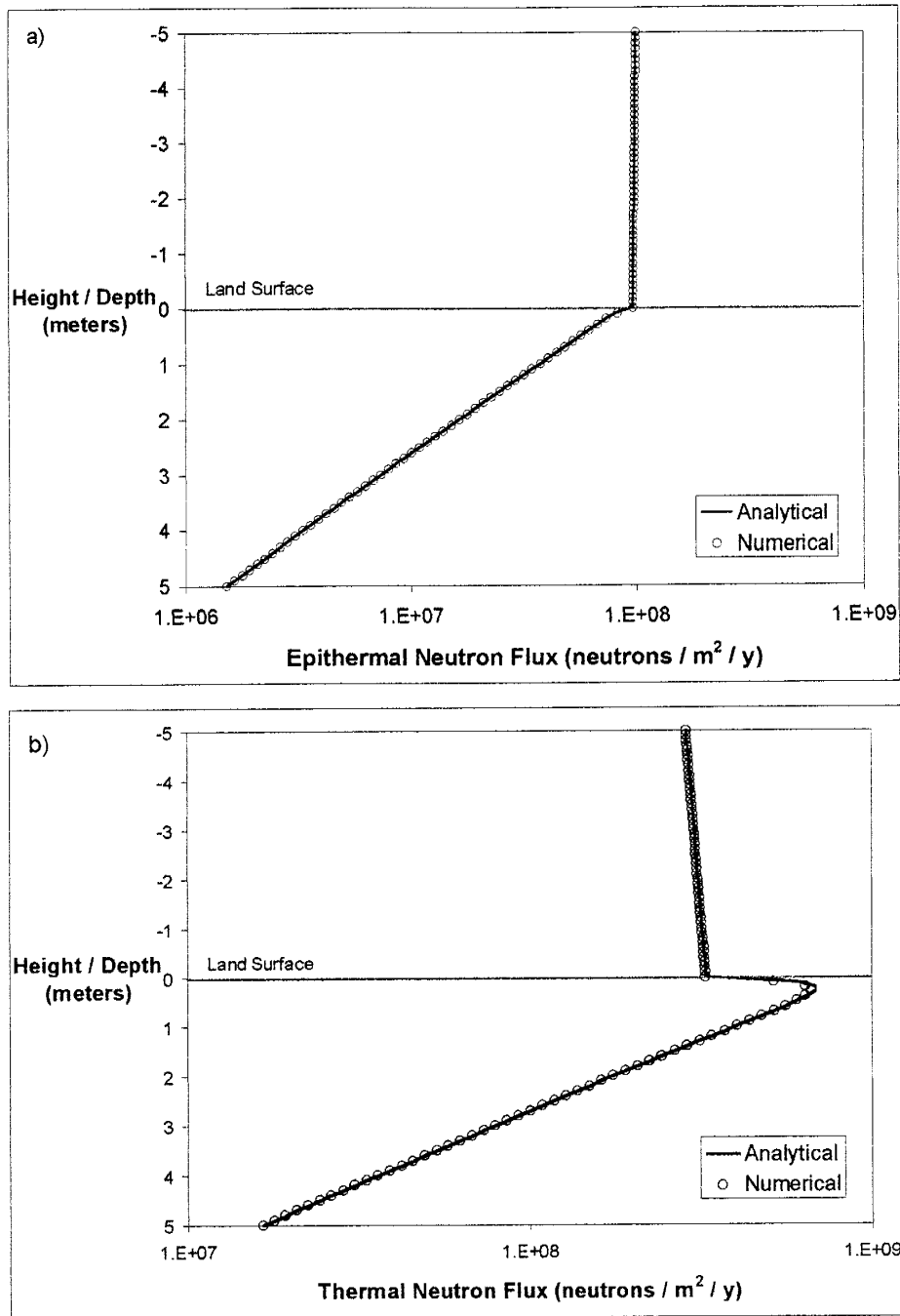
#### 2.4 Cosmogenic $^{36}\text{Cl}$ Accumulation and Redistribution

CLARA assesses the build-up of cosmogenic  $^{36}\text{Cl}$  beneath a fault scarp by summing the amount of cosmogenic  $^{36}\text{Cl}$  produced minus the amount of  $^{36}\text{Cl}$  radioactively decayed over each timestep from the initial offset to the present (Equation 2.28).

$$N_{i,j}^k = \sum_{k=1}^{k=q} (P_{t,(i,j)} - \lambda_{decay} N_{i,j}^{k-1}) \Delta t_k \quad (2.28)$$

In Equation 2.28,  $P_{t,(i,j)}$  is the total production of cosmogenic  $^{36}\text{Cl}$  from spallation and low-energy neutron capture (atoms  $\text{g}^{-1} \text{y}^{-1}$ ),  $N$  is the  $^{36}\text{Cl}$  concentration (atoms  $^{36}\text{Cl} \text{g}^{-1} \text{y}^{-1}$ ) at node- $i,j$ ,  $k$  indexes time,  $\Delta t_k$  is the size of the timestep (years),  $q$  is the total number of timesteps, and  $\lambda_{decay}$  is the decay coefficient of  $^{36}\text{Cl}$ .

CLARA weights the amount of cosmogenic  $^{36}\text{Cl}$  produced and decayed for a given timestep by the  $\Delta t$  for that timestep. In assessing the accumulation of cosmogenic  $^{36}\text{Cl}$ , the size of the timestep varies. This variability in  $\Delta t$  enhances the computational efficiency of the model. Immediately after an offset the geometry of a fault scarp is rapidly changing; however, as time passes the fault scarp evolves more slowly and CLARA increases the timestep without



**Figure 2.7.** Verification of the numerical solutions for the epithermal (a) and thermal (b) neutron fluxes. The average absolute deviation between the numerical and analytical solutions for the epithermal and thermal neutron fluxes is 0.034% and 0.29%, respectively.

sacrificing accuracy. For instance, for the first 5,000 years after an offset  $\Delta t$  is 1,000 years. Then CLARA increases  $\Delta t$  to 2,000 years for the next 10,000 years, and, finally, CLARA increases  $\Delta t$  to 5,000 years until another rupture occurs or until the end of the modeled time has been reached.

The amount of cosmogenic  $^{36}\text{Cl}$  produced at each timestep is scaled to account for the effects of topographic shielding ( $S_t$ ) and the latitude and elevation of a fault scarp ( $S_{el}$ ) (Equation 2.29). The values  $S_t$  and  $S_{el}$  are required input. The polynomials of Lal (1991) are used to scale cosmogenic  $^{36}\text{Cl}$  production for the latitude and elevation of a fault. The spreadsheet model CHLOE can be used to calculate the scaling factor for topographic shielding given the horizon angles and azimuths of landscape features that intercept cosmic radiation (Phillip and Plummer, 1996). In addition to calculating these parameters, CHLOE calculates the high-energy and low-energy production and flux parameter values given the average chemical composition of the material of a fault scarp. Using CHLOE to calculate these parameter values requires the user to convert the low-energy diffusion and attenuation coefficients to units of volume per area as described in section 2.3.2. In addition, the unit of length used in CHLOE is the centimeter, and in CLARA, the unit of length is the meter; therefore, the user must make the appropriate conversions.

$$P_{t,(i,j)} = S_{el} S_t (P_{sp,(i,j)} + P_{epi,(i,j)} + P_{thn,(i,j)}) \quad (2.29)$$

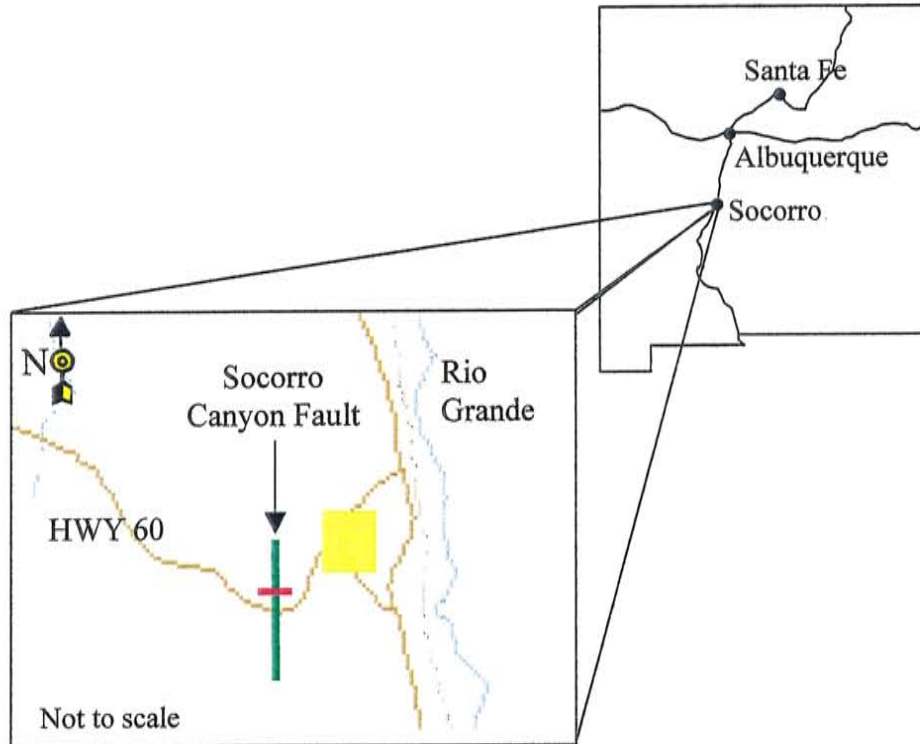
CLARA uses the fault-scarp morphologies of consecutive timesteps to simulate the erosion of material from the footwall and its deposition onto the hanging wall. The cosmogenic  $^{36}\text{Cl}$  concentration of nodes located between two consecutive fault-scarp profiles of the footwall are weighted and summed, and this quantity added to those nodes between consecutive profiles of the hanging wall.

### 3.0 Socorro Canyon Fault

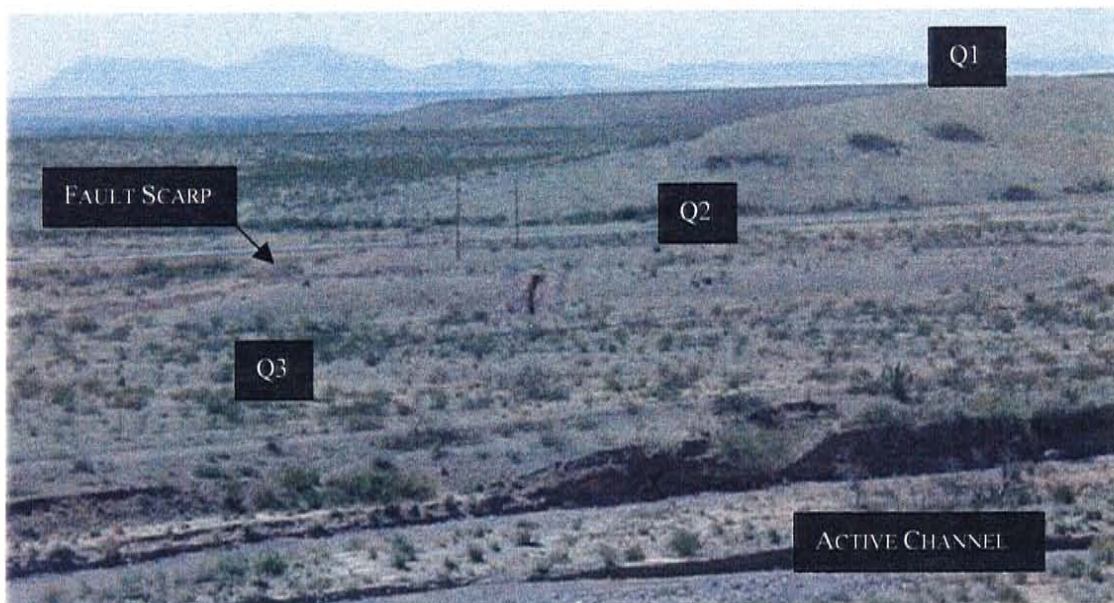
The Socorro Canyon fault (Machette, 1982) is an active normal fault of the central Rio Grande rift. This fault can be traced for 40 km along the west flank of the Socorro Basin (Chamberlin and Harrison, 1996). The fault runs north-northwest and dips to the east. Greater offset with increasing age of Quaternary surfaces is evidence of recurrent movement along the fault (Chamberlin and Harrison, 1996). The portion of the Socorro Canyon fault scarp analyzed in this study is approximately 8 km southwest of Socorro, New Mexico, USA (Figure 3.1) where the fault has displaced two Pleistocene terraces (Qt2 and Qt3) and an alluvial fan (Qf1) (Figure 3.2). We use the Q notation to reference the different geomorphic surfaces. The number after the Q indicates the relative age of a surface. The numbering starts at one for the oldest surface and ascends with decreasing surface age. The *t* represents terrace and the *f* alluvial fan. At the study site, backhoe trenches were oriented perpendicular to two fault scarps and a terrace-riser scarp. These trenches have exposed the soil stratigraphy associated with two geomorphic surfaces (i.e., Qt2 and Qt3).

From the trench cut perpendicular to the fault scarp on Qt2, we collected samples for  $^{36}\text{Cl}$  analysis. By matching the measured cosmogenic  $^{36}\text{Cl}$  concentrations and fault-scarp profile to those predicted from CLARA, we determined the rupture chronology of the Qt2 fault scarp. In addition, the trench exposed the soil stratigraphy of the fault scarp and allowed us to compare the chronology from CLARA to relative ages inferred from the soil geomorphology and stratigraphy.

The colluvium of the Qt2 fault scarp consists of clay to cobble sized material (Appendix 5). The average bulk density of the colluvium is  $1.42 \pm 0.14 \text{ g cm}^{-3}$  (Goldstein, 1998).



**Figure 3.1.** Field site (red line is the approximate location of the trench where samples were collected for  $^{36}\text{Cl}$  analysis).



**Figure 3.2.** Socorro Canyon fault-scarp field site. The view is to the south, in the direction of the fault. The trench in the center of the photo (terrace trench) cuts the terrace scarp between Q2 and Q3. The trench perpendicular to the Q2 fault scarp is to the left of the terrace trench



The soils of the footwall of Qt2 are well developed and exhibit stage III carbonate morphology (Figures 3.3 and 3.4). Other soils formed in gravelly alluvial deposits in the middle and lower Rio Grande Valley that exhibit a similar stage of carbonate development have been dated to the middle to late Pleistocene (Birkland, 1984). A buried soil in the hanging wall and the presence of two colluvial wedges suggest recurrent movement along this fault scarp (Figures 3.3 and 3.4). We obtained the facies map of Figure 3.3 from the stratigraphic log of the Qt2 trench, presented in Appendix 5. From sedimentary textures and geometry of the coarser deposits, we delineated the colluvial wedges shown in Figure 3.3. A colluvial wedge consists of two stratigraphic units, the debris facies and wash facies (McCalpin and Berry, 1996). The debris facies is the material slumped from the footwall during a mass movement, forming a wedge-shaped deposit on the hanging wall. The wedge-shaped deposit results from mass failure shortly after a rupture as the slope of the scarp retreats from the steep 'free face' to the angle of repose (Wallace, 1977). Wash facies forms atop debris facies once the scarp has attained the angle of repose, and slower material transport mechanisms dominate (e.g. soil creep). The slower material transport mechanisms allow soil to develop. Thus, multiple rupture events are recorded by a vertical sequence of mass failures separated by buried soils (McCalpin and Berry, 1996). The presence of two colluvial wedges and buried soil suggest that this fault scarp is the product of a least two ruptures. The greater accumulation of carbonate in the K-horizon of the footwall than the C<sub>k</sub>-horizon of the hanging wall suggests that the first rupture occurred shortly after abandonment of the Qt2 surface (Figure 3.4). Therefore, the first rupture appears to have happened in the middle to late Pleistocene. A small graben located near the land surface (Figure 3.5) has accommodated a third displacement. On the footwall edge of the graben, clasts dip in the direction of the fault plane, evidence of down-faulting and material transport. The opening

created by down-faulting of the graben has been filled with material derived from the footwall, creating a debris facies (Figure 3.3). We believe the fault scarp on the younger terrace (Qt3) adjacent to and north of the Qt2 fault scarp (Figure 3.2) was produced by the same event that created the small graben. The trench perpendicular to the fault-scarp on Qt3 surface has exposed a soil exhibiting stage I carbonate morphology. This degree of soil development in the lower and middle Rio Grande valley is indicative of Holocene age (Birkland, 1984). Therefore, the third rupture is likely Holocene in age.

The Qt2 trench extends ~27 m west of the fault plane into the footwall of the fault and ~10 m into the hanging wall of the fault. At the western extent of the trench, we collected alluvial samples along a vertical transect for  $^{36}\text{Cl}$  analysis. We refer to this transect as the 'control profile'. At the western extent of the trench, the slope of the terrace is gentle ( $<2^\circ$ ), and the soils are well developed (stage III carbonate morphology). The soil horizons descend vertically from an A-horizon (0 m - 0.10 m) to a B<sub>t</sub>-horizon (0.10 m - 0.34 m) to a B<sub>tk</sub>-horizon (0.34 m - 0.49 m) to a K-horizon (0.49 m - 1.09 m) and finally a C<sub>k</sub>-horizon (1.09 m - bottom of the trench). This vertically stacking of horizons is typical of soil stratigraphy where surficial processes and tectonics have little influence on soil development. Based on the degree of soil development where the control profile was sampled, it appears that the surface is stable (i.e. little erosion and aggradation). For example, if there were significant aggradation due to loess accumulation, the A-horizon would be over-thickened ( $>0.10$  m) as pedogenic processes would not keep pace with the deposition of loess. On the other hand, if erosion rates were high, the soil development would be poor and the surface would appear younger than the late Pleistocene. High erosion rates remove material at rates greater than pedogenic processes and therefore B-horizons are either thin or absent.

**Figure 3.3. Facies Map near Fault Plane**

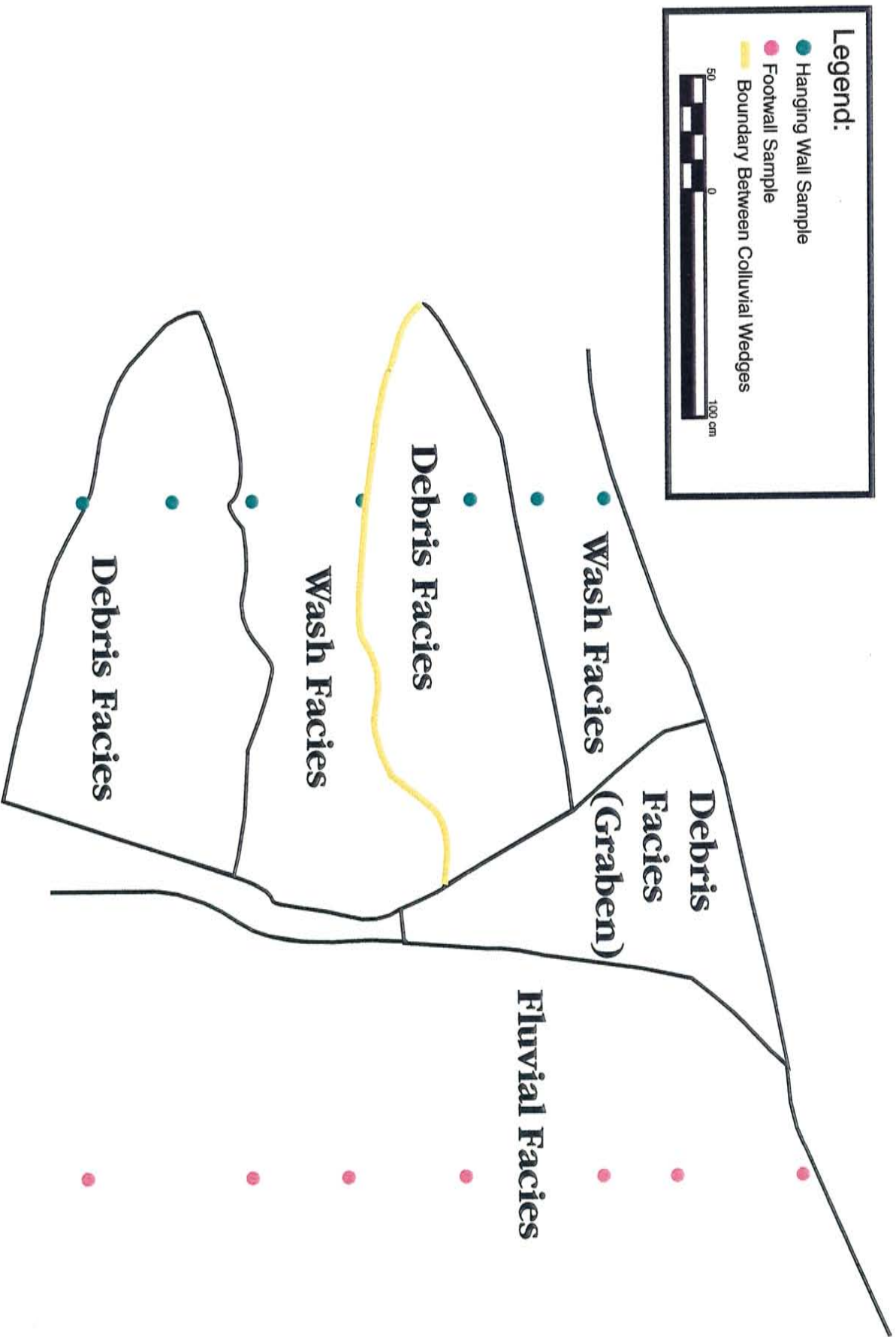
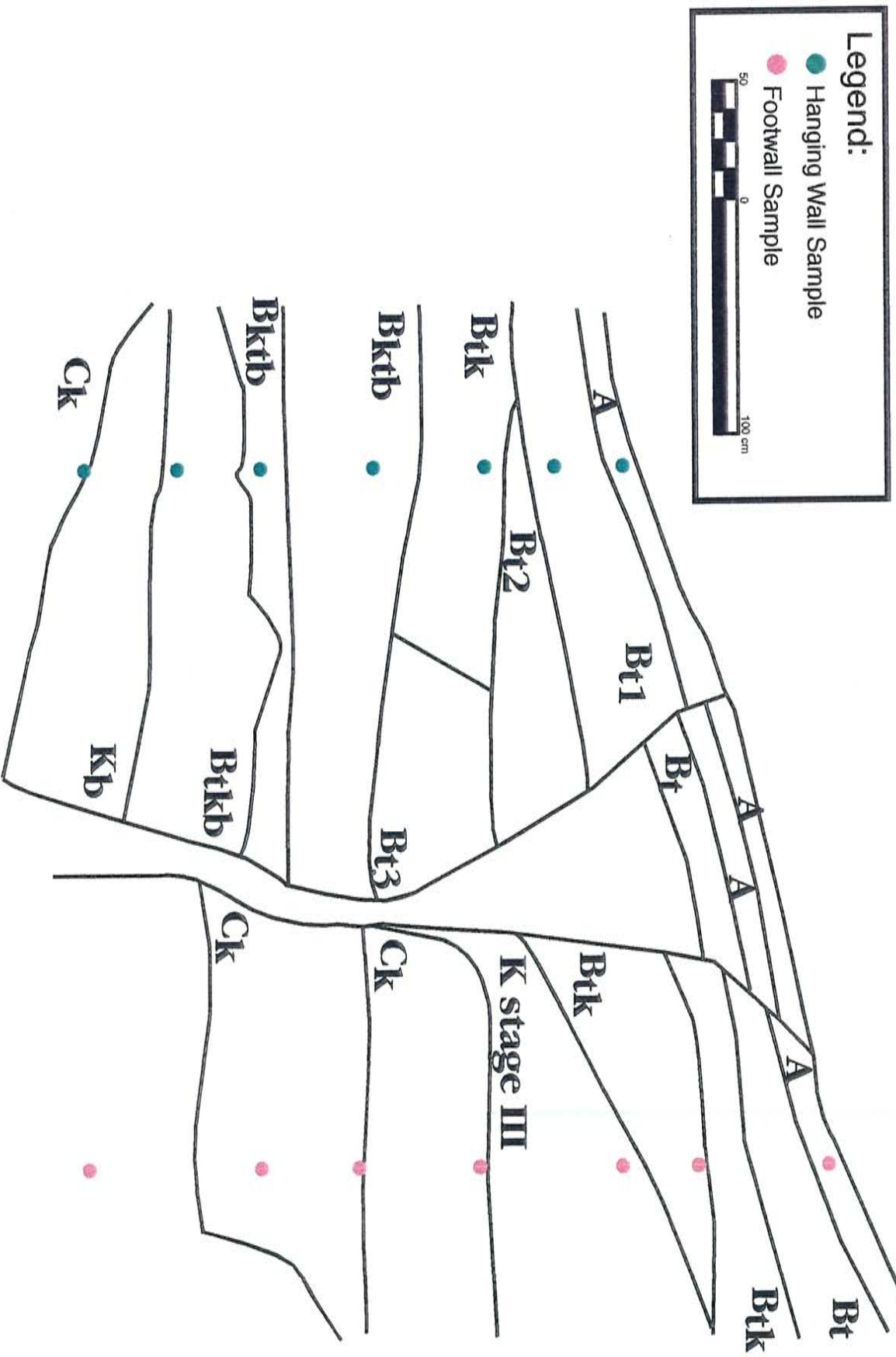


Figure 3.4. Soil Log near the Fault Plane (see Birkland, 1984 for notation)





**Figure 3.5.** Picture of trench showing the stage III carbonate of the footwall, ~2 meters west of the fault plane. String lengths are a meter from nail to nail.

**Figure 3.6.** Picture of graben adjacent to the fault plane.



As part of an extensive study on Quaternary and Pliocene faults in the Albuquerque and Belen Basins, Machette (1982) assessed fault scarp ages of those formed from the Socorro Canyon fault (Figure 3.2). He used the approach of Bucknam and Anderson (1979), plotting maximum scarp slope against scarp height. Bucknam and Anderson (1979) showed the relationship between the two parameters to be linear. Machette (1981) concluded that the smallest scarps (our Qt2 and Qt3) might have formed in the Holocene or latest Pleistocene. However, due to little variability in height over the short length of the fault scarps, they did not provide a well-defined data set for the analysis of Bucknam and Anderson (1979).

Recently, Clark (1998) estimated the ages of the fault scarps on Qt3 and Qt2 at 1.4 to 1.6 ka and 16 to 18 ka, respectively. To obtain these ages, Clark (1998) used previously determined Basin-and-Range geomorphic diffusivities from Hanks and Wallace (1985) and assumed the fault scarps were produced from single displacements. Based on the small size of the offset on the Qt3 surface (0.56 m), the fault scarp of this surface appears to have been created from a single displacement; however, the older terrace (Qt2) is the result of multiple ruptures as discussed above. Therefore, Clark's (1998) age estimate for the Qt2 fault scarp is incorrect.

## 4.0 Methods and Materials

### 4.1 Chlorine-36 and Chemical Analyses

We sampled three vertical transects for  $^{36}\text{Cl}$  and chemical analyses. The samples were collected from the trench cut perpendicular to the Socorro Canyon fault scarp where the fault has displaced the Pleistocene terrace Qt2 (see Section 3). Samples were collected within ~1.5 m of the fault plane for both the footwall and hanging wall. These two profiles were used to calibrate the model CLARA. The third profile was sampled on the terrace tread of the footwall, ~27 m west of the fault. This profile served as a control for verifying the expected shape of the  $^{36}\text{Cl}$  profile under a stable surface, for testing the success of amalgamating many individual clasts, and was used to determine the age of the displaced terrace. Each sample was collected over a ten-centimeter vertical interval.

We retained clasts between 1.5 cm and 0.5 cm for analysis. The minimum number of clasts per sample was specified to be greater than 150. In order to meet the greater than 150 clasts per sample criterion, some fragments chipped from larger clasts were included. The numerous small clasts comprising each sample were homogenized in order to average over the many different individual exposure histories of each clast and thus minimize random variations. The deepest control sample was split and the two aliquots processed independently to test the reproducibility of the sampling and analytical procedures. Samples were ground to a size fraction between 150  $\mu\text{m}$  and 1 mm. Samples were leached with 3% nitric acid to remove meteoric  $^{36}\text{Cl}$  and carbonate. Appendix 6.1 describes the sample collection, preparation, and grinding protocol, and Appendix 6.2 contains the leaching procedure.

Prior to chloride extraction, we removed a portion of each sample for chemical analysis. Boron (B) and gadolinium (Gd) were analyzed by Prompt Gamma Emission Spectrometry

(PGES), and major oxides, uranium (U), and thorium (Th) were measured by X-Ray Florescence (XRF). Carbon as carbonate was analyzed gravimetrically. Whole rock analyzes are needed, because the concentrations of the above elements are necessary to determine cosmogenic  $^{36}\text{Cl}$  production parameter. U and Th are used to calculate the radiogenic  $^{36}\text{Cl}$  inventory.

To analyze for  $^{36}\text{Cl}$ , we followed the procedure of Lui (1994) and extracted chloride from each crushed sample. The samples were dissolved in HF and  $\text{HNO}_3$ , and the solution decanted from residual fluorosilicates. A  $^{35}\text{Cl}$  spike of known concentration and purity was added to each sample. This addition assured that enough  $\text{AgCl}$  was recovered for  $^{36}\text{Cl}/\text{Cl}$  analysis. Chloride was separated from solution by adding  $\text{AgNO}_3$  in order to precipitate  $\text{AgCl}$ .  $\text{AgCl}$  was cleaned of S, because  $^{36}\text{S}$  is an interfering isobar, by dissolving the  $\text{AgCl}$  in  $\text{NH}_4\text{OH}$  and adding  $\text{Ba}(\text{NO}_3)_2$  to precipitate  $\text{Ba}(\text{SO}_4)$ . This was done twice per sample. The  $^{36}\text{Cl}/^{35}\text{Cl}$  ratio and the  $^{37}\text{Cl}/^{35}\text{Cl}$  ratio were measured at the Purdue Rare Isotope Measurement Laboratory (PRIME Lab). Appendix 6 contains a more detailed description of the chloride extraction procedure.

To determine the amount of topographic shielding of the cosmic-ray flux at the study site, we measured horizon angles along the azimuth (compass directions). We measured the horizon angles as the angle from the top of landscape features, such as mountain ranges, to the horizon. The horizon and azimuth angles were entered into CHLOE (Phillips and Plummer, 1996) and a shielding correction factor calculated. In addition to calculating a shielding correction factor, we used CHLOE to determine the sample ratio of  $^{36}\text{Cl}/\text{Cl}$  based on the AMS results, the nucleogenic input of  $^{36}\text{Cl}$ , and the scaling factor for elevation and latitude based on Lal (1991). CHLOE was also used to calculate the amount of chloride in the samples based on the AMS results.



## 4.2 *Fault Scarp Profile*

We surveyed a profile of the Socorro Canyon fault ~2-3 meters north of the Qt2 trench with a theodolite. In addition to using the surveyed profile to calibrate CLARA (section 4.3), we used the profile to determine the total fault displacement and far-field (regional) slope of the offset terrace. For comparison, we also used the Socorro N. Mex. 1:24,000 Quadrangle (USGS, 1971) to determine the far-field slope.

## 4.3 *Model Domain*

To determine a rupture history for the Socorro Canyon fault scarp, we based the space and time domains of CLARA on the sensitivity analysis we performed in Section 2. We used a vertical and horizontal discretization of 0.1 m and 0.5 m, respectively. The lateral specified height boundaries for the numerical solution to the diffusion equation for fault-scarp morphology were located 60 m from the fault plane. The lateral specified flux boundary conditions for the epithermal and thermal neutron fluxes were located 20 m from the fault plane. The upper atmospheric and lower subsurface boundaries were located 10 m from the maximum scarp height and 5 m below the minimum scarp height, respectively. The delta  $\phi$  and delta  $\theta$  in the numerical integration of the cosmic-radiation flux were  $6^\circ$  and  $10^\circ$ , respectively. The timestep used in the numerical solution for fault-scarp morphology was 1 ka; however, the timestep used in determining the spatial distribution of cosmogenic  $^{36}\text{Cl}$  was allowed to vary in order to enhance the computation efficiency of CLARA. After a rupture, the timestep for the first 5 ka was 1 ka; for the next 10 ka, the timestep was 2 ka; and more than 15 ka after a rupture, the timestep was 5 ka. Section 2.4 describes the variable timestep used to more efficiently access  $^{36}\text{Cl}$  production and accumulation.

## 5.0 Results and Modeling

### 5.1 Analytical Results

Tables A7.1 and A7.2, in Appendix 7, present the results from the XRF and PGES analyses for each alluvial sample collected from the Socorro Canyon fault scarp. In Table A7.1, the results from the XRF and PGES analyses are expressed in atoms  $g^{-1}$ , and in Table A7.2, the results are presented as weight percent.  $SiO_2$  is the most abundant (i.e., ~73.1%) oxide in the alluvial material of the Socorro Canyon fault scarp. The average concentrations of K, Ca, and Cl are  $9.34 \times 10^{20} \pm 4.44 \times 10^{19}$  atom  $g^{-1}$ ,  $4.54 \times 10^{19} \pm 1.79 \times 10^{19}$  atom  $g^{-1}$ , and  $4.08 \times 10^{17} \pm 0.61 \times 10^{17}$  atoms  $g^{-1}$ , respectively. The quoted uncertainties represent one standard deviation, calculated from the results of multiple analyses (i.e. 21), and not analytical precision (Table A8.1).

Based on the average chemistry of the alluvium, the total surface production rate is  $23.1 \pm 1.4$  atoms  $g^{-1} yr^{-1}$ . The surface production rates from spallation of K and Ca are  $21.1 \pm 1.0$  atoms  $g^{-1} yr^{-1}$  and  $0.500 \pm 0.195$  atoms  $g^{-1} yr^{-1}$ , respectively. The sum of epithermal and thermal neutron surface production rates is  $1.52 \pm 0.23$  atoms  $g^{-1} yr^{-1}$ , and the surface production rate from muon capture by K and Ca is  $0.0260 \pm 0.0114$  atoms  $g^{-1} yr^{-1}$ . We scaled these production rates to the elevation and latitude of the Socorro Canyon fault study area. We based the uncertainties associated with the production rates on the K, Ca, and Cl standard deviations (Table A8.1)

Tables A7.3 and A7.4, in Appendix 7, contain the results from the AMS analysis and the radiogenic and cosmogenic inventories of  $^{36}Cl$ . The average radiogenic  $^{36}Cl$  concentration, based on the sample concentrations of the U and Th, is  $9.38 \times 10^3 \pm 1.92 \times 10^3$  atoms  $g^{-1}$  (Table A7.3). Figure 5.1 shows the observed cosmogenic  $^{36}Cl$  depth profiles. The control profile shows an exponential decrease in cosmogenic  $^{36}Cl$  concentration with depth and fits an exponential regression with a  $r^2$  of 0.99. The footwall cosmogenic  $^{36}Cl$  depth profile shows a lower

cosmogenic  $^{36}\text{Cl}$  inventory than the control. On the other hand, except for the shallowest sample, the hanging wall concentrations are greater than the concentrations of the control profile. While the footwall and control profiles show a continuous exponential decrease with increasing depth, the hanging wall profile shows discontinuity between the two colluvial wedges and near the land surface.

The cosmogenic  $^{36}\text{Cl}$  concentrations of the two aliquots obtained from splitting the deepest sample of the control profile are within the analytical uncertainty of their AMS results and differ by only 5% (Table A7.3). The cosmogenic  $^{36}\text{Cl}$  concentrations of these two aliquots are  $1.22 \times 10^6 \pm 4.3 \times 10^4$  and  $1.16 \times 10^6 \pm 4.7 \times 10^4$  atom  $\text{g}^{-1}$ . The whole rock chemistries of these two samples are also similar.

## **5.2 Modeling**

In order to compare output from CLARA and CHLOE to the observed cosmogenic  $^{36}\text{Cl}$  depth profiles, we normalized the cosmogenic  $^{36}\text{Cl}$  concentrations of each sample (Table A7.4). CLARA and CHLOE assume a homogeneous subsurface; therefore, in the models, we used average production parameters calculated from the average chemical composition of the samples. Appendix 8.1 contains the average cosmogenic  $^{36}\text{Cl}$  production parameters for the Socorro Canyon fault scarp. Because the production parameters are based on an average chemistry, we normalized each observed cosmogenic  $^{36}\text{Cl}$  concentration to the average surface production in order to account for small differences in the chemical compositions of the samples. We performed the normalization by multiplying the observed cosmogenic  $^{36}\text{Cl}$  concentrations by the ratio of the average surface production to the sample surface production. We based the average surface production on the average chemical composition and the sample surface production rates on the individual sample chemistries.

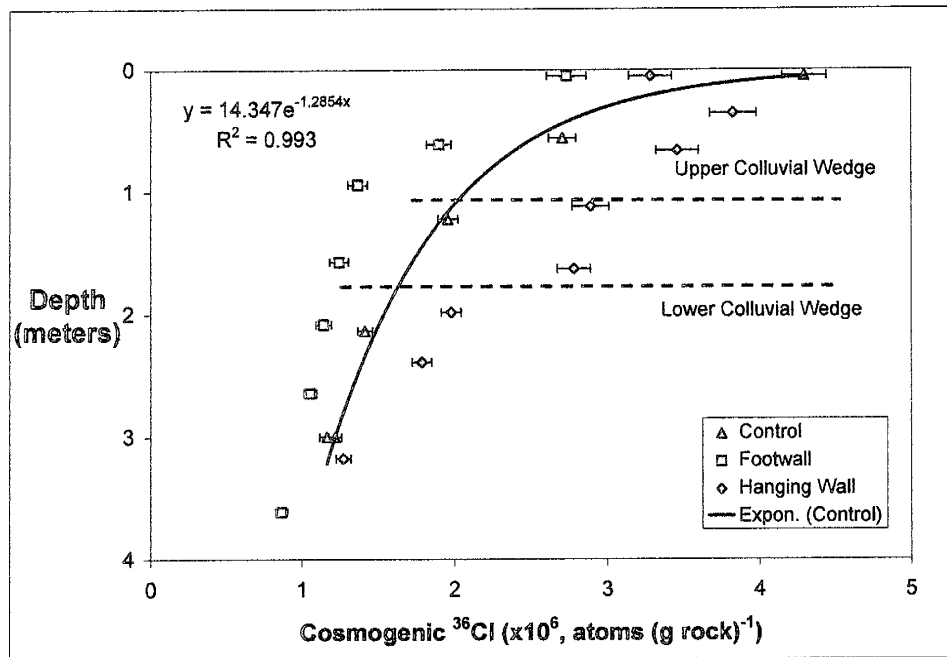


Figure 5.1. Cosmogenic  $^{36}\text{Cl}$  results (data not normalized). Error bars represent the AMS uncertainty. The equation and  $R^2$  value are for the exponential regression of the control profile.

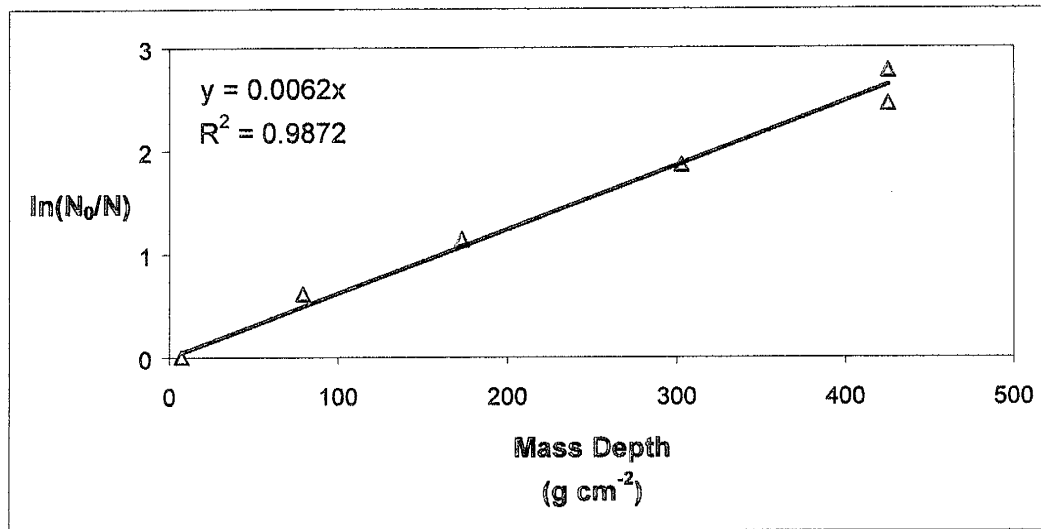


Figure 5.2. Regression analysis of the control profile. Red triangles are the observed values and solid line is a linear regression.  $N$  is the normalized cosmogenic  $^{36}\text{Cl}$  concentration of the samples and  $N_0$  is the surface concentration.  $\lambda_e = 161 \text{ g cm}^{-2}$ , calculated from the regression analysis.

### 5.2.1 Analysis of the Control Profile (Sample Inheritance and Terrace Age)

Using the control profile, we performed a regression analysis to calculate the effective attenuation coefficient ( $\lambda_e$ ) of the secondary cosmic-radiation flux. Figure 5.2 shows the regression analysis. The  $\lambda_e$ , calculated from the slope of the linear regression of Figure 5.2, is  $161 \pm 6 \text{ g cm}^{-2}$ . The uncertainty associated with the attenuation coefficient is based on the maximum AMS uncertainty of the control profile. The  $\lambda_e$  used in CLARA and CHLOE ( $170 \text{ g cm}^{-2}$ ) is  $\sim 5\%$  greater and slightly beyond the uncertainty of the attenuation coefficient calculated from the regression analysis; however, the cosmogenic  $^{36}\text{Cl}$  concentrations of the regression analysis include components from low-energy neutron and muon production.

In addition to the regression analysis, we used the control profile to determine the age of the displaced terrace and an average cosmogenic  $^{36}\text{Cl}$  sample inheritance. The  $^{36}\text{Cl}$  inheritance of a clast is the amount of cosmogenic  $^{36}\text{Cl}$  accumulated by the clast prior to being deposited and incorporated into the alluvial material of the terrace or alluvial fan. Because  $^{36}\text{Cl}$  concentrations can vary between clasts of the same sample due to variations in the exposure history of individual clasts, each sample was amalgamated from many clasts in order to average over the many individual exposure histories (Section 4.1). The sample inheritance represents the asymptotic cosmogenic  $^{36}\text{Cl}$  concentration at depth. For example, if a profile contained no inheritance the asymptotic concentration would be  $\sim 0$  due to the lack of inheritance and attenuation of the cosmic-ray flux at depth. We obtained the sample inheritance and age of the displaced terrace by fitting a modeled cosmogenic  $^{36}\text{Cl}$  profile to the control profile. To perform the profile matching, we used the spreadsheet model CHLOE (Phillips and Plummer, 1996) and assumed aggradation and erosion of the terrace tread have been negligible. The soil stratigraphy exposed at the western extent of the backhoe trench supports the assumption of little aggradation

and erosion (Section 3). The sample inheritance and terrace age were determined by minimizing the chi-squared-error between modeled (M) and observed (O) cosmogenic  $^{36}\text{Cl}$  concentrations using the terrace age and sample inheritance as fitting parameters (Equation 5.1).

$$Error = \sum_{i=1}^n \frac{(O_i - M_i)^2}{S_i^2} \quad (5.1)$$

In equation 4.1,  $S_i$  is the standard deviation of the  $i^{\text{th}}$  sample. We specified the standard deviation of each sample at 15% the observed concentration. We arrived at a 15% standard deviation by adding 2% to a mean-corrected standard deviation of Phillips et al. (in press). By comparing cosmogenic  $^{36}\text{Cl}$  ages to independent ages, Phillips et al. (in press) calculated a mean deviation (bias) of ~5% between  $^{36}\text{Cl}$  and independent ages with a standard deviation of 18%. Correcting the standard deviation to zero mean yields 13%. We added 2% to the corrected standard deviation to provide a conservative estimate of the sample standard deviation. This standard deviation includes uncertainty associated with  $^{36}\text{Cl}$  production rates, sample depths, and analytical protocols.

In determining the terrace age and inherited cosmogenic  $^{36}\text{Cl}$ , we omitted the upper most sample of the control profile when minimizing the chi-squared-error (Equation 5.1). We excluded the upper most sample because the cosmogenic  $^{36}\text{Cl}$  concentration of that sample appeared anomalously high when compared to the exponential trend of the deeper samples of the control profile. Phillips (personal communication) has observed this phenomenon (i.e., high cosmogenic  $^{36}\text{Cl}$  surface concentrations) elsewhere in samples collected from alluvium. The anomalous concentrations commonly observed in shallow samples are apparently because the top few centimeters of the soil are actively creeping downslope.

Figure 5.3 shows the agreement between the observed and modeled cosmogenic  $^{36}\text{Cl}$  depth profiles. The combination of terrace age and inherited cosmogenic  $^{36}\text{Cl}$  that yields the minimum

chi-squared-error is  $122 \pm 18$  ka and  $9.87 \times 10^5 \pm 3.9 \times 10^4$  atoms  $g^{-1}$ , respectively. We base the uncertainty associated with the sample inheritance on the maximum AMS uncertainty (4.0%) of the control profile. The uncertainty associated with the terrace age is based on the standard deviation of cosmogenic  $^{36}Cl$  ages, estimated as described above from the data of Phillips et. al (in press). In Figure 5.3, the value of  $9.87 \times 10^5$  atoms  $g^{-1}$  is the asymptotic cosmogenic  $^{36}Cl$  concentration at depth. The inherited concentration is equivalent to  $43 \pm 2$  ka of surface exposure to cosmic radiation, given the average bulk density of the alluvium and average chemical composition of the clasts.

### 5.2.2 Analysis of the Footwall and Hanging Wall Profiles (Rupture History)

To determine a rupture chronology for the Socorro Canyon fault scarp on the Qt2 surface, we used the geomorphic diffusivity and timing of two ruptures as fitting parameters in the model CLARA. As discussed in Section 3, the Socorro Canyon fault has ruptured three times since abandonment of the Qt2 surface. However, we simulated only two ruptures for the following two reasons: 1) a small graben appears to have accommodated the third, most recent rupture (Figure 3.3 and 3.6) and, (2) geological evidence indicates that the most recent rupture was quite recent (a few thousand years ago) and therefore it has had little effect on the cosmogenic nuclide profiles except eroding some alluvium off of the footwall of the scarp. To accommodate the geomorphic effects of the third, most recent rupture we added 50 cm to the sample depths of the footwall profile. Fifty centimeters is the amount of displacement on the Qt3 surface. As discussed in Section 3, we believe the tectonic event that created the graben also produced the fault scarp on the Qt3 surface. Figure 3.3 shows the proximity of the sampled footwall profile to the graben (~50 cm). The location where we collected samples from the hanging wall is more than a meter east of the graben. It appears that after the most recent rupture material was

deposited in the opening created by the graben rather than above the location where we collected the hanging wall samples. Therefore, we did not adjust the sample depths of the hanging wall profile. To recapitulate, our reconstruction indicates that the only significant effect of the most recent rupture, a few thousand years ago, was to cause ~50 cm of alluvium to be eroded off the footwall of the fault scarp (at the location of the footwall profile). Given the short time since that rupture, little buildup of cosmogenic nuclides has occurred and we have therefore accounted for the effects of the rupture only by “adding back” the 50 cm of alluvium that recently eroded from the footwall.

The remaining offset (~3.5 m) we attribute to displacement during the first and second ruptures. Our estimate of the size of the first rupture was based on the thickness of the lower colluvial wedge (~1.7 m). The second offset (~1.8 m) was assigned the difference between the total offset and first offset.

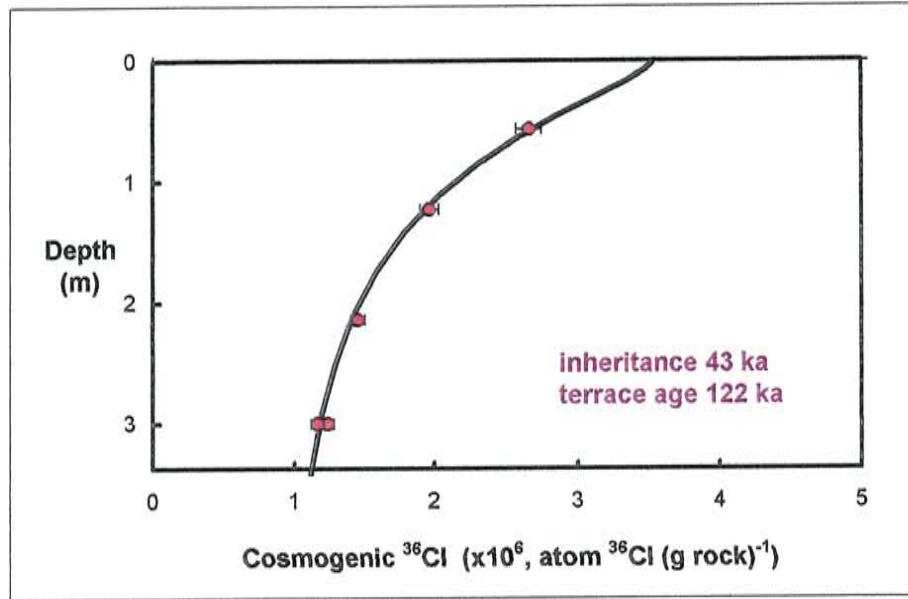
We obtained the rupture history and geomorphic diffusivity by fitting modeled and observed cosmogenic  $^{36}\text{Cl}$  depth profiles of the footwall and hanging wall, and modeled and observed profiles for the Socorro Canyon fault scarp. Each combination of geomorphic diffusivity and rupture ages generated a modeled fault-scarp profile that matched the observed profile. While each combination of rupture ages and geomorphic diffusivity produced similar fault-scarp profiles, the combinations when entered into CLARA gave different spatial distributions for the accumulation of cosmogenic  $^{36}\text{Cl}$ . By minimizing the chi-squared-error between the modeled (M) and observed (O) cosmogenic  $^{36}\text{Cl}$  concentrations (Equation 5.1), we obtained the rupture chronology and geomorphic diffusivity of the Socorro Canyon fault scarp. The modeled profiles of the footwall and hanging wall, used for comparison against the observed profiles, were located 1.5 m on either side of the fault plane (the same location as the observed profiles). In order to



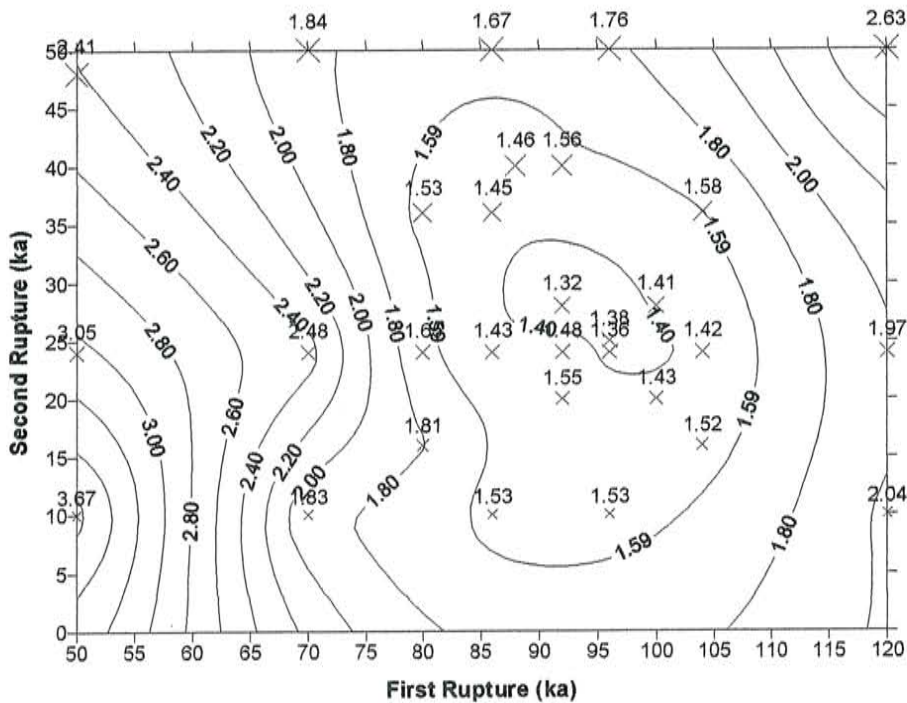
avoid discretization errors, we linearly interpolated the calculated cosmogenic  $^{36}\text{Cl}$  concentrations between nodes above and below the sample depths to obtain our modeled values for comparison to the observed. The rupture ages and geomorphic diffusivity of each CLARA simulation, along with output from CLARA, are in the Excel file 'model outputs' on the appended 3.5" diskette.

We did not use the soil surface samples in the profile fitting of either the hanging wall or footwall profiles because they came from the active layer of the soil and gave anomalous cosmogenic  $^{36}\text{Cl}$  concentrations. The deepest footwall samples also appeared anomalous and were not used in the chi-squared. When we subtracted the sample inheritance from the cosmogenic  $^{36}\text{Cl}$  concentration of the deepest footwall sample, the result was a negative concentration. When we included the second deepest footwall sample in the calculation of the chi-squared, the value was two orders of magnitude greater than the chi-squared calculated without the sample. Therefore, we excluded the sample because it so strongly biased the final rupture history.

In Figure 5.4, we plot the reduced chi-squared-error as a function of the Socorro Canyon fault rupture history. The reduced chi-squared-error is the chi-squared-error of equation 4.1 divided by  $n-2$  degrees of freedom where  $n$  is the number of samples (i.e., 11). The rupture history that yields the best fit between modeled and observed cosmogenic  $^{36}\text{Cl}$  of the footwall and hanging wall is  $92^{+16}_{-13}$  ka for the first rupture and  $28^{+18}_{-23}$  ka for the second rupture. This rupture history yields the smallest value of the reduced chi-squared-error seen in the contour plot of Figure 5.4. Table A9.1 in Appendix 9 provides a summary of the results from each simulation and includes reduced chi-square-errors calculated from only the footwall samples, only the hanging wall samples, and both profiles (i.e., the values of Figure 5.4). The geomorphic



**Figure 5.3.** Cosmogenic  $^{36}\text{Cl}$  age of the displaced terrace (Q2 surface). Solid line is the modeled inventory and the red circles are the observed concentrations. The modeled profile was generated with an exposure age of 122 ka and  $9.87 \times 10^5$  atoms  $^{36}\text{Cl}$   $\text{g}^{-1}$  of inheritance.



**Figure 5.4.** Values above the symbols represent the reduced chi-squared-error as a function of the Socorro Canyon fault rupture history. The reduced chi-squared-error was calculated from equation 4.1 and normalizing the chi-squared-error from equation 4.1 by 9 degrees of freedom. The 1.59 contour confines the 70% confidence region.

diffusivity associated with the above rupture history is  $0.4_{-0.1}^{+0.4} \text{ m}^2 \text{ ka}^{-1}$ . The uncertainty limits calculated for the rupture event ages and the geomorphic diffusivity were obtained from the limits of the region bound by the 1.59 contour in the Figure 5.4 (Press, et. al, 1992) and are significant at the 70% confidence level. The value of 1.59 represents the sum of the smallest reduced chi-square-error from the rupture history analysis (1.32) plus the value of the chi-squared-error at a 70% confidence level minimized by 2 degrees of freedom (0.27). The 2 degrees of freedom are to account for the use of the timing of the two ruptures as fitting parameters. The confidence limits on the rupture ages were determined by projecting the boundary of the 70% confidence region onto the horizontal and vertical axes of Figure 5.4. The use of higher confidence levels (e.g., 90%) would have resulted in possible negative ages for the second rupture event. We based the limits on the geomorphic diffusivity on the minimum and maximum values from the simulations bound by the 1.59 contour. Figure 5.5 shows the modeled and observed profiles of the hanging wall and footwall. Figure 5.6 shows modeled and observed fault-scarp profiles.

In Figure 5.4, values of the reduced chi-squared-error surrounding the minimum show minor oscillations (i.e., hills and valleys). The oscillations are probably a consequence of numerical errors in CLARA. Although we may not have exactly identified the true minimum, the region surrounding 92 ka and 28 ka does define an area where the reduced chi-squared-error is minimized.

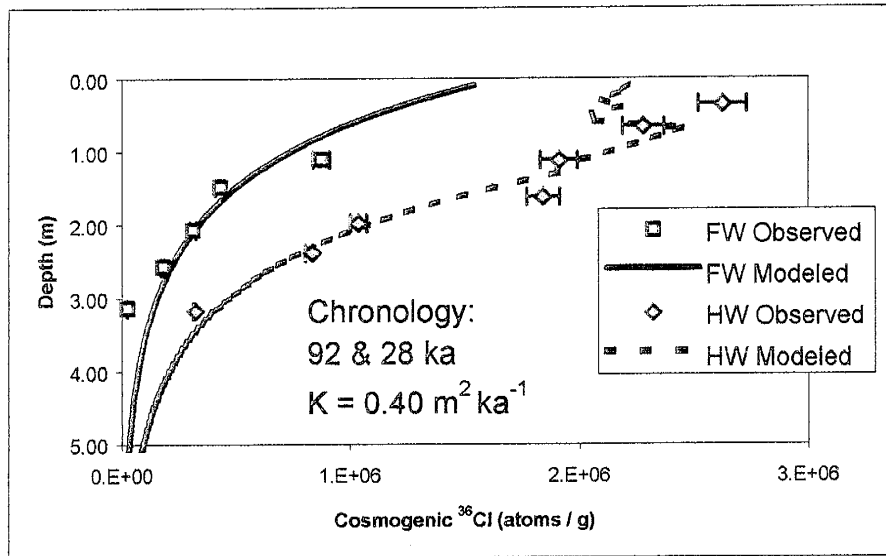


Figure 5.5. Cosmogenic  $^{36}\text{Cl}$  inventories of the footwall and hanging wall. Solid and dashed lines represent the modeled profiles for the footwall and hanging wall respectively. For the modeled profiles, the rupture history that yields the lowest sum of the chi-squared-error is plotted (see Figure 5.4). The symbols are the observed inventories and error bars represent the AMS analytical uncertainty.

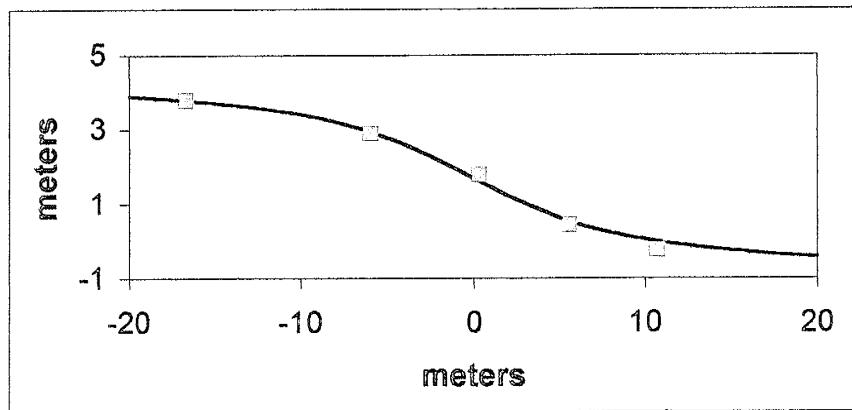


Figure 5.6. Modeled (solid line) and observed (symbols) fault-scarp profiles of the Socorro Canyon fault

## 6.0 Discussion

By specifying the minimum number of clasts per sample to be greater than 150, we obtained alluvial samples representative of the exposure history of the Socorro Canyon fault scarp and the displaced terrace. This is evidenced by the spatial patterns of the three sampled profiles, which show predicted trends, and the AMS results of the two aliquots split from the deepest control sample. The two aliquots, which were processed and analyzed independently, are within the analytical uncertainty of their AMS results demonstrating the reproducibility of the sampling and laboratory protocols. By homogenizing the numerous small clasts of each sample, we were able to discern the inherited cosmogenic  $^{36}\text{Cl}$  inventory from that due to abandonment and displacement of the terrace. The average inherited exposure age of the clasts is  $42\pm 2$  ka (equivalent to a surface concentration of  $9.87\times 10^5\pm 3.9\times 10^4$  atoms  $^{36}\text{Cl g}^{-1}$ ).

The  $122\pm 18$  ka terrace age is coincident with the Eemian interglacial period revealed in the delta  $^{18}\text{O}$  record of the Greenland Ice-core Project Summit ice core (Dansgaard, 1993). The calculated age of the displaced terrace is consistent with the stage III carbonate morphology of the terrace soil. Other soils formed in similar gravelly alluvial deposits in the middle and lower Rio Grande Valley that exhibit a similar stage of carbonate development have been dated to the late Pleistocene (Birkland, 1984).

To determine the terrace age, we assumed that where the control profile was sampled erosion has been negligible. To examine the assumption, we used the diffusion equation (Equation 1.1) and the geomorphic diffusivity ( $0.4 \text{ m}^2 \text{ ka}^{-1}$ ) we determined from CLARA to calculate an erosion rate of  $\sim 3.3\times 10^{-3} \text{ mm ka}^{-1}$ . Based on this erosion rate, since the time of abandonment ( $\sim 122$  ka ago) to the present  $\sim 0.4$  mm of material has been eroded from the surface where the control

profile was sampled. This small amount of erosion has an insignificant influence on observed cosmogenic  $^{36}\text{Cl}$  concentrations.

In using CLARA to determine the rupture history of the Socorro Canyon fault scarp on the Qt2 surface, we arrived at ages for the first and second rupture of  $92_{-13}^{+16}$  ka and  $28_{-23}^{+18}$  ka, respectively. The age estimates concur with the soil geomorphology and stratigraphy. For example, the difference between the  $^{36}\text{Cl}$  terrace and first rupture ages is only 30 ka. The age difference is consistent with the contrast in carbonate development between the K-horizon of the footwall and the  $C_k$ -horizon of the hanging wall. The difference in carbonate development suggests that the first rupture is likely late Pleistocene in age, occurring shortly after abandonment of the Qt2 surface (Figure 3.4). Additionally, a buried soil atop the lower colluvial wedge (Figure 3.4) indicates a period of tectonic quiescence between the first and second ruptures. CLARA shows a 64-ka period of tectonic inactivity between the first two ruptures. Previous chronological studies on this portion of the Socorro Canyon fault scarp, provided age estimates of latest Pleistocene to Holocene (Machette, 1982) and 16 to 18 ka (Clark, 1998). However, these age estimates assume the fault scarp was created from a single rupture. Interestingly, applying the geomorphic diffusivity we determined ( $0.4 \text{ m}^2 \text{ ka}^{-1}$ ) to the morphologic ages (i.e. product of age and diffusivity) of Clark (1998) yields an fault scarp age of  $\sim 42$  ka. This age estimate is only slightly greater (1.5 times) than age of the second rupture ( $28_{-23}^{+18}$  ka).

Using the morphologic dating technique, the age of the fault scarp on the Qt3 surface has been estimated at 1.4 to 1.6 ka ago (Clark, 1998). The age estimate is reasonable because the Qt3 terrace soil is weakly developed, exhibiting stage I carbonate morphology that is indicative of Holocene age for soils in the lower and middle Rio Grande valley (Birkland, 1984). Although

the age estimate is based on a geomorphic diffusivity ( $1.1\text{--}1.0 \text{ m}^2 \text{ ka}^{-1}$ ) twice the value we determined for the fault scarp on the Qt2 surface, the range seems responsible given the poor cohesiveness of the alluvium of the Qt3 surface.

Our study of the rupture history of the Socorro Canyon fault scarp required the analyses of the  $^{36}\text{Cl}$  content and whole rock chemistry of 21 samples. This number of analyses imposed a significant cost on the project, but was necessary due to the complex rupture history of the portion of the Socorro Canyon fault scarp we analyzed. We hypothesize that for a fault scarp produced from a single rupture, a much smaller number of samples may be required to determine the age of the fault scarp and geomorphic diffusivity, thereby, reducing project cost. One possible approach would be to collect only two samples, located near the land surface and on the footwall, one near the fault plane and the second distal the fault plane. These positions are similar to the control and footwall sample locations used in this study. The samples should be collected at shallow depths rather than from the surface due to the anomalously high cosmogenic  $^{36}\text{Cl}$  concentrations of surface samples (Phillips, personal communication). In addition to the samples, a surveyed profile of the scarp would also be needed.

Figures 6.1 and 6.2 demonstrate how the fault-scarp age and geomorphic diffusivity might be determined based on the collection of two footwall samples and a survey of the fault scarp. Figure 6.2 shows age and geomorphic diffusivity contours as function of dimensionless width ( $W_d$ ) and normalized cosmogenic  $^{36}\text{Cl}$  concentrations of the footwall. The dimensionless width is given by

$$W_d = \frac{|X_{86} - X_{16}|}{2a} \quad (5.1)$$

where  $X_{86}$  and  $X_{16}$  are the horizontal locations where the heights are 86% ( $Z_{86}$ ) and 16% ( $Z_{16}$ ) of the total offset ( $2a$ ), respectively. The reduced cosmogenic  $^{36}\text{Cl}$  concentration, calculated from

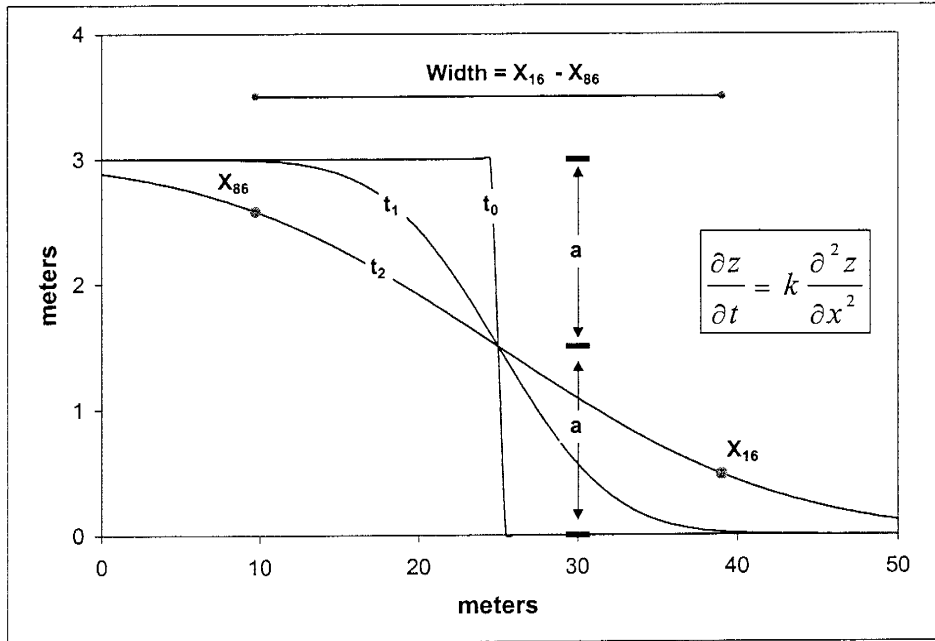
the two footwall samples, is calculated as the difference between the concentration distal to the fault plane and the concentration near the fault plane, normalized by the surface production rate of cosmogenic  $^{36}\text{Cl}$  at the field site (Equation 5.2).

$$N_r = \frac{N_c - N_f}{P_s} \quad (5.2)$$

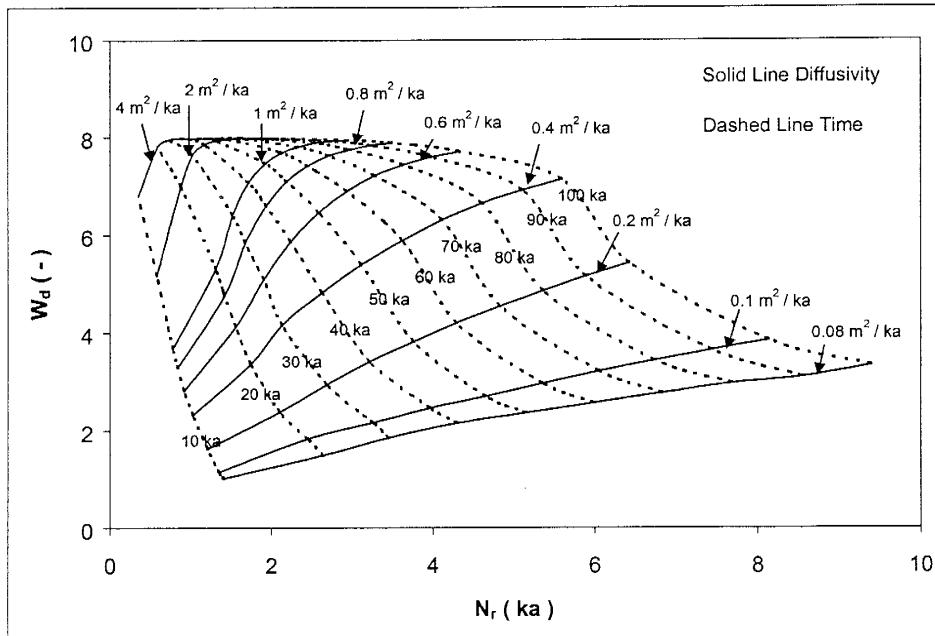
In Equation 5.2,  $N_c$  and  $N_f$  are the cosmogenic  $^{36}\text{Cl}$  concentrations of the control (distal to the fault plane) and footwall (near the fault plane) and  $P_s$  is the surface production rate. The difference between  $N_c$  and  $N_f$  represents the  $^{36}\text{Cl}$  concentration due to exposure after the rupture. The difference removes the cosmogenic  $^{36}\text{Cl}$  inventory due to sample inheritance and the exposure period between the abandonment and rupture of the surface. By representing the normalized cosmogenic  $^{36}\text{Cl}$  concentration and dimensionless width of a fault scarp on a plot similar to Figure 5.2, which was generated from CLARA, it may be possible to determine a unique fault scarp age and geomorphic diffusivity.

CLARA provides a new means for assessing rupture chronologies. By coupling fault-scarp diffusion with the production and accumulation of a cosmogenic nuclide, we determined the rupture chronology for a portion of the Socorro Canyon fault scarp that is consistent with soil geomorphology and stratigraphy. Although we collected numerous samples, we hypothesize that for a fault scarp produced from a single rupture CLARA can be used to determine the age of the fault scarp from only a few samples.





**Figure 6.1.** Parameters used in the analysis of single offset scarps.  $a$  is half the total offset and  $W_d = \text{Width}/2a$ .



**Figure 6.2.** Plot illustrating the analysis of single-offset scarps. Contour plot of age and geomorphic diffusivity as a function of the normalized fault-scarp diffusion and cosmogenic  $^{36}\text{Cl}$  accumulation parameters.

## Bibliography

## Bibliography

- Andrews, D. J. and Buchnam, R. C. (1987) Fitting degradation of shoreline scarps by a model with nonlinear diffusion: *J. Geophys. Res.* **90** 12,857-12,867.
- Andrews, D. J. and Hanks, T. C. (1985) Scarp degraded by linear diffusion: Inverse solution for age: *J. Geophys. Res.* **90** 10,193-10,208.
- Aruscavage, P.J. and Campbell, E.Y. (1987) An ion-selective electrode method for determination of chlorine in geological materials: *Talanta* v. 28, p. 745-749.
- Avouac J.-P. (1993) Analysis of scarp profiles: Evaluation of errors in morphologic dating: *J. Geophys. Res.* **98** 6745-6754.
- Bell, J. W., Brune, J. N., Liu, T., Zreda, M., and Yount J. C. (1998) Dating precariously balanced rocks in seismically active parts of California and Nevada: *Geology* **26** 495-498.
- Bierman, P. R., Gillespie, A. R., and Caffee, M. W. (1995) Cosmogenic ages for earthquake recurrence intervals and debris flow fan deposition, Owens Valley, California: *Science* **270** 447-449.
- Birkland, P. W. (1984) *Soil and Geomorphology*, Oxford University Press New York, pp. 372.
- Bucknam R.C. and Anderson R. E. (1979) Estimation of fault-scarp ages from a scarp-height-slope-angle relationship: *Geology* **7** 11-14.
- Chamberlin, R. M. and Harrison, J. B. J. (1996) Pliocene and Pleistocene displacement history of the Socorro Canyon fault, central Rio Grande Rift: *New Mexico Geology* **18** 45.
- Clark, J. A. (1998) Morphologic dating of fault scarps along the Socorro Canyon fault, Socorro, NM: In *Soil, Water, and Earthquakes around Socorro, New Mexico: Field Trip Guidebook for Rocky Mountain Cell, Friends of the Pleistocene, September 10-13, 1998* (ed. J.B.J Harrison), Socorro, New Mexico, pp. .
- Cerling T. E. and Craig H. (1994) Geomorphology and in-situ cosmogenic isotopes: *Ann. Rev. Earth Planet. Sci.* **22** 273-317.
- Colman, S. M. and Watson, Ken (1983) Ages estimated from a diffusion equation model for scarp degradation: *Science* **221** 263-265.
- Coulson, K. L. (1975) *Solar and Terrestrial Radiation*, Academic Press, New York, pp. 312.
- Dansgaard, W., Johnsen, S. J., Clausen, H. B., Dahl-Jensen, D., Gundestrup, N. S., Hammer, C. U., Hvidberg, C. S., Steffensen, J. P., Sveinbjornsdottir, A. E., Jouzel, J., and Bond, G. (1993) Evidence for general instability of past climate from a 250-kyr ice-core record: *Letters to Nature* **364** 218-220.
- Elmore, D. and Phillips, F. M. (1987) Accelerator mass spectrometry for measurement of long-lived radioisotopes: *Science* **236** 543-550.
- Elsheimer, H.N. (1987) Application of an ion-selective electrode method to the determination of chloride in 41 international geochemical reference materials: *Geostandards Newsletter*, v. 11, p. 115-122.
- Enzel Y., Amit, R., Harrison, J.B.J., Porat, N. (1994) Morphologic dating of fault scarps and terrace risers in the southern Arava, Israel: Comparison to other age-dating techniques and implications for paleoseismicity: *Isr. J. Earth Sci.* **43** 91-103.

- Goldstein, H. (1998) Socorro Canyon fault summary: In *Soil, Water, and Earthquakes around Socorro, New Mexico: Field Trip Guidebook for Rocky Mountain Cell, Friends of the Pleistocene, September 10-13, 1998* (ed. J.B.J Harrison), Socorro, New Mexico, pp. .
- Gosse, J. C. and Phillips, F. M. (in press) Terrestrial cosmogenic nuclides: Theory and application: submitted to: *Quaternary Science Review*.
- Hanks, T. C. (1998) The age of scarplike landforms from diffusion-equation analysis: In *Dating and Earthquakes: Review of Quaternary Geochronology and Its Application to Paleoseismology*, NUREG/CR-5562 (ed. J.M. Sowers, J.S. Noller, and W.R. Lettis) Office of Nuclear Regulatory Research, U.S. Nuclear Regulatory Commission, Washington, D.C., pp. 2-497 – 2-536.
- Hanks, T. C. and Andrew D. J. (1989) Effect of far-field slope on morphologic dating of scarplike landforms: *J. Geophys. Res.* **94** 565-573.
- Hanks, T. C. and Wallace, R. E. (1985) Morphologic analysis of the Lake Lahontan and Beachfront fault scarps, Pershing County, Nevada: *Bull. Seismol. Soc. Am.* **75** 835-846.
- Lal, D. (1991) Cosmic ray labeling of erosion surfaces: *in situ* nuclide production rates and erosion models: *Earth and Planetary Science Letters* **104** 424-439.
- Lui, B. (1994) Cosmogenic  $^{36}\text{Cl}$  dating of geomorphic surfaces and isotopic investigation of soil water and paleoclimate, Ajo Mountains, southern Arizona: Ph.D. Dissertation, New Mexico Institute of Mining and Technology.
- Liu, B., Phillips, F. M., Fabryka-Martin J. T., Fowler M. M., and Stone W. D. (1994) Cosmogenic  $^{36}\text{Cl}$  accumulation in unstable landforms, 1. Effects of the thermal neutron distribution: *Water Resour. Res.* **30** 3115-3125.
- Martin, Y. and Church M. (1997) Diffusion in landscape development models: on the nature of basic transport relations: *Earth Surf. Processes Landforms* **22** 273-279.
- McCalpin, J. P. and Berry, E. M. (1996) Soil catenas to estimate ages of movements on normal fault scarps, with an example from the Wasatch fault zone, Utah, USA: *Catena* **27** 265-286.
- Nash, David B. (1980) Morphologic dating of degraded normal fault scarps: *Geology* **88** 353-360.
- Nash, David B. (1984) Morphologic dating of fluvial terrace scarps and fault scarps near West Yellowstone, Montana: *Geol. Soc. Am. Bull.* **95** 1413-1424.
- Nash, David B. (1986) Morphologic dating and modeling degradation of fault scarps: In *Active Tectonics: National Research Council Studies in Geophysics*. National Academy Press, Washington, D.C., pp. 181-194.
- Niviere, B., Marquis G., and Maurin J.-C. (1998) Morphologic dating of slowly evolving scarps using a diffusive analogue: *Geophys. Res. Lett.* **25** 2325-2328.
- Machette, M.N. (1982) Quaternary and Pliocene faults in the La Jencia and southern part of the Albuquerque-Belen Basins, New Mexico: Evidence of fault history from fault-scarp morphology and Quaternary geology: in Albuquerque Country II, In *New Mexico Geological Society Thirty-Third Annual Field Conference Guide Book* (Grambling, J.A. and Wells, S.G.; eds.), 4-6 November 1982, New Mexico Bureau of Mines and Mineral Resources, Socorro, p. 161-169.

- Phillips, F. M., Stone, W. D., and Fabryka-Martin J. T. (in press) An improved approach to calculating low-energy cosmic-ray neutron fluxes near the land/atmosphere interface: submitted to: *Chem. Geol.*
- Phillips, F. M., Leavy B. D., Jannik, N. O., Elmore, D., and Kubik, P.W. (1986) The accumulation of cosmogenic chlorine-36 in rocks: A method for surface exposure dating: *Science* **231** 41-43.
- Phillips F. M. and Plummer M. A. (1996) CHLOE: A program for interpreting in-situ cosmogenic nuclide data for surface exposure dating and erosion studies: *Radiocarbon (Abstr. 7th Int. Conf. Accel. Mass Spectrom.)* **38** 98-99.
- Pierce, K. L. and Colman, S. M. (1986) Effect of height and orientation (microclimate) on geomorphic degradation rates and processes, late-glacial terrace scarps in central Idaho: *Geol. Soc. Am. Bull.* **97** 869-885,
- Press, W. H., Teukolsky, S. A, Vetterling, W. T., and Flannery, B. P. (1992) *Numerical recipes in fortan 77: The art of scientific computing*, Cambridge University Press New York, pp. 684-694.
- Siame, L. L., Bourles, D. L., Sebrier, M., Bellier, O., Castano, J. C., Araujo, M., Perez, M., Raisbeck, G. M., and Yiou, F. (1997) Cosmogenic dating ranging from 20 to 700 ka of a series of alluvial fan surfaces affected by the El Tigre fault, Argentina: *Geology* **25** 975-978.
- Stone, J. O. H., Evans, J. M., Fifield, L. K., Allan, G. L., and Cresswell, R. G. (1998) Cosmogenic chlorine-36 production in calcite by muons: *Geochim. Cosmochim. Acta.* **62** 433-454.
- Van der Woerd, J., Ryerson, F. J., Tapponnier P., Gaudemer, Y., Finkel, R., Meriaux, A. S., Caffee, M., Guoguang, Z., and Qunlu, H. (1998) Holocene left-slip rate determined by cosmogenic surface dating on the Xidatan segment of the Kunlun fault (Qinghai, China): *Geology* **26** 695-698.
- Wallace, Robert E. (1977) Profile and ages of young fault scarps, north-central Nevada: *Geol. Soc. Am. Bull.* **88** 1267-1281.
- Wang, H. F., and Anderson, M. P. (1982) *Introduction to groundwater modeling: Finite difference and finite element methods*, W.H. Freeman and Co. San Francisco, pp. 237.
- Zreda, M.G. (1994) Development and calibration of the cosmogenic <sup>36</sup>Cl surface exposure dating method and its application to the chronology of late Quaternary glaciations: Ph.D. dissertation, New Mexico Institute of Mining and Technology, Socorro, 318 p.
- Zreda, M. G. and Noller, J. S. (1998) Ages of prehistoric earthquakes revealed by cosmogenic chlorine-36 in a bedrock fault scarp at Hebgen Lake. *Science* **282**, 1097-1099.
- Zreda, M. G. and Phillips, F. M. (1998) Quaternary dating by cosmogenic nuclide buildup in surficial materials: In *Dating and Earthquakes: Review of Quaternary Geochronology and Its Application to Paleoseismology*, NUREG/CR-5562 (ed. J.M. Sowers, J.S. Noller, and W.R. Lettis) Office of Nuclear Regulatory Research, U.S. Nuclear Regulatory Commision, Washington, D.C., pp. 2-101 – 2-127.
- Zreda, M. G., Phillips, F. M., Elmore D., Kubik, P. W., Sharma P., and Dorn, R. I. (1991) Cosmogenic chlorine-36 production rates in terrestrial rocks: *Earth Planet. Sci. Lett.* **105** 94-109.

## Table of Appendices:

Appendix 1.1. CLARA README FILE .....	A2
Appendix 2.1. Analytical Solution to the Diffusion Equation for Fault-Scarp Morphology.....	A4
Appendix 2.2. Analytical Solution for Spallation Production.....	A5
Appendix 2.3. Analytical Solution for the Epithermal Neutron Flux.....	A6
Appendix 2.4. Analytical Solution for the Thermal Neutron Flux.....	A7
Appendix 3.1. Trigonometric Relationships .....	A8
Appendix 3.2. Validation of CLARA's Numerical Solution .....	A12
Appendix 4.1. Influence of Boundary Locations on the Accuracy of the Fault-Scarp Diffusion Numerical Solution.....	A13
Appendix 4.2. Sensitivity to $\Delta\phi$ and $\Delta\theta$ .....	A14
Appendix 4.3. Source Term for High-Energy Neutrons .....	A17
Appendix 4.4. Upper and Lower Boundary Locations for the Numerical Low-Energy Flux Solutions...	A20
Appendix 5.1. Grain Size Log of Entire Trench .....	A22
Appendix 5.2. Grain Size Log near Fault Plane .....	A23
Appendix 5.3. Legend for the Grain Size Logs of Appendices 5.2 and 5.3 .....	A24
Appendix 6.1. Protocol for Sample Collection, Preparation, and Grinding (Zreda, 1994) .....	A26
Appendix 6.2. Protocol for Sample Leaching .....	A28
Appendix 6.3. Protocol for Extracting Cl for $^{36}\text{Cl}/\text{Cl}$ Analysis (Lui, 1994; and Zreda, 1994).....	A29
Appendix 6.4. Estimation of the Expected $^{36}\text{Cl}/\text{Cl}$ .....	A32
Appendix 6.5. Estimation of Chloride Content with a Chloride Electrode (Aruscavage and Campbell, 1983; and Elsheimer, 1987) .....	A33
Appendix 7.1. Tables of Sample Chemistry.....	A35
Appendix 8.1. Cosmogenic $^{36}\text{Cl}$ Accumulation and Production Parameters.....	A43
Appendix 9.1. Reduced Chi-Squared-Error Calculated from the Individual Profiles and Both Profiles ..	A45

## Appendix 1.1. CLARA README FILE

CLARA (acronym for Chlorine-36 Accumulation and Rupture Ages) is a program that simulates  $^{36}\text{Cl}$  accumulation under fault scarps using Matlab, a software package with programming language constructs and built-in mathematical routines. Matlab is a registered trademark of The Math Works, Inc. The program couples cosmogenic  $^{36}\text{Cl}$  production and accumulation to a model for fault-scarp morphology. The model for fault-scarp morphology creates a surface for each timestep from the initial rupture to the present. At nodes, beneath each of these surfaces, CLARA assesses the production, accumulation, and redistribution of  $^{36}\text{Cl}$ . These nodes are spaced through discretization in the vertical ( $z$ ) and horizontal ( $x$ ) directions and are referenced by the row and column indexes  $i$  and  $j$ , respectively. The production of cosmogenic  $^{36}\text{Cl}$  is determined from the spallation of K and Ca and thermal neutron capture by  $^{35}\text{Cl}$ . Thermal neutron capture is assessed by considering two distinct energy ranges for these low-energy neutrons, epithermal ( $\sim 0.1$  MeV to 0.5 eV) and thermal ( $< 0.5$  eV). By summing the production of all timesteps minus radioactive decay, CLARA accumulates cosmogenic  $^{36}\text{Cl}$ . Using the fault-scarp morphologies of consecutive timesteps, CLARA simulates the erosion of material from the footwall and its deposition onto the hanging wall and the effects of this redistribution on the spatial pattern of the cosmogenic  $^{36}\text{Cl}$  concentration.

CLARA consists of seven principal Matlab functions: *clara*, *bldupdk*, *fsdiffm*, *import*, *redstrbt*, *totalPn*, *totalPa* (all these functions have a *.m* extension). Within the function *clara*, the size and discretization of the time and spatial domains are specified. This function serves as the model's hub, making calls to other functions, obtaining data from those functions, and sending this information to other functions. The function

*bldupdk* computes the buildup and decay of  $^{36}\text{Cl}$  beneath a fault scarp as a function of time. The function *fsdiffm* solves the diffusion model for fault-scarp morphology using implicit finite difference and provides surfaces from the initial rupture to the present. The numerical production of cosmogenic  $^{36}\text{Cl}$  is calculated in the function *totalPn*. The function *totalPa* contains analytical solutions for cosmogenic  $^{36}\text{Cl}$  production from Phillips et al. (in press) and Gosse and Phillips (in press). CLARA uses the analytical solutions to specify the boundary conditions and initial conditions for the low-energy neutron fluxes and calculate cosmogenic  $^{36}\text{Cl}$  accumulation before the first rupture. The redistribution of  $^{36}\text{Cl}$  concentrations between nodes of the footwall and those of the hanging wall is performed by the function *redstrbt*.

The output from CLARA is saved as well as plotted. The function *plot36Cl* produces a contour plot of  $^{36}\text{Cl}$  concentrations and comparisons between the observed and modeled fault scarp profiles and  $^{36}\text{Cl}$  depth profiles. The function *import* reads parameters necessary for modeling fault-scarp diffusion and  $^{36}\text{Cl}$  production. The files *inClpara.prn* and *infspara.prn* contain  $^{36}\text{Cl}$  production parameters and the morphological properties and estimated rupture ages of a fault-scarp, respectively. The files *hangwall.prn*, *footwall.prn*, and *fstop.prn* contain the observed  $^{36}\text{Cl}$  and fault-scarp profiles.



## Appendix 2.1. Analytical Solution to the Diffusion Equation for Fault-Scarp Morphology

Equation A2.1 is the analytical solution given in Hanks (1998) to Equation 1.1.

$$u(x,t) = a * \operatorname{erf}\left(\frac{x}{2\sqrt{Kt}}\right) + bx \quad (\text{A2.1})$$

In Equation A2.1,  $a$  is half the offset,  $t$  is time,  $b$  is the regional or far-field slope,  $K$  is the geomorphic diffusivity,  $x$  is the horizontal coordinate,  $u$  is the scarp height, and  $\operatorname{erf}$  is the error function. The initial condition for this solution is a step in topography ( $2a$ ) superimposed on surface with a preexisting slope ( $b$ ). The boundaries for the solution are specified at  $-\infty$  and  $+\infty$ .

$$\text{as } x \rightarrow -\infty, z = bx - a, \text{ and}$$

$$\text{as } x \rightarrow +\infty, z = a + bx$$

The solution of Hanks (1998) was modified using the relationship

$$\operatorname{erf}(x) + \operatorname{erfc}(x) = 1 \quad (\text{A2.2})$$

where  $x$  is a dummy variable and  $\operatorname{erfc}$  is the complimentary error function. This was done to give the analytical solution the same orientation as the numerical solution (footwall to the left and hanging wall to the right, see Figure 1.1). The resulting analytical expression is

$$z = a * \operatorname{erfc}\left(\frac{x}{2\sqrt{Kt}}\right) - bx \quad (\text{A2.3})$$

where

$$\text{as } x \rightarrow -\infty, z = 2a - bx, \text{ and}$$

$$\text{as } x \rightarrow +\infty, z = -bx$$

## Appendix 2.2. Analytical Solution for Spallation Production

The analytical solution presented in Gosse and Phillips (in press) for the production of a cosmogenic nuclide from spallation of a target element ( $k$ ) is:

$$P_{sp,m} = \Psi_{m,k} C_k \exp\left(\frac{-Z}{\lambda_{f,e}}\right) \quad (\text{A2.4})$$

where  $sp$  denotes spallation,  $m$  is the nuclide being produced (e.g.,  $^{36}\text{Cl}$ ), and  $f$  and  $e$  denote fast and effective, respectively.  $C_k$  is the concentration of target element  $k$ ,  $\Psi_{m,k}$  is the surface production rate from spallation of the target  $k$ ,  $Z$  is termed the mass depth and is the product of the surficial material's bulk density and vertical depth beneath the land surface, and  $\lambda_{f,e}$  is the effective attenuation coefficient of the cosmic radiation. By replacing the  $\Psi_{m,k} C_k$  with the surface production rate of high-energy neutrons, Equation A2.4 can also be used to calculate the distribution of high-energy neutrons in the atmosphere and subsurface.

### Appendix 2.3. Analytical Solution for the Epithermal Neutron Flux

The analytical of solution for the epithermal neutron (*eth*) flux from Phillips et al. (in press) is given by

$$\Phi_{eth,i} = \Phi_{eth,i}^* \exp\left(\frac{-Z}{\lambda_{f,e}}\right) + (F\Delta\Phi)_{eth,i}^* \exp\left(\frac{-|Z|}{L_{eth,i}}\right) \quad (A2.5)$$

where  $i$  refers to atmosphere or subsurface,  $Z$  is termed the mass depth (product of the vertical depth or height and the material density of the medium  $i$ ),  $\lambda_{f,e}$  is the effective attenuation coefficient of the cosmic-ray intensity, and  $L_{eth,i}$  is the epithermal neutron diffusion length in the medium  $i$ . The quantity  $\Phi_{eth,i}^*$  is a hypothetical epithermal neutron flux (neutrons  $\text{cm}^{-2} \text{ y}$ ). For instance,  $\Phi_{eth,ss}^*$  is the subsurface epithermal neutron flux that would be observed at the land surface if the material properties of the atmosphere and the subsurface were the same. The term  $(F\Delta\Phi)_{eth,i}^*$  is the difference between the hypothetical neutron flux ( $\Phi_{eth,i}^*$ ) and the actual flux that is the result of neutron diffusion across the atmosphere/subsurface interface. Details of the theory behind the calculations of the parameters of Equation A2.5 are presented in Phillips et al. (in press).

## Appendix 2.4. Analytical Solution for the Thermal Neutron Flux

The analytical solution for the thermal neutron (*thn*) flux is given by (Phillips et al., in review)

$$\Phi_{thn,i} = \Phi_{thn,i}^* \exp\left(\frac{-Z}{\lambda_{f,e}}\right) + (\mathfrak{I}\Delta\Phi)_{eth,i}^* \exp\left(\frac{-|Z|}{L_{eth,i}}\right) + (\mathfrak{I}\Delta\Phi)_{thn,i}^* \exp\left(\frac{-|Z|}{L_{thn,i}}\right) \quad (\text{A2.6})$$

where  $i$  refers to atmosphere or subsurface,  $Z$  is termed the mass depth (product of the vertical depth or height and the material density of the medium),  $\lambda_{f,e}$  is the effective attenuation coefficient of the cosmic-ray intensity,  $L_{eth,i}$  and  $L_{thn,i}$  are the epithermal and thermal neutron diffusion lengths, respectively, in the medium  $i$ . The quantity  $\Phi_{thn,i}^*$  is a hypothetical thermal neutron flux (neutrons  $\text{cm}^{-2} \text{y}$ ). For instance,  $\Phi_{thn,ss}^*$  is the subsurface thermal neutron flux that would be observed at the land surface if the material properties of the atmosphere and the subsurface were the same. The quantities  $(\mathfrak{I}\Delta\Phi)_{eth,i}^*$  and  $(\mathfrak{I}\Delta\Phi)_{thn,i}^*$  represent the perturbations in the thermal neutron profile due to neutron diffusion across the atmosphere/subsurface interface. Details of the theory behind the calculations of the parameters of Equation A2.6 are presented in Phillips et al. (in press).

## Appendix 3.1. Trigonometric Relationships

The following three expressions are used to relate  $\phi$  and  $\phi'$ . This is done so that  $z_{int}$  can be determined in order for  $d_t$  (linear distance traveled by a cosmic ray in the subsurface) to be calculated.  $\phi$  is the actual inclination angle, and  $\phi'$  is  $\phi$  projected back onto the  $xz$ -plane. Equation A3.1 is derived from the green right triangle depicted in Figure A3.1. The parameters of Equation A3.1, as well as the other expressions that follow, are illustrated and defined in Figure A3.1.

$$\cos(\phi) = \frac{\Delta z}{d_t} \quad (\text{A3.1})$$

Equation A3.2 is derived from the red right triangle (Figure A3.1) where  $\Delta x$  (the short red segment) is the difference between  $x_{int}$  and  $x_j$ .

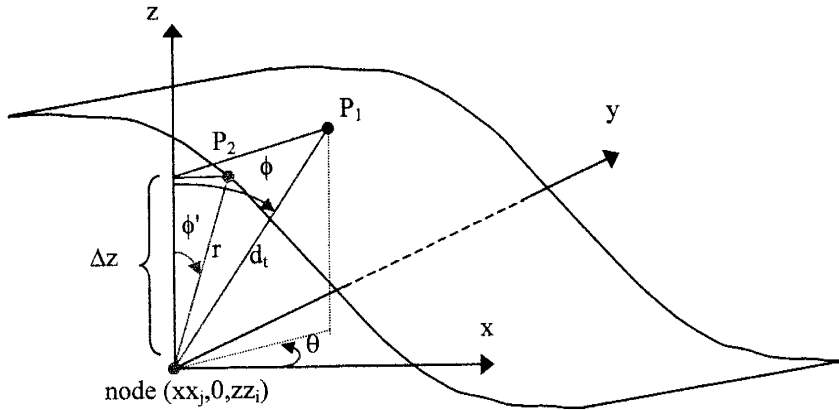
$$\tan(\phi') = \frac{\Delta x}{\Delta z} \quad (\text{A3.2})$$

Equation A3.3 is a spherical coordinate relationship.

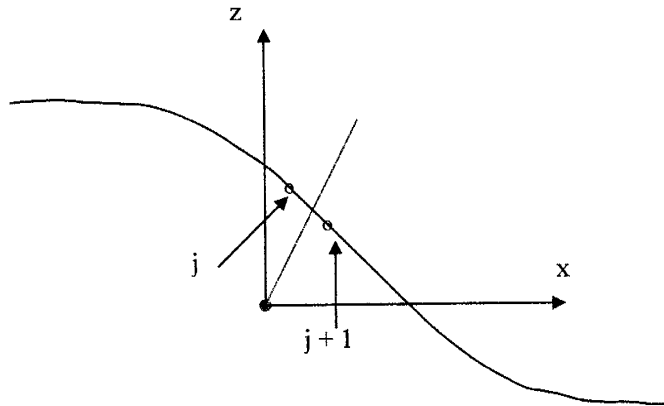
$$\Delta x = d_t \cos(\theta) \sin(\phi) \quad (\text{A3.3})$$

By substituting Equation A3.3 for  $\Delta x$  and Equation A3.1 for  $\Delta z$  in Equation A3.2, the following expression is derived

$$\tan(\phi') = \cos(\theta) \tan(\phi) \quad (\text{A3.4})$$



**Figure A3.1.** Trigonometric relationships used to express  $\phi'$  as a function of  $\phi$  and  $\theta$ . The segment  $\Delta z$  is a leg for both the green and red right triangles and is the difference between  $zz_i$  and  $z_{int}$ . The point  $P_1$  is defined by the spherical coordinates  $(d_t, \phi, \theta)$  and the Cartesian coordinates  $(x_{int}, y_{int}, z_{int})$  (*int* denotes interception with the surface). The parameter  $d_t$  is the distance from  $P_1$  to  $(xx_j, 0, zz_i)$ , When  $\phi$  is projected onto the  $xz$ -plane ( $\phi'$ ), the point  $P_2$  is defined by the spherical and Cartesian coordinates  $(r, \phi', 0)$  and  $(x_{int}, 0, z_{int})$ , respectively.



**Figure A3.2.** Interception of the projected cosmic ray (red) defined by Equation A3.2 with the surface interval  $j$  and  $j+1$ .

Equations A3.2 and A3.5 (below) are used to calculate  $z_{int}$ . Figure A3.2 shows the interception of the projected trajectory with the surface. The surface interval containing  $(x_{int}, 0, z_{int})$  is linearly interpolated (Equation A3.5). The surface is defined from the diffusion equation for fault-scarp morphology and is represented by  $(x_s, z_s)$  in Equations A3.5, A3.6 and A3.7. The subscript  $s$  denotes surface.

$$z_s = \frac{\Delta z_s}{\Delta x_s} (x_s - x_{s,j}) + z_{s,j} \quad (\text{A3.5})$$

In Equation A3.5,  $\Delta z_s / \Delta x_s$  defines the slope of the line where  $\Delta z_s$  and  $\Delta x_s$  are the differences between  $z_{s,j}$  and  $z_{s,j+1}$ , and  $x_{s,j}$  and  $x_{s,j+1}$ , respectively. The index  $j$  represents the surface node to the left of  $(x_{int}, z_{int})$ , and  $j+1$  is the node to the right of  $(x_{int}, z_{int})$ . By setting  $z_s$  equal to  $z_{int}$  and  $x_s$  equal to  $x_{int}$  in Equation A3.5 and substituting Equation A3.2 for  $x_{int}$  in Equation A3.5, the following expression for  $z_{int}$  is derived

$$z_{int} = \frac{\frac{\Delta z_s}{\Delta x_s} (x_{s,j} - x_{s,j+1} - z_{s,j} \tan(\phi')) + z_{s,j}}{1 - \frac{\Delta z_s}{\Delta x_s} \tan(\phi')} \quad (\text{A3.6})$$

Equation A3.6 is limited by the condition

$$\frac{\Delta z_s}{\Delta x_s} \tan(\phi') < 1 \quad (\text{A3.7})$$

This condition confines Equation A3.6 to large surface slopes and small inclination angles or larger inclination angles and small surface slopes. To account for this limitation, an *if* statement is used in CLARA to stop the integration of the cosmic-ray flux when the left-hand side of Equation A3.7 is greater than one. This results in a slight under-prediction of the cosmic-ray flux because, except in the vicinity of the fault plane, the surface slope is gentle (far-field slope generally  $< 5^\circ$ ). For example, with a surface

slope of  $5^\circ$ ,  $\phi'$  must be less than  $85^\circ$  in order to satisfy the condition of Equation A3.7.  $\phi'$  equals  $85^\circ$  at large  $\phi$  (reference Equation A3.4), and the majority (87%) of the cosmic-radiation flux is at inclination between  $0^\circ$  and  $60^\circ$ ; therefore, under-estimation of the flux is slight. Near the fault plane the surface slope is steep; however,  $\phi$  and  $\phi'$  are small so the left-hand side of Equation A3.7 is less than 1.



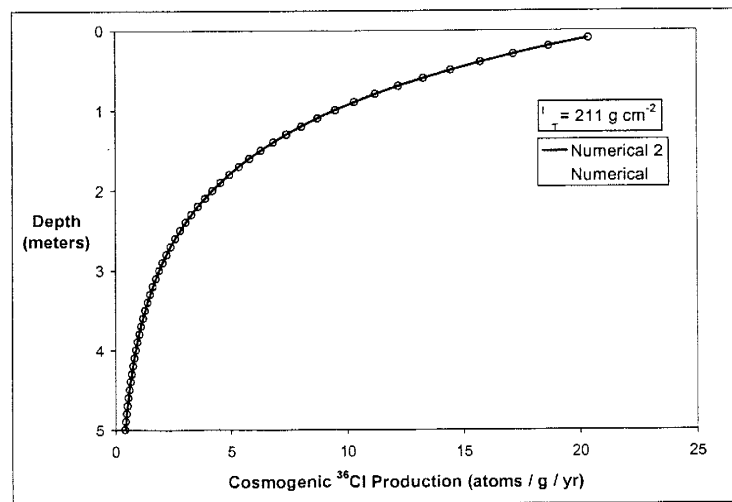
## Appendix 3.2. Validation of CLARA's Numerical Solution

We used Equations A3.8 and A3.9 to validate the numerical integration used by CLARA, Equation 2.10. Equation A3.8 is a simplified form of Equation 2.10. The simplification is possible because a horizontal surface is assumed. Because a horizontal surface is assumed, the trigonometry necessary to calculate  $d_t$  reduces to the single expression of Equation A3.9. Parameters of Equation A3.8 and A3.9 are defined in Section 2.

$$\Phi = 2 \sum_j^n \sum_{i=1}^m F_0 \cos^{m+1}(\phi) \exp(d_t \rho_b / \lambda_t) \sin(\phi) \Delta\theta \Delta\phi \quad (\text{A3.8})$$

$$d_t = \frac{\Delta z}{\cos(\phi)} \quad (\text{A3.9})$$

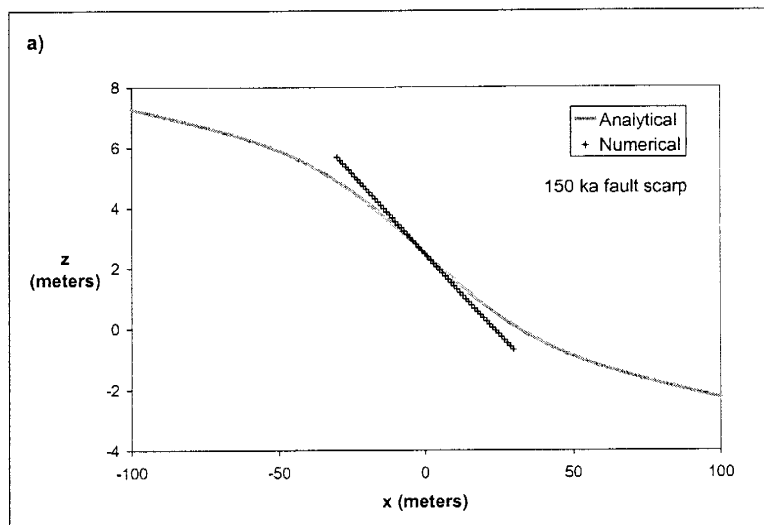
We evaluated the cosmic-ray flux using Equations A3.8 and A3.9 and used this flux to calculate spallation production for comparison against the solution for spallation production used in CLARA and discussed in Section 2. Figure A3.3 presents the comparison. The average deviation between the two solutions is 0.32%.



**Figure A3.3.** Agreement between the numerical solution present here and the solution of CLARA.

## Appendix 4.1. Influence of Boundary Locations on the Accuracy of the Fault-Scarp Diffusion Numerical Solution

In Figure A4.1, we demonstrate the sensitivity of the numerical solution for fault-scarp morphology to placement of the two-boundary conditions (Section 2.2). To perform the analysis, we used the same parameters as model verification (see Section 2.2). However, we placed the model boundaries nearer the fault plane. Figure A4.1 shows the error introduced by placing the boundaries too close to the fault plane. Users of CLARA should verify that the placements of the boundaries are not impacting the accuracy of the fault-scarp diffusion solution.



**Figure A4.1.** Sensitivity of the numerical solution for fault-scarp morphology to the placement of the model domain boundaries

## Appendix 4.2. Sensitivity to $\Delta\phi$ and $\Delta\theta$

In order to enhance the computational efficiency of CLARA, we explored sensitivity of the numerical solution for the cosmic-ray flux (Equation 2.10) to the size of the discretization parameters,  $\Delta\phi$  and  $\Delta\theta$ . The smaller the discretization the more accurate the solution; however, a smaller discretization requires greater CPU time. The objective of the sensitivity analysis was to find values for  $\Delta\phi$  and  $\Delta\theta$  that yield an accurate solution while conserving CPU time.

For the sensitivity analysis, we assessed spallation production along the depth profile depicted in Figure A4.2a. We selected a high angle scarp for the analysis because we expected the value of  $d_i$ , distance between the topographic surface and the node- $i,j$ , to show greater sensitivity to both  $\Delta\phi$  and  $\Delta\theta$  for a high angle scarp than a low angle scarp or horizontal surface. We based the expectation on the fact that for a horizontal surface  $d_i$  is insensitive to  $\Delta\theta$  and is only a function of  $\phi$ .

Table A4.1 and Figure A4.2b show the results of the sensitivity analysis. In Figure A4.2b, fine represents a discretization of  $\Delta\phi = 1.0^\circ$  and  $\Delta\theta = 1.0^\circ$ ; coarser is  $\Delta\phi = 4.0^\circ$  and  $\Delta\theta = 5.0^\circ$ , and coarsest is  $\Delta\phi = 6.0^\circ$  and  $\Delta\theta = 10.0^\circ$ . In Table A4.1, the average absolute deviation represents the average percent difference between spallation production values calculated from the finest and coarser discretization. The results show that a discretization of  $\Delta\phi = 6.0^\circ$  and  $\Delta\theta = 10.0^\circ$  provides a similar solution as the finest discretization. The average difference is  $\sim 0.40\%$  with a  $\sim 38$ -fold savings in CPU time. Therefore, implementing the coarser discretization into CLARA, reduces computational

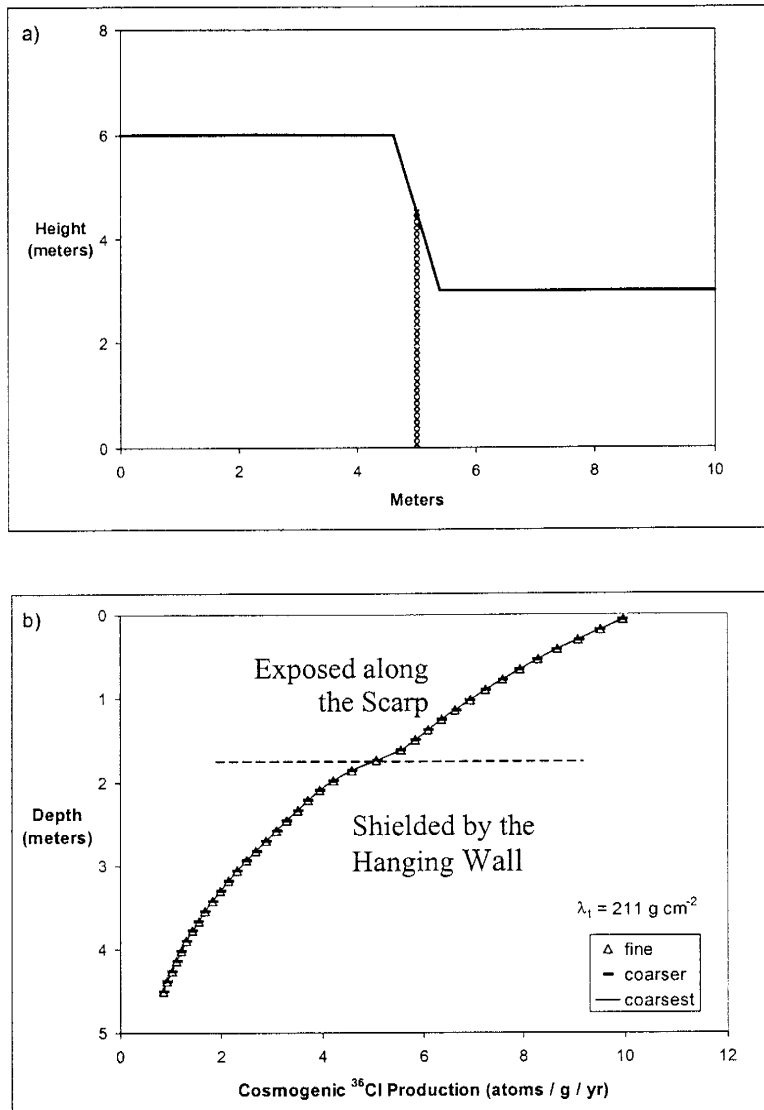
cost, making CLARA more practical for common use, while preserving the accuracy of the numerical solution for spallation production.

**Table A4.1. Results of the sensitivity analysis**

$\Delta\phi$ (degrees)	$\Delta\theta$ (degrees)	CPU time (minutes)	FLOPS ( $\times 10^8$ )	Average Absolute Deviation (%)
1	1	137	5.42	-
4	5	7.36	0.288	0.18
6	10	3.61	0.001	0.40

\*FLOPS is the number of floating point operations.

Apparent in the spallation production profile of Figure A4.2b is an inflection at a depth of 1.5 m. The inflection is coincident with the surface height of the hanging wall in Figure A4.2a. Below 1.5 m, cosmic rays intercept the material of the hanging wall, reducing the intensity of the cosmic-ray flux and thus spallation production. The reduction in spallation production produces the observed “kink” in the depth profile.



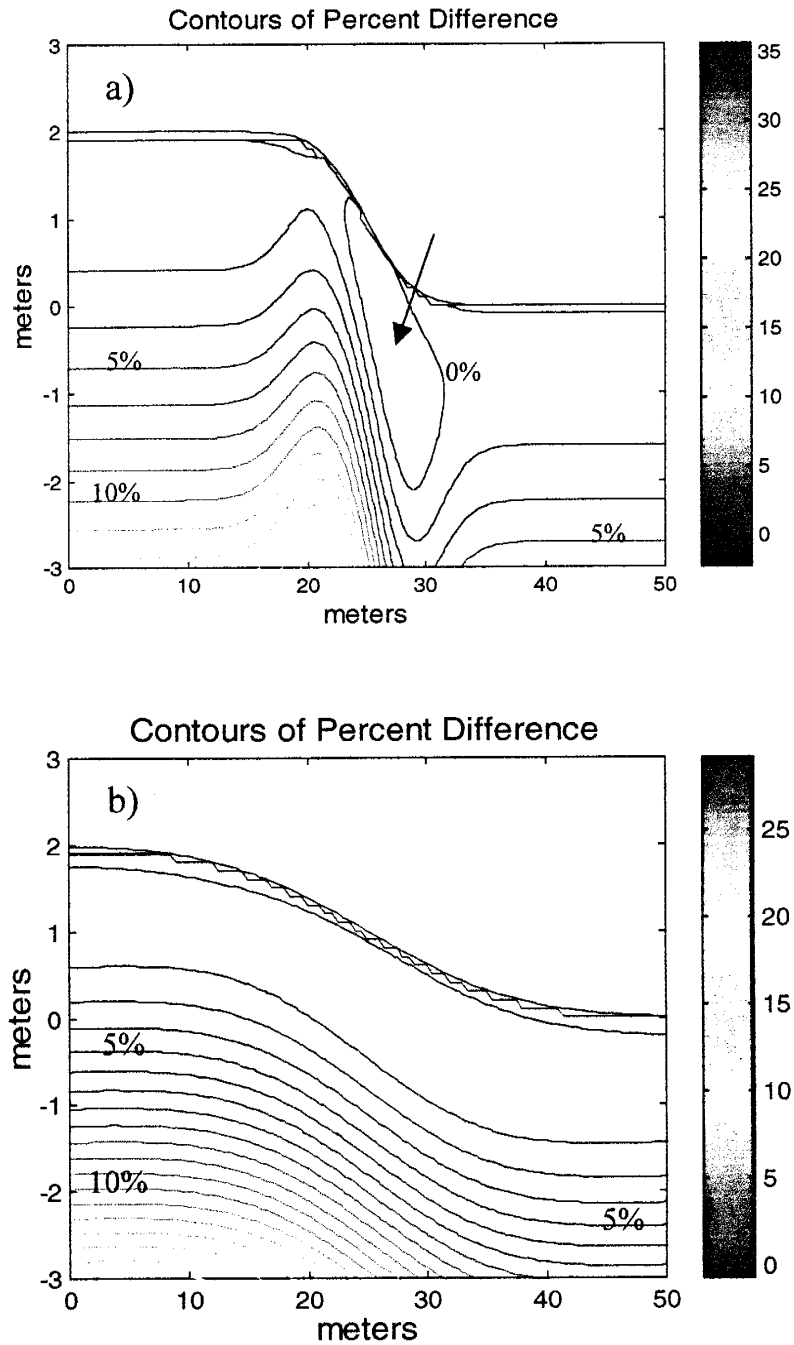
**Figure A4.2.** Sensitivity of Equation 2.10 to the values of the discretization parameters. a) Surface used during the sensitivity analysis; x's denote the depth profile shown in b. b) Spallation production as a function of depth. Fine, coarser, and coarsest refer to the size of  $\Delta\phi$  and  $\Delta\theta$  (see text). The dashed line marks the location below which the material of the hanging wall shields the profile (see text).

### Appendix 4.3. Source Term for High-Energy Neutrons

In Figures A4.2a and A4.2b, we explore the difference in calculating the high-energy neutron component of cosmogenic  $^{36}\text{Cl}$  production from an analytical solution (Gosse and Phillips (in press)) and the numerical solution presented in Section 2. High-energy neutrons contribute to cosmogenic  $^{36}\text{Cl}$  production in two ways: 1) through spallation reactions, and 2) as a source of epithermal neutrons. As a scarp evolves, its slope becomes shallower and the geometry of the scarp begins to resemble a horizontal surface. Therefore, the production of cosmogenic  $^{36}\text{Cl}$  from high-energy neutrons may be approximated by the analytical solution of Gosse and Phillips (in press) presented in Appendix 2.1. In CLARA, the approximation reduces computational cost but is only accurate at small scarp slopes.

Figure A4.2 shows the difference in cosmogenic  $^{36}\text{Cl}$  production for two scarps of different geomorphic age and therefore with different maximum scarp slopes. The contours of Figure A4.2 represent the percent difference between calculating the high-energy component of  $^{36}\text{Cl}$  production with the analytical and numerical solutions (i.e.,  $(\text{numerical} - \text{analytical}) / \text{numerical} * 100\%$ ). The figure shows that as the scarp evolves the difference between the two solutions decreases and that the contours begin to conform to the shape of the scarp. In Figure A4.2a, the arrow identifies a region beneath the scarp where the analytical solution overestimates the amount of spallation production as the solution underestimates the amount of shielding caused by the footwall. In addition, on the footwall of the scarp near the fault plane the contours ramp as the analytical solution underestimates the amount of production. Here, because the analytical solution assumes the surface is a flat plane, it overestimates the amount of shielding to

the right of the scarp. Foreshortening of the cosmic-ray flux due to the slope of the scarp is another cause for the differences observed in Figure A4.3. At depth, the difference in cosmogenic  $^{36}\text{Cl}$  production is due to the systematic overestimation of the cosmic-ray flux at depth introduced by the numerical solution using a  $\lambda_t$  of  $211 \text{ g cm}^{-2}$  (see Section 2.3.1). Although the numerical solution overestimates the cosmic-ray flux at depth, the solution does accurately (<5% difference) predict the high-energy neutron flux at depths less than 3 m where the majority of cosmogenic  $^{36}\text{Cl}$  is produced.



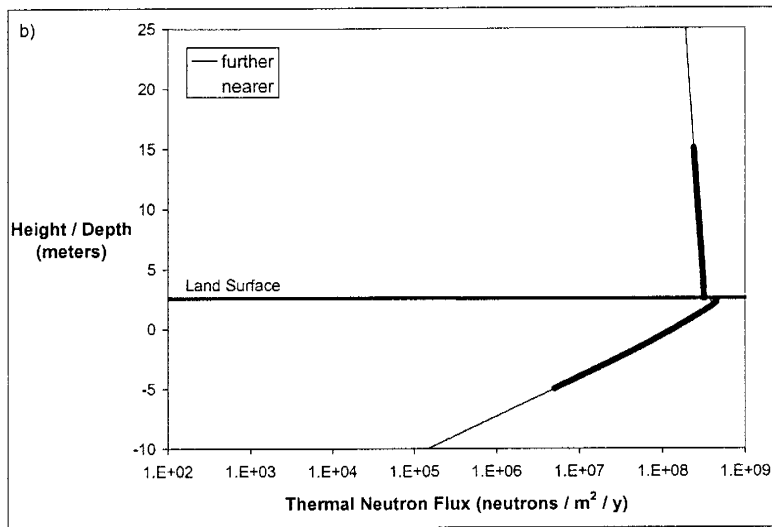
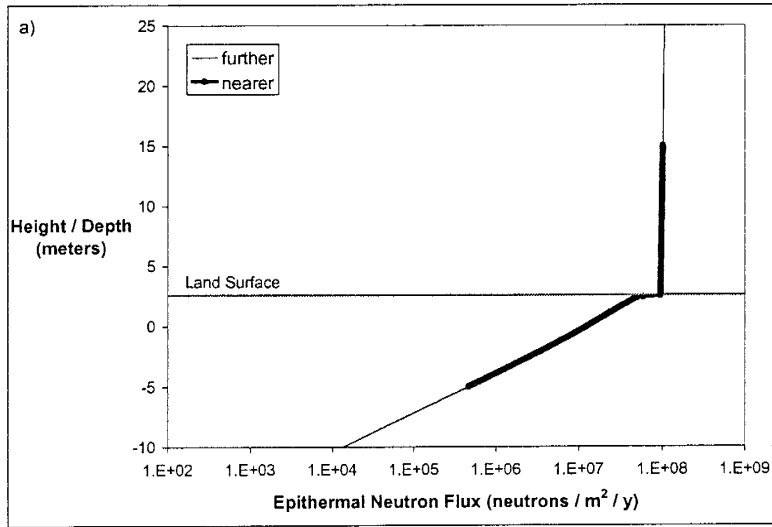
**Figure A4.3.** Illustration of the difference between numerical and analytical solutions for the calculation of high-energy neutron production: a) morphologic age of  $5 \text{ m}^2$  (maximum scarp slope of  $14^\circ$ ), and b) morphologic age of  $50 \text{ m}^2$  (maximum scarp slope of  $5^\circ$ ).



## Appendix 4.4. Upper and Lower Boundary Locations for the Numerical Low-Energy Flux Solutions

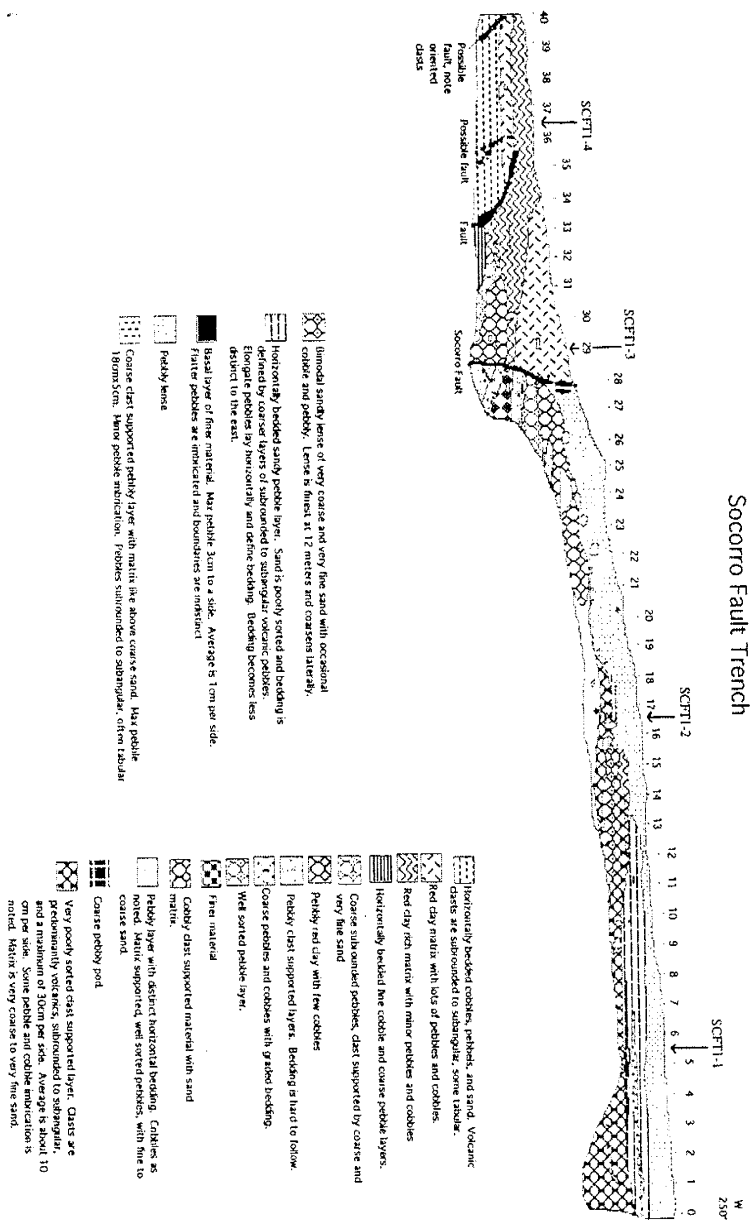
Prior to using CLARA to determine a rupture chronology for the Socorro Canyon fault scarp, we explored the sensitivity of the numerical solutions for the lower-energy neutron fluxes to the placement of the upper atmospheric and lower subsurface boundaries. For the analysis, we used a 1 ka fault scarp as the surface beneath which the production of cosmogenic  $^{36}\text{Cl}$  from low-energy neutrons was calculated. The offset was 5 meters, and we used a spatial discretization of 0.5 meters for  $\Delta x$  and 0.1 meters for  $\Delta z$ . We performed the analysis by adjusting the boundary locations relative to the surface of the footwall and hanging wall. We varied the position of the boundaries in order to identify boundary location that were close to the topographic surface but did not influence the numerical solutions.

The upper boundary was placed 10 meters from the maximum height of the footwall, and the lower boundary was located 5 meters below the minimum height of the hanging wall. These conditions are defined as "nearer" in Figure A4.3. The "further" condition consisted of an upper boundary located 20 meters from the maximum height of the footwall and the lower boundary placed 10 meters below the minimum height of the hanging wall. The results show that placing the boundaries 10 meters above the maximum footwall height and 5 meters below the minimum hanging wall height does not influence the low-energy neutron fluxes near the land surface.

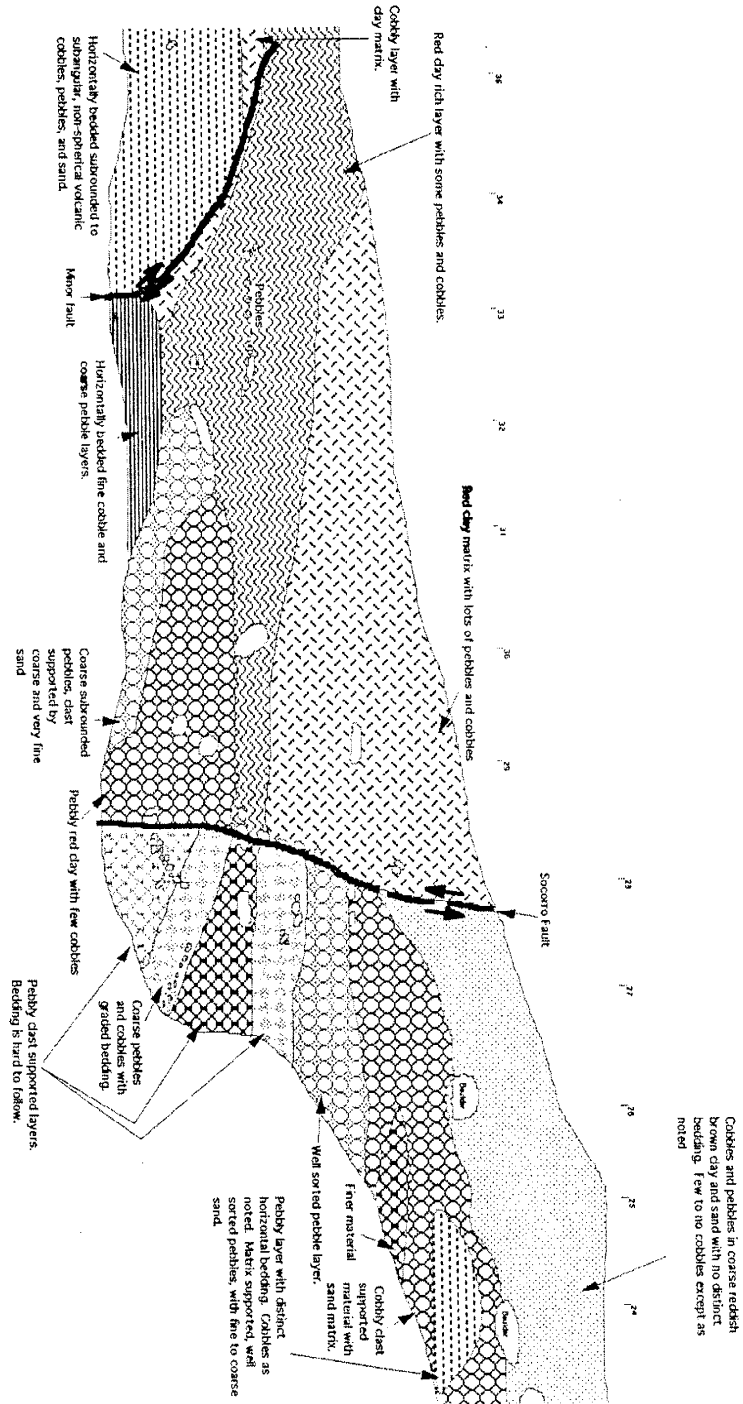


**Figure A4.4.** Sensitivity of the numerical low-energy flux solutions to the placement of the boundaries: a) epithermal neutron flux with an average absolute deviation of  $2.6 \times 10^{-5}\%$  between the two solutions and b) thermal neutron flux with an average absolute deviation of  $1.8 \times 10^{-3}\%$  between the two solutions.








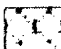






# Appendix 5.1. Grain Size Log of Entire Trench (Harrison, 1998) (note: legend of a larger font is provided as Appendix 5.3)



## Appendix 5.2. Grain Size Log near Fault Plane (Harrison, 1998)



### Appendix 5.3. Legend for the Grain Size Logs of Appendices 5.1 and 5.2 (Harrison, 1998)

- 
 Horizontally bedded cobbles, pebbles, and sand. Volcanic clasts are subrounded to subangular, some tabular.
- 
 Red clay matrix with lots of pebbles and cobbles.
- 
 Red clay rich matrix with minor pebbles and cobbles
- 
 Horizontally bedded fine cobble and coarse pebble layers.
- 
 Coarse subrounded pebbles, clast supported by coarse and very fine sand
- 
 Pebbly red clay with few cobbles
- 
 Pebbly clast supported layers. Bedding is hard to follow.
- 
 Coarse pebbles and cobbles with graded bedding.
- 
 Well sorted pebble layer.
- 
 Finer material
- 
 Cobbly clast supported material with sand matrix.
- 
 Pebbly layer with distinct horizontal bedding. Cobbles as noted. Matrix supported, well sorted pebbles, with fine to coarse sand.
- 
 Coarse pebbly pod.
- 
 Very poorly sorted clast supported layer. Clasts are predominantly volcanics, subrounded to subangular, and a maximum of 30cm per side. Average is about 10 cm per side. Some pebble and cobble imbrication is noted. Matrix is very coarse to very fine sand.



Bimodal sandy lense of very coarse and very fine sand with occasional cobble and pebbly. Lense is finest at 12 meters and coarsens laterally.



Horizontally bedded sandy pebble layer. Sand is poorly sorted and bedding is defined by coarser layers of subrounded to subangular volcanic pebbles. Elongate pebbles lay horizontally and define bedding. Bedding becomes less distinct to the east.



Basal layer of finer material. Max pebble 3cm to a side. Average is 1cm per side. Flatter pebbles are imbricated and boundaries are indistinct.



Pebbly lense



Coarse clast supported pebbly layer with matrix like above coarse sand. Max pebble 18cmx5cm. Minor pebble imbrication. Pebbles subrounded to subangular, often tabular.

## Appendix 6.1. Protocol for Sample Collection, Preparation, and Grinding (Zreda, 1994)

- Collect samples along vertical transects with the number of samples per transect large enough that the samples define a representative cosmogenic  $^{36}\text{Cl}$  depth profile, which can be compared to a modeled profile.
- Avoid sampling soil horizons where carbonate accumulation is excessive. The carbonate neutralizes the acids used in the laboratory protocol.
- The sample size should be large enough that it contains many (>150) small clast.
- In order to collect a large enough sample at the Socorro Canyon fault, the area from which a sample was collected was defined by vertical distance of ~10 cm and a horizontal distance of ~50 cm. The vertical distance should be minimized due to the exponential dependence of cosmogenic  $^{36}\text{Cl}$  with depth.
- Separate numerous small clasts for chemical and cosmogenic  $^{36}\text{Cl}$  analyses. The size of the numerous small clasts should be similar. Due to possible different individual exposure histories of the clasts, large clasts might bias the cosmogenic  $^{36}\text{Cl}$  results. If necessary, include fragments from larger clasts.
- Clean the clast of loose soil, organic matter, and carbonate. If necessary, rinse the clast.
- Grind the small clasts to a size fraction <1 mm. We used a TEMA mill (shatterbox).
- Separate the <150  $\mu\text{m}$  size fraction from the >150  $\mu\text{m}$  size fraction.
- The >150  $\mu\text{m}$  size fraction is retained for analysis; however, store the <150  $\mu\text{m}$  size fraction in case additional sample is needed.

- Between samples, the TEMA mill was cleaned by place a OTTAWA quartz sand in the shatterbox and allow the shatterbox to run for ~30 minutes.



## Appendix 6.2. Protocol for Sample Leaching

- Add 3% HNO<sub>3</sub> at 3 – 4 times the sample volume to a beaker or other glassware containing the sample.
- Mix the sample well and cover the sample.
- Allow the sample to leach for 8 – 12 hours.
- Decant the leachate and rinse the sample with deionized water.
- While decanting the leachate and during the sample rinse, suspended fines are washed out of the sample.
- Add a small volume of 3% HNO<sub>3</sub> and watch for effervescence.
- If effervescence is observed, a second leaching is necessary and repeat the first 5 steps.
- If effervescence is not observed, add 1% NaOH to the sample until the pH is between 7 and 9.
- Decant the NaOH and rinse the sample 2 – 3 times with deionized water. The final pH should be between 5 and 6.
- Oven dry the samples (105 °C).

### Appendix 6.3. Protocol for Extracting Cl for $^{36}\text{Cl}/\text{Cl}$ Analysis (Lui, 1994; and Zreda, 1994)

- Prior to the extraction, all laboratory ware used in this protocol should be clean so that any residual chloride present on the glassware is removed. Acid washing with hot  $\text{HNO}_3$ , and then rinsing with  $\text{NH}_4\text{OH}$  and a final deionized water rinse will accomplish this.
- Weigh the sample into a Teflon bottle. The sample size fraction at this point is between 1 mm and 150  $\mu\text{m}$ . The amount of sample to digest is based on the expected  $^{36}\text{Cl}/\text{Cl}$  ratio. Determination of the expected  $^{36}\text{Cl}/\text{Cl}$  ratio is presented in Appendix 4.3.
- Add deionized water to just cover the sample and swirl.
- Weigh the appropriate amount of  $^{35}\text{Cl}$  spike and add it to the sample. The amount of spike added is based on the following: estimated  $^{36}\text{Cl}/\text{Cl}$ , estimated sample Cl concentration, amount of  $\text{AgCl}$  need for AMS, and the total amount of sample remaining after grinding and leaching. The amount of spike added was selected so that the final  $^{35}\text{Cl}/^{37}\text{Cl}$  would be approximately 6.0, the anticipated quantity of  $\text{AgCl}$  would be greater than 10 mg, there would be a representative sample, and the  $^{36}\text{Cl}/\text{Cl}$  ratio would be greater than  $50 \times 10^{-15}$ . These calculations were performed using the spreadsheet model LABCALCS developed by Plummer and Phillips (unpublished).
- Pour concentrated  $\text{HNO}_3$  (70%) into a separatory funnel at a ratio of 1 part acid to 2 parts sample by mass.
- Pour concentrated  $\text{HF}$  (48%) into a separatory funnel at a ratio of  $2\frac{1}{2}$  parts acid to 1 part sample by mass.

- Drip the acid solution from the separatory funnel into the Teflon bottle containing the sample. This solution needs to be added to the sample slowly due to the possibility of a violent reaction with silicates within the sample. A cool water bath should be present in case the Teflon bottle becomes too hot.
- Once all of the acid solution has been dripped into the Teflon bottle, replace the bottle cap (keep the cap loose) and allow the sample to cool.
- Place the sample on a hot plate at a low temperature ( $\sim 60$  °C) setting.
- Allow the samples to dissolve. This normally takes 48 to 72 hours.
- After complete dissolution, transfer the sample and any solids into a Teflon centrifuge bottle.
- Centrifuge the sample at  $\sim 2500$  rpm for at least 10 minutes to separate the solution from remaining fluorosilicates.
- Decant the solution into a Teflon beaker and add 10 mL of 0.2 M  $\text{AgNO}_3$  to precipitate  $\text{AgCl}$ .
- Place the beaker with cover on a hot plate ( $\sim 60$  °C) to flocculate  $\text{AgCl}$  and to evaporate excess solution.
- Allow the sample to remain on the hot plate for approximately 12 hours.
- Once significant  $\text{AgCl}$  has precipitated, transfer the solution and  $\text{AgCl}$  into a Teflon centrifuge bottle.
- Centrifuge for 10 minutes at  $\sim 2500$  rpm.
- Decant the solution and retain the  $\text{AgCl}$  precipitate.
- Rinse the precipitate using deionized water and centrifuge the sample. Then remove the excess water.

- To separate AgCl from any remaining fluorosilicates, add a few mL of NH<sub>4</sub>OH to dissolve the AgCl, centrifuge and decant the solution.
- Add concentrated HNO<sub>3</sub> to the solution to re-precipitate AgCl.
- To remove sulfur from the solution, re-dissolve the precipitate by adding ~3 mL of NH<sub>4</sub>OH and 1.0 mL of a saturated Ba(NO<sub>3</sub>)<sub>2</sub>. Allow the solution to react for at least 8 hours. Removal of sulfur is necessary because <sup>36</sup>S is an interfering isobar during the AMS analysis.
- Centrifuge the sample for at least 10 minutes, transfer the supernatant with a pipette, re-precipitate AgCl by add concentrated HNO<sub>3</sub> and let the solution stand for 2 hours.
- Pour off the remaining acid, rinse with deionized water and centrifuge.
- If ample AgCl is remaining, the last three steps (sulfur removal) can be repeated.
- When sulfur removal has been completed, rinse the sample, which has been precipitated in HNO<sub>3</sub>, at least 3 times in deionized water. Centrifuge between each rinse. The pH of the final solution should be approximately 7.
- Transfer the AgCl to a watch glass, carefully remove excess water with a pipette, cover the watch glass with aluminum foil and place the sample in an oven at ~60 °C for approximately 24 hours or until the sample is dry.
- The sample is ready for <sup>36</sup>Cl analysis.

## Appendix 6.4. Estimation of the Expected $^{36}\text{Cl}/\text{Cl}$

- To estimate the expected  $^{36}\text{Cl}/\text{Cl}$ , an estimate of the age of the sample, the sample chemistry, and the cosmogenic  $^{36}\text{Cl}$  production rate are needed.
- The age can be approximated from knowledge of the site's geology. For instance, the degree of soil development was used to constrain the age estimate, 100 ka, in this study.
- The chemistry is determined via XRF and is used to calculate production rates.
- The amount of chloride can be measured with a chloride electrode after dissolving the sample and capturing the chloride in a reducing solution. This procedure is described in Appendix 6.5.
- Cosmogenic  $^{36}\text{Cl}$  production rates were calculated the analytical solution in CHLOE (Phillips and Plummer, 1996). This solution uses effective attenuation coefficients and mass depth (the product of the sample depth and the sample density).
- The concentration of cosmogenic  $^{36}\text{Cl}$  (atoms / g sample) is calculated using the following equation:

$$N = \frac{P}{\lambda}(1 - e^{-\lambda t})$$

where P is the cosmogenic  $^{36}\text{Cl}$  production rate,  $\lambda$  is the  $^{36}\text{Cl}$  decay coefficient equal to  $\ln(2) / \text{half-life of } ^{36}\text{Cl}$ , t is time (or the estimated age) and N is the cosmogenic  $^{36}\text{Cl}$  concentration.

- By dividing the cosmogenic  $^{36}\text{Cl}$  concentration by the chloride concentration measured with the chloride electrode, an estimate of the ratio is obtained.

## Appendix 6.5. Estimation of Chloride Content with a Chloride Electrode (Aruscavage and Campbell, 1983; and Elsheimer, 1987)

- In this study, a portable Beckman meter and an Orion model 96-17BN combination chloride electrode were used to measure the amount of sample chloride.
- Grind the sample to a size fraction  $< 150 \mu\text{m}$ . For samples consisting of many small clasts, the numerous clasts should be homogenized.
- This analysis should be carried out in airtight Teflon containers that consist of two separate chambers. The chambers keep separate oxidizing and reducing solutions. The containers used in this study are termed diffusion cells.
- Prior to use and between samples the diffusion cells should be cleaned.
  - The cleaning solution is prepared by combining 375 mL of concentrated  $\text{H}_2\text{SO}_4$  with 13 mL of saturated  $\text{K}_2\text{Cr}_2\text{O}_7$  solution.
  - Heat the cleaning solution, and then add it to the diffusion cells.
  - Replace the lid, tilt the cell back and forth and allow the solution to sit in the cells for 10 – 15 minutes.
  - Empty the cleaning solution and rinse the cells in deionized water.
  - Rinse the solution with a second solution. This solution is prepared by mixing 300 mL of heated  $\text{HNO}_3$  with 50 mL of  $\text{H}_2\text{O}_2$ .
  - Finally, rinse the cells again with deionized water.
- Prepare standards in order to construct a voltage/concentration log-linear regression. This regression is necessary to convert the voltage reading of the meter to a chloride

concentration. In this study the following aqueous standards were used: 10, 25, 50 and 100 ppm.

- Weigh 0.2 ( $\pm 0.0004$ ) grams of standard solution or sample into the oxidizing chamber of the diffusion cell.
- Add 2.5 mL of reducing solution to the reducing chamber.
  - Prepare the reducing solution by combining 5.8 g of KOH pellets, 0.29 g of  $\text{Na}_2\text{SO}_3$  with 31 g of deionized water.
- Add 3 mL of the oxidizing solution to the oxidizing chamber.
  - Make sure the oxidizing solution does not contact the standard or sample until the lid is on and the cell is airtight.
  - Prepare the oxidizing solution by combining 0.4 g of  $\text{KMnO}_4$  with 5.6g of deionized water, 1.85 mL of 50%  $\text{H}_2\text{SO}_4$ , and 32 mL of HF.
- Replace the lids, place the diffusion cells on a orbital shaker and let the samples digest for 16 – 20 hours. During the digestion, the standard or sample is oxidized releasing  $\text{Cl}_2$  that is captured by the reducing solution to produce  $\text{Cl}^-$ .
- Using a voltage meter and chloride electrode, take voltage readings of the reducing solution.
- Rinse the electrode between sample and make sure the base of the electrode is totally submersed in the reducing solution.

Table A7.1. Chemical Composition of the Socorro Canyon Fault Scarp (HW = hanging wall, FW = footwall, & C = control).

Sample	C	Na	Mg	Al	Si	P	K	Ca	Ti
#	(atoms / g)	(atoms / g)	(atoms / g)	(atoms / g)	(atoms / g)	(atoms / g)	(atoms / g)	(atoms / g)	(atoms / g)
HW-a	8.80E+18	4.23E+20	9.56E+19	1.05E+21	7.22E+21	3.39E+18	8.82E+20	6.44E+19	4.07E+19
HW-b	8.80E+18	3.86E+20	8.07E+19	1.03E+21	7.26E+21	2.54E+18	8.97E+20	5.90E+19	3.99E+19
HW-c	7.30E+18	3.69E+20	6.13E+19	9.98E+20	7.39E+21	2.54E+18	8.91E+20	5.26E+19	3.69E+19
HW-d	6.70E+18	3.50E+20	6.27E+19	1.04E+21	7.31E+21	2.54E+18	1.01E+21	4.08E+19	3.46E+19
HW-e	6.90E+18	3.32E+20	3.88E+19	9.76E+20	7.49E+21	2.54E+18	9.42E+20	2.47E+19	2.94E+19
HW-f	6.00E+18	3.34E+20	6.42E+19	1.01E+21	7.33E+21	2.54E+18	9.93E+20	3.76E+19	3.24E+19
HW-g	5.80E+18	3.50E+20	3.74E+19	1.01E+21	7.38E+21	2.54E+18	9.99E+20	2.04E+19	2.86E+19
HW-h	6.00E+18	3.18E+20	2.99E+19	9.47E+20	7.54E+21	1.70E+18	9.53E+20	1.93E+19	2.56E+19
FW-a	6.20E+18	4.06E+20	5.98E+19	1.03E+21	7.33E+21	2.54E+18	9.05E+20	4.40E+19	3.54E+19
FW-b	5.80E+18	3.71E+20	4.78E+19	1.03E+21	7.33E+21	3.39E+18	9.84E+20	2.90E+19	3.39E+19
FW-c	6.40E+18	4.02E+20	5.83E+19	1.03E+21	7.34E+21	2.54E+18	9.20E+20	4.18E+19	3.54E+19
FW-d	8.10E+18	4.25E+20	8.37E+19	1.05E+21	7.20E+21	3.39E+18	8.82E+20	5.79E+19	4.07E+19
FW-e	7.20E+18	4.29E+20	6.87E+19	1.03E+21	7.32E+21	2.54E+18	8.95E+20	4.72E+19	3.46E+19
FW-f	6.80E+18	4.27E+20	7.32E+19	1.08E+21	7.13E+21	4.24E+18	9.57E+20	5.26E+19	4.37E+19
FW-g	6.10E+18	3.63E+20	4.48E+19	1.00E+21	7.41E+21	2.54E+18	9.41E+20	3.86E+19	3.01E+19
C-a-1	6.70E+18	4.12E+20	5.53E+19	1.02E+21	7.32E+21	2.54E+18	8.96E+20	3.86E+19	3.39E+19
C-a-2	6.80E+18	4.41E+20	1.00E+20	1.06E+21	7.17E+21	2.54E+18	8.96E+20	8.69E+19	4.22E+19
C-b	8.20E+18	4.04E+20	8.37E+19	1.04E+21	7.23E+21	3.39E+18	8.96E+20	5.69E+19	3.99E+19
C-c	7.00E+18	4.14E+20	8.52E+19	1.04E+21	7.22E+21	2.54E+18	9.05E+20	7.30E+19	3.77E+19
C-d	6.00E+18	3.96E+20	5.83E+19	1.04E+21	7.27E+21	2.54E+18	9.52E+20	5.04E+19	3.46E+19
C-e	4.90E+18	3.13E+20	2.99E+19	9.89E+20	7.45E+21	1.70E+18	1.01E+21	1.82E+19	2.71E+19
Average	6.79E+18	3.84E+20	6.28E+19	1.02E+21	7.32E+21	2.71E+18	9.34E+20	4.54E+19	3.51E+19
Standard Deviation	1.02E+18	3.95E+19	2.04E+19	2.97E+19	1.04E+20	5.76E+17	4.44E+19	1.79E+19	5.03E+18



Table A7.1 (continued). Chemical Composition of the Socorro Canyon Fault Scarp.

Sample	Mn	Fe	Cl	B	Gd	U	Th
#	(atoms / g)	(atoms / g)	(atoms / g)	(atoms / g)	(atoms / g)	(atoms / g)	(atoms / g)
HW-a	3.39E+18	2.43E+20	4.02E+17	na	na	7.59E+15	3.63E+16
HW-b	3.39E+18	2.22E+20	3.75E+17	na	na	1.01E+16	3.37E+16
HW-c	3.39E+18	2.09E+20	4.12E+17	na	na	1.01E+16	3.63E+16
HW-d	3.39E+18	2.04E+20	3.26E+17	na	na	7.59E+15	3.63E+16
HW-e	2.55E+18	1.69E+20	3.37E+17	na	na	7.59E+15	3.89E+16
HW-f	3.39E+18	1.90E+20	3.67E+17	na	na	1.01E+16	3.63E+16
HW-g	3.39E+18	1.61E+20	3.72E+17	na	na	1.01E+16	3.89E+16
HW-h	2.55E+18	1.50E+20	3.21E+17	na	na	7.59E+15	3.63E+16
FW-a	3.56E+18	1.99E+20	4.92E+17	9.47E+17	2.49E+16	9.61E+15	3.48E+16
FW-b	3.05E+18	1.91E+20	3.96E+17	4.18E+17	1.15E+16	1.01E+16	3.99E+16
FW-c	3.14E+18	2.00E+20	3.63E+17	6.96E+17	9.57E+15	1.06E+16	3.50E+16
FW-d	8.23E+18	2.38E+20	4.38E+17	9.74E+17	1.15E+16	9.61E+15	3.48E+16
FW-e	3.22E+18	1.95E+20	4.22E+17	8.07E+17	2.11E+16	9.10E+15	3.63E+16
FW-f	3.39E+18	2.44E+20	3.96E+17	9.74E+17	1.72E+16	9.36E+15	3.14E+16
FW-g	3.48E+18	1.70E+20	4.13E+17	8.07E+17	2.11E+16	1.01E+16	3.76E+16
C-a-1	3.22E+18	1.89E+20	5.03E+17	9.47E+17	1.72E+16	9.61E+15	3.94E+16
C-a-2	3.90E+18	2.38E+20	5.40E+17	9.74E+17	2.11E+16	9.61E+15	3.50E+16
C-b	3.14E+18	2.25E+20	4.58E+17	1.11E+18	2.49E+16	9.10E+15	3.40E+16
C-c	3.48E+18	2.18E+20	4.90E+17	9.19E+17	2.87E+16	9.61E+15	3.66E+16
C-d	3.31E+18	1.92E+20	4.00E+17	9.47E+17	2.49E+16	1.01E+16	3.84E+16
C-e	3.90E+18	1.55E+20	3.41E+17	9.74E+17	2.49E+16	9.61E+15	3.68E+16
Average	3.55E+18	2.00E+20	4.08E+17	8.84E+17	1.99E+16	9.38E+15	3.63E+16
Standard Deviation	1.12E+18	2.86E+19	6.10E+16	1.74E+17	6.08E+15	9.66E+14	2.09E+15

\*na is not analyzed

Table A7.2. Chemical Composition of the Socorro Canyon Fault Scarp.

Sample	C	Na <sub>2</sub> O	MgO	Al <sub>2</sub> O <sub>3</sub>	SiO <sub>2</sub>	P <sub>2</sub> O <sub>5</sub>	K <sub>2</sub> O	CaO	TiO <sub>2</sub>	MnO	Fe <sub>2</sub> O <sub>3</sub>
#	(wt.%)	(wt.%)	(wt.%)	(wt.%)	(wt.%)	(wt.%)	(wt.%)	(wt.%)	(wt.%)	(wt.%)	(wt.%)
HW-a	0.88	2.18	0.64	13.06	72.11	0.04	6.90	0.60	0.54	0.040	3.22
HW-b	0.88	1.99	0.54	12.79	72.56	0.03	7.02	0.55	0.53	0.040	2.94
HW-c	0.73	1.90	0.41	12.43	73.81	0.03	6.97	0.49	0.49	0.040	2.77
HW-d	0.67	1.80	0.42	12.98	73.00	0.03	7.92	0.38	0.46	0.040	2.71
HW-e	0.69	1.71	0.26	12.16	74.81	0.03	7.37	0.23	0.39	0.030	2.24
HW-f	0.60	1.72	0.43	12.56	73.25	0.03	7.77	0.35	0.43	0.040	2.52
HW-g	0.58	1.80	0.25	12.57	73.73	0.03	7.82	0.19	0.38	0.040	2.14
HW-h	0.60	1.64	0.20	11.79	75.32	0.02	7.46	0.18	0.34	0.030	1.99
FW-a	0.62	2.09	0.40	12.83	73.18	0.03	7.08	0.41	0.47	0.042	2.64
FW-b	0.58	1.91	0.32	12.77	73.21	0.04	7.70	0.27	0.45	0.036	2.53
FW-c	0.64	2.07	0.39	12.78	73.34	0.03	7.20	0.39	0.47	0.037	2.65
FW-d	0.81	2.19	0.56	13.13	71.88	0.04	6.90	0.54	0.54	0.097	3.15
FW-e	0.72	2.21	0.46	12.80	73.16	0.03	7.00	0.44	0.46	0.038	2.58
FW-f	0.68	2.20	0.49	13.41	71.24	0.05	7.49	0.49	0.58	0.040	3.23
FW-g	0.61	1.87	0.30	12.49	74.01	0.03	7.36	0.36	0.40	0.041	2.26
C-a-1	0.67	2.12	0.37	12.71	73.17	0.03	7.10	0.36	0.45	0.038	2.50
C-a-2	0.68	2.27	0.67	13.21	71.63	0.03	7.01	0.81	0.56	0.046	3.15
C-b	0.82	2.08	0.56	12.91	72.23	0.04	7.01	0.53	0.53	0.037	2.98
C-c	0.70	2.13	0.57	12.93	72.10	0.03	7.08	0.68	0.50	0.041	2.89
C-d	0.60	2.04	0.39	12.93	72.63	0.03	7.45	0.47	0.46	0.039	2.55
C-e	0.49	1.61	0.20	12.32	74.38	0.02	7.91	0.17	0.36	0.046	2.05
Average	0.68	1.98	0.42	12.74	73.08	0.03	7.31	0.42	0.47	0.042	2.65
Standard Deviation	0.10	0.20	0.14	0.37	1.04	0.01	0.35	0.17	0.07	0.013	0.38

Table A7.2 (continued). Chemical Composition of the Socorro Canyon Fault Scarp.

Sample	Cl	B	Gd	U	Th
#	(ppm)	(ppm)	(ppm)	(ppm)	(ppm)
HW-a	23.7	na	na	3.0	14.0
HW-b	22.1	na	na	4.0	13.0
HW-c	24.3	na	na	4.0	14.0
HW-d	19.2	na	na	3.0	14.0
HW-e	19.8	na	na	3.0	15.0
HW-f	21.6	na	na	4.0	14.0
HW-g	21.9	na	na	4.0	15.0
HW-h	18.9	na	na	3.0	14.0
FW-a	29.0	17.0	6.5	3.8	13.4
FW-b	23.3	7.5	3.0	4.0	15.4
FW-c	21.4	12.5	2.5	4.2	13.5
FW-d	25.8	17.5	3.0	3.8	13.4
FW-e	24.9	14.5	5.5	3.6	14.0
FW-f	23.4	17.5	4.5	3.7	12.1
FW-g	24.3	14.5	5.5	4.0	14.5
C-a-1	29.7	17.0	4.5	3.8	15.2
C-a-2	31.8	17.5	5.5	3.8	13.5
C-b	27.0	20.0	6.5	3.6	13.1
C-c	28.8	16.5	7.5	3.8	14.1
C-d	23.6	17.0	6.5	4.0	14.8
C-e	20.1	17.5	6.5	3.8	14.2
Average	24.0	15.9	5.2	3.7	14.0
Standard Deviation	3.6	3.1	1.6	0.4	0.8

Table A7.3. AMS results and Cosmogenic <sup>36</sup>Cl.

Sample #	Depth (meters)	Analytical Ratio x 10 <sup>15</sup> ( <sup>36</sup> Cl / Cl)	Analytical Uncertainty (%)	Sample Ratio x 10 <sup>15</sup> ( <sup>36</sup> Cl / Cl)	Radiogenic <sup>36</sup> Cl (x10 <sup>6</sup> atoms/g)	Total Sample <sup>36</sup> Cl (x10 <sup>6</sup> atoms/g)	Cosmogenic <sup>36</sup> Cl (x10 <sup>6</sup> atoms/g)
HW-a	3.17	1830	3.8	3190	0.011 +/- 0.0004	1.28 +/- 0.05	1.27 +/- 0.05
HW-b	2.39	2500	3.6	4790	0.011 +/- 0.0004	1.80 +/- 0.06	1.78 +/- 0.06
HW-c	1.98	2400	3.3	4830	0.013 +/- 0.0004	1.99 +/- 0.07	1.98 +/- 0.07
HW-d	1.63	3800	3.9	8560	0.009 +/- 0.0003	2.79 +/- 0.11	2.78 +/- 0.11
HW-e	1.12	4490	4.2	8620	0.010 +/- 0.0004	2.90 +/- 0.12	2.89 +/- 0.12
HW-f	0.66	5240	4.0	9450	0.011 +/- 0.0004	3.47 +/- 0.14	3.46 +/- 0.14
HW-g	0.36	5770	4.0	10300	0.012 +/- 0.0005	3.83 +/- 0.15	3.82 +/- 0.15
HW-h	0.05	5360	4.3	10300	0.009 +/- 0.0004	3.31 +/- 0.14	3.30 +/- 0.14
FW-a	3.61	708	4.5	1780	0.010 +/- 0.0005	0.88 +/- 0.04	0.87 +/- 0.04
FW-b	2.64	1370	3.9	2690	0.011 +/- 0.0004	1.07 +/- 0.04	1.05 +/- 0.04
FW-c	2.08	1050	4.4	3170	0.009 +/- 0.0004	1.15 +/- 0.05	1.14 +/- 0.05
FW-d	1.57	1070	4.9	2860	0.009 +/- 0.0005	1.25 +/- 0.06	1.24 +/- 0.06
FW-e	0.94	1500	4.7	3250	0.009 +/- 0.0004	1.37 +/- 0.06	1.36 +/- 0.06
FW-f	0.61	2140	4.2	4800	0.008 +/- 0.0003	1.90 +/- 0.08	1.90 +/- 0.08
FW-g	0.05	3870	4.7	6640	0.009 +/- 0.0004	2.74 +/- 0.13	2.73 +/- 0.13
C-a-1	3.00	1670	3.5	2440	0.012 +/- 0.0004	1.23 +/- 0.04	1.22 +/- 0.04
C-a-2	3.00	1510	4.0	2170	0.011 +/- 0.0005	1.17 +/- 0.05	1.16 +/- 0.05
C-b	2.13	2060	3.4	3100	0.009 +/- 0.0003	1.42 +/- 0.05	1.41 +/- 0.05
C-c	1.22	2730	3.3	4010	0.010 +/- 0.0003	1.96 +/- 0.06	1.95 +/- 0.06
C-d	0.56	4200	3.3	6780	0.009 +/- 0.0003	2.72 +/- 0.09	2.71 +/- 0.09
C-e	0.05	7540	3.4	12600	0.003 +/- 0.0001	4.30 +/- 0.15	4.29 +/- 0.15

\*The analytical ratio is the AMS result returned from PRIME lab and includes the chloride spike in the ratio. In the sample ratio, the ratio has been adjusted to account for the addition of the spike (equation 5.1), and the ratio represents the bulk ratio of the sample.

$$\text{Ratio}_{\text{colluvium}} = \left( \frac{\text{Cl}_{\text{sample}} + \text{Cl}_{\text{spike}}}{\text{Cl}_{\text{spike}}} \right) \text{Ratio}_{\text{measured}} \quad (5.1)$$

The cosmogenic  $^{36}\text{Cl}$  concentration was calculated by subtracting the radiogenic inventory of  $^{36}\text{Cl}$  from the total sample concentration.

The radiogenic inventory of  $^{36}\text{Cl}$  is calculated based on the U and Th concentrations of each sample. The radiogenic inventories as well as the sample ratio were calculated using CHLOE (Phillip and Plummer, 1996). The uncertainties expressed in the cosmogenic and radiogenic  $^{36}\text{Cl}$  concentrations are calculated based on the analytical uncertainty of the AMS analysis.

Table A7.4. Normalized Cosmogenic  $^{36}\text{Cl}$  and Inheritance Removed.

Sample #	Depth (meters)	Cosmogenic $^{36}\text{Cl}$ Surface Production (atoms/g/yr)	Normalized Cosmogenic $^{36}\text{Cl}$ ( $\times 10^6$ atoms/g)	Minus Inheritance Cosmogenic $^{36}\text{Cl}$ ( $\times 10^6$ atoms/g)
HW-a	3.17	22.5	1.31 +/- 0.05	0.32 +/- 0.01
HW-b	2.39	22.7	1.82 +/- 0.07	0.84 +/- 0.03
HW-c	1.98	22.7	2.02 +/- 0.07	1.04 +/- 0.03
HW-d	1.63	22.8	2.83 +/- 0.11	1.84 +/- 0.07
HW-e	1.12	23.2	2.90 +/- 0.12	1.91 +/- 0.08
HW-f	0.66	24.6	3.27 +/- 0.13	2.28 +/- 0.09
HW-g	0.36	24.5	3.62 +/- 0.14	2.63 +/- 0.11
HW-h	0.05	23.3	3.27 +/- 0.14	2.29 +/- 0.10
FW-a	3.61	22.7	0.88 +/- 0.04	-0.10 +/- -0.005
FW-b	2.64	24.2	1.01 +/- 0.04	0.02 +/- 0.00
FW-c	2.08	22.7	1.17 +/- 0.05	0.18 +/- 0.01
FW-d	1.57	22.2	1.30 +/- 0.06	0.31 +/- 0.02
FW-e	0.94	22.3	1.42 +/- 0.07	0.43 +/- 0.02
FW-f	0.61	23.7	1.86 +/- 0.08	0.87 +/- 0.04
FW-g	0.05	23.2	2.73 +/- 0.13	1.74 +/- 0.08
C-a-1	3.00	22.8	1.24 +/- 0.04	0.25 +/- 0.01
C-a-2	3.00	23.2	1.16 +/- 0.05	0.18 +/- 0.01
C-b	2.13	22.5	1.45 +/- 0.05	0.47 +/- 0.02
C-c	1.22	23.0	1.97 +/- 0.07	0.98 +/- 0.03
C-d	0.56	23.5	2.67 +/- 0.09	1.68 +/- 0.06
C-e	0.05	24.3	4.11 +/- 0.14	3.12 +/- 0.11

To normalize the  $^{36}\text{Cl}$  concentrations, we multiplied the cosmogenic  $^{36}\text{Cl}$  concentrations of table 5.3 by the ratio of average surface production to the sample surface production. Each sample surface production was determined from the chemical composition of that sample. The average surface production was calculated based on the average chemical composition of all the samples. Surface productions and the average production were calculated using CHLOE. The uncertainties expressed in the cosmogenic  $^{36}\text{Cl}$  concentrations are calculated based on the analytical uncertainty of the AMS analysis.

## Appendix 8.1. Cosmogenic $^{36}\text{Cl}$ Accumulation and Production Parameters

```
%  $^{36}\text{Cl}$  production parameters
% Constants:
1.420E+06 % rhob, bulk density (g / m3)
1.225E+03 % rhoa, density of air (g / m3)
2.616E+00 % Sel, elevation and latitude scaling factor (-)
1.000E+00 % ST, topographic shielding scaling factor (-)
2.303E-06 % lambda, decay constant of  $^{36}\text{Cl}$  (per y)
% Spallation production parameters:
1.700E+06 % Lfe, effective attenuation length of a cosmic ray (g / m2)
2.080E+06 % Lft, true attenuation length of a cosmic ray, from the calibration of the numerical solution (g / m2)
6.260E+02 % Pf0, production from fast neutrons (neutrons / g / y)
9.343E+20 % Nk, atoms of K / gram rock
4.542E+19 % Nca, atoms of Ca / gram rock
9.120E-21 % PsK0,  $^{36}\text{Cl}$  production rate from K (atoms of  $^{36}\text{Cl}$  / g of K / y), from Phillips et al., 1999
4.450E-21 % PsCa0,  $^{36}\text{Cl}$  production rate from Ca (atoms of  $^{36}\text{Cl}$  / g of Ca / y), from Phillips et al., 1999
% Epithermal flux and production parameters:
8.745E-02 % alepis, epithermal neutron attenuation length in the subsurface (m)
1.133E+00 % Repis, ratio of epithermal neutron production in the subsurface to that in the atmosphere (-)
1.501E-02 % Depis, epithermal neutron diffusion coefficient in the subsurface (m)
5.052E+04 % dlepis, epithermal neutron diffusion length of the subsurface (g / m2)
8.814E+07 % Fstr_esP, hypothetical epithermal neutron flux at the land surface (neutrons / m2 / y)
8.506E+06 % Fdstr_es, difference between Fstar_es and actual epithermal neutron flux at the land surface (neutrons / m2 / yr)
1.346E-03 % fepis, fraction of epithermal neutrons absorbed by chlorine and producing  $^{36}\text{Cl}$ ,
1.490E+02 % alepia, epithermal neutron attenuation length in the atmosphere (m)
7.560E+00 % Depia, epithermal neutron diffusion coefficient in the atmosphere (m)
4.015E+04 % dlepia, epithermal neutron diffusion length of the atmosphere (g / m2)
1.143E+08 % Fstr_eaP, hypothetical epithermal neutron flux in the air at the land/atm interface (neutrons / m2 / y)
-1.766E+07 % Fdstr_ea, difference between Fstar_ea and actual epithermal neutron flux at the land surface (neutrons / m2 / y)
% Thermal flux and production parameters:
9.901E-01 % althns, thermal neutron attenuation length in the subsurface (m)
9.485E-01 % pEthns, subsurface resonance escape probability (-)
1.694E+00 % Rthns, ratio of thermal neutron production in subsurface to that in atmosphere (-)
1.501E-02 % Dthns, thermal neutron diffusion coefficient in subsurface (m)
```



1.731E+05 % dlthns, thermal neutron diffusion length in subsurface (g / m<sup>2</sup>)  
 9.564E+08 % Fstr\_tsP, hypothetical equilibrium thermal neutron flux at land surface (neutrons / m<sup>2</sup> / y)  
 -8.503E+06 % depis, difference between Fstar\_es and actual flux due to the epithermal flux profile (neutrons / m<sup>2</sup> / y)  
 -6.189E+08 % dthns, difference between Fstar\_es and actual flux due to the thermal flux profile (neutrons / m<sup>2</sup> / y)  
 1.921E-03 % fthns, fraction of thermal neutrons absorbed by chlorine and producing <sup>36</sup>Cl,  
 1.355E+02 % althna, thermal neutron attenuation in atmosphere (m)  
 5.600E-01 % pEthna, atmosphere resonance escape probability (-)  
 7.560E+00 % Dthna, thermal neutron diffusion coefficient in the atmosphere (m)  
 3.900E+04 % dlthna, thermal neutron diffusion length of atmosphere (g / m<sup>2</sup>)  
 5.822E+07 % Fstr\_taP, hypothetical thermal neutron flux in atmosphere at the land/atm interface (neutrons / m<sup>2</sup> / y)  
 -1.935E+08 % depia, difference between Fstar\_ea and the actual flux due to the epithermal flux profile (neutrons / m<sup>2</sup> / y)  
 4.643E+08 % dthna, difference between Fstar\_ea and the actual flux due to the thermal flux profile (neutrons / m<sup>2</sup> / y)

## Appendix 9.1. Reduced Chi-Squared of Individual Profiles and Both Profiles

Fitting Parameters of Each Simulation:				Chi-Square-Error / (degrees of freedom - 2)		
K (m <sup>2</sup> ka <sup>-1</sup> )	first rupture (ka)	second rupture (ka)	Footwall (-)	Hanging Wall		Total (-)
				(-)	(-)	
1.00	50	10	4.37	4.86	3.67	3.67
0.60	50	24	3.17	4.22	3.05	3.05
0.50	50	48	2.15	3.48	2.41	2.41
0.70	70	10	2.36	2.34	1.83	1.83
0.60	70	24	2.30	3.54	2.48	2.48
0.40	70	50	2.74	2.22	1.84	1.84
0.68	80	16	2.21	2.37	1.81	1.81
0.47	80	24	2.17	2.10	1.65	1.65
0.38	80	36	2.46	1.77	1.53	1.53
0.80	86	10	2.12	1.53	1.53	1.53
0.50	86	24	2.20	1.70	1.43	1.43
0.30	86	50	3.96	1.43	1.67	1.67
0.37	86	36	2.79	1.50	1.45	1.45
0.35	88	40	3.08	1.40	1.46	1.46
0.54	92	20	2.23	1.90	1.55	1.55
0.45	92	24	2.39	1.70	1.48	1.48
0.40	92	28	2.57	1.35	1.32	1.32
0.31	92	40	3.48	1.41	1.56	1.56
0.80	96	10	2.16	1.90	1.53	1.53
0.50	96	24	2.43	1.48	1.36	1.36
0.50	96	25	2.47	1.50	1.38	1.38
0.30	96	50	4.84	1.23	1.76	1.76
0.50	100	20	2.52	1.56	1.43	1.43
0.39	100	28	2.98	1.34	1.41	1.41
0.52	104	16	2.67	1.67	1.52	1.52
0.48	104	24	2.81	1.43	1.42	1.42
0.34	104	36	3.91	1.28	1.58	1.58
0.60	120	10	4.07	2.04	2.04	2.04
0.40	120	24	4.24	1.85	1.97	1.97
0.30	120	50	7.68	1.66	2.63	2.63

## Appendix 8

### Profile 1.5 m from the fault plane

% Fault-scarp parameters, 0 is second column is necessary but meaningless.

% Age estimates need to be to the nearest 1 ka.

0.7	0	% geomorphic diffusivity (m <sup>2</sup> / ka)
1.3	0	% far-field slope (degrees)
122	0	% age of displaced terrace (ka)
2	0	% number of displacements
1.7	70	% magnitude (meters) and age estimate (ka)
1.8	10	% list each event on a separate row, start with the oldest

<b>Footwall</b>		<b>Hanging Wall</b>		<b>Topography</b>	
Depth (meters)	36Cl (atoms/g)	Depth (meters)	36Cl (atoms/g)	x (meters)	Z (meters)
5.13E-02	1.61E+06	5.04E-02	2.39E+06	-2.00E+01	3.94E+00
1.51E-01	1.49E+06	1.50E-01	2.22E+06	-1.95E+01	3.93E+00
2.51E-01	1.38E+06	2.50E-01	2.23E+06	-1.90E+01	3.92E+00
3.51E-01	1.27E+06	3.50E-01	2.20E+06	-1.85E+01	3.90E+00
4.51E-01	1.17E+06	4.50E-01	2.00E+06	-1.80E+01	3.89E+00
5.51E-01	1.08E+06	5.50E-01	1.96E+06	-1.75E+01	3.87E+00
6.51E-01	9.96E+05	6.50E-01	1.82E+06	-1.70E+01	3.86E+00
7.51E-01	9.18E+05	7.50E-01	1.74E+06	-1.65E+01	3.84E+00
8.51E-01	8.47E+05	8.50E-01	2.12E+06	-1.60E+01	3.82E+00
9.51E-01	7.81E+05	9.50E-01	2.07E+06	-1.55E+01	3.80E+00
1.05E+00	7.21E+05	1.05E+00	2.00E+06	-1.50E+01	3.78E+00
1.15E+00	6.66E+05	1.15E+00	1.95E+06	-1.45E+01	3.76E+00
1.25E+00	6.15E+05	1.25E+00	1.85E+06	-1.40E+01	3.73E+00
1.35E+00	5.68E+05	1.35E+00	1.96E+06	-1.35E+01	3.71E+00
1.45E+00	5.24E+05	1.45E+00	1.83E+06	-1.30E+01	3.68E+00
1.55E+00	4.84E+05	1.55E+00	1.70E+06	-1.25E+01	3.65E+00
1.65E+00	4.48E+05	1.65E+00	1.57E+06	-1.20E+01	3.62E+00
1.75E+00	4.14E+05	1.75E+00	1.44E+06	-1.15E+01	3.58E+00
1.85E+00	3.82E+05	1.85E+00	1.33E+06	-1.10E+01	3.54E+00
1.95E+00	3.53E+05	1.95E+00	1.22E+06	-1.05E+01	3.50E+00
2.05E+00	3.27E+05	2.05E+00	1.13E+06	-1.00E+01	3.45E+00
2.15E+00	3.02E+05	2.15E+00	1.04E+06	-9.50E+00	3.40E+00
2.25E+00	2.80E+05	2.25E+00	9.54E+05	-9.00E+00	3.35E+00
2.35E+00	2.59E+05	2.35E+00	8.78E+05	-8.50E+00	3.29E+00
2.45E+00	2.39E+05	2.45E+00	8.08E+05	-8.00E+00	3.23E+00
2.55E+00	2.21E+05	2.55E+00	7.44E+05	-7.50E+00	3.16E+00
2.65E+00	2.05E+05	2.65E+00	6.85E+05	-7.00E+00	3.09E+00
2.75E+00	1.90E+05	2.75E+00	6.30E+05	-6.50E+00	3.02E+00
2.85E+00	1.75E+05	2.85E+00	5.81E+05	-6.00E+00	2.94E+00
2.95E+00	1.62E+05	2.95E+00	5.35E+05	-5.50E+00	2.85E+00
3.05E+00	1.50E+05	3.05E+00	4.92E+05	-5.00E+00	2.76E+00
3.15E+00	1.39E+05	3.15E+00	4.54E+05	-4.50E+00	2.67E+00
3.25E+00	1.29E+05	3.25E+00	4.18E+05	-4.00E+00	2.57E+00
3.35E+00	1.19E+05	3.35E+00	3.85E+05	-3.50E+00	2.47E+00
3.45E+00	1.11E+05	3.45E+00	3.55E+05	-3.00E+00	2.37E+00
3.55E+00	1.02E+05	3.55E+00	3.27E+05	-2.50E+00	2.26E+00
3.65E+00	9.49E+04	3.65E+00	3.01E+05	-2.00E+00	2.15E+00

Appendix 8

3.75E+00	8.80E+04	3.75E+00	2.78E+05	-1.50E+00	2.04E+00
3.85E+00	8.15E+04	3.85E+00	2.56E+05	-1.00E+00	1.93E+00
3.95E+00	7.55E+04	3.95E+00	2.36E+05	-5.00E-01	1.81E+00
4.05E+00	7.00E+04	4.05E+00	2.17E+05	0.00E+00	1.70E+00
4.15E+00	6.49E+04	4.15E+00	2.00E+05	5.00E-01	1.58E+00
4.25E+00	6.01E+04	4.25E+00	1.85E+05	1.00E+00	1.47E+00
4.35E+00	5.57E+04	4.35E+00	1.70E+05	1.50E+00	1.36E+00
4.45E+00	5.16E+04	4.45E+00	1.57E+05	2.00E+00	1.25E+00
4.55E+00	4.79E+04	4.55E+00	1.45E+05	2.50E+00	1.14E+00
4.65E+00	4.44E+04	4.65E+00	1.33E+05	3.00E+00	1.04E+00
4.75E+00	4.12E+04	4.75E+00	1.23E+05	3.50E+00	9.38E-01
4.85E+00	3.82E+04	4.85E+00	1.14E+05	4.00E+00	8.41E-01
4.95E+00	3.54E+04	4.95E+00	1.05E+05	4.50E+00	7.47E-01
5.05E+00	3.28E+04	5.05E+00	9.66E+04	5.00E+00	6.58E-01
5.15E+00	3.04E+04	5.15E+00	8.91E+04	5.50E+00	5.73E-01
5.25E+00	2.82E+04	5.25E+00	8.22E+04	6.00E+00	4.93E-01
5.35E+00	2.62E+04	5.35E+00	7.58E+04	6.50E+00	4.18E-01
5.45E+00	2.43E+04	5.45E+00	6.99E+04	7.00E+00	3.47E-01
5.55E+00	2.25E+04	5.55E+00	6.45E+04	7.50E+00	2.80E-01
5.65E+00	2.09E+04	5.65E+00	5.95E+04	8.00E+00	2.18E-01
5.75E+00	1.94E+04	5.75E+00	5.49E+04	8.50E+00	1.60E-01
5.85E+00	1.80E+04	5.85E+00	5.07E+04	9.00E+00	1.07E-01
5.95E+00	1.67E+04	5.95E+00	4.68E+04	9.50E+00	5.73E-02
6.05E+00	1.55E+04	6.05E+00	4.32E+04	1.00E+01	1.16E-02
6.15E+00	1.44E+04	6.15E+00	3.99E+04	1.05E+01	-3.06E-02
6.25E+00	1.33E+04	6.25E+00	3.68E+04	1.10E+01	-6.95E-02
6.35E+00	1.24E+04			1.15E+01	-1.05E-01
6.45E+00	1.15E+04			1.20E+01	-1.38E-01
6.55E+00	1.07E+04			1.25E+01	-1.69E-01
6.65E+00	9.89E+03			1.30E+01	-1.97E-01
6.75E+00	9.19E+03			1.35E+01	-2.23E-01
6.85E+00	8.53E+03			1.40E+01	-2.47E-01
6.95E+00	7.92E+03			1.45E+01	-2.69E-01
7.05E+00	7.35E+03			1.50E+01	-2.90E-01
7.15E+00	6.82E+03			1.55E+01	-3.09E-01
				1.60E+01	-3.27E-01
				1.65E+01	-3.45E-01
				1.70E+01	-3.61E-01
				1.75E+01	-3.77E-01
				1.80E+01	-3.92E-01
				1.85E+01	-4.06E-01
				1.90E+01	-4.20E-01
				1.95E+01	-4.33E-01
				2.00E+01	-4.46E-01

Lookup modeled  $^{36}\text{Cl}$  accumulation at sample depths:

Footwall		Hanging Wall	
Depth (meters)	$^{36}\text{Cl}$ (atoms/g)	Depth (meters)	$^{36}\text{Cl}$ (atoms/g)
6.51E-01	9.96E+05	3.50E-01	2.20E+06
1.05E+00	7.21E+05	6.50E-01	1.82E+06
1.65E+00	4.48E+05	1.05E+00	2.00E+06
2.15E+00	3.02E+05	1.55E+00	1.70E+06
2.75E+00	1.90E+05	1.95E+00	1.22E+06
		2.35E+00	8.78E+05
		3.15E+00	4.54E+05

## Difference between modeled and observed:

1.05E+05	-4.40E+05
2.71E+05	-4.82E+05
1.19E+05	8.38E+04
1.05E+05	-1.61E+05
1.47E+05	1.74E+05
	2.37E+04
	1.12E+05

## Squared Difference:

1.10E+10	1.94E+11
7.35E+10	2.32E+11
1.41E+10	7.03E+09
1.11E+10	2.60E+10
2.17E+10	3.02E+10
	5.62E+08
	1.25E+10

## Chi-square residuals:

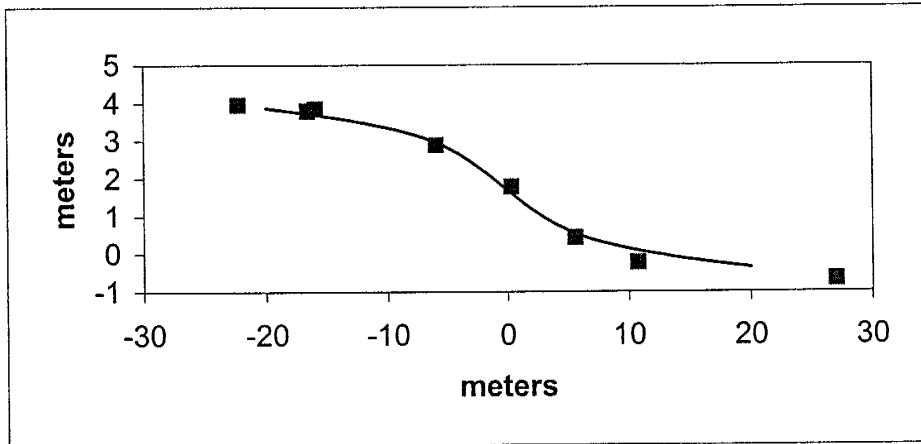
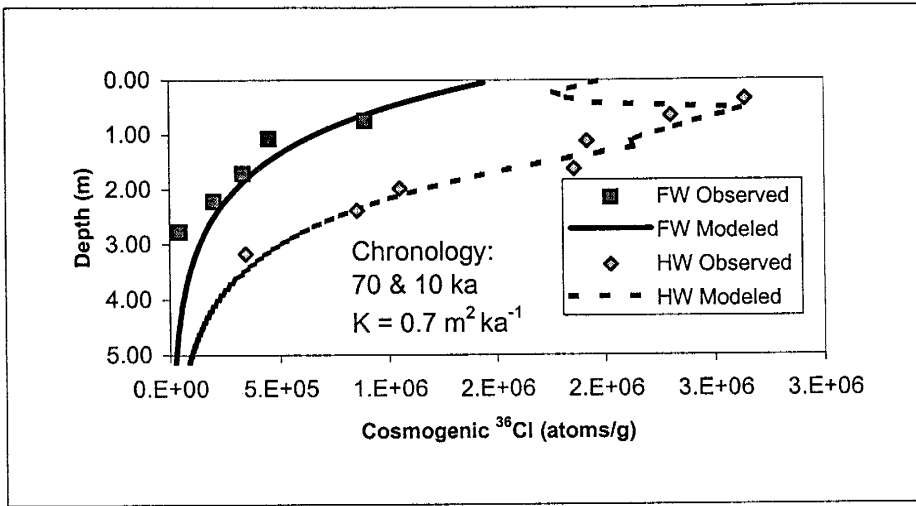
1.10E+04	8.82E+04
1.02E+05	1.28E+05
3.14E+04	3.51E+03
3.66E+04	1.53E+04
1.14E+05	2.47E+04
	6.40E+02
	2.75E+04

## Chi-square value:

2.95E+05	2.87E+05
----------	----------

**Total Chi-square:** 5.83E+05

Appendix 8



Appendix 8

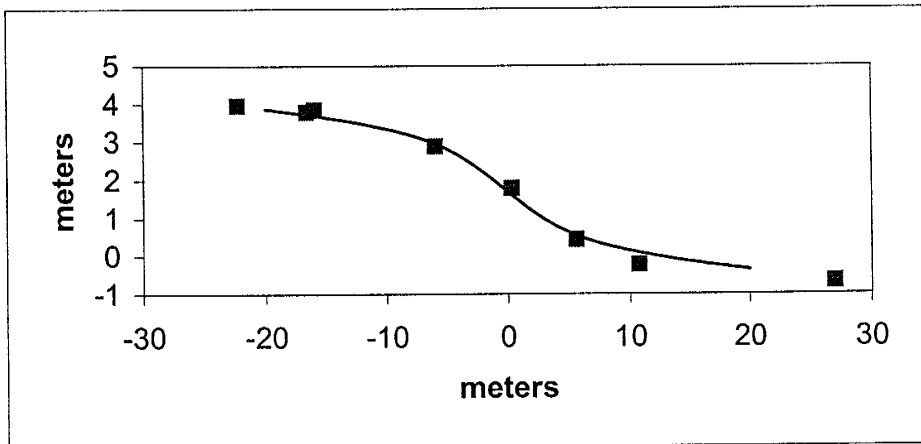
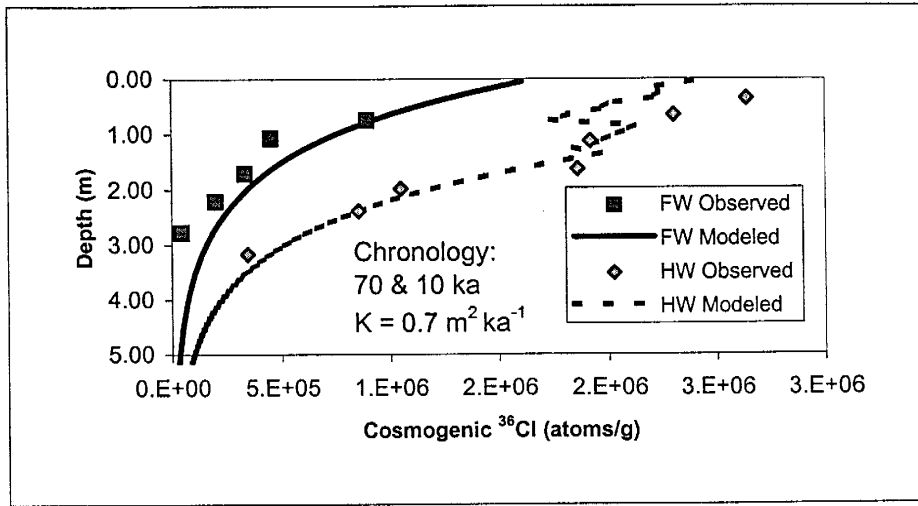


Table A8.4. Normalized Cosmogenic  $^{36}\text{Cl}$  and Inheritance Removed.

Sample #	Depth (meters)	Cosmogenic $^{36}\text{Cl}$ Surface Production (atoms/g/yr)	Normalized Cosmogenic $^{36}\text{Cl}$ (x10 <sup>6</sup> atoms/g)	Minus Inheritance Cosmogenic $^{36}\text{Cl}$ (x10 <sup>6</sup> atoms/g)
HW-a	3.17	22.5	1.31 +/- 0.05	0.34 +/- 0.01
HW-b	2.39	22.7	1.82 +/- 0.07	0.85 +/- 0.03
HW-c	1.98	22.7	2.02 +/- 0.07	1.05 +/- 0.03
HW-d	1.63	22.8	2.82 +/- 0.11	1.86 +/- 0.07
HW-e	1.12	23.2	2.89 +/- 0.12	1.92 +/- 0.08
HW-f	0.66	24.6	3.26 +/- 0.13	2.30 +/- 0.09
HW-g	0.36	24.5	3.61 +/- 0.14	2.64 +/- 0.11
HW-h	0.05	23.3	3.26 +/- 0.14	2.30 +/- 0.10
FW-a	3.74	22.7	0.88 +/- 0.04	-0.08 +/- -0.004
FW-b	2.77	24.2	1.01 +/- 0.04	0.04 +/- 0.00
FW-c	2.21	22.7	1.16 +/- 0.05	0.20 +/- 0.01
FW-d	1.71	22.2	1.29 +/- 0.06	0.33 +/- 0.02
FW-e	1.07	22.3	1.41 +/- 0.07	0.45 +/- 0.02
FW-f	0.74	23.7	1.86 +/- 0.08	0.89 +/- 0.04
FW-g	0.18	23.2	2.72 +/- 0.13	1.76 +/- 0.08
C-a-1	3.00	22.8	1.23 +/- 0.04	0.27 +/- 0.01
C-a-2	3.00	23.2	1.16 +/- 0.05	0.20 +/- 0.01
C-b	2.13	22.5	1.45 +/- 0.05	0.49 +/- 0.02
C-c	1.22	23.0	1.96 +/- 0.06	1.00 +/- 0.03
C-d	0.56	23.5	2.66 +/- 0.09	1.70 +/- 0.06
C-e	0.05	24.3	4.09 +/- 0.14	3.13 +/- 0.11



To normalize the  $^{36}\text{Cl}$  concentrations, we multiplied the cosmogenic  $^{36}\text{Cl}$  concentrations of table 5.3 by the ratio of average surface production to the sample surface production. Each sample surface production was determined from the chemical composition of that sample. The average surface production was calculated based on the average chemical composition of the all the samples. Surface productions and the average production were calculated using CHLOE. The uncertainties expressed in the cosmogenic  $^{36}\text{Cl}$  concentrations are calculated based on the analytical uncertainty of the AMS analysis.

## Appendix 8.2. CLARA Simulations

Appendix 8

Profile 1.5 m from the fault plane

% Fault-scarp parameters, 0 is second column is necessary but meaningless.

% Age estimates need to be to the nearest 1 ka.

0.5	0	% geomorphic diffusivity (m <sup>2</sup> / ka)
1.3	0	% far-field slope (degrees)
122	0	% age of displaced terrace (ka)
2	0	% number of displacements
1.7	96	% magnitude (meters) and age estimate (ka)
1.8	24	% list each event on a separate row, start with the oldest

Footwall		Hanging Wall		Topography	
Depth (meters)	36Cl (atoms/g)	Depth (meters)	36Cl (atoms/g)	x (meters)	Z (meters)
7.17E-02	1.56E+06	2.61E-02	2.10E+06	-2.00E+01	3.92E+00
1.72E-01	1.44E+06	1.26E-01	2.45E+06	-1.95E+01	3.90E+00
2.72E-01	1.33E+06	2.26E-01	2.10E+06	-1.90E+01	3.88E+00
3.72E-01	1.23E+06	3.26E-01	2.12E+06	-1.85E+01	3.87E+00
4.72E-01	1.13E+06	4.26E-01	2.09E+06	-1.80E+01	3.85E+00
5.72E-01	1.04E+06	5.26E-01	1.99E+06	-1.75E+01	3.83E+00
6.72E-01	9.60E+05	6.26E-01	2.52E+06	-1.70E+01	3.81E+00
7.72E-01	8.85E+05	7.26E-01	2.49E+06	-1.65E+01	3.79E+00
8.72E-01	8.16E+05	8.26E-01	2.38E+06	-1.60E+01	3.77E+00
9.72E-01	7.53E+05	9.26E-01	2.25E+06	-1.55E+01	3.75E+00
1.07E+00	6.95E+05	1.03E+00	2.12E+06	-1.50E+01	3.73E+00
1.17E+00	6.41E+05	1.13E+00	1.97E+06	-1.45E+01	3.70E+00
1.27E+00	5.92E+05	1.23E+00	1.88E+06	-1.40E+01	3.68E+00
1.37E+00	5.47E+05	1.33E+00	1.86E+06	-1.35E+01	3.65E+00
1.47E+00	5.05E+05	1.43E+00	1.72E+06	-1.30E+01	3.62E+00
1.57E+00	4.66E+05	1.53E+00	1.59E+06	-1.25E+01	3.59E+00
1.67E+00	4.31E+05	1.63E+00	1.46E+06	-1.20E+01	3.56E+00
1.77E+00	3.98E+05	1.73E+00	1.35E+06	-1.15E+01	3.53E+00
1.87E+00	3.68E+05	1.83E+00	1.24E+06	-1.10E+01	3.49E+00
1.97E+00	3.40E+05	1.93E+00	1.14E+06	-1.05E+01	3.45E+00
2.07E+00	3.14E+05	2.03E+00	1.05E+06	-1.00E+01	3.41E+00
2.17E+00	2.91E+05	2.13E+00	9.65E+05	-9.50E+00	3.37E+00
2.27E+00	2.69E+05	2.23E+00	8.88E+05	-9.00E+00	3.32E+00
2.37E+00	2.49E+05	2.33E+00	8.17E+05	-8.50E+00	3.27E+00
2.47E+00	2.30E+05	2.43E+00	7.53E+05	-8.00E+00	3.22E+00
2.57E+00	2.13E+05	2.53E+00	6.93E+05	-7.50E+00	3.16E+00
2.67E+00	1.97E+05	2.63E+00	6.38E+05	-7.00E+00	3.09E+00
2.77E+00	1.82E+05	2.73E+00	5.88E+05	-6.50E+00	3.03E+00
2.87E+00	1.69E+05	2.83E+00	5.42E+05	-6.00E+00	2.95E+00
2.97E+00	1.56E+05	2.93E+00	4.99E+05	-5.50E+00	2.87E+00
3.07E+00	1.44E+05	3.03E+00	4.60E+05	-5.00E+00	2.79E+00
3.17E+00	1.34E+05	3.13E+00	4.24E+05	-4.50E+00	2.70E+00
3.27E+00	1.24E+05	3.23E+00	3.91E+05	-4.00E+00	2.60E+00
3.37E+00	1.15E+05	3.33E+00	3.61E+05	-3.50E+00	2.50E+00
3.47E+00	1.06E+05	3.43E+00	3.33E+05	-3.00E+00	2.40E+00
3.57E+00	9.83E+04	3.53E+00	3.07E+05	-2.50E+00	2.29E+00
3.67E+00	9.11E+04	3.63E+00	2.83E+05	-2.00E+00	2.17E+00

## Appendix 8

3.77E+00	8.44E+04	3.73E+00	2.61E+05	-1.50E+00	2.06E+00
3.87E+00	7.82E+04	3.83E+00	2.41E+05	-1.00E+00	1.94E+00
3.97E+00	7.24E+04	3.93E+00	2.22E+05	-5.00E-01	1.82E+00
4.07E+00	6.71E+04	4.03E+00	2.05E+05	0.00E+00	1.70E+00
4.17E+00	6.22E+04	4.13E+00	1.89E+05	5.00E-01	1.58E+00
4.27E+00	5.76E+04	4.23E+00	1.75E+05	1.00E+00	1.46E+00
4.37E+00	5.34E+04	4.33E+00	1.61E+05	1.50E+00	1.34E+00
4.47E+00	4.95E+04	4.43E+00	1.49E+05	2.00E+00	1.23E+00
4.57E+00	4.59E+04	4.53E+00	1.37E+05	2.50E+00	1.12E+00
4.67E+00	4.25E+04	4.63E+00	1.27E+05	3.00E+00	1.01E+00
4.77E+00	3.94E+04	4.73E+00	1.17E+05	3.50E+00	9.10E-01
4.87E+00	3.65E+04	4.83E+00	1.08E+05	4.00E+00	8.14E-01
4.97E+00	3.39E+04	4.93E+00	9.99E+04	4.50E+00	7.24E-01
5.07E+00	3.14E+04	5.03E+00	9.23E+04	5.00E+00	6.39E-01
5.17E+00	2.91E+04	5.13E+00	8.53E+04	5.50E+00	5.60E-01
5.27E+00	2.70E+04	5.23E+00	7.88E+04	6.00E+00	4.86E-01
5.37E+00	2.51E+04	5.33E+00	7.28E+04	6.50E+00	4.17E-01
5.47E+00	2.32E+04	5.43E+00	6.72E+04	7.00E+00	3.54E-01
5.57E+00	2.15E+04	5.53E+00	6.21E+04	7.50E+00	2.94E-01
5.67E+00	2.00E+04	5.63E+00	5.74E+04	8.00E+00	2.40E-01
5.77E+00	1.85E+04	5.73E+00	5.31E+04	8.50E+00	1.89E-01
5.87E+00	1.72E+04	5.83E+00	4.91E+04	9.00E+00	1.42E-01
5.97E+00	1.60E+04	5.93E+00	4.53E+04	9.50E+00	9.78E-02
6.07E+00	1.48E+04	6.03E+00	4.19E+04	1.00E+01	5.71E-02
6.17E+00	1.37E+04	6.13E+00	3.88E+04	1.05E+01	1.91E-02
6.27E+00	1.27E+04	6.23E+00	3.58E+04	1.10E+01	-1.65E-02
6.37E+00	1.18E+04			1.15E+01	-4.98E-02
6.47E+00	1.10E+04			1.20E+01	-8.11E-02
6.57E+00	1.02E+04			1.25E+01	-1.11E-01
6.67E+00	9.45E+03			1.30E+01	-1.39E-01
6.77E+00	8.77E+03			1.35E+01	-1.65E-01
6.87E+00	8.14E+03			1.40E+01	-1.90E-01
6.97E+00	7.56E+03			1.45E+01	-2.14E-01
7.07E+00	7.01E+03			1.50E+01	-2.37E-01
7.17E+00	6.51E+03			1.55E+01	-2.58E-01
				1.60E+01	-2.79E-01
				1.65E+01	-2.99E-01
				1.70E+01	-3.19E-01
				1.75E+01	-3.37E-01
				1.80E+01	-3.55E-01
				1.85E+01	-3.72E-01
				1.90E+01	-3.89E-01
				1.95E+01	-4.05E-01
				2.00E+01	-4.21E-01

Lookup modeled <sup>36</sup>Cl accumulation at sample depths:

Footwall		Hanging Wall	
Depth (meters)	<sup>36</sup> Cl (atoms/g)	Depth (meters)	<sup>36</sup> Cl (atoms/g)
6.72E-01	9.60E+05	3.26E-01	2.12E+06
9.72E-01	7.53E+05	6.26E-01	2.52E+06
1.67E+00	4.31E+05	1.03E+00	2.12E+06
2.17E+00	2.91E+05	1.53E+00	1.59E+06
2.67E+00	1.97E+05	1.93E+00	1.14E+06
		2.33E+00	8.17E+05
		3.13E+00	4.24E+05

Difference between modeled and observed:

6.86E+04	-5.15E+05
3.03E+05	2.18E+05
1.02E+05	2.05E+05
9.37E+04	-2.72E+05
1.55E+05	8.93E+04
	-3.65E+04
	8.23E+04

Squared Difference:

4.71E+09	2.65E+11
9.17E+10	4.76E+10
1.04E+10	4.20E+10
8.78E+09	7.41E+10
2.39E+10	7.98E+09
	1.33E+09
	6.77E+09

Chi-square residuals:

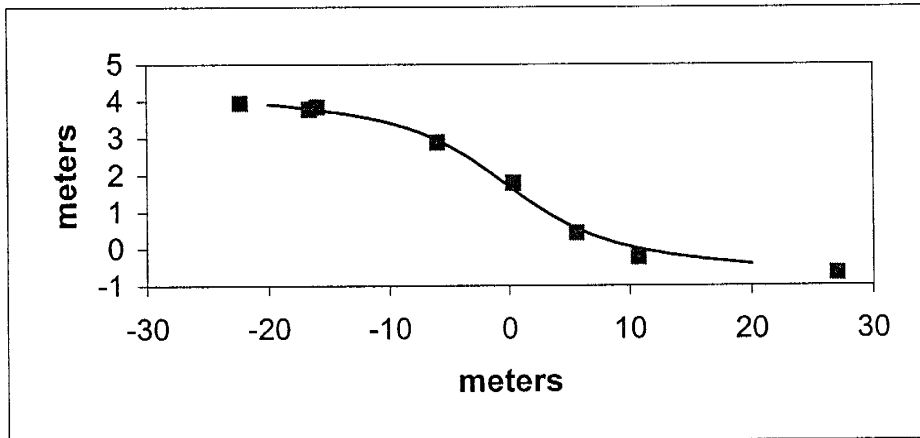
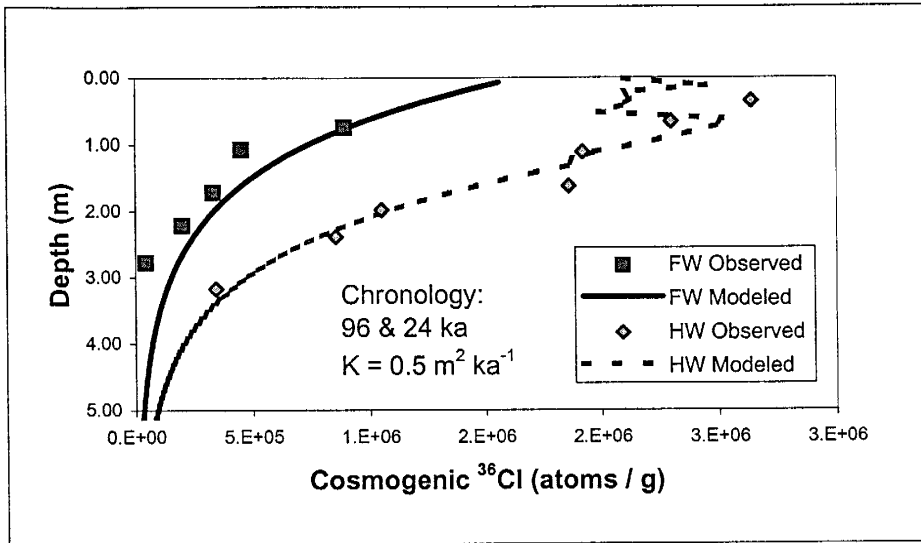
4.90E+03	1.25E+05
1.22E+05	1.89E+04
2.41E+04	1.98E+04
3.02E+04	4.67E+04
1.21E+05	7.00E+03
	1.63E+03
	1.60E+04

Chi-square value:

3.02E+05	2.35E+05
----------	----------

Total Chi-square: 5.37E+05

Appendix 8





Appendix 8

Profile 1.5 m from the fault plane

% Fault-scarp parameters, 0 is second column is necessary but meaningless.

% Age estimates needs to be to the nearest 1 ka.

0.3	0	% geomorphic diffusivity (m <sup>2</sup> / ka)
1.3	0	% far-field slope (degrees)
122	0	% age of displaced terrace (ka)
2	0	% number of displacements
1.7	96	% magnitude (meters) and age estimate (ka)
1.8	50	% list each event on a separate row, start with the oldest

<u>Footwall</u>		<u>Hanging Wall</u>		<u>Topography</u>	
<u>Depth</u> <u>(meters)</u>	<u>36Cl</u> <u>(atoms/g)</u>	<u>Depth</u> <u>(meters)</u>	<u>36Cl</u> <u>(atoms/g)</u>	<u>x</u> <u>(meters)</u>	<u>Z</u> <u>(meters)</u>
7.86E-02	1.70E+06	1.64E-02	2.32E+06	-2.00E+01	3.95E+00
1.79E-01	1.57E+06	1.16E-01	2.28E+06	-1.95E+01	3.93E+00
2.79E-01	1.45E+06	2.16E-01	2.25E+06	-1.90E+01	3.92E+00
3.79E-01	1.34E+06	3.16E-01	2.25E+06	-1.85E+01	3.90E+00
4.79E-01	1.23E+06	4.16E-01	2.26E+06	-1.80E+01	3.89E+00
5.79E-01	1.14E+06	5.16E-01	2.02E+06	-1.75E+01	3.88E+00
6.79E-01	1.05E+06	6.16E-01	1.93E+06	-1.70E+01	3.86E+00
7.79E-01	9.69E+05	7.16E-01	2.31E+06	-1.65E+01	3.84E+00
8.79E-01	8.94E+05	8.16E-01	2.22E+06	-1.60E+01	3.83E+00
9.79E-01	8.25E+05	9.16E-01	2.16E+06	-1.55E+01	3.81E+00
1.08E+00	7.62E+05	1.02E+00	2.02E+06	-1.50E+01	3.79E+00
1.18E+00	7.04E+05	1.12E+00	1.91E+06	-1.45E+01	3.77E+00
1.28E+00	6.51E+05	1.22E+00	1.83E+06	-1.40E+01	3.75E+00
1.38E+00	6.01E+05	1.32E+00	1.79E+06	-1.35E+01	3.72E+00
1.48E+00	5.56E+05	1.42E+00	1.66E+06	-1.30E+01	3.70E+00
1.58E+00	5.14E+05	1.52E+00	1.54E+06	-1.25E+01	3.67E+00
1.68E+00	4.75E+05	1.62E+00	1.41E+06	-1.20E+01	3.64E+00
1.78E+00	4.39E+05	1.72E+00	1.30E+06	-1.15E+01	3.61E+00
1.88E+00	4.06E+05	1.82E+00	1.20E+06	-1.10E+01	3.57E+00
1.98E+00	3.76E+05	1.92E+00	1.10E+06	-1.05E+01	3.53E+00
2.08E+00	3.48E+05	2.02E+00	1.01E+06	-1.00E+01	3.49E+00
2.18E+00	3.22E+05	2.12E+00	9.33E+05	-9.50E+00	3.45E+00
2.28E+00	2.98E+05	2.22E+00	8.58E+05	-9.00E+00	3.40E+00
2.38E+00	2.76E+05	2.32E+00	7.90E+05	-8.50E+00	3.34E+00
2.48E+00	2.55E+05	2.42E+00	7.27E+05	-8.00E+00	3.28E+00
2.58E+00	2.37E+05	2.52E+00	6.70E+05	-7.50E+00	3.22E+00
2.68E+00	2.19E+05	2.62E+00	6.17E+05	-7.00E+00	3.15E+00
2.78E+00	2.03E+05	2.72E+00	5.68E+05	-6.50E+00	3.07E+00
2.88E+00	1.88E+05	2.82E+00	5.24E+05	-6.00E+00	2.99E+00
2.98E+00	1.74E+05	2.92E+00	4.82E+05	-5.50E+00	2.91E+00
3.08E+00	1.61E+05	3.02E+00	4.45E+05	-5.00E+00	2.82E+00
3.18E+00	1.49E+05	3.12E+00	4.10E+05	-4.50E+00	2.72E+00
3.28E+00	1.39E+05	3.22E+00	3.78E+05	-4.00E+00	2.62E+00
3.38E+00	1.28E+05	3.32E+00	3.48E+05	-3.50E+00	2.52E+00
3.48E+00	1.19E+05	3.42E+00	3.21E+05	-3.00E+00	2.41E+00
3.58E+00	1.10E+05	3.52E+00	2.96E+05	-2.50E+00	2.29E+00
3.68E+00	1.02E+05	3.62E+00	2.73E+05	-2.00E+00	2.18E+00



## Appendix 8

3.78E+00	9.48E+04	3.72E+00	2.52E+05	-1.50E+00	2.06E+00
3.88E+00	8.79E+04	3.82E+00	2.32E+05	-1.00E+00	1.94E+00
3.98E+00	8.16E+04	3.92E+00	2.14E+05	-5.00E-01	1.82E+00
4.08E+00	7.56E+04	4.02E+00	1.98E+05	0.00E+00	1.69E+00
4.18E+00	7.01E+04	4.12E+00	1.83E+05	5.00E-01	1.57E+00
4.28E+00	6.51E+04	4.22E+00	1.69E+05	1.00E+00	1.45E+00
4.38E+00	6.04E+04	4.32E+00	1.56E+05	1.50E+00	1.33E+00
4.48E+00	5.60E+04	4.42E+00	1.44E+05	2.00E+00	1.22E+00
4.58E+00	5.19E+04	4.52E+00	1.33E+05	2.50E+00	1.10E+00
4.68E+00	4.82E+04	4.62E+00	1.22E+05	3.00E+00	9.94E-01
4.78E+00	4.47E+04	4.72E+00	1.13E+05	3.50E+00	8.89E-01
4.88E+00	4.15E+04	4.82E+00	1.04E+05	4.00E+00	7.88E-01
4.98E+00	3.85E+04	4.92E+00	9.64E+04	4.50E+00	6.93E-01
5.08E+00	3.57E+04	5.02E+00	8.91E+04	5.00E+00	6.02E-01
5.18E+00	3.32E+04	5.12E+00	8.23E+04	5.50E+00	5.17E-01
5.28E+00	3.08E+04	5.22E+00	7.60E+04	6.00E+00	4.37E-01
5.38E+00	2.86E+04	5.32E+00	7.02E+04	6.50E+00	3.63E-01
5.48E+00	2.65E+04	5.42E+00	6.49E+04	7.00E+00	2.94E-01
5.58E+00	2.46E+04	5.52E+00	5.99E+04	7.50E+00	2.30E-01
5.68E+00	2.29E+04	5.62E+00	5.54E+04	8.00E+00	1.71E-01
5.78E+00	2.12E+04	5.72E+00	5.12E+04	8.50E+00	1.16E-01
5.88E+00	1.97E+04	5.82E+00	4.73E+04	9.00E+00	6.62E-02
5.98E+00	1.83E+04	5.92E+00	4.37E+04	9.50E+00	2.03E-02
6.08E+00	1.70E+04	6.02E+00	4.04E+04	1.00E+01	-2.19E-02
6.18E+00	1.58E+04	6.12E+00	3.74E+04	1.05E+01	-6.06E-02
6.28E+00	1.47E+04	6.22E+00	3.46E+04	1.10E+01	-9.60E-02
6.38E+00	1.36E+04			1.15E+01	-1.29E-01
6.48E+00	1.26E+04			1.20E+01	-1.59E-01
6.58E+00	1.17E+04			1.25E+01	-1.86E-01
6.68E+00	1.09E+04			1.30E+01	-2.12E-01
6.78E+00	1.01E+04			1.35E+01	-2.35E-01
6.88E+00	9.41E+03			1.40E+01	-2.57E-01
6.98E+00	8.74E+03			1.45E+01	-2.78E-01
7.08E+00	8.12E+03			1.50E+01	-2.97E-01
7.18E+00	7.54E+03			1.55E+01	-3.15E-01
				1.60E+01	-3.32E-01
				1.65E+01	-3.49E-01
				1.70E+01	-3.64E-01
				1.75E+01	-3.79E-01
				1.80E+01	-3.93E-01
				1.85E+01	-4.07E-01
				1.90E+01	-4.21E-01
				1.95E+01	-4.34E-01
				2.00E+01	-4.47E-01

Lookup modeled <sup>36</sup>Cl accumulation at sample depths:

Footwall		Hanging Wall	
Depth (meters)	<sup>36</sup> Cl (atoms/g)	Depth (meters)	<sup>36</sup> Cl (atoms/g)
6.79E-01	1.05E+06	3.16E-01	2.25E+06
9.79E-01	8.25E+05	6.16E-01	1.93E+06
1.68E+00	4.75E+05	1.12E+00	1.91E+06
2.18E+00	3.22E+05	1.62E+00	1.41E+06
2.68E+00	2.19E+05	1.92E+00	1.10E+06
		2.32E+00	7.90E+05
		3.12E+00	4.10E+05

## Difference between modeled and observed:

1.59E+05	-3.95E+05
3.75E+05	-3.74E+05
1.46E+05	-1.21E+04
1.25E+05	-4.45E+05
1.77E+05	5.16E+04
	-6.39E+04
	6.78E+04

## Squared Difference:

2.53E+10	1.56E+11
1.41E+11	1.40E+11
2.13E+10	1.46E+08
1.56E+10	1.98E+11
3.12E+10	2.67E+09
	4.09E+09
	4.59E+09

## Chi-square residuals:

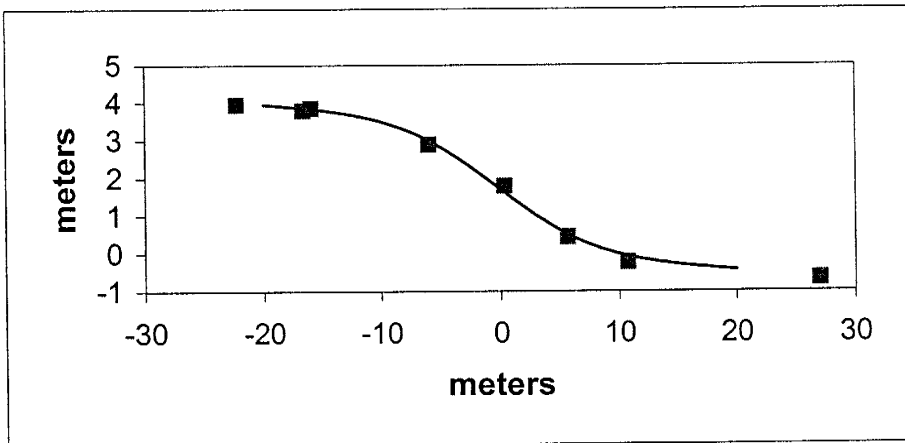
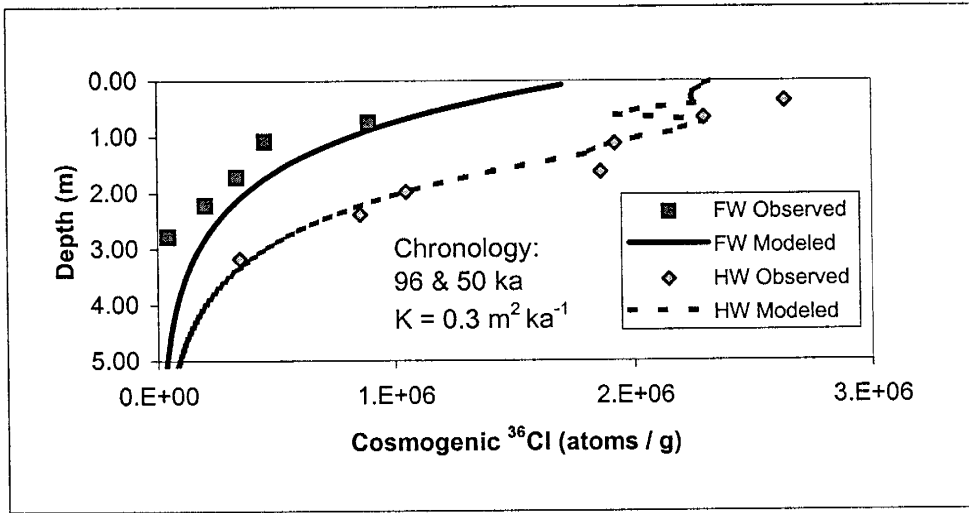
2.41E+04	6.94E+04
1.71E+05	7.27E+04
4.49E+04	7.65E+01
4.85E+04	1.40E+05
1.43E+05	2.42E+03
	5.17E+03
	1.12E+04

## Chi-square value:

4.31E+05	3.01E+05
----------	----------

**Total Chi-square:** 7.32E+05

Appendix 8



Appendix 8

Profile 1.5 m from the fault plane

% Fault-scarp parameters, 0 is second column is necessary but meaningless.

% Age estimates need to be to the nearest 1 ka.

0.8	0	% geomorphic diffusivity (m <sup>2</sup> / ka)
1.3	0	% far-field slope (degrees)
140	0	% age of displaced terrace (ka)
2	0	% number of displacements
1.7	96	% magnitude (meters) and age estimate (ka)
1.8	10	% list each event on a separate row, start with the oldest

Footwall		Hanging Wall		Topography	
Depth (meters)	<sup>36</sup> Cl (atoms/g)	Depth (meters)	<sup>36</sup> Cl (atoms/g)	x (meters)	Z (meters)
6.86E-03	1.63E+06	8.53E-02	2.06E+06	-2.00E+01	3.86E+00
1.07E-01	1.50E+06	1.85E-01	2.04E+06	-1.95E+01	3.84E+00
2.07E-01	1.38E+06	2.85E-01	1.97E+06	-1.90E+01	3.82E+00
3.07E-01	1.27E+06	3.85E-01	2.00E+06	-1.85E+01	3.80E+00
4.07E-01	1.17E+06	4.85E-01	2.17E+06	-1.80E+01	3.78E+00
5.07E-01	1.08E+06	5.85E-01	2.66E+06	-1.75E+01	3.76E+00
6.07E-01	9.94E+05	6.85E-01	2.55E+06	-1.70E+01	3.74E+00
7.07E-01	9.16E+05	7.85E-01	2.45E+06	-1.65E+01	3.71E+00
8.07E-01	8.44E+05	8.85E-01	2.30E+06	-1.60E+01	3.69E+00
9.07E-01	7.78E+05	9.85E-01	2.16E+06	-1.55E+01	3.67E+00
1.01E+00	7.17E+05	1.09E+00	2.01E+06	-1.50E+01	3.64E+00
1.11E+00	6.61E+05	1.19E+00	1.93E+06	-1.45E+01	3.62E+00
1.21E+00	6.10E+05	1.29E+00	1.87E+06	-1.40E+01	3.59E+00
1.31E+00	5.63E+05	1.39E+00	1.73E+06	-1.35E+01	3.56E+00
1.41E+00	5.19E+05	1.49E+00	1.60E+06	-1.30E+01	3.54E+00
1.51E+00	4.79E+05	1.59E+00	1.47E+06	-1.25E+01	3.51E+00
1.61E+00	4.43E+05	1.69E+00	1.35E+06	-1.20E+01	3.48E+00
1.71E+00	4.09E+05	1.79E+00	1.25E+06	-1.15E+01	3.45E+00
1.81E+00	3.77E+05	1.89E+00	1.15E+06	-1.10E+01	3.41E+00
1.91E+00	3.49E+05	1.99E+00	1.06E+06	-1.05E+01	3.38E+00
2.01E+00	3.22E+05	2.09E+00	9.71E+05	-1.00E+01	3.35E+00
2.11E+00	2.98E+05	2.19E+00	8.94E+05	-9.50E+00	3.31E+00
2.21E+00	2.75E+05	2.29E+00	8.23E+05	-9.00E+00	3.27E+00
2.31E+00	2.54E+05	2.39E+00	7.58E+05	-8.50E+00	3.23E+00
2.41E+00	2.35E+05	2.49E+00	6.98E+05	-8.00E+00	3.18E+00
2.51E+00	2.17E+05	2.59E+00	6.43E+05	-7.50E+00	3.13E+00
2.61E+00	2.01E+05	2.69E+00	5.93E+05	-7.00E+00	3.08E+00
2.71E+00	1.86E+05	2.79E+00	5.46E+05	-6.50E+00	3.02E+00
2.81E+00	1.72E+05	2.89E+00	5.03E+05	-6.00E+00	2.96E+00
2.91E+00	1.59E+05	2.99E+00	4.64E+05	-5.50E+00	2.89E+00
3.01E+00	1.47E+05	3.09E+00	4.28E+05	-5.00E+00	2.81E+00
3.11E+00	1.36E+05	3.19E+00	3.94E+05	-4.50E+00	2.73E+00
3.21E+00	1.26E+05	3.29E+00	3.64E+05	-4.00E+00	2.64E+00
3.31E+00	1.16E+05	3.39E+00	3.35E+05	-3.50E+00	2.54E+00
3.41E+00	1.08E+05	3.49E+00	3.09E+05	-3.00E+00	2.44E+00
3.51E+00	9.96E+04	3.59E+00	2.85E+05	-2.50E+00	2.33E+00
3.61E+00	9.21E+04	3.69E+00	2.63E+05	-2.00E+00	2.21E+00

## Appendix 8

3.71E+00	8.53E+04	3.79E+00	2.43E+05	-1.50E+00	2.08E+00
3.81E+00	7.90E+04	3.89E+00	2.24E+05	-1.00E+00	1.95E+00
3.91E+00	7.31E+04	3.99E+00	2.07E+05	-5.00E-01	1.82E+00
4.01E+00	6.77E+04	4.09E+00	1.91E+05	0.00E+00	1.69E+00
4.11E+00	6.27E+04	4.19E+00	1.76E+05	5.00E-01	1.56E+00
4.21E+00	5.80E+04	4.29E+00	1.63E+05	1.00E+00	1.43E+00
4.31E+00	5.37E+04	4.39E+00	1.50E+05	1.50E+00	1.30E+00
4.41E+00	4.98E+04	4.49E+00	1.39E+05	2.00E+00	1.19E+00
4.51E+00	4.61E+04	4.59E+00	1.28E+05	2.50E+00	1.07E+00
4.61E+00	4.27E+04	4.69E+00	1.18E+05	3.00E+00	9.67E-01
4.71E+00	3.96E+04	4.79E+00	1.09E+05	3.50E+00	8.69E-01
4.81E+00	3.67E+04	4.89E+00	1.01E+05	4.00E+00	7.79E-01
4.91E+00	3.40E+04	4.99E+00	9.31E+04	4.50E+00	6.96E-01
5.01E+00	3.15E+04	5.09E+00	8.60E+04	5.00E+00	6.21E-01
5.11E+00	2.92E+04	5.19E+00	7.95E+04	5.50E+00	5.52E-01
5.21E+00	2.70E+04	5.29E+00	7.34E+04	6.00E+00	4.89E-01
5.31E+00	2.50E+04	5.39E+00	6.79E+04	6.50E+00	4.31E-01
5.41E+00	2.32E+04	5.49E+00	6.27E+04	7.00E+00	3.79E-01
5.51E+00	2.15E+04	5.59E+00	5.79E+04	7.50E+00	3.30E-01
5.61E+00	1.99E+04	5.69E+00	5.36E+04	8.00E+00	2.85E-01
5.71E+00	1.85E+04	5.79E+00	4.95E+04	8.50E+00	2.43E-01
5.81E+00	1.71E+04	5.89E+00	4.58E+04	9.00E+00	2.03E-01
5.91E+00	1.59E+04	5.99E+00	4.23E+04	9.50E+00	1.66E-01
6.01E+00	1.47E+04	6.09E+00	3.91E+04	1.00E+01	1.31E-01
6.11E+00	1.37E+04	6.19E+00	3.62E+04	1.05E+01	9.73E-02
6.21E+00	1.27E+04			1.10E+01	6.52E-02
6.31E+00	1.17E+04			1.15E+01	3.43E-02
6.41E+00	1.09E+04			1.20E+01	4.55E-03
6.51E+00	1.01E+04			1.25E+01	-2.42E-02
6.61E+00	9.37E+03			1.30E+01	-5.20E-02
6.71E+00	8.69E+03			1.35E+01	-7.89E-02
6.81E+00	8.06E+03			1.40E+01	-1.05E-01
6.91E+00	7.48E+03			1.45E+01	-1.30E-01
7.01E+00	6.94E+03			1.50E+01	-1.55E-01
7.11E+00	6.44E+03			1.55E+01	-1.79E-01
7.21E+00	5.97E+03			1.60E+01	-2.02E-01
				1.65E+01	-2.25E-01
				1.70E+01	-2.47E-01
				1.75E+01	-2.68E-01
				1.80E+01	-2.89E-01
				1.85E+01	-3.09E-01
				1.90E+01	-3.29E-01
				1.95E+01	-3.48E-01
				2.00E+01	-3.67E-01

**Lookup modeled <sup>36</sup>Cl accumulation at sample depths:**

<b>Footwall</b>		<b>Hanging Wall</b>	
<b>Depth</b>	<b>36Cl</b>	<b>Depth</b>	<b>36Cl</b>
<b>(meters)</b>	<b>(atoms/g)</b>	<b>(meters)</b>	<b>(atoms/g)</b>
7.07E-01	9.16E+05	2.85E-01	1.97E+06
1.01E+00	7.17E+05	5.85E-01	2.66E+06
1.71E+00	4.09E+05	1.09E+00	2.01E+06
2.21E+00	2.75E+05	1.59E+00	1.47E+06
2.71E+00	1.86E+05	1.89E+00	1.15E+06
		2.39E+00	7.58E+05
		3.09E+00	4.28E+05

**Difference between modeled and observed:**

2.46E+04	-6.67E+05
2.67E+05	3.61E+05
7.97E+04	9.14E+04
7.79E+04	-3.88E+05
1.43E+05	9.69E+04
	-9.58E+04
	8.56E+04

**Squared Difference:**

6.06E+08	4.45E+11
7.14E+10	1.30E+11
6.35E+09	8.36E+09
6.07E+09	1.51E+11
2.05E+10	9.40E+09
	9.18E+09
	7.34E+09

**Chi-square residuals:**

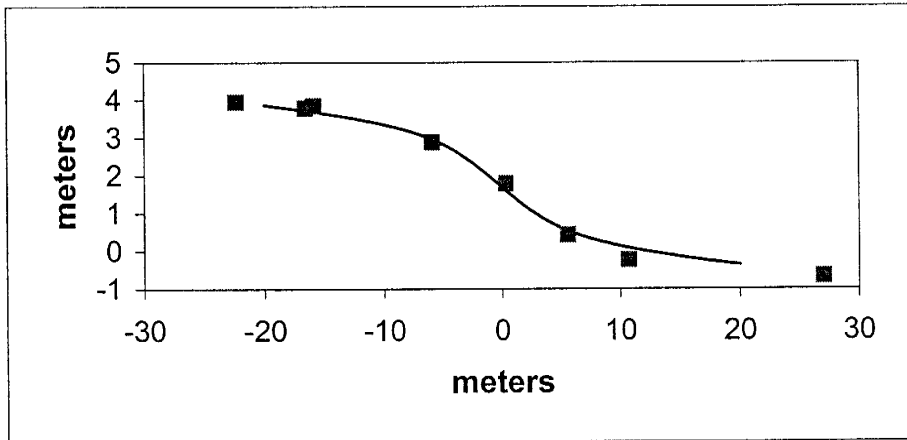
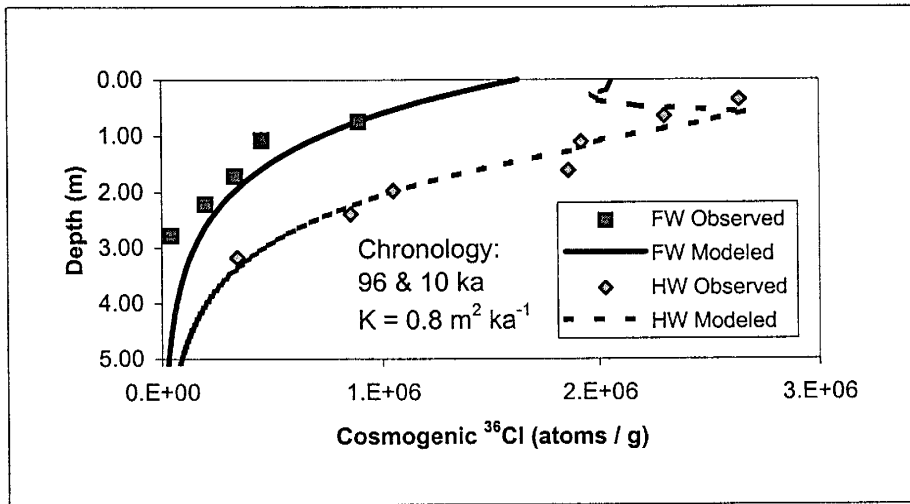
6.62E+02	2.26E+05
9.95E+04	4.89E+04
1.55E+04	4.16E+03
2.21E+04	1.02E+05
1.11E+05	8.19E+03
	1.21E+04
	1.72E+04

**Chi-square value:**

2.48E+05	4.19E+05
----------	----------

**Total Chi-square:** 6.67E+05

Appendix 8



Appendix 8



Appendix 8

Profile 1.5 m from the fault plane

% Fault-scarp parameters, 0 is second column is necessary but meaningless.

% Age estimates need to be to the nearest 1 ka.

0.6	0	% geomorphic diffusivity (m <sup>2</sup> / ka)
1.3	0	% far-field slope (degrees)
122	0	% age of displaced terrace (ka)
2	0	% number of displacements
1.7	50	% magnitude (meters) and age estimate (ka)
1.8	24	% list each event on a separate row, start with the oldest

Footwall		Hanging Wall		Topography	
Depth (meters)	<sup>36</sup> Cl (atoms/g)	Depth (meters)	<sup>36</sup> Cl (atoms/g)	x (meters)	Z (meters)
8.24E-02	1.32E+06	1.18E-02	2.12E+06	-2.00E+01	3.94E+00
1.82E-01	1.21E+06	1.12E-01	2.12E+06	-1.95E+01	3.93E+00
2.82E-01	1.12E+06	2.12E-01	1.89E+06	-1.90E+01	3.92E+00
3.82E-01	1.03E+06	3.12E-01	2.03E+06	-1.85E+01	3.90E+00
4.82E-01	9.51E+05	4.12E-01	1.85E+06	-1.80E+01	3.89E+00
5.82E-01	8.76E+05	5.12E-01	1.74E+06	-1.75E+01	3.87E+00
6.82E-01	8.07E+05	6.12E-01	1.70E+06	-1.70E+01	3.86E+00
7.82E-01	7.44E+05	7.12E-01	2.37E+06	-1.65E+01	3.84E+00
8.82E-01	6.86E+05	8.12E-01	2.34E+06	-1.60E+01	3.82E+00
9.82E-01	6.33E+05	9.12E-01	2.26E+06	-1.55E+01	3.80E+00
1.08E+00	5.84E+05	1.01E+00	2.23E+06	-1.50E+01	3.79E+00
1.18E+00	5.39E+05	1.11E+00	2.12E+06	-1.45E+01	3.76E+00
1.28E+00	4.97E+05	1.21E+00	2.18E+06	-1.40E+01	3.74E+00
1.38E+00	4.59E+05	1.31E+00	2.26E+06	-1.35E+01	3.72E+00
1.48E+00	4.23E+05	1.41E+00	2.11E+06	-1.30E+01	3.69E+00
1.58E+00	3.91E+05	1.51E+00	1.96E+06	-1.25E+01	3.67E+00
1.68E+00	3.61E+05	1.61E+00	1.81E+06	-1.20E+01	3.64E+00
1.78E+00	3.33E+05	1.71E+00	1.67E+06	-1.15E+01	3.60E+00
1.88E+00	3.08E+05	1.81E+00	1.54E+06	-1.10E+01	3.57E+00
1.98E+00	2.84E+05	1.91E+00	1.41E+06	-1.05E+01	3.53E+00
2.08E+00	2.63E+05	2.01E+00	1.30E+06	-1.00E+01	3.49E+00
2.18E+00	2.43E+05	2.11E+00	1.20E+06	-9.50E+00	3.44E+00
2.28E+00	2.24E+05	2.21E+00	1.10E+06	-9.00E+00	3.39E+00
2.38E+00	2.07E+05	2.31E+00	1.01E+06	-8.50E+00	3.34E+00
2.48E+00	1.91E+05	2.41E+00	9.33E+05	-8.00E+00	3.28E+00
2.58E+00	1.77E+05	2.51E+00	8.59E+05	-7.50E+00	3.22E+00
2.68E+00	1.63E+05	2.61E+00	7.90E+05	-7.00E+00	3.15E+00
2.78E+00	1.51E+05	2.71E+00	7.27E+05	-6.50E+00	3.08E+00
2.88E+00	1.40E+05	2.81E+00	6.70E+05	-6.00E+00	3.00E+00
2.98E+00	1.29E+05	2.91E+00	6.16E+05	-5.50E+00	2.91E+00
3.08E+00	1.19E+05	3.01E+00	5.67E+05	-5.00E+00	2.82E+00
3.18E+00	1.10E+05	3.11E+00	5.22E+05	-4.50E+00	2.73E+00
3.28E+00	1.02E+05	3.21E+00	4.81E+05	-4.00E+00	2.63E+00
3.38E+00	9.45E+04	3.31E+00	4.43E+05	-3.50E+00	2.52E+00
3.48E+00	8.74E+04	3.41E+00	4.08E+05	-3.00E+00	2.41E+00
3.58E+00	8.08E+04	3.51E+00	3.75E+05	-2.50E+00	2.30E+00
3.68E+00	7.48E+04	3.61E+00	3.46E+05	-2.00E+00	2.18E+00

## Appendix 8

3.78E+00	6.92E+04	3.71E+00	3.18E+05	-1.50E+00	2.06E+00
3.88E+00	6.40E+04	3.81E+00	2.93E+05	-1.00E+00	1.94E+00
3.98E+00	5.92E+04	3.91E+00	2.70E+05	-5.00E-01	1.82E+00
4.08E+00	5.48E+04	4.01E+00	2.49E+05	0.00E+00	1.69E+00
4.18E+00	5.07E+04	4.11E+00	2.29E+05	5.00E-01	1.57E+00
4.28E+00	4.70E+04	4.21E+00	2.11E+05	1.00E+00	1.45E+00
4.38E+00	4.35E+04	4.31E+00	1.95E+05	1.50E+00	1.33E+00
4.48E+00	4.02E+04	4.41E+00	1.79E+05	2.00E+00	1.21E+00
4.58E+00	3.72E+04	4.51E+00	1.65E+05	2.50E+00	1.10E+00
4.68E+00	3.45E+04	4.61E+00	1.52E+05	3.00E+00	9.88E-01
4.78E+00	3.19E+04	4.71E+00	1.40E+05	3.50E+00	8.83E-01
4.88E+00	2.96E+04	4.81E+00	1.29E+05	4.00E+00	7.82E-01
4.98E+00	2.74E+04	4.91E+00	1.19E+05	4.50E+00	6.87E-01
5.08E+00	2.53E+04	5.01E+00	1.10E+05	5.00E+00	5.97E-01
5.18E+00	2.35E+04	5.11E+00	1.01E+05	5.50E+00	5.13E-01
5.28E+00	2.17E+04	5.21E+00	9.32E+04	6.00E+00	4.34E-01
5.38E+00	2.01E+04	5.31E+00	8.59E+04	6.50E+00	3.60E-01
5.48E+00	1.86E+04	5.41E+00	7.92E+04	7.00E+00	2.92E-01
5.58E+00	1.73E+04	5.51E+00	7.30E+04	7.50E+00	2.29E-01
5.68E+00	1.60E+04	5.61E+00	6.72E+04	8.00E+00	1.71E-01
5.78E+00	1.48E+04	5.71E+00	6.20E+04	8.50E+00	1.17E-01
5.88E+00	1.37E+04	5.81E+00	5.71E+04	9.00E+00	6.78E-02
5.98E+00	1.27E+04	5.91E+00	5.27E+04	9.50E+00	2.25E-02
6.08E+00	1.18E+04	6.01E+00	4.86E+04	1.00E+01	-1.91E-02
6.18E+00	1.09E+04	6.11E+00	4.48E+04	1.05E+01	-5.73E-02
6.28E+00	1.01E+04	6.21E+00	4.13E+04	1.10E+01	-9.24E-02
6.38E+00	9.37E+03			1.15E+01	-1.25E-01
6.48E+00	8.68E+03			1.20E+01	-1.54E-01
6.58E+00	8.05E+03			1.25E+01	-1.82E-01
6.68E+00	7.46E+03			1.30E+01	-2.07E-01
6.78E+00	6.92E+03			1.35E+01	-2.31E-01
6.88E+00	6.41E+03			1.40E+01	-2.53E-01
6.98E+00	5.94E+03			1.45E+01	-2.74E-01
7.08E+00	5.51E+03			1.50E+01	-2.93E-01
7.18E+00	5.11E+03			1.55E+01	-3.12E-01
				1.60E+01	-3.29E-01
				1.65E+01	-3.46E-01
				1.70E+01	-3.61E-01
				1.75E+01	-3.77E-01
				1.80E+01	-3.91E-01
				1.85E+01	-4.05E-01
				1.90E+01	-4.19E-01
				1.95E+01	-4.32E-01
				2.00E+01	-4.45E-01

Lookup modeled  $^{36}\text{Cl}$  accumulation at sample depths:

Footwall		Hanging Wall	
Depth (meters)	$^{36}\text{Cl}$ (atoms/g)	Depth (meters)	$^{36}\text{Cl}$ (atoms/g)
6.82E-01	8.07E+05	3.12E-01	2.03E+06
9.82E-01	6.33E+05	6.12E-01	1.70E+06
1.68E+00	3.61E+05	1.11E+00	2.12E+06
2.18E+00	2.43E+05	1.61E+00	1.81E+06
2.68E+00	1.63E+05	1.91E+00	1.41E+06
		2.31E+00	1.01E+06
		3.11E+00	5.22E+05

## Difference between modeled and observed:

-8.35E+04	-6.05E+05
1.83E+05	-6.01E+05
3.18E+04	2.03E+05
4.55E+04	-4.76E+04
1.21E+05	3.65E+05
	1.60E+05
	1.80E+05

## Squared Difference:

6.98E+09	3.66E+11
3.35E+10	3.61E+11
1.01E+09	4.11E+10
2.07E+09	2.26E+09
1.47E+10	1.33E+11
	2.56E+10
	3.25E+10

## Chi-square residuals:

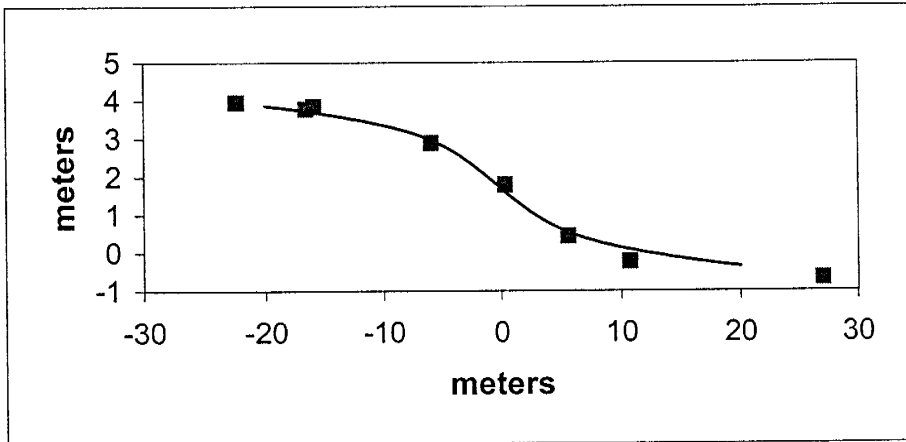
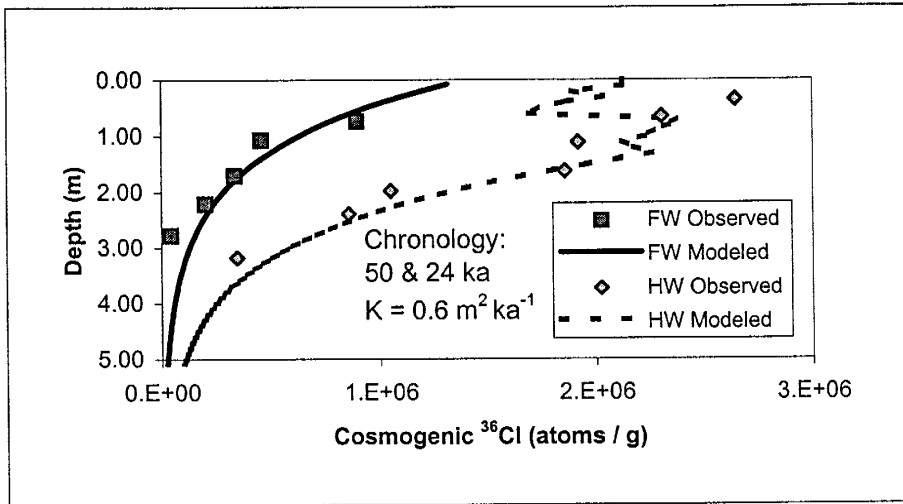
8.64E+03	1.80E+05
5.29E+04	2.13E+05
2.81E+03	1.94E+04
8.55E+03	1.25E+03
8.98E+04	9.41E+04
	2.52E+04
	6.23E+04

## Chi-square value:

1.63E+05	5.95E+05
----------	----------

Total Chi-square: 7.58E+05

Appendix 8



Appendix 8

Profile 1.5 m from the fault plane

% Fault-scarp parameters, 0 is second column is necessary but meaningless.

% Age estimates need to be to the nearest 1 ka.

0.4	0	% geomorphic diffusivity (m <sup>2</sup> / ka)
1.3	0	% far-field slope (degrees)
122	0	% age of displaced terrace (ka)
2	0	% number of displacements
1.7	120	% magnitude (meters) and age estimate (ka)
1.8	24	% list each event on a separate row, start with the oldest

<u>Footwall</u>		<u>Hanging Wall</u>		<u>Topography</u>	
<u>Depth</u> <u>(meters)</u>	<u>36Cl</u> <u>(atoms/g)</u>	<u>Depth</u> <u>(meters)</u>	<u>36Cl</u> <u>(atoms/g)</u>	<u>x</u> <u>(meters)</u>	<u>Z</u> <u>(meters)</u>
2.23E-04	1.80E+06	9.12E-02	2.18E+06	-2.00E+01	3.92E+00
1.00E-01	1.66E+06	1.91E-01	2.12E+06	-1.95E+01	3.90E+00
2.00E-01	1.53E+06	2.91E-01	2.12E+06	-1.90E+01	3.88E+00
3.00E-01	1.41E+06	3.91E-01	2.08E+06	-1.85E+01	3.87E+00
4.00E-01	1.30E+06	4.91E-01	2.16E+06	-1.80E+01	3.85E+00
5.00E-01	1.20E+06	5.91E-01	2.61E+06	-1.75E+01	3.83E+00
6.00E-01	1.11E+06	6.91E-01	2.53E+06	-1.70E+01	3.81E+00
7.00E-01	1.02E+06	7.91E-01	2.41E+06	-1.65E+01	3.79E+00
8.00E-01	9.40E+05	8.91E-01	2.26E+06	-1.60E+01	3.77E+00
9.00E-01	8.67E+05	9.91E-01	2.11E+06	-1.55E+01	3.75E+00
1.00E+00	8.00E+05	1.09E+00	1.96E+06	-1.50E+01	3.73E+00
1.10E+00	7.39E+05	1.19E+00	1.81E+06	-1.45E+01	3.70E+00
1.20E+00	6.82E+05	1.29E+00	1.68E+06	-1.40E+01	3.68E+00
1.30E+00	6.30E+05	1.39E+00	1.55E+06	-1.35E+01	3.65E+00
1.40E+00	5.82E+05	1.49E+00	1.42E+06	-1.30E+01	3.63E+00
1.50E+00	5.38E+05	1.59E+00	1.31E+06	-1.25E+01	3.60E+00
1.60E+00	4.97E+05	1.69E+00	1.20E+06	-1.20E+01	3.57E+00
1.70E+00	4.59E+05	1.79E+00	1.11E+06	-1.15E+01	3.54E+00
1.80E+00	4.25E+05	1.89E+00	1.02E+06	-1.10E+01	3.50E+00
1.90E+00	3.93E+05	1.99E+00	9.36E+05	-1.05E+01	3.47E+00
2.00E+00	3.63E+05	2.09E+00	8.61E+05	-1.00E+01	3.43E+00
2.10E+00	3.36E+05	2.19E+00	7.93E+05	-9.50E+00	3.39E+00
2.20E+00	3.11E+05	2.29E+00	7.30E+05	-9.00E+00	3.35E+00
2.30E+00	2.88E+05	2.39E+00	6.73E+05	-8.50E+00	3.30E+00
2.40E+00	2.66E+05	2.49E+00	6.20E+05	-8.00E+00	3.25E+00
2.50E+00	2.46E+05	2.59E+00	5.71E+05	-7.50E+00	3.19E+00
2.60E+00	2.28E+05	2.69E+00	5.26E+05	-7.00E+00	3.13E+00
2.70E+00	2.11E+05	2.79E+00	4.85E+05	-6.50E+00	3.07E+00
2.80E+00	1.95E+05	2.89E+00	4.47E+05	-6.00E+00	3.00E+00
2.90E+00	1.81E+05	2.99E+00	4.13E+05	-5.50E+00	2.92E+00
3.00E+00	1.68E+05	3.09E+00	3.81E+05	-5.00E+00	2.83E+00
3.10E+00	1.55E+05	3.19E+00	3.51E+05	-4.50E+00	2.74E+00
3.20E+00	1.44E+05	3.29E+00	3.24E+05	-4.00E+00	2.65E+00
3.30E+00	1.33E+05	3.39E+00	2.99E+05	-3.50E+00	2.54E+00
3.40E+00	1.23E+05	3.49E+00	2.76E+05	-3.00E+00	2.44E+00
3.50E+00	1.14E+05	3.59E+00	2.55E+05	-2.50E+00	2.32E+00
3.60E+00	1.06E+05	3.69E+00	2.35E+05	-2.00E+00	2.20E+00

## Appendix 8

3.70E+00	9.82E+04	3.79E+00	2.17E+05	-1.50E+00	2.08E+00
3.80E+00	9.10E+04	3.89E+00	2.01E+05	-1.00E+00	1.95E+00
3.90E+00	8.44E+04	3.99E+00	1.86E+05	-5.00E-01	1.82E+00
4.00E+00	7.82E+04	4.09E+00	1.71E+05	0.00E+00	1.69E+00
4.10E+00	7.25E+04	4.19E+00	1.58E+05	5.00E-01	1.56E+00
4.20E+00	6.72E+04	4.29E+00	1.46E+05	1.00E+00	1.44E+00
4.30E+00	6.23E+04	4.39E+00	1.35E+05	1.50E+00	1.31E+00
4.40E+00	5.78E+04	4.49E+00	1.25E+05	2.00E+00	1.19E+00
4.50E+00	5.36E+04	4.59E+00	1.16E+05	2.50E+00	1.08E+00
4.60E+00	4.97E+04	4.69E+00	1.07E+05	3.00E+00	9.67E-01
4.70E+00	4.61E+04	4.79E+00	9.90E+04	3.50E+00	8.63E-01
4.80E+00	4.28E+04	4.89E+00	9.15E+04	4.00E+00	7.67E-01
4.90E+00	3.97E+04	4.99E+00	8.47E+04	4.50E+00	6.76E-01
5.00E+00	3.68E+04	5.09E+00	7.83E+04	5.00E+00	5.93E-01
5.10E+00	3.42E+04	5.19E+00	7.25E+04	5.50E+00	5.15E-01
5.20E+00	3.17E+04	5.29E+00	6.70E+04	6.00E+00	4.44E-01
5.30E+00	2.94E+04	5.39E+00	6.20E+04	6.50E+00	3.78E-01
5.40E+00	2.73E+04	5.49E+00	5.74E+04	7.00E+00	3.18E-01
5.50E+00	2.53E+04	5.59E+00	5.31E+04	7.50E+00	2.63E-01
5.60E+00	2.35E+04	5.69E+00	4.92E+04	8.00E+00	2.12E-01
5.70E+00	2.18E+04	5.79E+00	4.55E+04	8.50E+00	1.64E-01
5.80E+00	2.03E+04	5.89E+00	4.22E+04	9.00E+00	1.21E-01
5.90E+00	1.88E+04	5.99E+00	3.90E+04	9.50E+00	8.00E-02
6.00E+00	1.75E+04	6.09E+00	3.61E+04	1.00E+01	4.21E-02
6.10E+00	1.62E+04	6.19E+00	3.35E+04	1.05E+01	6.64E-03
6.20E+00	1.50E+04			1.10E+01	-2.67E-02
6.30E+00	1.40E+04			1.15E+01	-5.81E-02
6.40E+00	1.30E+04			1.20E+01	-8.78E-02
6.50E+00	1.20E+04			1.25E+01	-1.16E-01
6.60E+00	1.12E+04			1.30E+01	-1.43E-01
6.70E+00	1.04E+04			1.35E+01	-1.68E-01
6.80E+00	9.64E+03			1.40E+01	-1.93E-01
6.90E+00	8.95E+03			1.45E+01	-2.16E-01
7.00E+00	8.31E+03			1.50E+01	-2.38E-01
7.10E+00	7.72E+03			1.55E+01	-2.60E-01
7.20E+00	7.17E+03			1.60E+01	-2.80E-01
				1.65E+01	-3.00E-01
				1.70E+01	-3.19E-01
				1.75E+01	-3.37E-01
				1.80E+01	-3.55E-01
				1.85E+01	-3.72E-01
				1.90E+01	-3.89E-01
				1.95E+01	-4.05E-01
				2.00E+01	-4.21E-01

Lookup modeled <sup>36</sup>Cl accumulation at sample depths:

Footwall		Hanging Wall	
Depth (meters)	<sup>36</sup> Cl (atoms/g)	Depth (meters)	<sup>36</sup> Cl (atoms/g)
7.00E-01	1.02E+06	2.91E-01	2.12E+06
1.00E+00	8.00E+05	5.91E-01	2.61E+06
1.70E+00	4.59E+05	1.09E+00	1.96E+06
2.20E+00	3.11E+05	1.59E+00	1.31E+06
2.70E+00	2.11E+05	1.89E+00	1.02E+06
		2.29E+00	7.30E+05
		3.09E+00	3.81E+05

## Difference between modeled and observed:

1.28E+05	-5.20E+05
3.50E+05	3.13E+05
1.30E+05	3.97E+04
1.14E+05	-5.52E+05
1.69E+05	-3.28E+04
	-1.24E+05
	3.87E+04

## Squared Difference:

1.65E+10	2.71E+11
1.23E+11	9.78E+10
1.70E+10	1.58E+09
1.29E+10	3.05E+11
2.85E+10	1.07E+09
	1.53E+10
	1.50E+09

## Chi-square residuals:

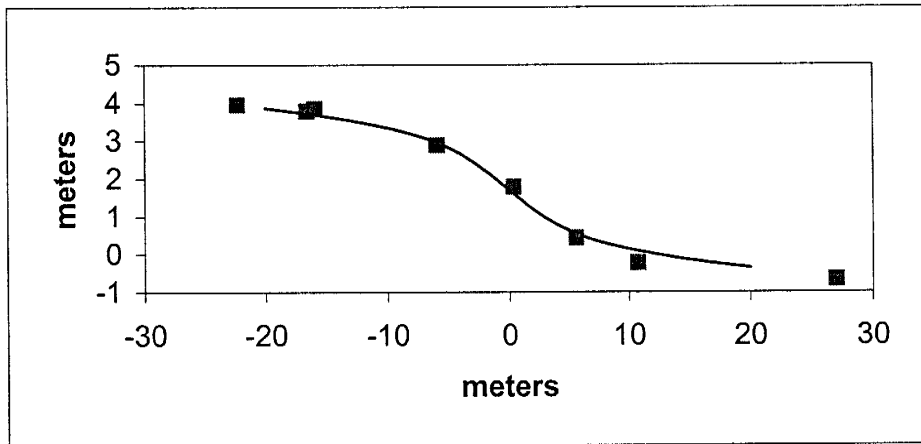
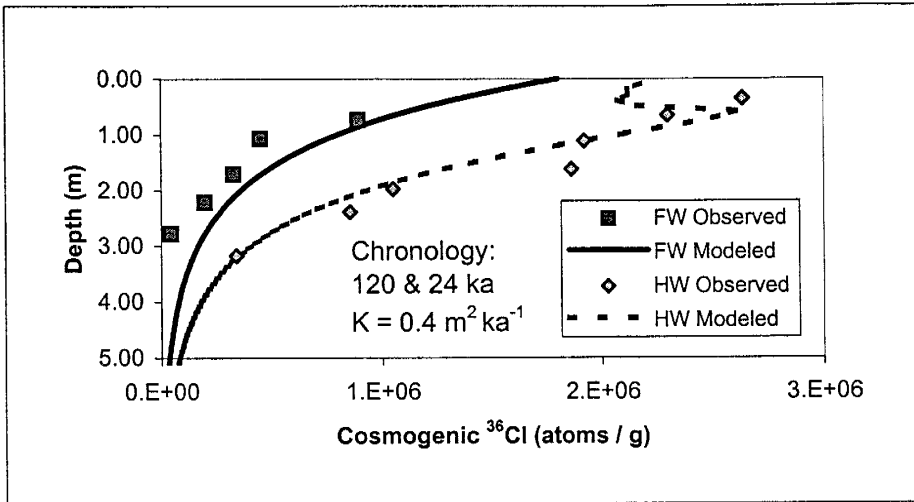
1.61E+04	1.28E+05
1.53E+05	3.74E+04
3.70E+04	8.05E+02
4.17E+04	2.33E+05
1.35E+05	1.06E+03
	2.10E+04
	3.94E+03

## Chi-square value:

3.83E+05	4.25E+05
----------	----------

Total Chi-square: 8.08E+05

Appendix 8





Appendix 8

Profile 1.5 m from the fault plane

% Fault-scarp parameters, 0 is second column is necessary but meaningless.

% Age estimates need to be to the nearest 1 ka.

0.3	0	% geomorphic diffusivity (m <sup>2</sup> / ka)
1.3	0	% far-field slope (degrees)
122	0	% age of displaced terrace (ka)
2	0	% number of displacements
1.7	120	% magnitude (meters) and age estimate (ka)
1.8	50	% list each event on a separate row, start with the oldest

Footwall		Hanging Wall		Topography	
Depth (meters)	<sup>36</sup> Cl (atoms/g)	Depth (meters)	<sup>36</sup> Cl (atoms/g)	x (meters)	Z (meters)
6.23E-02	1.83E+06	3.70E-02	2.17E+06	-2.00E+01	3.94E+00
1.62E-01	1.70E+06	1.37E-01	2.36E+06	-1.95E+01	3.92E+00
2.62E-01	1.57E+06	2.37E-01	2.22E+06	-1.90E+01	3.91E+00
3.62E-01	1.44E+06	3.37E-01	2.28E+06	-1.85E+01	3.89E+00
4.62E-01	1.33E+06	4.37E-01	2.17E+06	-1.80E+01	3.88E+00
5.62E-01	1.23E+06	5.37E-01	2.18E+06	-1.75E+01	3.86E+00
6.62E-01	1.13E+06	6.37E-01	2.09E+06	-1.70E+01	3.84E+00
7.62E-01	1.05E+06	7.37E-01	2.35E+06	-1.65E+01	3.82E+00
8.62E-01	9.65E+05	8.37E-01	2.24E+06	-1.60E+01	3.80E+00
9.62E-01	8.91E+05	9.37E-01	2.12E+06	-1.55E+01	3.78E+00
1.06E+00	8.22E+05	1.04E+00	1.98E+06	-1.50E+01	3.76E+00
1.16E+00	7.59E+05	1.14E+00	1.85E+06	-1.45E+01	3.74E+00
1.26E+00	7.02E+05	1.24E+00	1.71E+06	-1.40E+01	3.72E+00
1.36E+00	6.48E+05	1.34E+00	1.59E+06	-1.35E+01	3.69E+00
1.46E+00	5.99E+05	1.44E+00	1.47E+06	-1.30E+01	3.66E+00
1.56E+00	5.54E+05	1.54E+00	1.35E+06	-1.25E+01	3.63E+00
1.66E+00	5.12E+05	1.64E+00	1.24E+06	-1.20E+01	3.60E+00
1.76E+00	4.74E+05	1.74E+00	1.14E+06	-1.15E+01	3.57E+00
1.86E+00	4.38E+05	1.84E+00	1.05E+06	-1.10E+01	3.53E+00
1.96E+00	4.06E+05	1.94E+00	9.64E+05	-1.05E+01	3.49E+00
2.06E+00	3.75E+05	2.04E+00	8.87E+05	-1.00E+01	3.45E+00
2.16E+00	3.47E+05	2.14E+00	8.16E+05	-9.50E+00	3.40E+00
2.26E+00	3.22E+05	2.24E+00	7.52E+05	-9.00E+00	3.35E+00
2.36E+00	2.98E+05	2.34E+00	6.92E+05	-8.50E+00	3.29E+00
2.46E+00	2.76E+05	2.44E+00	6.37E+05	-8.00E+00	3.24E+00
2.56E+00	2.55E+05	2.54E+00	5.87E+05	-7.50E+00	3.17E+00
2.66E+00	2.37E+05	2.64E+00	5.41E+05	-7.00E+00	3.10E+00
2.76E+00	2.19E+05	2.74E+00	4.99E+05	-6.50E+00	3.03E+00
2.86E+00	2.03E+05	2.84E+00	4.60E+05	-6.00E+00	2.95E+00
2.96E+00	1.88E+05	2.94E+00	4.24E+05	-5.50E+00	2.87E+00
3.06E+00	1.74E+05	3.04E+00	3.91E+05	-5.00E+00	2.78E+00
3.16E+00	1.62E+05	3.14E+00	3.61E+05	-4.50E+00	2.69E+00
3.26E+00	1.50E+05	3.24E+00	3.33E+05	-4.00E+00	2.59E+00
3.36E+00	1.39E+05	3.34E+00	3.07E+05	-3.50E+00	2.49E+00
3.46E+00	1.29E+05	3.44E+00	2.84E+05	-3.00E+00	2.38E+00
3.56E+00	1.19E+05	3.54E+00	2.62E+05	-2.50E+00	2.27E+00
3.66E+00	1.11E+05	3.64E+00	2.42E+05	-2.00E+00	2.16E+00

## Appendix 8

3.76E+00	1.03E+05	3.74E+00	2.23E+05	-1.50E+00	2.05E+00
3.86E+00	9.52E+04	3.84E+00	2.06E+05	-1.00E+00	1.93E+00
3.96E+00	8.83E+04	3.94E+00	1.91E+05	-5.00E-01	1.81E+00
4.06E+00	8.19E+04	4.04E+00	1.76E+05	0.00E+00	1.70E+00
4.16E+00	7.59E+04	4.14E+00	1.63E+05	5.00E-01	1.58E+00
4.26E+00	7.05E+04	4.24E+00	1.50E+05	1.00E+00	1.46E+00
4.36E+00	6.54E+04	4.34E+00	1.39E+05	1.50E+00	1.35E+00
4.46E+00	6.07E+04	4.44E+00	1.28E+05	2.00E+00	1.24E+00
4.56E+00	5.63E+04	4.54E+00	1.19E+05	2.50E+00	1.13E+00
4.66E+00	5.22E+04	4.64E+00	1.10E+05	3.00E+00	1.02E+00
4.76E+00	4.85E+04	4.74E+00	1.02E+05	3.50E+00	9.21E-01
4.86E+00	4.50E+04	4.84E+00	9.39E+04	4.00E+00	8.23E-01
4.96E+00	4.18E+04	4.94E+00	8.68E+04	4.50E+00	7.30E-01
5.06E+00	3.88E+04	5.04E+00	8.03E+04	5.00E+00	6.42E-01
5.16E+00	3.60E+04	5.14E+00	7.43E+04	5.50E+00	5.59E-01
5.26E+00	3.34E+04	5.24E+00	6.88E+04	6.00E+00	4.81E-01
5.36E+00	3.10E+04	5.34E+00	6.36E+04	6.50E+00	4.08E-01
5.46E+00	2.88E+04	5.44E+00	5.89E+04	7.00E+00	3.39E-01
5.56E+00	2.67E+04	5.54E+00	5.45E+04	7.50E+00	2.76E-01
5.66E+00	2.48E+04	5.64E+00	5.04E+04	8.00E+00	2.17E-01
5.76E+00	2.31E+04	5.74E+00	4.67E+04	8.50E+00	1.62E-01
5.86E+00	2.14E+04	5.84E+00	4.32E+04	9.00E+00	1.11E-01
5.96E+00	1.99E+04	5.94E+00	4.00E+04	9.50E+00	6.41E-02
6.06E+00	1.85E+04	6.04E+00	3.71E+04	1.00E+01	2.07E-02
6.16E+00	1.72E+04	6.14E+00	3.43E+04	1.05E+01	-1.94E-02
6.26E+00	1.59E+04	6.24E+00	3.18E+04	1.10E+01	-5.65E-02
6.36E+00	1.48E+04			1.15E+01	-9.09E-02
6.46E+00	1.38E+04			1.20E+01	-1.23E-01
6.56E+00	1.28E+04			1.25E+01	-1.52E-01
6.66E+00	1.19E+04			1.30E+01	-1.80E-01
6.76E+00	1.10E+04			1.35E+01	-2.06E-01
6.86E+00	1.03E+04			1.40E+01	-2.30E-01
6.96E+00	9.53E+03			1.45E+01	-2.52E-01
7.06E+00	8.85E+03			1.50E+01	-2.74E-01
7.16E+00	8.23E+03			1.55E+01	-2.94E-01
				1.60E+01	-3.13E-01
				1.65E+01	-3.31E-01
				1.70E+01	-3.48E-01
				1.75E+01	-3.65E-01
				1.80E+01	-3.80E-01
				1.85E+01	-3.96E-01
				1.90E+01	-4.11E-01
				1.95E+01	-4.25E-01
				2.00E+01	-4.39E-01

**Lookup modeled  $^{36}\text{Cl}$  accumulation at sample depths:**

<b>Footwall</b>		<b>Hanging Wall</b>	
<b>Depth</b>	<b><math>^{36}\text{Cl}</math></b>	<b>Depth</b>	<b><math>^{36}\text{Cl}</math></b>
<b>(meters)</b>	<b>(atoms/g)</b>	<b>(meters)</b>	<b>(atoms/g)</b>
6.62E-01	1.13E+06	3.37E-01	2.28E+06
1.06E+00	8.22E+05	6.37E-01	2.09E+06
1.66E+00	5.12E+05	1.04E+00	1.98E+06
2.16E+00	3.47E+05	1.54E+00	1.35E+06
2.76E+00	2.19E+05	1.94E+00	9.64E+05
		2.34E+00	6.92E+05
		3.14E+00	3.61E+05

**Difference between modeled and observed:**

2.42E+05	-3.61E+05
3.72E+05	-2.12E+05
1.83E+05	6.28E+04
1.50E+05	-5.12E+05
1.77E+05	-8.60E+04
	-1.62E+05
	1.89E+04

**Squared Difference:**

5.86E+10	1.30E+11
1.39E+11	4.48E+10
3.36E+10	3.95E+09
2.26E+10	2.62E+11
3.12E+10	7.39E+09
	2.62E+10
	3.57E+08

**Chi-square residuals:**

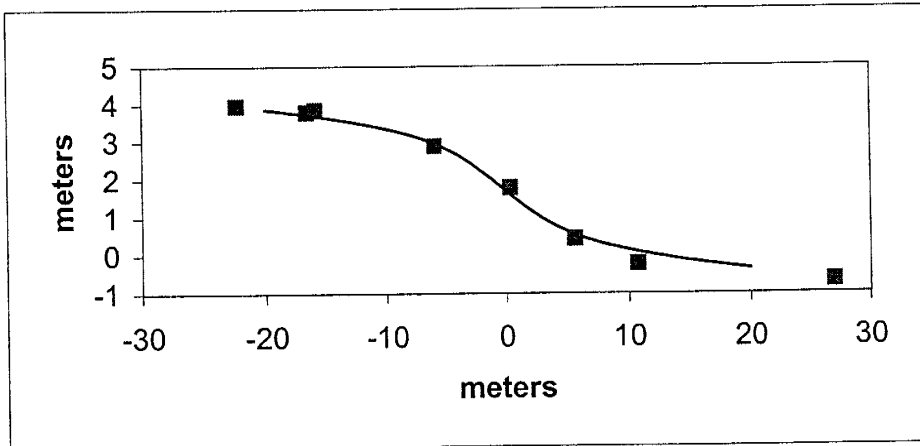
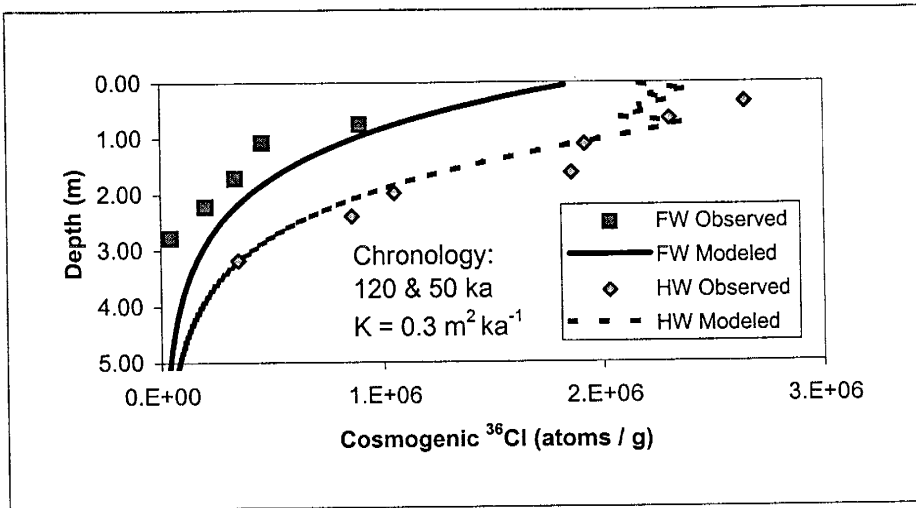
5.17E+04	5.71E+04
1.69E+05	2.15E+04
6.56E+04	1.99E+03
6.51E+04	1.94E+05
1.43E+05	7.66E+03
	3.79E+04
	9.89E+02

**Chi-square value:**

4.94E+05	3.22E+05
----------	----------

**Total Chi-square:** 8.15E+05

Appendix 8



Appendix 8

Profile 1.5 m from the fault plane

% Fault-scarp parameters, 0 is second column is necessary but meaningless.

% Age estimates need to be to the nearest 1 ka.

0.6	0	% geomorphic diffusivity (m <sup>2</sup> / ka)
1.3	0	% far-field slope (degrees)
122	0	% age of displaced terrace (ka)
2	0	% number of displacements
1.7	120	% magnitude (meters) and age estimate (ka)
1.8	10	% list each event on a separate row, start with the oldest

<u>Footwall</u>		<u>Hanging Wall</u>		<u>Topography</u>	
<u>Depth</u> <u>(meters)</u>	<u>36Cl</u> <u>(atoms/g)</u>	<u>Depth</u> <u>(meters)</u>	<u>36Cl</u> <u>(atoms/g)</u>	<u>x</u> <u>(meters)</u>	<u>Z</u> <u>(meters)</u>
5.47E-02	1.75E+06	2.86E-02	2.17E+06	-2.00E+01	3.87E+00
1.55E-01	1.61E+06	1.29E-01	2.21E+06	-1.95E+01	3.85E+00
2.55E-01	1.48E+06	2.29E-01	2.19E+06	-1.90E+01	3.83E+00
3.55E-01	1.36E+06	3.29E-01	2.18E+06	-1.85E+01	3.81E+00
4.55E-01	1.25E+06	4.29E-01	2.37E+06	-1.80E+01	3.79E+00
5.55E-01	1.16E+06	5.29E-01	2.71E+06	-1.75E+01	3.77E+00
6.55E-01	1.06E+06	6.29E-01	2.60E+06	-1.70E+01	3.75E+00
7.55E-01	9.81E+05	7.29E-01	2.46E+06	-1.65E+01	3.73E+00
8.55E-01	9.04E+05	8.29E-01	2.29E+06	-1.60E+01	3.70E+00
9.55E-01	8.34E+05	9.29E-01	2.13E+06	-1.55E+01	3.68E+00
1.05E+00	7.69E+05	1.03E+00	1.97E+06	-1.50E+01	3.65E+00
1.15E+00	7.09E+05	1.13E+00	1.82E+06	-1.45E+01	3.63E+00
1.25E+00	6.54E+05	1.23E+00	1.69E+06	-1.40E+01	3.60E+00
1.35E+00	6.04E+05	1.33E+00	1.55E+06	-1.35E+01	3.58E+00
1.45E+00	5.58E+05	1.43E+00	1.43E+06	-1.30E+01	3.55E+00
1.55E+00	5.15E+05	1.53E+00	1.31E+06	-1.25E+01	3.52E+00
1.65E+00	4.76E+05	1.63E+00	1.21E+06	-1.20E+01	3.49E+00
1.75E+00	4.39E+05	1.73E+00	1.11E+06	-1.15E+01	3.46E+00
1.85E+00	4.06E+05	1.83E+00	1.02E+06	-1.10E+01	3.43E+00
1.95E+00	3.75E+05	1.93E+00	9.40E+05	-1.05E+01	3.40E+00
2.05E+00	3.47E+05	2.03E+00	8.65E+05	-1.00E+01	3.37E+00
2.15E+00	3.20E+05	2.13E+00	7.96E+05	-9.50E+00	3.33E+00
2.25E+00	2.96E+05	2.23E+00	7.33E+05	-9.00E+00	3.30E+00
2.35E+00	2.74E+05	2.33E+00	6.76E+05	-8.50E+00	3.26E+00
2.45E+00	2.53E+05	2.43E+00	6.23E+05	-8.00E+00	3.22E+00
2.55E+00	2.34E+05	2.53E+00	5.74E+05	-7.50E+00	3.17E+00
2.65E+00	2.17E+05	2.63E+00	5.29E+05	-7.00E+00	3.12E+00
2.75E+00	2.01E+05	2.73E+00	4.88E+05	-6.50E+00	3.07E+00
2.85E+00	1.86E+05	2.83E+00	4.50E+05	-6.00E+00	3.01E+00
2.95E+00	1.72E+05	2.93E+00	4.15E+05	-5.50E+00	2.95E+00
3.05E+00	1.59E+05	3.03E+00	3.83E+05	-5.00E+00	2.88E+00
3.15E+00	1.47E+05	3.13E+00	3.53E+05	-4.50E+00	2.80E+00
3.25E+00	1.36E+05	3.23E+00	3.26E+05	-4.00E+00	2.71E+00
3.35E+00	1.26E+05	3.33E+00	3.01E+05	-3.50E+00	2.61E+00
3.45E+00	1.17E+05	3.43E+00	2.78E+05	-3.00E+00	2.50E+00
3.55E+00	1.08E+05	3.53E+00	2.56E+05	-2.50E+00	2.38E+00
3.65E+00	1.00E+05	3.63E+00	2.37E+05	-2.00E+00	2.25E+00

## Appendix 8

3.75E+00	9.27E+04	3.73E+00	2.19E+05	-1.50E+00	2.12E+00
3.85E+00	8.59E+04	3.83E+00	2.02E+05	-1.00E+00	1.98E+00
3.95E+00	7.95E+04	3.93E+00	1.87E+05	-5.00E-01	1.83E+00
4.05E+00	7.37E+04	4.03E+00	1.73E+05	0.00E+00	1.68E+00
4.15E+00	6.83E+04	4.13E+00	1.59E+05	5.00E-01	1.54E+00
4.25E+00	6.33E+04	4.23E+00	1.47E+05	1.00E+00	1.39E+00
4.35E+00	5.86E+04	4.33E+00	1.36E+05	1.50E+00	1.26E+00
4.45E+00	5.43E+04	4.43E+00	1.26E+05	2.00E+00	1.13E+00
4.55E+00	5.04E+04	4.53E+00	1.16E+05	2.50E+00	1.01E+00
4.65E+00	4.67E+04	4.63E+00	1.08E+05	3.00E+00	9.01E-01
4.75E+00	4.33E+04	4.73E+00	9.96E+04	3.50E+00	8.02E-01
4.85E+00	4.01E+04	4.83E+00	9.21E+04	4.00E+00	7.13E-01
4.95E+00	3.72E+04	4.93E+00	8.52E+04	4.50E+00	6.33E-01
5.05E+00	3.45E+04	5.03E+00	7.88E+04	5.00E+00	5.62E-01
5.15E+00	3.20E+04	5.13E+00	7.29E+04	5.50E+00	4.98E-01
5.25E+00	2.97E+04	5.23E+00	6.75E+04	6.00E+00	4.40E-01
5.35E+00	2.75E+04	5.33E+00	6.25E+04	6.50E+00	3.87E-01
5.45E+00	2.55E+04	5.43E+00	5.78E+04	7.00E+00	3.39E-01
5.55E+00	2.37E+04	5.53E+00	5.35E+04	7.50E+00	2.95E-01
5.65E+00	2.19E+04	5.63E+00	4.95E+04	8.00E+00	2.54E-01
5.75E+00	2.04E+04	5.73E+00	4.58E+04	8.50E+00	2.15E-01
5.85E+00	1.89E+04	5.83E+00	4.24E+04	9.00E+00	1.79E-01
5.95E+00	1.75E+04	5.93E+00	3.93E+04	9.50E+00	1.44E-01
6.05E+00	1.63E+04	6.03E+00	3.64E+04	1.00E+01	1.11E-01
6.15E+00	1.51E+04	6.13E+00	3.37E+04	1.05E+01	7.87E-02
6.25E+00	1.40E+04			1.10E+01	4.78E-02
6.35E+00	1.30E+04			1.15E+01	1.79E-02
6.45E+00	1.21E+04			1.20E+01	-1.10E-02
6.55E+00	1.12E+04			1.25E+01	-3.91E-02
6.65E+00	1.04E+04			1.30E+01	-6.63E-02
6.75E+00	9.63E+03			1.35E+01	-9.28E-02
6.85E+00	8.94E+03			1.40E+01	-1.18E-01
6.95E+00	8.30E+03			1.45E+01	-1.43E-01
7.05E+00	7.71E+03			1.50E+01	-1.68E-01
7.15E+00	7.15E+03			1.55E+01	-1.91E-01
7.25E+00	6.64E+03			1.60E+01	-2.14E-01
				1.65E+01	-2.37E-01
				1.70E+01	-2.58E-01
				1.75E+01	-2.79E-01
				1.80E+01	-3.00E-01
				1.85E+01	-3.20E-01
				1.90E+01	-3.39E-01
				1.95E+01	-3.58E-01
				2.00E+01	-3.76E-01

Lookup modeled <sup>36</sup>Cl accumulation at sample depths:

Footwall		Hanging Wall	
Depth (meters)	<sup>36</sup> Cl (atoms/g)	Depth (meters)	<sup>36</sup> Cl (atoms/g)
6.55E-01	1.06E+06	3.29E-01	2.18E+06
1.05E+00	7.69E+05	6.29E-01	2.60E+06
1.65E+00	4.76E+05	1.03E+00	1.97E+06
2.15E+00	3.20E+05	1.53E+00	1.31E+06
2.75E+00	2.01E+05	1.93E+00	9.40E+05
		2.33E+00	6.76E+05
		3.13E+00	3.53E+05

## Difference between modeled and observed:

1.73E+05	-4.62E+05
3.19E+05	2.96E+05
1.47E+05	4.97E+04
1.23E+05	-5.48E+05
1.58E+05	-1.10E+05
	-1.78E+05
	1.12E+04

## Squared Difference:

3.00E+10	2.14E+11
1.02E+11	8.76E+10
2.15E+10	2.47E+09
1.52E+10	3.00E+11
2.50E+10	1.22E+10
	3.18E+10
	1.24E+08

## Chi-square residuals:

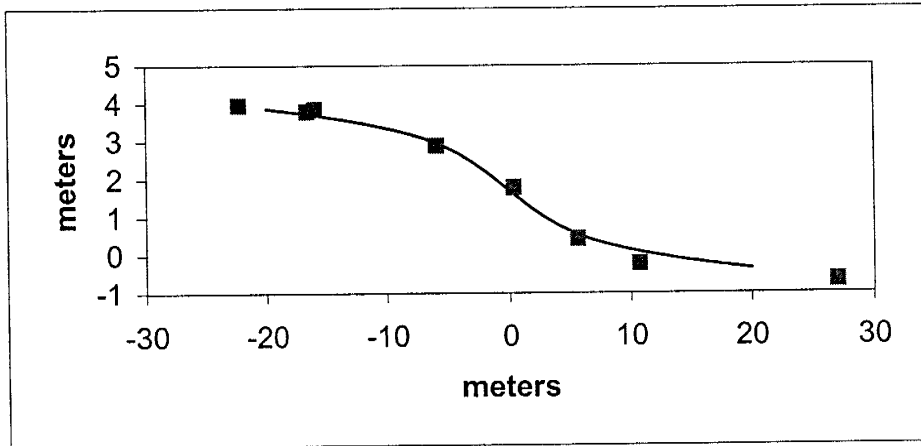
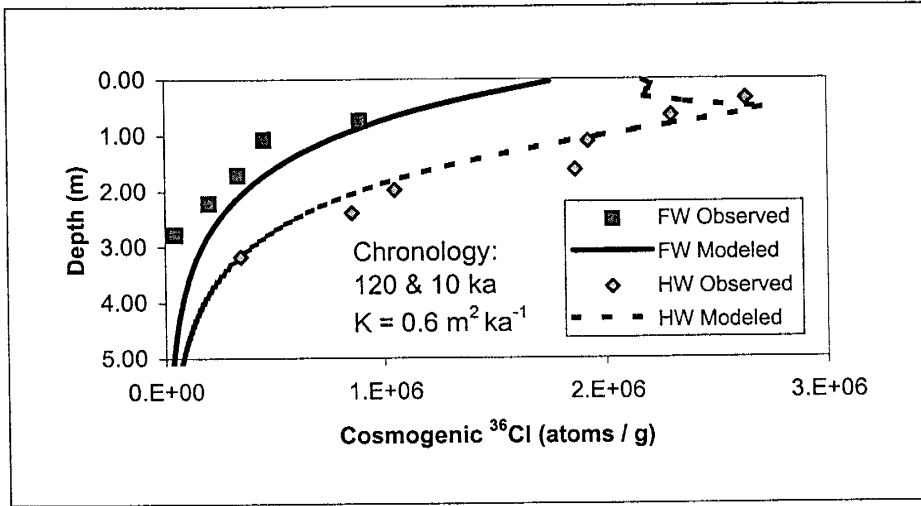
2.82E+04	9.80E+04
1.32E+05	3.37E+04
4.52E+04	1.25E+03
4.75E+04	2.29E+05
1.25E+05	1.30E+04
	4.71E+04
	3.52E+02

## Chi-square value:

3.78E+05	4.22E+05
----------	----------

Total Chi-square: 8.00E+05

Appendix 8





Appendix 8

Profile 1.5 m from the fault plane

% Fault-scarp parameters, 0 is second column is necessary but meaningless.

% Age estimates need to be to the nearest 1 ka.

1	0	% geomorphic diffusivity (m <sup>2</sup> / ka)
1.3	0	% far-field slope (degrees)
122	0	% age of displaced terrace (ka)
2	0	% number of displacements
1.7	50	% magnitude (meters) and age estimate (ka)
1.8	10	% list each event on a separate row, start with the oldest

<u>Footwall</u>		<u>Hanging Wall</u>		<u>Topography</u>	
<u>Depth</u> <u>(meters)</u>	<u>36Cl</u> <u>(atoms/g)</u>	<u>Depth</u> <u>(meters)</u>	<u>36Cl</u> <u>(atoms/g)</u>	<u>x</u> <u>(meters)</u>	<u>Z</u> <u>(meters)</u>
9.86E-02	1.24E+06	9.36E-02	1.84E+06	-2.00E+01	3.91E+00
1.99E-01	1.14E+06	1.94E-01	1.79E+06	-1.95E+01	3.90E+00
2.99E-01	1.05E+06	2.94E-01	1.65E+06	-1.90E+01	3.88E+00
3.99E-01	9.67E+05	3.94E-01	1.66E+06	-1.85E+01	3.86E+00
4.99E-01	8.91E+05	4.94E-01	1.78E+06	-1.80E+01	3.84E+00
5.99E-01	8.21E+05	5.94E-01	2.54E+06	-1.75E+01	3.82E+00
6.99E-01	7.56E+05	6.94E-01	2.46E+06	-1.70E+01	3.81E+00
7.99E-01	6.96E+05	7.94E-01	2.50E+06	-1.65E+01	3.79E+00
8.99E-01	6.42E+05	8.94E-01	2.23E+06	-1.60E+01	3.76E+00
9.99E-01	5.92E+05	9.94E-01	2.28E+06	-1.55E+01	3.74E+00
1.10E+00	5.45E+05	1.09E+00	2.17E+06	-1.50E+01	3.72E+00
1.20E+00	5.03E+05	1.19E+00	2.20E+06	-1.45E+01	3.70E+00
1.30E+00	4.64E+05	1.29E+00	2.29E+06	-1.40E+01	3.67E+00
1.40E+00	4.28E+05	1.39E+00	2.15E+06	-1.35E+01	3.65E+00
1.50E+00	3.94E+05	1.49E+00	1.99E+06	-1.30E+01	3.62E+00
1.60E+00	3.64E+05	1.59E+00	1.84E+06	-1.25E+01	3.59E+00
1.70E+00	3.36E+05	1.69E+00	1.70E+06	-1.20E+01	3.56E+00
1.80E+00	3.10E+05	1.79E+00	1.56E+06	-1.15E+01	3.53E+00
1.90E+00	2.86E+05	1.89E+00	1.44E+06	-1.10E+01	3.49E+00
2.00E+00	2.64E+05	1.99E+00	1.32E+06	-1.05E+01	3.46E+00
2.10E+00	2.44E+05	2.09E+00	1.22E+06	-1.00E+01	3.42E+00
2.20E+00	2.25E+05	2.19E+00	1.12E+06	-9.50E+00	3.38E+00
2.30E+00	2.08E+05	2.29E+00	1.03E+06	-9.00E+00	3.33E+00
2.40E+00	1.92E+05	2.39E+00	9.47E+05	-8.50E+00	3.29E+00
2.50E+00	1.77E+05	2.49E+00	8.72E+05	-8.00E+00	3.24E+00
2.60E+00	1.63E+05	2.59E+00	8.02E+05	-7.50E+00	3.18E+00
2.70E+00	1.51E+05	2.69E+00	7.39E+05	-7.00E+00	3.12E+00
2.80E+00	1.39E+05	2.79E+00	6.80E+05	-6.50E+00	3.06E+00
2.90E+00	1.29E+05	2.89E+00	6.26E+05	-6.00E+00	2.99E+00
3.00E+00	1.19E+05	2.99E+00	5.76E+05	-5.50E+00	2.91E+00
3.10E+00	1.10E+05	3.09E+00	5.31E+05	-5.00E+00	2.83E+00
3.20E+00	1.02E+05	3.19E+00	4.89E+05	-4.50E+00	2.74E+00
3.30E+00	9.38E+04	3.29E+00	4.50E+05	-4.00E+00	2.64E+00
3.40E+00	8.67E+04	3.39E+00	4.14E+05	-3.50E+00	2.54E+00
3.50E+00	8.01E+04	3.49E+00	3.81E+05	-3.00E+00	2.43E+00
3.60E+00	7.41E+04	3.59E+00	3.51E+05	-2.50E+00	2.32E+00
3.70E+00	6.84E+04	3.69E+00	3.24E+05	-2.00E+00	2.20E+00

## Appendix 8

3.80E+00	6.33E+04	3.79E+00	2.98E+05	-1.50E+00	2.08E+00
3.90E+00	5.85E+04	3.89E+00	2.75E+05	-1.00E+00	1.95E+00
4.00E+00	5.41E+04	3.99E+00	2.53E+05	-5.00E-01	1.82E+00
4.10E+00	5.00E+04	4.09E+00	2.33E+05	0.00E+00	1.69E+00
4.20E+00	4.62E+04	4.19E+00	2.15E+05	5.00E-01	1.56E+00
4.30E+00	4.27E+04	4.29E+00	1.98E+05	1.00E+00	1.44E+00
4.40E+00	3.95E+04	4.39E+00	1.82E+05	1.50E+00	1.31E+00
4.50E+00	3.66E+04	4.49E+00	1.68E+05	2.00E+00	1.19E+00
4.60E+00	3.38E+04	4.59E+00	1.55E+05	2.50E+00	1.08E+00
4.70E+00	3.13E+04	4.69E+00	1.43E+05	3.00E+00	9.71E-01
4.80E+00	2.89E+04	4.79E+00	1.31E+05	3.50E+00	8.69E-01
4.90E+00	2.68E+04	4.89E+00	1.21E+05	4.00E+00	7.74E-01
5.00E+00	2.48E+04	4.99E+00	1.12E+05	4.50E+00	6.84E-01
5.10E+00	2.29E+04	5.09E+00	1.03E+05	5.00E+00	6.02E-01
5.20E+00	2.12E+04	5.19E+00	9.48E+04	5.50E+00	5.25E-01
5.30E+00	1.96E+04	5.29E+00	8.73E+04	6.00E+00	4.55E-01
5.40E+00	1.81E+04	5.39E+00	8.05E+04	6.50E+00	3.90E-01
5.50E+00	1.68E+04	5.49E+00	7.42E+04	7.00E+00	3.30E-01
5.60E+00	1.55E+04	5.59E+00	6.84E+04	7.50E+00	2.75E-01
5.70E+00	1.44E+04	5.69E+00	6.31E+04	8.00E+00	2.24E-01
5.80E+00	1.33E+04	5.79E+00	5.81E+04	8.50E+00	1.76E-01
5.90E+00	1.23E+04	5.89E+00	5.36E+04	9.00E+00	1.33E-01
6.00E+00	1.14E+04	5.99E+00	4.94E+04	9.50E+00	9.16E-02
6.10E+00	1.06E+04	6.09E+00	4.56E+04	1.00E+01	5.33E-02
6.20E+00	9.77E+03	6.19E+00	4.20E+04	1.05E+01	1.74E-02
6.30E+00	9.04E+03			1.10E+01	-1.64E-02
6.40E+00	8.37E+03			1.15E+01	-4.83E-02
6.50E+00	7.75E+03			1.20E+01	-7.85E-02
6.60E+00	7.18E+03			1.25E+01	-1.07E-01
6.70E+00	6.64E+03			1.30E+01	-1.34E-01
6.80E+00	6.15E+03			1.35E+01	-1.60E-01
6.90E+00	5.70E+03			1.40E+01	-1.85E-01
7.00E+00	5.28E+03			1.45E+01	-2.09E-01
7.10E+00	4.89E+03			1.50E+01	-2.31E-01
7.20E+00	4.53E+03			1.55E+01	-2.53E-01
				1.60E+01	-2.74E-01
				1.65E+01	-2.94E-01
				1.70E+01	-3.14E-01
				1.75E+01	-3.32E-01
				1.80E+01	-3.50E-01
				1.85E+01	-3.68E-01
				1.90E+01	-3.85E-01
				1.95E+01	-4.01E-01
				2.00E+01	-4.17E-01

**Lookup modeled <sup>36</sup>Cl accumulation at sample depths:**

<b>Footwall</b>		<b>Hanging Wall</b>	
<b>Depth</b>	<b>36Cl</b>	<b>Depth</b>	<b>36Cl</b>
<b>(meters)</b>	<b>(atoms/g)</b>	<b>(meters)</b>	<b>(atoms/g)</b>
6.99E-01	7.56E+05	2.94E-01	1.65E+06
9.99E-01	5.92E+05	5.94E-01	2.54E+06
1.70E+00	3.36E+05	1.09E+00	2.17E+06
2.20E+00	2.25E+05	1.59E+00	1.84E+06
2.70E+00	1.51E+05	1.89E+00	1.44E+06
		2.29E+00	1.03E+06
		3.09E+00	5.31E+05

**Difference between modeled and observed:**

-1.35E+05	-9.88E+05
1.42E+05	2.35E+05
6.73E+03	2.50E+05
2.78E+04	-2.04E+04
1.09E+05	3.86E+05
	1.76E+05
	1.89E+05

**Squared Difference:**

1.82E+10	9.75E+11
2.01E+10	5.54E+10
4.53E+07	6.25E+10
7.74E+08	4.16E+08
1.18E+10	1.49E+11
	3.08E+10
	3.56E+10

**Chi-square residuals:**

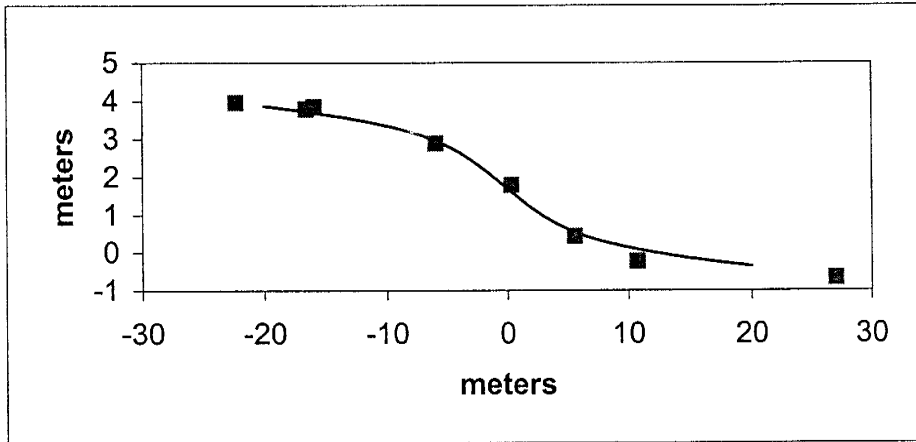
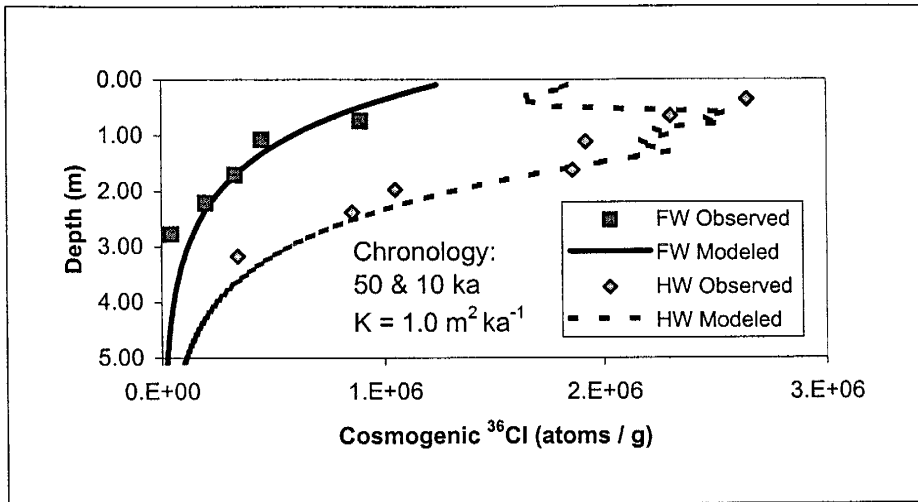
2.41E+04	5.90E+05
3.39E+04	2.19E+04
1.35E+02	2.88E+04
3.44E+03	2.26E+02
7.82E+04	1.04E+05
	2.99E+04
	6.70E+04

**Chi-square value:**

1.40E+05	8.42E+05
----------	----------

**Total Chi-square:** 9.82E+05

Appendix 8



## Appendix 8

### Profile 1.5 m from the fault plane

% Fault-scarp parameters, 0 is second column is necessary but meaningless.

% Age estimates need to be to the nearest 1 ka.

0.5	0	% geomorphic diffusivity (m <sup>2</sup> / ka)
1.3	0	% far-field slope (degrees)
122	0	% age of displaced terrace (ka)
2	0	% number of displacements
1.7	50	% magnitude (meters) and age estimate (ka)
1.8	48	% list each event on a separate row, start with the oldest

Footwall		Hanging Wall		Topography	
Depth (meters)	36Cl (atoms/g)	Depth (meters)	36Cl (atoms/g)	x (meters)	Z (meters)
4.39E-02	1.50E+06	5.97E-02	2.26E+06	-2.00E+01	3.94E+00
1.44E-01	1.39E+06	1.60E-01	2.24E+06	-1.95E+01	3.93E+00
2.44E-01	1.28E+06	2.60E-01	2.16E+06	-1.90E+01	3.92E+00
3.44E-01	1.18E+06	3.60E-01	2.20E+06	-1.85E+01	3.90E+00
4.44E-01	1.09E+06	4.60E-01	1.97E+06	-1.80E+01	3.89E+00
5.44E-01	1.01E+06	5.60E-01	2.03E+06	-1.75E+01	3.87E+00
6.44E-01	9.28E+05	6.60E-01	1.97E+06	-1.70E+01	3.86E+00
7.44E-01	8.55E+05	7.60E-01	2.04E+06	-1.65E+01	3.84E+00
8.44E-01	7.89E+05	8.60E-01	1.81E+06	-1.60E+01	3.82E+00
9.44E-01	7.27E+05	9.60E-01	1.75E+06	-1.55E+01	3.80E+00
1.04E+00	6.71E+05	1.06E+00	1.72E+06	-1.50E+01	3.78E+00
1.14E+00	6.19E+05	1.16E+00	1.66E+06	-1.45E+01	3.75E+00
1.24E+00	5.71E+05	1.26E+00	1.90E+06	-1.40E+01	3.73E+00
1.34E+00	5.27E+05	1.36E+00	2.11E+06	-1.35E+01	3.70E+00
1.44E+00	4.87E+05	1.46E+00	1.98E+06	-1.30E+01	3.67E+00
1.54E+00	4.50E+05	1.56E+00	1.84E+06	-1.25E+01	3.64E+00
1.64E+00	4.15E+05	1.66E+00	1.70E+06	-1.20E+01	3.61E+00
1.74E+00	3.84E+05	1.76E+00	1.57E+06	-1.15E+01	3.57E+00
1.84E+00	3.54E+05	1.86E+00	1.44E+06	-1.10E+01	3.53E+00
1.94E+00	3.28E+05	1.96E+00	1.33E+06	-1.05E+01	3.49E+00
2.04E+00	3.03E+05	2.06E+00	1.22E+06	-1.00E+01	3.44E+00
2.14E+00	2.80E+05	2.16E+00	1.13E+06	-9.50E+00	3.39E+00
2.24E+00	2.59E+05	2.26E+00	1.04E+06	-9.00E+00	3.34E+00
2.34E+00	2.39E+05	2.36E+00	9.54E+05	-8.50E+00	3.28E+00
2.44E+00	2.21E+05	2.46E+00	8.78E+05	-8.00E+00	3.22E+00
2.54E+00	2.05E+05	2.56E+00	8.08E+05	-7.50E+00	3.15E+00
2.64E+00	1.89E+05	2.66E+00	7.44E+05	-7.00E+00	3.08E+00
2.74E+00	1.75E+05	2.76E+00	6.85E+05	-6.50E+00	3.00E+00
2.84E+00	1.62E+05	2.86E+00	6.31E+05	-6.00E+00	2.92E+00
2.94E+00	1.50E+05	2.96E+00	5.81E+05	-5.50E+00	2.84E+00
3.04E+00	1.39E+05	3.06E+00	5.34E+05	-5.00E+00	2.75E+00
3.14E+00	1.28E+05	3.16E+00	4.92E+05	-4.50E+00	2.66E+00
3.24E+00	1.19E+05	3.26E+00	4.53E+05	-4.00E+00	2.56E+00
3.34E+00	1.10E+05	3.36E+00	4.17E+05	-3.50E+00	2.46E+00
3.44E+00	1.02E+05	3.46E+00	3.84E+05	-3.00E+00	2.36E+00
3.54E+00	9.43E+04	3.56E+00	3.54E+05	-2.50E+00	2.25E+00
3.64E+00	8.73E+04	3.66E+00	3.26E+05	-2.00E+00	2.14E+00

## Appendix 8

3.74E+00	8.08E+04	3.76E+00	3.00E+05	-1.50E+00	2.03E+00
3.84E+00	7.49E+04	3.86E+00	2.76E+05	-1.00E+00	1.92E+00
3.94E+00	6.93E+04	3.96E+00	2.55E+05	-5.00E-01	1.81E+00
4.04E+00	6.42E+04	4.06E+00	2.35E+05	0.00E+00	1.70E+00
4.14E+00	5.95E+04	4.16E+00	2.16E+05	5.00E-01	1.59E+00
4.24E+00	5.51E+04	4.26E+00	1.99E+05	1.00E+00	1.48E+00
4.34E+00	5.11E+04	4.36E+00	1.83E+05	1.50E+00	1.37E+00
4.44E+00	4.73E+04	4.46E+00	1.69E+05	2.00E+00	1.26E+00
4.54E+00	4.38E+04	4.56E+00	1.56E+05	2.50E+00	1.15E+00
4.64E+00	4.06E+04	4.66E+00	1.43E+05	3.00E+00	1.05E+00
4.74E+00	3.76E+04	4.76E+00	1.32E+05	3.50E+00	9.52E-01
4.84E+00	3.49E+04	4.86E+00	1.22E+05	4.00E+00	8.55E-01
4.94E+00	3.23E+04	4.96E+00	1.12E+05	4.50E+00	7.63E-01
5.04E+00	3.00E+04	5.06E+00	1.03E+05	5.00E+00	6.74E-01
5.14E+00	2.78E+04	5.16E+00	9.53E+04	5.50E+00	5.89E-01
5.24E+00	2.58E+04	5.26E+00	8.78E+04	6.00E+00	5.09E-01
5.34E+00	2.39E+04	5.36E+00	8.09E+04	6.50E+00	4.33E-01
5.44E+00	2.21E+04	5.46E+00	7.46E+04	7.00E+00	3.62E-01
5.54E+00	2.05E+04	5.56E+00	6.87E+04	7.50E+00	2.95E-01
5.64E+00	1.90E+04	5.66E+00	6.34E+04	8.00E+00	2.32E-01
5.74E+00	1.76E+04	5.76E+00	5.84E+04	8.50E+00	1.73E-01
5.84E+00	1.64E+04	5.86E+00	5.38E+04	9.00E+00	1.19E-01
5.94E+00	1.52E+04	5.96E+00	4.96E+04	9.50E+00	6.83E-02
6.04E+00	1.41E+04	6.06E+00	4.57E+04	1.00E+01	2.16E-02
6.14E+00	1.31E+04	6.16E+00	4.22E+04	1.05E+01	-2.17E-02
6.24E+00	1.21E+04	6.26E+00	3.89E+04	1.10E+01	-6.16E-02
6.34E+00	1.12E+04			1.15E+01	-9.83E-02
6.44E+00	1.04E+04			1.20E+01	-1.32E-01
6.54E+00	9.66E+03			1.25E+01	-1.64E-01
6.64E+00	8.97E+03			1.30E+01	-1.92E-01
6.74E+00	8.32E+03			1.35E+01	-2.19E-01
6.84E+00	7.72E+03			1.40E+01	-2.44E-01
6.94E+00	7.16E+03			1.45E+01	-2.66E-01
7.04E+00	6.65E+03			1.50E+01	-2.88E-01
7.14E+00	6.17E+03			1.55E+01	-3.08E-01
				1.60E+01	-3.26E-01
				1.65E+01	-3.44E-01
				1.70E+01	-3.60E-01
				1.75E+01	-3.76E-01
				1.80E+01	-3.91E-01
				1.85E+01	-4.06E-01
				1.90E+01	-4.20E-01
				1.95E+01	-4.33E-01
				2.00E+01	-4.46E-01

Lookup modeled  $^{36}\text{Cl}$  accumulation at sample depths:

Footwall		Hanging Wall	
Depth	$^{36}\text{Cl}$	Depth	$^{36}\text{Cl}$
(meters)	(atoms/g)	(meters)	(atoms/g)
6.44E-01	9.28E+05	2.60E-01	2.16E+06
1.04E+00	6.71E+05	6.60E-01	1.97E+06
1.64E+00	4.15E+05	1.06E+00	1.72E+06
2.14E+00	2.80E+05	1.56E+00	1.84E+06
2.74E+00	1.75E+05	1.96E+00	1.33E+06
		2.36E+00	9.54E+05
		3.16E+00	4.92E+05

## Difference between modeled and observed:

3.66E+04	-4.79E+05
2.21E+05	-3.33E+05
8.63E+04	-2.02E+05
8.28E+04	-1.88E+04
1.33E+05	2.80E+05
	1.00E+05
	1.50E+05

## Squared Difference:

1.34E+09	2.30E+11
4.88E+10	1.11E+11
7.44E+09	4.07E+10
6.86E+09	3.55E+08
1.76E+10	7.84E+10
	1.00E+10
	2.25E+10

## Chi-square residuals:

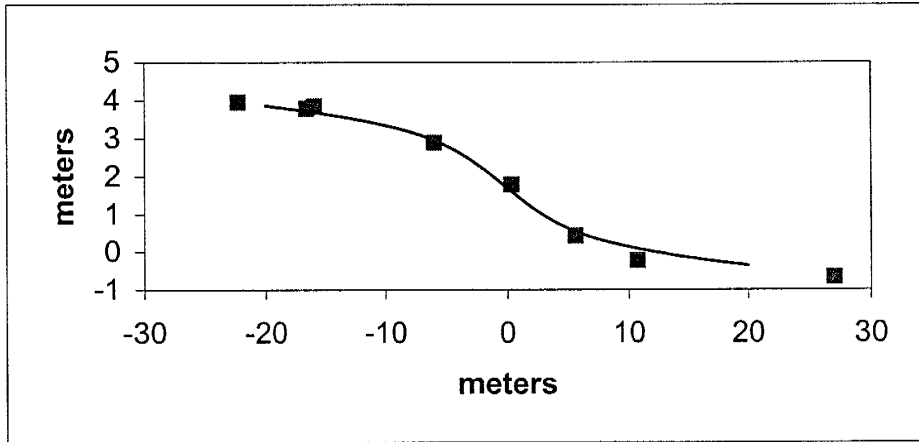
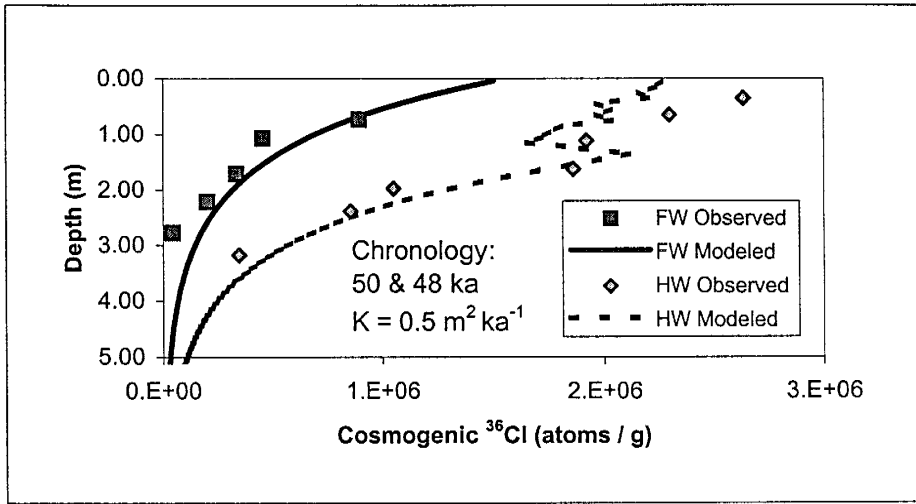
1.45E+03	1.06E+05
7.27E+04	5.63E+04
1.79E+04	2.37E+04
2.45E+04	1.93E+02
1.01E+05	5.90E+04
	1.05E+04
	4.58E+04

## Chi-square value:

2.17E+05	3.02E+05
----------	----------

Total Chi-square: 5.19E+05

Appendix 8





## Appendix 8

### Profile 1.5 m from the fault plane

% Fault-scarp parameters, 0 is second column is necessary but meaningless.

% Age estimates need to be to the nearest 1 ka.

0.8	0	% geomorphic diffusivity (m <sup>2</sup> / ka)
1.3	0	% far-field slope (degrees)
122	0	% age of displaced terrace (ka)
2	0	% number of displacements
1.7	86	% magnitude (meters) and age estimate (ka)
1.8	10	% list each event on a separate row, start with the oldest

Footwall		Hanging Wall		Topography	
Depth (meters)	36Cl (atoms/g)	Depth (meters)	36Cl (atoms/g)	x (meters)	Z (meters)
1.23E-02	1.56E+06	7.84E-02	2.01E+06	-2.00E+01	3.88E+00
1.12E-01	1.44E+06	1.78E-01	1.92E+06	-1.95E+01	3.86E+00
2.12E-01	1.33E+06	2.78E-01	1.84E+06	-1.90E+01	3.84E+00
3.12E-01	1.22E+06	3.78E-01	1.94E+06	-1.85E+01	3.82E+00
4.12E-01	1.12E+06	4.78E-01	2.09E+06	-1.80E+01	3.80E+00
5.12E-01	1.04E+06	5.78E-01	2.64E+06	-1.75E+01	3.78E+00
6.12E-01	9.54E+05	6.78E-01	2.54E+06	-1.70E+01	3.76E+00
7.12E-01	8.79E+05	7.78E-01	2.46E+06	-1.65E+01	3.73E+00
8.12E-01	8.10E+05	8.78E-01	2.32E+06	-1.60E+01	3.71E+00
9.12E-01	7.47E+05	9.78E-01	2.19E+06	-1.55E+01	3.69E+00
1.01E+00	6.89E+05	1.08E+00	2.05E+06	-1.50E+01	3.66E+00
1.11E+00	6.35E+05	1.18E+00	2.00E+06	-1.45E+01	3.64E+00
1.21E+00	5.86E+05	1.28E+00	1.96E+06	-1.40E+01	3.61E+00
1.31E+00	5.40E+05	1.38E+00	1.82E+06	-1.35E+01	3.59E+00
1.41E+00	4.99E+05	1.48E+00	1.69E+06	-1.30E+01	3.56E+00
1.51E+00	4.60E+05	1.58E+00	1.55E+06	-1.25E+01	3.53E+00
1.61E+00	4.25E+05	1.68E+00	1.43E+06	-1.20E+01	3.50E+00
1.71E+00	3.92E+05	1.78E+00	1.32E+06	-1.15E+01	3.47E+00
1.81E+00	3.62E+05	1.88E+00	1.21E+06	-1.10E+01	3.44E+00
1.91E+00	3.35E+05	1.98E+00	1.11E+06	-1.05E+01	3.40E+00
2.01E+00	3.09E+05	2.08E+00	1.03E+06	-1.00E+01	3.37E+00
2.11E+00	2.85E+05	2.18E+00	9.44E+05	-9.50E+00	3.33E+00
2.21E+00	2.64E+05	2.28E+00	8.69E+05	-9.00E+00	3.29E+00
2.31E+00	2.44E+05	2.38E+00	8.00E+05	-8.50E+00	3.25E+00
2.41E+00	2.25E+05	2.48E+00	7.37E+05	-8.00E+00	3.20E+00
2.51E+00	2.08E+05	2.58E+00	6.78E+05	-7.50E+00	3.15E+00
2.61E+00	1.92E+05	2.68E+00	6.25E+05	-7.00E+00	3.10E+00
2.71E+00	1.78E+05	2.78E+00	5.76E+05	-6.50E+00	3.04E+00
2.81E+00	1.64E+05	2.88E+00	5.30E+05	-6.00E+00	2.98E+00
2.91E+00	1.52E+05	2.98E+00	4.89E+05	-5.50E+00	2.91E+00
3.01E+00	1.41E+05	3.08E+00	4.50E+05	-5.00E+00	2.83E+00
3.11E+00	1.30E+05	3.18E+00	4.15E+05	-4.50E+00	2.74E+00
3.21E+00	1.20E+05	3.28E+00	3.83E+05	-4.00E+00	2.65E+00
3.31E+00	1.11E+05	3.38E+00	3.53E+05	-3.50E+00	2.55E+00
3.41E+00	1.03E+05	3.48E+00	3.25E+05	-3.00E+00	2.45E+00
3.51E+00	9.53E+04	3.58E+00	3.00E+05	-2.50E+00	2.33E+00
3.61E+00	8.82E+04	3.68E+00	2.77E+05	-2.00E+00	2.21E+00

## Appendix 8

3.71E+00	8.16E+04	3.78E+00	2.55E+05	-1.50E+00	2.09E+00
3.81E+00	7.55E+04	3.88E+00	2.35E+05	-1.00E+00	1.96E+00
3.91E+00	6.99E+04	3.98E+00	2.17E+05	-5.00E-01	1.82E+00
4.01E+00	6.47E+04	4.08E+00	2.00E+05	0.00E+00	1.69E+00
4.11E+00	5.99E+04	4.18E+00	1.85E+05	5.00E-01	1.56E+00
4.21E+00	5.54E+04	4.28E+00	1.70E+05	1.00E+00	1.43E+00
4.31E+00	5.13E+04	4.38E+00	1.57E+05	1.50E+00	1.30E+00
4.41E+00	4.75E+04	4.48E+00	1.45E+05	2.00E+00	1.18E+00
4.51E+00	4.40E+04	4.58E+00	1.34E+05	2.50E+00	1.06E+00
4.61E+00	4.08E+04	4.68E+00	1.24E+05	3.00E+00	9.57E-01
4.71E+00	3.78E+04	4.78E+00	1.14E+05	3.50E+00	8.58E-01
4.81E+00	3.50E+04	4.88E+00	1.05E+05	4.00E+00	7.67E-01
4.91E+00	3.24E+04	4.98E+00	9.72E+04	4.50E+00	6.83E-01
5.01E+00	3.00E+04	5.08E+00	8.98E+04	5.00E+00	6.06E-01
5.11E+00	2.78E+04	5.18E+00	8.29E+04	5.50E+00	5.36E-01
5.21E+00	2.58E+04	5.28E+00	7.65E+04	6.00E+00	4.72E-01
5.31E+00	2.39E+04	5.38E+00	7.07E+04	6.50E+00	4.13E-01
5.41E+00	2.21E+04	5.48E+00	6.53E+04	7.00E+00	3.60E-01
5.51E+00	2.05E+04	5.58E+00	6.03E+04	7.50E+00	3.10E-01
5.61E+00	1.90E+04	5.68E+00	5.57E+04	8.00E+00	2.64E-01
5.71E+00	1.76E+04	5.78E+00	5.14E+04	8.50E+00	2.22E-01
5.81E+00	1.63E+04	5.88E+00	4.75E+04	9.00E+00	1.82E-01
5.91E+00	1.51E+04	5.98E+00	4.39E+04	9.50E+00	1.44E-01
6.01E+00	1.40E+04	6.08E+00	4.06E+04	1.00E+01	1.09E-01
6.11E+00	1.30E+04	6.18E+00	3.75E+04	1.05E+01	7.49E-02
6.21E+00	1.20E+04			1.10E+01	4.26E-02
6.31E+00	1.12E+04			1.15E+01	1.16E-02
6.41E+00	1.03E+04			1.20E+01	-1.81E-02
6.51E+00	9.59E+03			1.25E+01	-4.68E-02
6.61E+00	8.90E+03			1.30E+01	-7.44E-02
6.71E+00	8.25E+03			1.35E+01	-1.01E-01
6.81E+00	7.65E+03			1.40E+01	-1.27E-01
6.91E+00	7.10E+03			1.45E+01	-1.52E-01
7.01E+00	6.58E+03			1.50E+01	-1.76E-01
7.11E+00	6.10E+03			1.55E+01	-2.00E-01
7.21E+00	5.66E+03			1.60E+01	-2.22E-01
				1.65E+01	-2.44E-01
				1.70E+01	-2.66E-01
				1.75E+01	-2.87E-01
				1.80E+01	-3.07E-01
				1.85E+01	-3.27E-01
				1.90E+01	-3.46E-01
				1.95E+01	-3.64E-01
				2.00E+01	-3.82E-01

Lookup modeled <sup>36</sup>Cl accumulation at sample depths:

Footwall		Hanging Wall	
Depth (meters)	<sup>36</sup> Cl (atoms/g)	Depth (meters)	<sup>36</sup> Cl (atoms/g)
7.12E-01	8.79E+05	2.78E-01	1.84E+06
1.01E+00	6.89E+05	5.78E-01	2.64E+06
1.61E+00	4.25E+05	1.08E+00	2.05E+06
2.21E+00	2.64E+05	1.58E+00	1.55E+06
2.71E+00	1.78E+05	1.98E+00	1.11E+06
		2.38E+00	8.00E+05
		3.08E+00	4.50E+05

## Difference between modeled and observed:

-1.18E+04	-7.96E+05
2.39E+05	3.45E+05
9.59E+04	1.27E+05
6.67E+04	-3.07E+05
1.36E+05	6.42E+04
	-5.41E+04
	1.08E+05

## Squared Difference:

1.40E+08	6.34E+11
5.69E+10	1.19E+11
9.19E+09	1.62E+10
4.45E+09	9.42E+10
1.84E+10	4.12E+09
	2.92E+09
	1.17E+10

## Chi-square residuals:

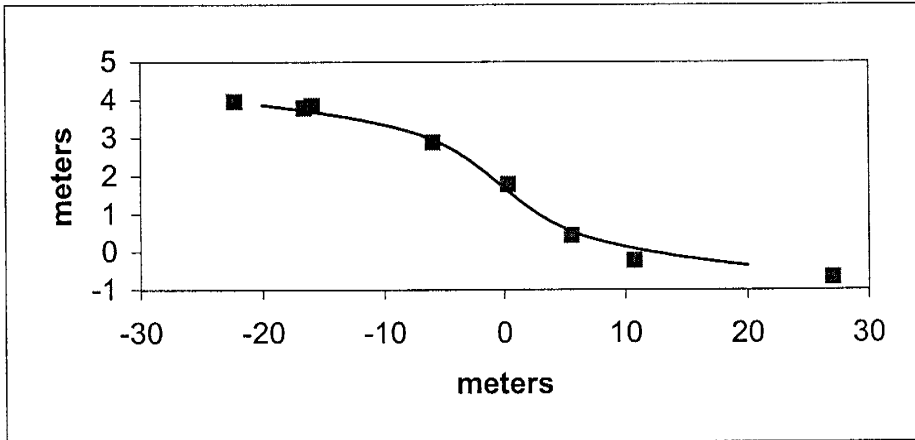
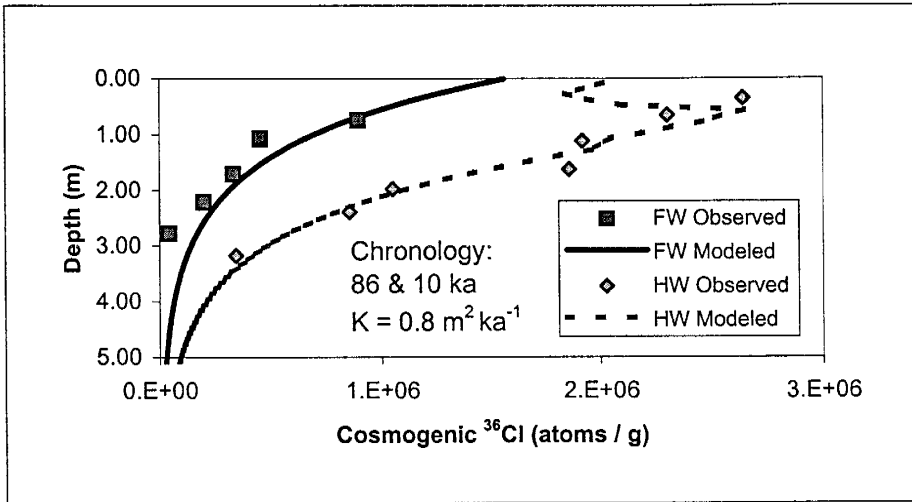
1.59E+02	3.44E+05
8.27E+04	4.50E+04
2.16E+04	7.92E+03
1.69E+04	6.07E+04
1.03E+05	3.70E+03
	3.65E+03
	2.61E+04

## Chi-square value:

2.25E+05	4.91E+05
----------	----------

Total Chi-square: 7.15E+05

Appendix 8



## Appendix 8

### Profile 1.5 m from the fault plane

% Fault-scarp parameters, 0 is second column is necessary but meaningless.

% Age estimates need to be to the nearest 1 ka.

0.5	0	% geomorphic diffusivity (m <sup>2</sup> / ka)
1.3	0	% far-field slope (degrees)
122	0	% age of displaced terrace (ka)
2	0	% number of displacements
1.7	86	% magnitude (meters) and age estimate (ka)
1.8	24	% list each event on a separate row, start with the oldest

Footwall		Hanging Wall		Topography	
Depth (meters)	36Cl (atoms/g)	Depth (meters)	36Cl (atoms/g)	x (meters)	Z (meters)
7.85E-02	1.51E+06	1.74E-02	2.13E+06	-2.00E+01	3.93E+00
1.78E-01	1.39E+06	1.17E-01	2.03E+06	-1.95E+01	3.91E+00
2.78E-01	1.28E+06	2.17E-01	1.96E+06	-1.90E+01	3.89E+00
3.78E-01	1.18E+06	3.17E-01	2.15E+06	-1.85E+01	3.88E+00
4.78E-01	1.09E+06	4.17E-01	1.95E+06	-1.80E+01	3.86E+00
5.78E-01	1.00E+06	5.17E-01	1.90E+06	-1.75E+01	3.84E+00
6.78E-01	9.24E+05	6.17E-01	2.49E+06	-1.70E+01	3.82E+00
7.78E-01	8.52E+05	7.17E-01	2.48E+06	-1.65E+01	3.81E+00
8.78E-01	7.86E+05	8.17E-01	2.38E+06	-1.60E+01	3.79E+00
9.78E-01	7.25E+05	9.17E-01	2.26E+06	-1.55E+01	3.76E+00
1.08E+00	6.69E+05	1.02E+00	2.15E+06	-1.50E+01	3.74E+00
1.18E+00	6.17E+05	1.12E+00	1.99E+06	-1.45E+01	3.72E+00
1.28E+00	5.70E+05	1.22E+00	1.92E+06	-1.40E+01	3.70E+00
1.38E+00	5.26E+05	1.32E+00	1.95E+06	-1.35E+01	3.67E+00
1.48E+00	4.86E+05	1.42E+00	1.81E+06	-1.30E+01	3.64E+00
1.58E+00	4.49E+05	1.52E+00	1.67E+06	-1.25E+01	3.61E+00
1.68E+00	4.15E+05	1.62E+00	1.54E+06	-1.20E+01	3.58E+00
1.78E+00	3.83E+05	1.72E+00	1.42E+06	-1.15E+01	3.55E+00
1.88E+00	3.54E+05	1.82E+00	1.31E+06	-1.10E+01	3.51E+00
1.98E+00	3.27E+05	1.92E+00	1.20E+06	-1.05E+01	3.48E+00
2.08E+00	3.03E+05	2.02E+00	1.11E+06	-1.00E+01	3.44E+00
2.18E+00	2.80E+05	2.12E+00	1.02E+06	-9.50E+00	3.39E+00
2.28E+00	2.59E+05	2.22E+00	9.36E+05	-9.00E+00	3.35E+00
2.38E+00	2.39E+05	2.32E+00	8.61E+05	-8.50E+00	3.29E+00
2.48E+00	2.21E+05	2.42E+00	7.93E+05	-8.00E+00	3.24E+00
2.58E+00	2.05E+05	2.52E+00	7.30E+05	-7.50E+00	3.18E+00
2.68E+00	1.89E+05	2.62E+00	6.72E+05	-7.00E+00	3.11E+00
2.78E+00	1.75E+05	2.72E+00	6.19E+05	-6.50E+00	3.05E+00
2.88E+00	1.62E+05	2.82E+00	5.70E+05	-6.00E+00	2.97E+00
2.98E+00	1.50E+05	2.92E+00	5.26E+05	-5.50E+00	2.89E+00
3.08E+00	1.39E+05	3.02E+00	4.84E+05	-5.00E+00	2.80E+00
3.18E+00	1.29E+05	3.12E+00	4.46E+05	-4.50E+00	2.71E+00
3.28E+00	1.19E+05	3.22E+00	4.11E+05	-4.00E+00	2.62E+00
3.38E+00	1.10E+05	3.32E+00	3.79E+05	-3.50E+00	2.51E+00
3.48E+00	1.02E+05	3.42E+00	3.49E+05	-3.00E+00	2.41E+00
3.58E+00	9.44E+04	3.52E+00	3.22E+05	-2.50E+00	2.29E+00
3.68E+00	8.75E+04	3.62E+00	2.97E+05	-2.00E+00	2.18E+00

## Appendix 8

3.78E+00	8.10E+04	3.72E+00	2.74E+05	-1.50E+00	2.06E+00
3.88E+00	7.50E+04	3.82E+00	2.53E+05	-1.00E+00	1.94E+00
3.98E+00	6.95E+04	3.92E+00	2.33E+05	-5.00E-01	1.82E+00
4.08E+00	6.44E+04	4.02E+00	2.15E+05	0.00E+00	1.69E+00
4.18E+00	5.96E+04	4.12E+00	1.98E+05	5.00E-01	1.57E+00
4.28E+00	5.53E+04	4.22E+00	1.83E+05	1.00E+00	1.45E+00
4.38E+00	5.12E+04	4.32E+00	1.69E+05	1.50E+00	1.33E+00
4.48E+00	4.74E+04	4.42E+00	1.56E+05	2.00E+00	1.22E+00
4.58E+00	4.40E+04	4.52E+00	1.44E+05	2.50E+00	1.11E+00
4.68E+00	4.08E+04	4.62E+00	1.33E+05	3.00E+00	9.99E-01
4.78E+00	3.78E+04	4.72E+00	1.22E+05	3.50E+00	8.96E-01
4.88E+00	3.50E+04	4.82E+00	1.13E+05	4.00E+00	7.99E-01
4.98E+00	3.25E+04	4.92E+00	1.04E+05	4.50E+00	7.08E-01
5.08E+00	3.01E+04	5.02E+00	9.62E+04	5.00E+00	6.22E-01
5.18E+00	2.79E+04	5.12E+00	8.88E+04	5.50E+00	5.41E-01
5.28E+00	2.59E+04	5.22E+00	8.20E+04	6.00E+00	4.66E-01
5.38E+00	2.40E+04	5.32E+00	7.57E+04	6.50E+00	3.97E-01
5.48E+00	2.22E+04	5.42E+00	6.99E+04	7.00E+00	3.32E-01
5.58E+00	2.06E+04	5.52E+00	6.46E+04	7.50E+00	2.72E-01
5.68E+00	1.91E+04	5.62E+00	5.97E+04	8.00E+00	2.17E-01
5.78E+00	1.77E+04	5.72E+00	5.51E+04	8.50E+00	1.66E-01
5.88E+00	1.64E+04	5.82E+00	5.09E+04	9.00E+00	1.19E-01
5.98E+00	1.53E+04	5.92E+00	4.70E+04	9.50E+00	7.52E-02
6.08E+00	1.41E+04	6.02E+00	4.34E+04	1.00E+01	3.45E-02
6.18E+00	1.31E+04	6.12E+00	4.01E+04	1.05E+01	-3.22E-03
6.28E+00	1.22E+04	6.22E+00	3.71E+04	1.10E+01	-3.84E-02
6.38E+00	1.13E+04			1.15E+01	-7.13E-02
6.48E+00	1.05E+04			1.20E+01	-1.02E-01
6.58E+00	9.72E+03			1.25E+01	-1.31E-01
6.68E+00	9.02E+03			1.30E+01	-1.58E-01
6.78E+00	8.37E+03			1.35E+01	-1.84E-01
6.88E+00	7.77E+03			1.40E+01	-2.08E-01
6.98E+00	7.21E+03			1.45E+01	-2.31E-01
7.08E+00	6.69E+03			1.50E+01	-2.53E-01
7.18E+00	6.21E+03			1.55E+01	-2.74E-01
				1.60E+01	-2.94E-01
				1.65E+01	-3.13E-01
				1.70E+01	-3.32E-01
				1.75E+01	-3.49E-01
				1.80E+01	-3.66E-01
				1.85E+01	-3.83E-01
				1.90E+01	-3.98E-01
				1.95E+01	-4.14E-01
				2.00E+01	-4.29E-01

**Lookup modeled <sup>36</sup>Cl accumulation at sample depths:**

<b>Footwall</b>		<b>Hanging Wall</b>	
<b>Depth</b>	<b><sup>36</sup>Cl</b>	<b>Depth</b>	<b><sup>36</sup>Cl</b>
<b>(meters)</b>	<b>(atoms/g)</b>	<b>(meters)</b>	<b>(atoms/g)</b>
6.78E-01	9.24E+05	3.17E-01	2.15E+06
9.78E-01	7.25E+05	6.17E-01	2.49E+06
1.68E+00	4.15E+05	1.12E+00	1.99E+06
2.18E+00	2.80E+05	1.62E+00	1.54E+06
2.68E+00	1.89E+05	1.92E+00	1.20E+06
		2.32E+00	8.61E+05
		3.12E+00	4.46E+05

**Difference between modeled and observed:**

3.30E+04	-4.86E+05
2.75E+05	1.86E+05
8.57E+04	6.76E+04
8.28E+04	-3.19E+05
1.47E+05	1.51E+05
	7.46E+03
	1.04E+05

**Squared Difference:**

1.09E+09	2.36E+11
7.56E+10	3.44E+10
7.35E+09	4.58E+09
6.85E+09	1.02E+11
2.16E+10	2.28E+10
	5.57E+07
	1.09E+10

**Chi-square residuals:**

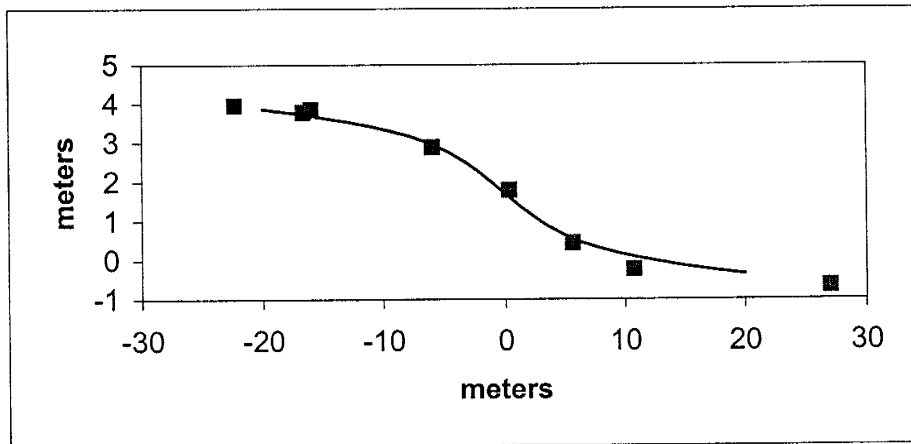
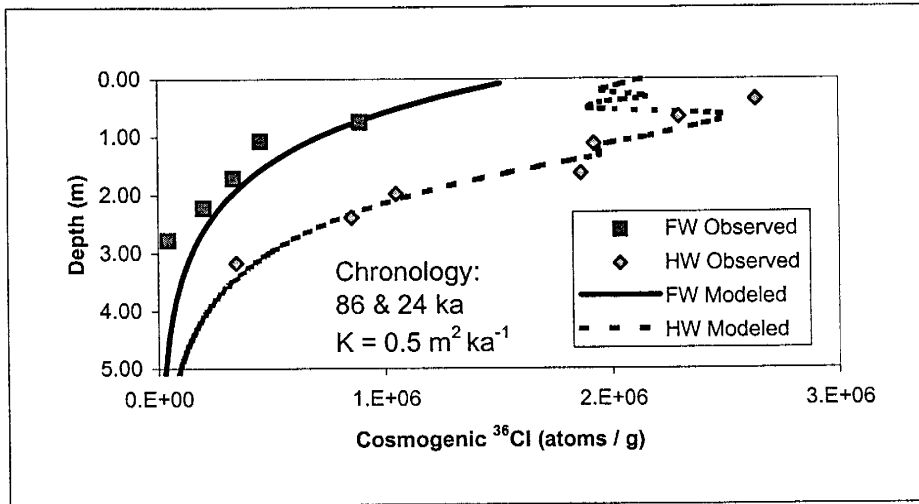
1.18E+03	1.10E+05
1.04E+05	1.38E+04
1.77E+04	2.30E+03
2.45E+04	6.60E+04
1.14E+05	1.90E+04
	6.46E+01
	2.43E+04

**Chi-square value:**

2.62E+05	2.35E+05
----------	----------

**Total Chi-square:** 4.97E+05

Appendix 8





## Appendix 8

### Profile 1.5 m from the fault plane

% Fault-scarp parameters, 0 is second column is necessary but meaningless.

% Age estimates need to be to the nearest 1 ka.

0.3	0	% geomorphic diffusivity (m <sup>2</sup> / ka)
1.3	0	% far-field slope (degrees)
122	0	% age of displaced terrace (ka)
2	0	% number of displacements
1.7	86	% magnitude (meters) and age estimate (ka)
1.8	50	% list each event on a separate row, start with the oldest

Footwall		Hanging Wall		Topography	
Depth (meters)	36Cl (atoms/g)	Depth (meters)	36Cl (atoms/g)	x (meters)	Z (meters)
8.73E-02	1.64E+06	5.38E-03	2.29E+06	-2.00E+01	3.95E+00
1.87E-01	1.52E+06	1.05E-01	2.31E+06	-1.95E+01	3.94E+00
2.87E-01	1.40E+06	2.05E-01	2.15E+06	-1.90E+01	3.92E+00
3.87E-01	1.29E+06	3.05E-01	2.25E+06	-1.85E+01	3.91E+00
4.87E-01	1.19E+06	4.05E-01	2.29E+06	-1.80E+01	3.90E+00
5.87E-01	1.10E+06	5.05E-01	1.90E+06	-1.75E+01	3.88E+00
6.87E-01	1.01E+06	6.05E-01	1.92E+06	-1.70E+01	3.87E+00
7.87E-01	9.36E+05	7.05E-01	1.90E+06	-1.65E+01	3.85E+00
8.87E-01	8.64E+05	8.05E-01	2.21E+06	-1.60E+01	3.83E+00
9.87E-01	7.98E+05	9.05E-01	2.17E+06	-1.55E+01	3.82E+00
1.09E+00	7.36E+05	1.01E+00	2.03E+06	-1.50E+01	3.80E+00
1.19E+00	6.80E+05	1.11E+00	1.93E+06	-1.45E+01	3.78E+00
1.29E+00	6.29E+05	1.21E+00	1.88E+06	-1.40E+01	3.76E+00
1.39E+00	5.81E+05	1.31E+00	1.88E+06	-1.35E+01	3.74E+00
1.49E+00	5.37E+05	1.41E+00	1.75E+06	-1.30E+01	3.71E+00
1.59E+00	4.96E+05	1.51E+00	1.61E+06	-1.25E+01	3.69E+00
1.69E+00	4.59E+05	1.61E+00	1.49E+06	-1.20E+01	3.66E+00
1.79E+00	4.24E+05	1.71E+00	1.37E+06	-1.15E+01	3.63E+00
1.89E+00	3.93E+05	1.81E+00	1.26E+06	-1.10E+01	3.59E+00
1.99E+00	3.63E+05	1.91E+00	1.16E+06	-1.05E+01	3.55E+00
2.09E+00	3.36E+05	2.01E+00	1.07E+06	-1.00E+01	3.51E+00
2.19E+00	3.11E+05	2.11E+00	9.81E+05	-9.50E+00	3.47E+00
2.29E+00	2.88E+05	2.21E+00	9.03E+05	-9.00E+00	3.42E+00
2.39E+00	2.66E+05	2.31E+00	8.31E+05	-8.50E+00	3.36E+00
2.49E+00	2.47E+05	2.41E+00	7.65E+05	-8.00E+00	3.30E+00
2.59E+00	2.28E+05	2.51E+00	7.05E+05	-7.50E+00	3.24E+00
2.69E+00	2.12E+05	2.61E+00	6.49E+05	-7.00E+00	3.17E+00
2.79E+00	1.96E+05	2.71E+00	5.97E+05	-6.50E+00	3.10E+00
2.89E+00	1.81E+05	2.81E+00	5.50E+05	-6.00E+00	3.02E+00
2.99E+00	1.68E+05	2.91E+00	5.07E+05	-5.50E+00	2.93E+00
3.09E+00	1.56E+05	3.01E+00	4.67E+05	-5.00E+00	2.84E+00
3.19E+00	1.44E+05	3.11E+00	4.30E+05	-4.50E+00	2.74E+00
3.29E+00	1.34E+05	3.21E+00	3.97E+05	-4.00E+00	2.64E+00
3.39E+00	1.24E+05	3.31E+00	3.65E+05	-3.50E+00	2.53E+00
3.49E+00	1.15E+05	3.41E+00	3.37E+05	-3.00E+00	2.42E+00
3.59E+00	1.06E+05	3.51E+00	3.11E+05	-2.50E+00	2.31E+00
3.69E+00	9.87E+04	3.61E+00	2.86E+05	-2.00E+00	2.19E+00

## Appendix 8

3.79E+00	9.15E+04	3.71E+00	2.64E+05	-1.50E+00	2.07E+00
3.89E+00	8.49E+04	3.81E+00	2.43E+05	-1.00E+00	1.94E+00
3.99E+00	7.87E+04	3.91E+00	2.25E+05	-5.00E-01	1.82E+00
4.09E+00	7.30E+04	4.01E+00	2.07E+05	0.00E+00	1.69E+00
4.19E+00	6.77E+04	4.11E+00	1.91E+05	5.00E-01	1.57E+00
4.29E+00	6.28E+04	4.21E+00	1.76E+05	1.00E+00	1.45E+00
4.39E+00	5.82E+04	4.31E+00	1.63E+05	1.50E+00	1.32E+00
4.49E+00	5.40E+04	4.41E+00	1.50E+05	2.00E+00	1.21E+00
4.59E+00	5.01E+04	4.51E+00	1.38E+05	2.50E+00	1.09E+00
4.69E+00	4.65E+04	4.61E+00	1.28E+05	3.00E+00	9.79E-01
4.79E+00	4.31E+04	4.71E+00	1.18E+05	3.50E+00	8.72E-01
4.89E+00	4.00E+04	4.81E+00	1.09E+05	4.00E+00	7.70E-01
4.99E+00	3.71E+04	4.91E+00	1.00E+05	4.50E+00	6.73E-01
5.09E+00	3.44E+04	5.01E+00	9.27E+04	5.00E+00	5.81E-01
5.19E+00	3.20E+04	5.11E+00	8.56E+04	5.50E+00	4.95E-01
5.29E+00	2.97E+04	5.21E+00	7.90E+04	6.00E+00	4.15E-01
5.39E+00	2.75E+04	5.31E+00	7.30E+04	6.50E+00	3.40E-01
5.49E+00	2.56E+04	5.41E+00	6.74E+04	7.00E+00	2.71E-01
5.59E+00	2.37E+04	5.51E+00	6.22E+04	7.50E+00	2.07E-01
5.69E+00	2.20E+04	5.61E+00	5.75E+04	8.00E+00	1.48E-01
5.79E+00	2.04E+04	5.71E+00	5.31E+04	8.50E+00	9.44E-02
5.89E+00	1.90E+04	5.81E+00	4.90E+04	9.00E+00	4.50E-02
5.99E+00	1.76E+04	5.91E+00	4.53E+04	9.50E+00	-2.64E-04
6.09E+00	1.64E+04	6.01E+00	4.18E+04	1.00E+01	-4.16E-02
6.19E+00	1.52E+04	6.11E+00	3.86E+04	1.05E+01	-7.93E-02
6.29E+00	1.41E+04	6.21E+00	3.57E+04	1.10E+01	-1.14E-01
6.39E+00	1.31E+04			1.15E+01	-1.45E-01
6.49E+00	1.22E+04			1.20E+01	-1.74E-01
6.59E+00	1.13E+04			1.25E+01	-2.00E-01
6.69E+00	1.05E+04			1.30E+01	-2.25E-01
6.79E+00	9.74E+03			1.35E+01	-2.47E-01
6.89E+00	9.05E+03			1.40E+01	-2.68E-01
6.99E+00	8.40E+03			1.45E+01	-2.88E-01
7.09E+00	7.80E+03			1.50E+01	-3.06E-01
7.19E+00	7.25E+03			1.55E+01	-3.23E-01
				1.60E+01	-3.39E-01
				1.65E+01	-3.55E-01
				1.70E+01	-3.70E-01
				1.75E+01	-3.84E-01
				1.80E+01	-3.98E-01
				1.85E+01	-4.11E-01
				1.90E+01	-4.24E-01
				1.95E+01	-4.37E-01
				2.00E+01	-4.49E-01

Lookup modeled  $^{36}\text{Cl}$  accumulation at sample depths:

Footwall		Hanging Wall	
Depth (meters)	$^{36}\text{Cl}$ (atoms/g)	Depth (meters)	$^{36}\text{Cl}$ (atoms/g)
6.87E-01	1.01E+06	3.05E-01	2.25E+06
9.87E-01	7.98E+05	6.05E-01	1.92E+06
1.69E+00	4.59E+05	1.11E+00	1.93E+06
2.19E+00	3.11E+05	1.61E+00	1.49E+06
2.69E+00	2.12E+05	1.91E+00	1.16E+06
		2.31E+00	8.31E+05
		3.11E+00	4.30E+05

## Difference between modeled and observed:

1.23E+05	-3.85E+05
3.48E+05	-3.78E+05
1.30E+05	1.10E+04
1.14E+05	-3.72E+05
1.69E+05	1.09E+05
	-2.27E+04
	8.83E+04

## Squared Difference:

1.52E+10	1.48E+11
1.21E+11	1.43E+11
1.69E+10	1.20E+08
1.30E+10	1.38E+11
2.86E+10	1.20E+10
	5.16E+08
	7.80E+09

## Chi-square residuals:

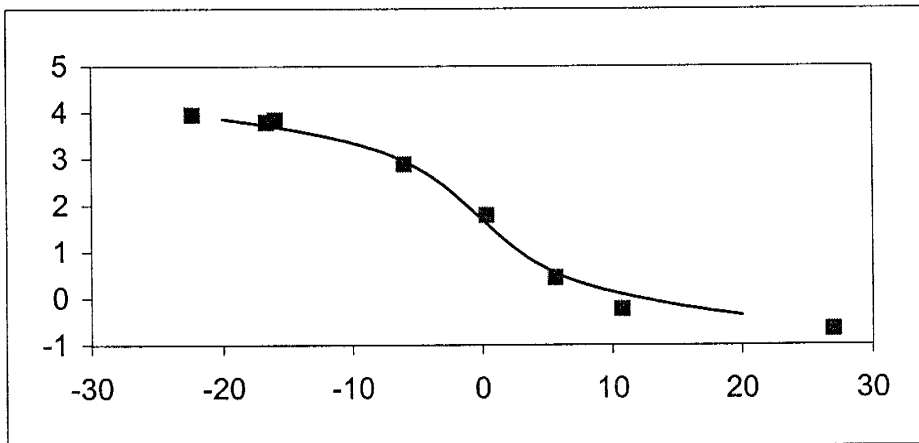
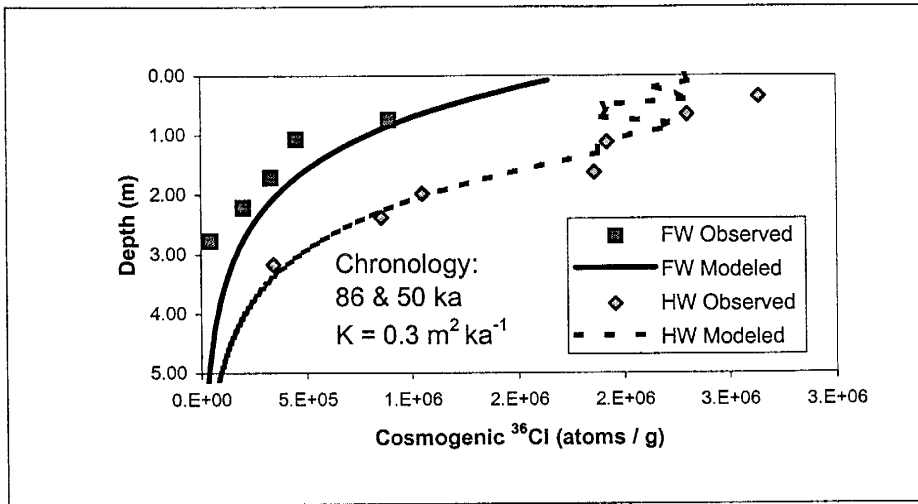
1.50E+04	6.58E+04
1.51E+05	7.43E+04
3.68E+04	6.22E+01
4.18E+04	9.30E+04
1.35E+05	1.03E+04
	6.21E+02
	1.81E+04

## Chi-square value:

3.80E+05	2.62E+05
----------	----------

**Total Chi-square:** 6.43E+05

Appendix 8



## Appendix 8

### Profile 1.5 m from the fault plane

% Fault-scarp parameters, 0 is second column is necessary but meaningless.

% Age estimates need to be to the nearest 1 ka.

0.6	0	% geomorphic diffusivity (m <sup>2</sup> / ka)
1.3	0	% far-field slope (degrees)
122	0	% age of displaced terrace (ka)
2	0	% number of displacements
1.7	70	% magnitude (meters) and age estimate (ka)
1.8	24	% list each event on a separate row, start with the oldest

<b>Footwall</b>		<b>Hanging Wall</b>		<b>Topography</b>	
Depth (meters)	36Cl (atoms/g)	Depth (meters)	36Cl (atoms/g)	x (meters)	Z (meters)
5.87E-02	1.44E+06	4.18E-02	2.18E+06	-2.00E+01	3.93E+00
1.59E-01	1.33E+06	1.42E-01	2.15E+06	-1.95E+01	3.91E+00
2.59E-01	1.22E+06	2.42E-01	1.98E+06	-1.90E+01	3.90E+00
3.59E-01	1.13E+06	3.42E-01	1.61E+06	-1.85E+01	3.88E+00
4.59E-01	1.04E+06	4.42E-01	1.98E+06	-1.80E+01	3.86E+00
5.59E-01	9.57E+05	5.42E-01	1.82E+06	-1.75E+01	3.84E+00
6.59E-01	8.82E+05	6.42E-01	2.59E+06	-1.70E+01	3.83E+00
7.59E-01	8.13E+05	7.42E-01	2.41E+06	-1.65E+01	3.81E+00
8.59E-01	7.50E+05	8.42E-01	2.35E+06	-1.60E+01	3.79E+00
9.59E-01	6.92E+05	9.42E-01	2.25E+06	-1.55E+01	3.77E+00
1.06E+00	6.38E+05	1.04E+00	2.18E+06	-1.50E+01	3.74E+00
1.16E+00	5.89E+05	1.14E+00	2.06E+06	-1.45E+01	3.72E+00
1.26E+00	5.43E+05	1.24E+00	2.05E+06	-1.40E+01	3.69E+00
1.36E+00	5.01E+05	1.34E+00	2.07E+06	-1.35E+01	3.67E+00
1.46E+00	4.63E+05	1.44E+00	1.93E+06	-1.30E+01	3.64E+00
1.56E+00	4.27E+05	1.54E+00	1.79E+06	-1.25E+01	3.61E+00
1.66E+00	3.95E+05	1.64E+00	1.65E+06	-1.20E+01	3.58E+00
1.76E+00	3.65E+05	1.74E+00	1.52E+06	-1.15E+01	3.54E+00
1.86E+00	3.37E+05	1.84E+00	1.40E+06	-1.10E+01	3.50E+00
1.96E+00	3.11E+05	1.94E+00	1.29E+06	-1.05E+01	3.46E+00
2.06E+00	2.87E+05	2.04E+00	1.18E+06	-1.00E+01	3.42E+00
2.16E+00	2.66E+05	2.14E+00	1.09E+06	-9.50E+00	3.38E+00
2.26E+00	2.46E+05	2.24E+00	1.00E+06	-9.00E+00	3.33E+00
2.36E+00	2.27E+05	2.34E+00	9.23E+05	-8.50E+00	3.27E+00
2.46E+00	2.10E+05	2.44E+00	8.50E+05	-8.00E+00	3.21E+00
2.56E+00	1.94E+05	2.54E+00	7.82E+05	-7.50E+00	3.15E+00
2.66E+00	1.79E+05	2.64E+00	7.20E+05	-7.00E+00	3.08E+00
2.76E+00	1.66E+05	2.74E+00	6.63E+05	-6.50E+00	3.01E+00
2.86E+00	1.53E+05	2.84E+00	6.11E+05	-6.00E+00	2.94E+00
2.96E+00	1.42E+05	2.94E+00	5.62E+05	-5.50E+00	2.85E+00
3.06E+00	1.31E+05	3.04E+00	5.18E+05	-5.00E+00	2.77E+00
3.16E+00	1.21E+05	3.14E+00	4.77E+05	-4.50E+00	2.68E+00
3.26E+00	1.12E+05	3.24E+00	4.39E+05	-4.00E+00	2.58E+00
3.36E+00	1.04E+05	3.34E+00	4.05E+05	-3.50E+00	2.48E+00
3.46E+00	9.62E+04	3.44E+00	3.73E+05	-3.00E+00	2.38E+00
3.56E+00	8.91E+04	3.54E+00	3.44E+05	-2.50E+00	2.27E+00
3.66E+00	8.24E+04	3.64E+00	3.17E+05	-2.00E+00	2.16E+00

## Appendix 8

3.76E+00	7.63E+04	3.74E+00	2.92E+05	-1.50E+00	2.05E+00
3.86E+00	7.06E+04	3.84E+00	2.69E+05	-1.00E+00	1.93E+00
3.96E+00	6.54E+04	3.94E+00	2.48E+05	-5.00E-01	1.81E+00
4.06E+00	6.05E+04	4.04E+00	2.29E+05	0.00E+00	1.70E+00
4.16E+00	5.61E+04	4.14E+00	2.11E+05	5.00E-01	1.58E+00
4.26E+00	5.19E+04	4.24E+00	1.94E+05	1.00E+00	1.47E+00
4.36E+00	4.81E+04	4.34E+00	1.79E+05	1.50E+00	1.35E+00
4.46E+00	4.45E+04	4.44E+00	1.65E+05	2.00E+00	1.24E+00
4.56E+00	4.12E+04	4.54E+00	1.52E+05	2.50E+00	1.13E+00
4.66E+00	3.82E+04	4.64E+00	1.40E+05	3.00E+00	1.03E+00
4.76E+00	3.54E+04	4.74E+00	1.29E+05	3.50E+00	9.30E-01
4.86E+00	3.28E+04	4.84E+00	1.19E+05	4.00E+00	8.34E-01
4.96E+00	3.04E+04	4.94E+00	1.10E+05	4.50E+00	7.43E-01
5.06E+00	2.81E+04	5.04E+00	1.02E+05	5.00E+00	6.57E-01
5.16E+00	2.61E+04	5.14E+00	9.37E+04	5.50E+00	5.75E-01
5.26E+00	2.42E+04	5.24E+00	8.65E+04	6.00E+00	4.99E-01
5.36E+00	2.24E+04	5.34E+00	7.98E+04	6.50E+00	4.27E-01
5.46E+00	2.07E+04	5.44E+00	7.36E+04	7.00E+00	3.60E-01
5.56E+00	1.92E+04	5.54E+00	6.79E+04	7.50E+00	2.98E-01
5.66E+00	1.78E+04	5.64E+00	6.27E+04	8.00E+00	2.40E-01
5.76E+00	1.65E+04	5.74E+00	5.78E+04	8.50E+00	1.86E-01
5.86E+00	1.53E+04	5.84E+00	5.34E+04	9.00E+00	1.36E-01
5.96E+00	1.42E+04	5.94E+00	4.93E+04	9.50E+00	8.99E-02
6.06E+00	1.32E+04	6.04E+00	4.55E+04	1.00E+01	4.68E-02
6.16E+00	1.22E+04	6.14E+00	4.20E+04	1.05E+01	6.80E-03
6.26E+00	1.13E+04	6.24E+00	3.87E+04	1.10E+01	-3.04E-02
6.36E+00	1.05E+04			1.15E+01	-6.51E-02
6.46E+00	9.72E+03			1.20E+01	-9.75E-02
6.56E+00	9.02E+03			1.25E+01	-1.28E-01
6.66E+00	8.36E+03			1.30E+01	-1.56E-01
6.76E+00	7.76E+03			1.35E+01	-1.83E-01
6.86E+00	7.19E+03			1.40E+01	-2.08E-01
6.96E+00	6.67E+03			1.45E+01	-2.31E-01
7.06E+00	6.19E+03			1.50E+01	-2.54E-01
7.16E+00	5.74E+03			1.55E+01	-2.75E-01
				1.60E+01	-2.95E-01
				1.65E+01	-3.15E-01
				1.70E+01	-3.33E-01
				1.75E+01	-3.51E-01
				1.80E+01	-3.68E-01
				1.85E+01	-3.84E-01
				1.90E+01	-4.00E-01
				1.95E+01	-4.15E-01
				2.00E+01	-4.30E-01

Lookup modeled <sup>36</sup>Cl accumulation at sample depths:

Footwall		Hanging Wall	
Depth (meters)	<sup>36</sup> Cl (atoms/g)	Depth (meters)	<sup>36</sup> Cl (atoms/g)
6.59E-01	8.82E+05	3.42E-01	1.61E+06
1.06E+00	6.38E+05	6.42E-01	2.59E+06
1.66E+00	3.95E+05	1.04E+00	2.18E+06
2.16E+00	2.66E+05	1.54E+00	1.79E+06
2.76E+00	1.66E+05	1.94E+00	1.29E+06
		2.34E+00	9.23E+05
		3.14E+00	4.77E+05

## Difference between modeled and observed:

-8.71E+03	-1.03E+06
1.88E+05	2.85E+05
6.57E+04	2.59E+05
6.86E+04	-7.14E+04
1.24E+05	2.37E+05
	6.91E+04
	1.35E+05

## Squared Difference:

7.58E+07	1.06E+12
3.53E+10	8.14E+10
4.31E+09	6.69E+10
4.71E+09	5.10E+09
1.53E+10	5.63E+10
	4.77E+09
	1.82E+10

## Chi-square residuals:

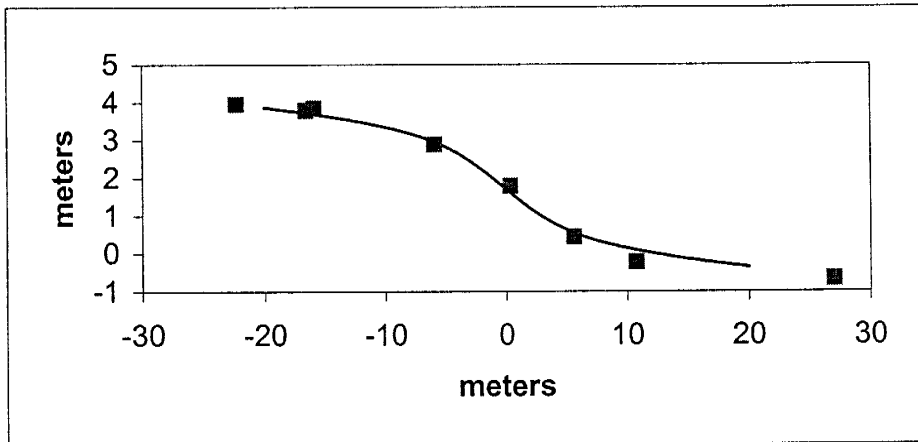
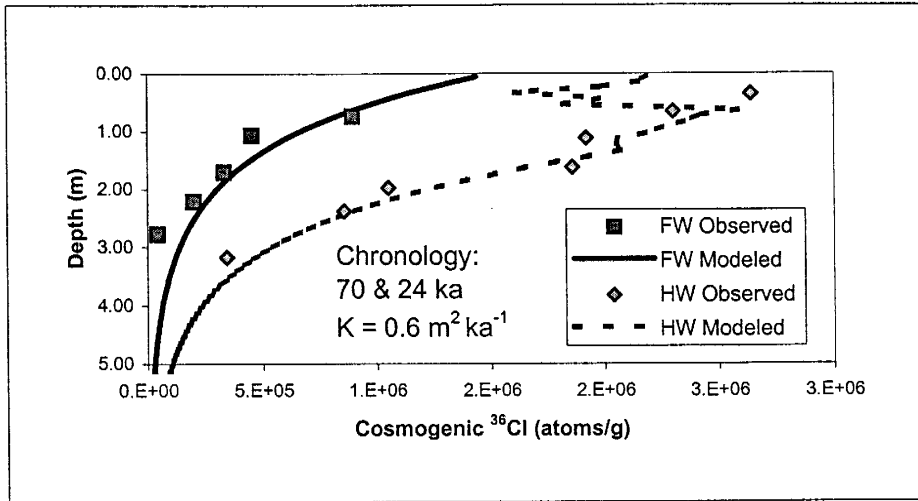
8.59E+01	6.60E+05
5.54E+04	3.15E+04
1.09E+04	3.07E+04
1.77E+04	2.85E+03
9.21E+04	4.38E+04
	5.17E+03
	3.82E+04

## Chi-square value:

1.76E+05	8.13E+05
----------	----------

**Total Chi-square:** 9.89E+05

Appendix 8





Appendix 8

Profile 1.5 m from the fault plane

% Fault-scarp parameters, 0 is second column is necessary but meaningless.

% Age estimates need to be to the nearest 1 ka.

0.7	0	% geomorphic diffusivity (m <sup>2</sup> / ka)
1.3	0	% far-field slope (degrees)
122	0	% age of displaced terrace (ka)
2	0	% number of displacements
1.7	70	% magnitude (meters) and age estimate (ka)
1.8	10	% list each event on a separate row, start with the oldest

<u>Footwall</u>		<u>Hanging Wall</u>		<u>Topography</u>	
<u>Depth</u> <u>(meters)</u>	<u>36Cl</u> <u>(atoms/g)</u>	<u>Depth</u> <u>(meters)</u>	<u>36Cl</u> <u>(atoms/g)</u>	<u>x</u> <u>(meters)</u>	<u>Z</u> <u>(meters)</u>
5.11E-02	1.44E+06	3.06E-02	1.97E+06	-2.00E+01	3.91E+00
1.51E-01	1.33E+06	1.31E-01	1.87E+06	-1.95E+01	3.90E+00
2.51E-01	1.23E+06	2.31E-01	1.77E+06	-1.90E+01	3.88E+00
3.51E-01	1.13E+06	3.31E-01	1.83E+06	-1.85E+01	3.86E+00
4.51E-01	1.04E+06	4.31E-01	1.96E+06	-1.80E+01	3.85E+00
5.51E-01	9.57E+05	5.31E-01	2.62E+06	-1.75E+01	3.83E+00
6.51E-01	8.82E+05	6.31E-01	2.54E+06	-1.70E+01	3.81E+00
7.51E-01	8.13E+05	7.31E-01	2.43E+06	-1.65E+01	3.79E+00
8.51E-01	7.49E+05	8.31E-01	2.34E+06	-1.60E+01	3.77E+00
9.51E-01	6.91E+05	9.31E-01	2.26E+06	-1.55E+01	3.75E+00
1.05E+00	6.37E+05	1.03E+00	2.16E+06	-1.50E+01	3.72E+00
1.15E+00	5.87E+05	1.13E+00	2.12E+06	-1.45E+01	3.70E+00
1.25E+00	5.42E+05	1.23E+00	2.13E+06	-1.40E+01	3.68E+00
1.35E+00	5.00E+05	1.33E+00	1.99E+06	-1.35E+01	3.65E+00
1.45E+00	4.61E+05	1.43E+00	1.84E+06	-1.30E+01	3.63E+00
1.55E+00	4.26E+05	1.53E+00	1.70E+06	-1.25E+01	3.60E+00
1.65E+00	3.93E+05	1.63E+00	1.56E+06	-1.20E+01	3.57E+00
1.75E+00	3.63E+05	1.73E+00	1.44E+06	-1.15E+01	3.54E+00
1.85E+00	3.35E+05	1.83E+00	1.32E+06	-1.10E+01	3.51E+00
1.95E+00	3.09E+05	1.93E+00	1.22E+06	-1.05E+01	3.48E+00
2.05E+00	2.86E+05	2.03E+00	1.12E+06	-1.00E+01	3.44E+00
2.15E+00	2.64E+05	2.13E+00	1.03E+06	-9.50E+00	3.40E+00
2.25E+00	2.44E+05	2.23E+00	9.49E+05	-9.00E+00	3.37E+00
2.35E+00	2.25E+05	2.33E+00	8.73E+05	-8.50E+00	3.32E+00
2.45E+00	2.08E+05	2.43E+00	8.04E+05	-8.00E+00	3.28E+00
2.55E+00	1.92E+05	2.53E+00	7.40E+05	-7.50E+00	3.23E+00
2.65E+00	1.78E+05	2.63E+00	6.81E+05	-7.00E+00	3.17E+00
2.75E+00	1.64E+05	2.73E+00	6.27E+05	-6.50E+00	3.12E+00
2.85E+00	1.52E+05	2.83E+00	5.78E+05	-6.00E+00	3.05E+00
2.95E+00	1.40E+05	2.93E+00	5.32E+05	-5.50E+00	2.98E+00
3.05E+00	1.30E+05	3.03E+00	4.90E+05	-5.00E+00	2.90E+00
3.15E+00	1.20E+05	3.13E+00	4.52E+05	-4.50E+00	2.81E+00
3.25E+00	1.11E+05	3.23E+00	4.16E+05	-4.00E+00	2.72E+00
3.35E+00	1.03E+05	3.33E+00	3.83E+05	-3.50E+00	2.62E+00
3.45E+00	9.49E+04	3.43E+00	3.53E+05	-3.00E+00	2.50E+00
3.55E+00	8.78E+04	3.53E+00	3.25E+05	-2.50E+00	2.38E+00
3.65E+00	8.12E+04	3.63E+00	3.00E+05	-2.00E+00	2.25E+00

## Appendix 8

3.75E+00	7.51E+04	3.73E+00	2.76E+05	-1.50E+00	2.11E+00
3.85E+00	6.95E+04	3.83E+00	2.55E+05	-1.00E+00	1.97E+00
3.95E+00	6.43E+04	3.93E+00	2.35E+05	-5.00E-01	1.83E+00
4.05E+00	5.95E+04	4.03E+00	2.17E+05	0.00E+00	1.68E+00
4.15E+00	5.51E+04	4.13E+00	2.00E+05	5.00E-01	1.54E+00
4.25E+00	5.10E+04	4.23E+00	1.84E+05	1.00E+00	1.40E+00
4.35E+00	4.72E+04	4.33E+00	1.70E+05	1.50E+00	1.26E+00
4.45E+00	4.37E+04	4.43E+00	1.57E+05	2.00E+00	1.13E+00
4.55E+00	4.04E+04	4.53E+00	1.44E+05	2.50E+00	1.01E+00
4.65E+00	3.74E+04	4.63E+00	1.33E+05	3.00E+00	8.96E-01
4.75E+00	3.46E+04	4.73E+00	1.23E+05	3.50E+00	7.92E-01
4.85E+00	3.21E+04	4.83E+00	1.13E+05	4.00E+00	6.96E-01
4.95E+00	2.97E+04	4.93E+00	1.04E+05	4.50E+00	6.10E-01
5.05E+00	2.75E+04	5.03E+00	9.64E+04	5.00E+00	5.31E-01
5.15E+00	2.55E+04	5.13E+00	8.89E+04	5.50E+00	4.60E-01
5.25E+00	2.36E+04	5.23E+00	8.20E+04	6.00E+00	3.95E-01
5.35E+00	2.18E+04	5.33E+00	7.57E+04	6.50E+00	3.37E-01
5.45E+00	2.02E+04	5.43E+00	6.98E+04	7.00E+00	2.83E-01
5.55E+00	1.87E+04	5.53E+00	6.44E+04	7.50E+00	2.34E-01
5.65E+00	1.74E+04	5.63E+00	5.95E+04	8.00E+00	1.88E-01
5.75E+00	1.61E+04	5.73E+00	5.49E+04	8.50E+00	1.46E-01
5.85E+00	1.49E+04	5.83E+00	5.07E+04	9.00E+00	1.07E-01
5.95E+00	1.38E+04	5.93E+00	4.68E+04	9.50E+00	6.97E-02
6.05E+00	1.28E+04	6.03E+00	4.32E+04	1.00E+01	3.49E-02
6.15E+00	1.19E+04	6.13E+00	3.98E+04	1.05E+01	1.88E-03
6.25E+00	1.10E+04			1.10E+01	-2.95E-02
6.35E+00	1.02E+04			1.15E+01	-5.93E-02
6.45E+00	9.43E+03			1.20E+01	-8.79E-02
6.55E+00	8.74E+03			1.25E+01	-1.15E-01
6.65E+00	8.10E+03			1.30E+01	-1.41E-01
6.75E+00	7.51E+03			1.35E+01	-1.66E-01
6.85E+00	6.96E+03			1.40E+01	-1.90E-01
6.95E+00	6.45E+03			1.45E+01	-2.13E-01
7.05E+00	5.98E+03			1.50E+01	-2.36E-01
7.15E+00	5.55E+03			1.55E+01	-2.57E-01
7.25E+00	5.14E+03			1.60E+01	-2.78E-01
				1.65E+01	-2.97E-01
				1.70E+01	-3.17E-01
				1.75E+01	-3.35E-01
				1.80E+01	-3.53E-01
				1.85E+01	-3.70E-01
				1.90E+01	-3.87E-01
				1.95E+01	-4.03E-01
				2.00E+01	-4.19E-01

Lookup modeled <sup>36</sup>Cl accumulation at sample depths:

Footwall		Hanging Wall	
Depth (meters)	<sup>36</sup> Cl (atoms/g)	Depth (meters)	<sup>36</sup> Cl (atoms/g)
6.51E-01	8.82E+05	3.31E-01	1.83E+06
1.05E+00	6.37E+05	6.31E-01	2.54E+06
1.65E+00	3.93E+05	1.03E+00	2.16E+06
2.15E+00	2.64E+05	1.53E+00	1.70E+06
2.75E+00	1.64E+05	1.93E+00	1.22E+06
		2.33E+00	8.73E+05
		3.13E+00	4.52E+05

## Difference between modeled and observed:

-9.13E+03	-8.11E+05
1.87E+05	2.40E+05
6.39E+04	2.41E+05
6.68E+04	-1.63E+05
1.22E+05	1.67E+05
	1.92E+04
	1.10E+05

## Squared Difference:

8.34E+07	6.57E+11
3.49E+10	5.74E+10
4.08E+09	5.79E+10
4.47E+09	2.67E+10
1.49E+10	2.80E+10
	3.68E+08
	1.20E+10

## Chi-square residuals:

9.46E+01	3.59E+05
5.48E+04	2.26E+04
1.04E+04	2.68E+04
1.69E+04	1.58E+04
9.05E+04	2.30E+04
	4.22E+02
	2.66E+04

## Chi-square value:

1.73E+05	4.74E+05
----------	----------

Total Chi-square: 6.47E+05